Copyright is owned by the Author of the thesis. Permission is given for a copy to be downloaded by an individual for the purpose of research and private study only. The thesis may not be reproduced elsewhere without the permission of the Author.

Understanding the provenance and trigger mechanisms of lahars at Mt. Ruapehu, NZ to construct new hazard analysis approaches.

A thesis presented in partial fulfilment of the requirements for the degree of

Doctor of Philosophy

In

Earth Science

at Massey University, Palmerston North, New Zealand

Brian Kai Perttu

2025





Abstract

Lahars (volcanic flows of mixed water and sediment) represent one of the most frequent and significant volcanic hazard at Mt. Ruapehu, New Zealand. However, modern hazard assessments primarily rely on short historical records (≤150 yr) despite the prehistoric record containing events that are orders of magnitude larger than those observed historically. This study addresses key knowledge gaps by integrating advanced stratigraphic and sedimentological understanding of the depositional characterics of historic and modern deposits, spectral geochemistry to determine the provenance and triggers of the flows, and numerical modelling to better understand the source conditions of lahars to refine the late Holocene lahar history (approximately the last 2,000 years) of Ruapehu, ultimately improving hazard risk assessment.

The research focused initially on the Onetapu Formation on the eastern ring plain, involving a reassessment of lahar deposition to refine stratigraphy and define the relationships between discrete deposits. Detailed grain-size and lithofacies analyses were used to characterize deposits and revealed evidence of downstream debulking and contributions from the Wahianoa catchment following the 232 CE Taupo Ignimbrite emplacement.

A key methodological contribution to better understand the provenance and triggers of lahars was the development of a multi-criteria analytical approach, employing Short-Wave Infrared Reflectance (SWIR) spectroscopy supported by X-ray fluorescence (XRF), to successfully "fingerprint" lahar provenance and infer triggering mechanisms. SWIR proved capable of resolving hydrothermal alteration signatures (e.g., smectite and kaolinite) at abundances below the detection limits of bulk X-ray diffraction (XRD) methods, offering a sensitive, globally applicable forensic toolset for distinguishing flow origins.

Complementary numerical simulations investigated the dynamics of Crater Lake eruption-induced waves, a frequent lahar trigger. Modelling underwater explosions using different cavity

size formulations demonstrated that even individually small, bore-generating eruptions can rapidly escalate lahar hazard through cumulative lake drainage, particularly within Ruapehu's multi-phase eruptive sequences.

The integrated results produce the most comprehensive analysis of Ruapehu's late Holocene lahar record to date. This work highlights the critical need for next-generation multi-trigger probabilistic models that explicitly account for changing physical conditions, such as lake volume, rainfall, eruptive state, and sediment availability, to provide more accurate evaluations of expected flow size and downstream impact for hazard management at Ruapehu and other lahar-prone volcanoes

Acknowledgements

This thesis was funded through the *Resilience to Nature's Challenges Āhea riri ai ngā maunga puia? (When will our volcanoes become angry?)* programme.

This thesis wouldn't have been possible without the support of Ngāti Rangi for access and sample collection, and especially Keith Wood at Karioi Forest for extensive help with logistics and pointing out fresh excavations.

My supervisory committee:

Thanks to Graham Leonard who helped shape some of the big ideas, arranging geochemical analysis with Matthew Hill (thanks as well!) at GNS Avalon, and introducing me to so many people in Geneva.

Thanks to Mark Bebbington for setting up the statistical modelling, explaining when (and when not) to use equations, as well as using lost luggage to explain Bayesian event trees.

Thanks to Anke Zernack for confirming and improving my interpretation of the Onetapu deposits on a great field day as well as thorough manuscript reviews.

Thanks to Stuart Mead for helping with all the setup on my modelling runs as well as being the only one to check the QR code.

Jon Procter, without your guidance I'd have never gotten out of the swamp at Dagobah. Metaphorically. And the trips, field work, and conversations in the car were all great, thank you.

Thank you Dr. Katy Hodgson, your commentary on papers and guidance in the field was what made the haze of data and ideas finally coalesce. I hope we can make it out to Rangipo one day.

Thank you to Anja Moebis for all the help on leachate, wet sieving, XRF, and everything lab related. Thanks to Gabor Kereszturi for the field and ASD help as well as geochemical data. Thank you Melody Whitehead for statistics guidance and initial paper reviews. Thanks to Matt Irwin for everything around the department, and on that note, thanks to Shannen Mills for general help on just about everything, especially when I first got here. Thanks to Matty Hayward for troubleshooting his Basilisk setup. Thanks to Joseph Fleming for stuff. Mike Smith, thank you for helping me feel like a little less of a foreigner here.

Thank you to Carol Stewart and David Johnston for being wonderful friends, David is greatly missed.

Thanks to Janine Krippner for being a fantastic scale for field photos, a great friend, and for bringing us into your family for holidays.

Un grand merci à Juliette, Jeff, Sam et Paul, and thanks to Rae, James, Dan, Carlos, Silvia, Nimeshika, Ermanno, Mustafa, Courtney, Tamsin, and Maia.

Anna Perttu, you've kept me going, so I'll thank you in the way you'll appreciate the most: cheese. I love you and can't wait to see what's next.

Table of Contents

Abstract i
Acknowledgements i
Table of Contents i
List of Figures iii
List of Tables vii

1 Introduction 1

1.1 Summary 1
1.2 Literature review 2
1.2.1 Lahars 2
1.2.2 Triggering mechanisms 4
1.2.3 Lahar Rheology 5
1.2.4 Flow Indicators and Sedimentological Signatures 7
1.2.5 Edifice Alteration, Mass Wasting Transformations, and Lahars 11
1.3 Geological background 13
1.3.1 Regional geology 13
1.3.2 Mount Ruapehu 16
1.3.2.1 Ring plain stratigraphy 17
1.3.2.2 Major Effusive Formations 20
1.3.2.2.1 Te Herenga Formation 20
1.3.2.2.2 Wahianoa Formation 21
1.3.2.2.3 Mangawhero Formation 21
1.3.2.2.4 Whakapapa Formation 21
1.3.2.3 Tephrostratigraphy and Marker Beds 21
1.3.2.3.1 Bullot Formation 22
1.3.2.3.2 Papakai Formation 22
1.3.2.3.3 Tufa Trig Formation 22
1.3.2.3.4 Ngauruhoe Formation 22
1.3.2.3.5 Taurewa Formation: Pourahu Member 23
1.3.2.4 Volcaniclastic formations 23
1.3.2.4.1 Sector collapse formations 23
1.3.2.4.1.1 Murimotu formation 23
1.3.2.4.1.2 Mangaio formation 23
1.3.2.4.2 Lahar formations 23
1.3.2.4.2.1 Te Heuheu 24
1.3.2.4.2.2 Tangatu Formation 24
1.3.2.4.2.3 Manutahi Formation 24
1.3.2.4.2.4 The Modern and Historical Onetapu Formation 24
1.4 Contemporary Lahar Hazards at Ruapehu 25
1.4.1 Infrastructure and Downstream Exposure 25
1.4.2 Monitoring Systems and Hazard Mitigation 26
1.4.3 Hazard Assessment and Forecasting Challenges 26
1.4.4 The Importance of the Geological Record for Modern Hazard Planning 30
1.5 Knowledge Gaps in Lahar Research at Ruapehu 31
1.5.1 Limited understanding of large-magnitude prehistoric lahars 31
1.5.2 Poorly resolved trigger mechanisms for prehistoric flows 31
1.5.3 Limited understanding of prehistoric Crater Lake eruptions 32
1.5.4 No probabilistic or magnitude-frequency model integrating geological and historical data 32
1.6 Thesis Objectives 32
1.7 Thesis structure 33

2 Deciphering Lahar Stratigraphy and Sedimentology on the Eastern Ring Plain of Mt. Ruapehu, New Zealand: New Insights from the Onetapu Formation 36

2.1 Abstract **37**
2.2 Introduction **37**
2.2.1 Regional setting 41
2.2.2 Background 41
2.2.3 Onetapu Formation 42
2.3 Methodology **49**
2.3.1 Lithofacies Designations 49
2.3.2 Grain-size analysis 53
2.4 Results and Findings **56**
2.4.1 Stratigraphy and Unit Correlation 56
2.4.2 Sedimentary Characteristics and Facies Analysis 65
2.5 Discussion **68**
2.5.1 Karioi lahars (interpretation of newly identified units) 69
2.5.2 Interplay with large rhyolitic eruptions and ignimbrites from neighbouring calderas 70
2.5.3 Deposit sedimentology and lithology 72
2.5.4 Trigger mechanisms 75
2.6 Conclusions **77**

3 Geochemical and spectral techniques for lahar fingerprinting at Mt. Ruapehu: Improving assessment of triggering mechanisms and provenance 80

3.1 Abstract **80**
3.2 Introduction **81**
3.2.1 Geological setting 85
3.2.2 Mineralogical and Spectral Techniques on Lahars 87
3.3 Methods **89**
3.3.1 Field sampling 90
3.3.2 X-ray fluorescence 91
3.3.3 VNIR & SWIR 93
3.3.4 XRD 94
3.4 Results and interpretations **94**
3.4.1 X-ray fluorescence and x-ray diffraction 94
3.4.2 VNIR & SWIR 100
3.5 Discussion **110**
3.5.1 Triggers 110
3.5.2 Fingerprints 113
3.5.3 Refining the lahar record 114
3.5.4 Applicability of methods 116
3.6 Conclusions **117**

4 Numerical modelling of eruption induced waves in Mt. Ruapehu's Crater Lake: Implications for lahar hazard models 120

4.1 Abstract **120**
4.2 Introduction **121**
4.2.1 Mt. Ruapehu 122
4.2.2 Crater lake eruptions 123
4.3 Methodology **124**
4.3.1 Underwater explosions 124
4.4 Modeling **128**
4.4.1 Numerical Model Setup 128
4.4.2 Model Domain and Resolution 129
4.4.3 Bathymetry and Initial Conditions 130
4.4.4 Explosion Parameter Definition 132
4.4.5 Data Collection and Analysis 133
4.5 Results and Findings **135**
4.6 Discussion **139**
4.6.1 Predictive hazard application of model 144

4.7 Conclusions 146
5 A new approach to lahar hazard assessment 148
5.1 Introduction 148
5.2 Lahar Frequency and Probability 150
5.3 Ruapehu Trigger Mechanisms and Dependencies 156
5.4 Magnitude-Frequency and Global Analog Comparisons 159
5.5 Hazard Implications 169
5.6 Conclusions 172
6 Conclusion 174
6.1 Objective (1) reassessing lahar deposits and revising stratigraphic relationships 174
6.2 Objectives (2 & 3) characterising these deposits and inferring triggering mechanisms 174
6.3 Objective (4) modelling typical Crater Lake eruption triggered lahar generation 175
6.4 Objective (5) synthesising these findings into a preliminary multi-trigger probabilistic model 176
6.5 Future work 176
6.5.1 Opportunistic field mapping to address preservation bias: 176
6.5.2 Quantify low abundance clay minerals using SWIR: 176
6.5.3 Link Crater Lake outflow to downstream lahar dynamics: 177
6.5.4 Develop and validate multi-trigger probabilistic model: 177
7 References 178
Appendix A 197
Appendix A1 Field sites, sample locations, and stratigraphic columns (.pptx) 197
Appendix A2 Weight size categories (.csv) 197
Appendix A3 Gradistat sample analysis results (.csv) 197
Appendix B 197
Appendix B1 XRD analysis spectra (.rasx) 197
Appendix B2 Individual sample SWIR spectra and sample matrix spectral angle similarity table (.csv) 197
Appendix B3 Leachate analysis results (.xlsx) 197
Appendix C 197
Appendix C1 Example Basilisk code (.c) 197
Appendix D 197
Appendix D1 Lahar events table (.xlsx) 197
Appendix E 197
Appendix E1 Statement of Contribution forms (.pdf) 197

List of Figures

Figure 1.1 Classification of mass movements on steep slopes as a function of solid fraction and material type. After Coussot and Meunier (1996). 4
Figure 1.2 Classification of sediment-laden flows based on shear strength and sediment concentration. After Costa (1988). 6
Figure 1.3 Examples of flow indicators and representative outcrop photos. A: Four common ripple mark textures (Boggs, 2009), B: longitudinal bars on the Whangaehu River, C: schematic of imbricated clasts (Boggs, 2009), D : cross bedding in sandstone with coin for scale (Boggs, 2009), E: terracing (Pierson, 2005a) F: Rain-triggered volcanic debris flow deposit (Pierson et al., 2025), G: Clay-poor volcanic debris flow deposit with trenching tool for scale (Pierson et al. 2025), H: Lower gray volcanic hyperconcentrated flow deposit and upper brown volcanic debris flow deposit (Pierson et al. 2025), I: Progressively coarsening volcanic hyperconcentrated flow deposit (Pierson et al., 2025), J: Plane-

parallel-bedded channel facies volcanic water flood deposit with pocket knife for scale (Pierson et al., 2025), K: Channel facies volcanic water flood deposit with trenching tool for scale (Pierson et al., 2025). 10
Figure 1.4 Location of Mt. Ruapehu (center) with fault lines from Earth Science New Zealand (Langridge et al., 2016), with inset showing Hikurangi-Kermadec subduction zone, Taupo Volcanic Zone, and major andesitic volcanoes. 14
Figure 1.5 Simplified timeline of modern eruptive and lahar units on the eastern Ruapehu ring plain. Tufa Trig nomenclature and dates from Voloschina (2020) with italicized names from Donoghue (1991) and Donoghue & Neall (2001), Onetapu Formation units and dates from Hodgson et al. (2007) with older nomenclature superscripts as cited by Hodgson et al. (2007): H Hodgson (1993), C97 Cronin et al. (1997b), D Donoghue (1991) & Donoghue & Neall (2001), and as cited by Hodgson (1993): C73 Campbell (1973), P Purves (1990). Trigger information simplified (Chapter 5) from Hodgson et al. (2007) and Lecointre et al. (2004). 18
Figure 1.6 Lithostratigraphy of Southeast Mt. Ruapehu ring plain lahar deposits (Hodgson, 1993). 19
Figure 1.7 Geological sketch map of Mt. Ruapehu's major effusive formations, after Hackett & Houghton, 1989. 20
Figure 1.8 Lahar hazard map from Neall et al. (1999). 28
Figure 1.9 Lahar hazard map from Neall et al. (2004). 29
Figure 2.1 Schematic representation of deposit facies resulting from the longitudinal transformation of a lahar. M_Z is mean grain size, σ_G is sorting, and C is concentration of sediment. Size units are in phi scale and categories are calculated after Folk (1965). Manville et al. (2013) after Pierson and Scott (1985). 38
Figure 2.2 Classification of sediment-laden flows based on shear strength and sediment concentration. Increases in smectite (swelling) clay volume have a much more pronounced contribution to rheology changes than similar volumes of kaolinite clays. After Costa (1988). 39
Figure 2.3 Comparison of particle size distributions of the upper 1 meter of the active flow and a marginal sediment deposit taken from an Onetapu e6 lahar 42 km downstream, near site 10 (this study). Size units are in phi scale and categories are calculated after Folk (1980). After Cronin et al. (2000). 39
Figure 2.4 A) Overview map of the North Island, New Zealand Mt. Ruapehu shown in relation to the Taupo Volcanic Zone and Hikurangi Subduction Zone. B) View of Mt. Ruapehu from the south, with the Karioi Forest in the foreground, Tangiwai is in the center-right, and the Whangaehu River in the lower right. C) 1969 Crown Survey 2192 (LINZ, 2015) DSM oblique view northwest of Whangaehu River (blue) and Rangipo Desert/fan (red), with Karioi Forest in the lower center and Wahianoa Valley mid-right D) Schematic stratigraphic section of Onetapu Formation units combining descriptions from Hodgson et al. (2007)(Table 2.1) and field relations observed in this study, plotted against eruptive deposits (Voloschina, 2020), with dates of observed deposits and upper and lower bounding radiocarbon dates: [HE]Hodgson et al. (2007), [DE]Donoghue et al. (1995), [D]Donoghue (1991), [C]Campbell (1973), [H]Hodgson (1993), [F]Froggatt & Lowe (1990). 43
Figure 2.5 Reference sites along the Whangaehu and Wahianoa rivers. Solid colored triangles are where stratigraphic columns were logged and samples were selected, hollow circles are surveyed sites that were visited to check presence of Taupo Ignimbrite and any subsequent deposits. Map projection is New Zealand Transverse Mercator 2000, the regional map is NZ 8m Digital Elevation Model (2012) from LINZ Data Service. Location map is a 1 meter photogrammetric DSM from LINZ historical aerial imagery flown in 2000 and 2003. 54
Figure 2.6 Mapped extent of Onetapu lahar deposits associated with the Wahianoa catchment. Lahar extents were observed from current stream exposures and Karioi Forest road sediment traps and inferred from satellite imagery. Moraine extents are generalized from field observations. Map projection is New Zealand Transverse Mercator 2000, the regional map is NZ 8m Digital Elevation Model (2012) from LINZ Data Service. Location map is a 1 meter photogrammetric DSM from LINZ historical aerial imagery flown in 2000 and 2003. 56
Figure 2.7 Example stratigraphic column with grain sizes, composition, field observations, and sieving results of sampled sections. Field grain size estimates were divided into <fine sand, fine sand, medium sand, coarse sand, and gravel with no upper size limit. Composition was noted based on

lith code analysis of clasts and matrix where applicable. Samples were sieved in full ϕ increments from maximum grain size to 1.5 ϕ, in 0.5 ϕ increments from 1.5ϕ to 4.0ϕ, inclusive, and sizes smaller than 4.0ϕ were determined by laser particle grain sizing. 57
Figure 2.8 Stratigraphy at reference sites along the Whangaehu and Wahianoa catchments. Unit colors are derived from field photos, diagnostic textures are approximated using USGS swatches (U.S. Geological Survey, 2006) for reproducibility, inferred trigger mechanisms are indicated by L: Lake Outbreak, E: Eruption-Crater Lake, R: Remobilised, M: Mass-wasting. Links between columns are shaded where units are readily identifiable via stratigraphic correlations or past studies. Sites 10a and 13a were not sampled, but stratigraphic correlations were logged. Site 10a (Fig. 2.10c) is the Whangaehu cut bank closest to site 10. Site 13a is an exposed track cutting next to an access road ~400 m downstream from site 13. 60
Figure 2.9 Onetapu Formation stratigraphy and radiocarbon dates from Hodgson et al. (2007). Stars mark radiocarbon date localities. Solid lines mark confident correlations between units; dashed lines mark tentative correlations. Column 1 was near site 5 (Fig. 2.5), column 2 was from river exposures between sites 8 and 10 (Fig. 2.5), column 3 was from exposures near site 14 (Fig. 2.5), column 4 is site 16 (Fig. 2.5)..... 61
Figure 2.10 Selected representative site photos with code descriptors for logged units. Thicknesses are the same as marked sites from Fig. 2.8. (A) Site 16 (Fig. 2.5) has sequence of Onetapu C hyperconcentrated flow deposits with a sequence of Onetapu D debris flow and hyperconcentrated flow deposits on top. (B) Site 15 (fig. 2.4) has Onetapu E3 hyperconcentrated flow deposits that underwent soft sediment deformation with the underlying soil layer, Onetapu E4 inversely graded hyperconcentrated flow deposits, and Onetapu E6 & E7 hyperconcentrated flow deposits. (C) Site 10a (fig. 2.4) has deposits of Onetapu A, B, C, and D over a thin layer of Taupo, approximately 4 meters above current river level. (D) Site 8 (fig. 2.4) has thin deposits of Onetapu A and B, and thicker layers of Onetapu C and D. (E) Site 4 (fig. 2.4) ~2 meters above current river level rounded to sub-angular clast supported boulders in Onetapu A overlie Taupo deposits. (F) Site 2 (fig. 2.4) Onetapu deposits overlie sequences of tephra and older lahar units. (G) KFB (fig. 2.4) a similar sequence to site 2 with older lahar units under pre-Taupo and Taupo deposits. (H) Site 19 (Fig. 2.5) Onetapu hyperconcentrated flow units (~1.6 m) and reworked Taupo ash and pumice (~5 m) overlie Taupo deposits 300 m up a tributary from the Whangaehu..... 62
Figure 2.11Reference site 1 on the upper Wahianoa, showing a sequence of events from the Taupo ash to several subsequent lahars. Pre-Taupo deposit, Taupo deposit, and Onetapu lahar are labelled, and the intermediate sequence is numbered based on interpreted order of events..... 65
Figure 2.12 Sedimentary deposit codes and dominant lithological types at selected sites. Lithological componentry was estimated (Terry & Chilingar, 1955) based on gravel size fractions, where available, or the coarsest sand fractions otherwise. Units of indeterminate age were assigned ''undiff'' as undifferentiated and plotted across the age ranges inferred from their stratigraphic relationships, sedimentary deposit types, and lithological componentry. Trigger mechanisms have been assigned after Hodgson et al. (2007). 71
Figure 3.1 Location map of samples and logged sections along Whangaehu and Wahianoa river drainages off Mt. Ruapehu. 84
Figure 3.2 Flow chart of methods applied. 93
Figure 3.3 TAS diagram of composition of samples (purple) excluding ≥5% LOI, Taupo pumice layers plotted as light blue. Plotted against whole rock major element data from Conway et al. (2016) WH: Whakapapa Formation, MA: Mangawhero Formation, WA: Wahianoa Formation, TH: Te Herenga Formation. 96
Figure 3.4 SiO_2 vs K_2O of major chronostratigraphic lava formations (Conway et al., 2018) and lahar units (Hodgson et al., 2007). Whakapapa formation (<15 ka) are red circles, Mangawhero formation (50 – 15 ka) are red squares, Wahianoa formation (160-80 ka) are red diamonds, Te Herenga formation (200-150 ka) are red triangles. Onetapu formation members are all represented by circles, with Onetapu A (>1530 ± 160 BP - <1850 BP) light green, Onetapu B (<1640 ± 60 yr BP - >1271 ± 56 yr BP) lavender, Onetapu C (<1271 ± 56 yr BP - >890 ± 50 yr BP) black, Onetapu D (<890 ± 50 yr BP- >380 ±

60 yr BP), and Onetapu E3 as pale blue, E4 as forest green, E6 as ochre, and E7 as violet (1861AD, 1953AD, 1995AD, 2007AD respectively)..... 98
Figure 3.5 XRD mineral phases in lahar matrix samples. Samples are dominated by plagiclase (orange) and clinopyroxene (purple). Other common mineral phases are quartz (dark blue), orthopyroxene (light blue), magnetite/spinel (grey-blue), kspar (dark green), and a broad peak alternatively identified as cristobalite or opal (green and violet, respectively). Onetapu C Tangiwai Swamp samples (TS) are TS2BSU and TS2BSB, Onetapu B Tangiwai Swamp (TS) samples are TS2SDT, TS2SDM, TS2SDB, Onetapu D Tangiwai Swamp (TS) samples are TS23, TS22, TS21, Onetapu C Marae Bridge Quarry (MQ) samples are MQE, MQC, and MQA..... 99
Figure 3.6 Pie charts of clay mineral assemblages progressing upstream. Sites duplicated in this study are: I = MQ, II = TS2, III = PON. After Hodgson et al. (2007) 100
Figure 3.7 Continuum removed SWIR spectra of >5% LOI lahar matrix (blue) vs. <5% LOI lahar matrix (red) showing comparitively greater absorption in the 1410 nm band, and much greater absobption in the 1910 nm band..... 101
Figure 3.8 Combined continuum removed 1300 – 2500 nm subset spectra of (a) matrix material (<4ϕ) and (b) clast material (>1.5 ϕ) of all samples. Individual spectra are plotted along with a mean line (red) and a blue ribbon representing one standard deviation. Gray bars and dashed lines at 1410 – 1450 nm, 1920 nm, and 2180 – 2400 nm are general absorption features of phyllosilicate minerals..... 102
Figure 3.9 Comparison of 1300 nm to 2500 nm subset of continuum removed spectra for clasts vs matrix from the same lahar unit and relative location within the column at two sampling sites. Blue line is matrix reflectance, pink line is clast reflectance, where pink shaded areas indicate where clasts have relatively greater absorption features (greater abundance), and blue shaded areas indicate where matrix has relatively greater absorption features (greater abundance). Black vertical lines are smectite absorption peaks, grey vertical lines and areas are kaolinite absorption peaks, and orange vertical lines are alunite absorption peaks. 103
Figure 3.10 Spectral angle mapping matches of matrix and clast samples with spectral database entries for pure samples with top 5 closest matches displayed. Reference samples (Kokaly et al. 2017) for montmorillonite (a & c) and kaolinite (b & d) are graphed against the top five best 350 nm to 2500 nm (fine, a & b) and 1300 nm to 2500 nm (coarse, c & d) continuum removed spectra spectral angle matches. 106
Figure 3.11 Spectral angle similarity distance heatmap, red showing greater similarity. Similarity clusters are denoted by dendrograms. 107
Figure 4.1 Overview map of the location of Mt. Ruapehu in North Island, New Zealand (left), with a 1969 Crown Survey 2192 (LINZ, 2015) DSM oblique view northwest of Mt. Ruapehu edifice (right) with the Crater lake visible in the upper-middle section..... 123
Figure 4.2 Graphical representation of subaqueous explosion parameters. (a) An explosion of yield E at depth z in a water column of depth h. (b) The initial surface elevation given by the parabolic equation. (c) The initial surface elevation given by the quadric equation. After Hayward et al. (2022). 126
Figure 4.3 Bathymetry and hillshade topopgraphy of Mt. Ruapehu's summit Crater Lake that was the basis for numerical simulations. Bathymetry contours are displayed in 6 meter increments with the outlet on the southern edge. Hillshade DEM is modified from Horizons LIDAR imagery, with raised topography on areas outside the Crater Lake basin to reduce computational load and numerical instabilities due to water level effects. Crater Lake bathymetry was unpublished data from Christenson (2012) as cited in, and digitized from, Ching (2022)..... 131
Figure 4.4 Numerical model gauge locations on Crater Lake outlet. 134
Figure 4.5 Mid-saddle gauges used for calculations from an example 30 meter cavity from an explosion from the west vent (star), 70 meters depth, water height 30 cm below outflow level, using a parabolic solver, along with gauge timeseries from gauges A3-E3, top to bottom, and a maximum height free surface plot (etamax). 135
Figure 4.6 Time series comparison of waves arriving at gauge C1 located on the crater lake surface near the outlet channel. Vent locations are organized by row (Center, Center North, North, West, East from top to bottom) and initial cavity radii are organized by column (10, 15, 17, 20, 30 meters) with

colors corresponding to initial water level and solver (Red - -1.3m, parabolic, Green - -30cm, parabolic, Blue - -1.3m quadric, Purple - -30cm quadric). 137
Figure 4.7 Cumulative outflow volume through the outflow channel of crater lake calculated from a simulated gauge transect across the scoured outlet and using a broad crested weir approximation. Water levels were 1.3 meters below the outflow (left half of the figure) and 30 cm below the outflow (right half of the figure), with each line corresponding to modelled vent location (Center, Center North, East, North, West) from top to bottom, and progressively greater cavity radii (10, 15, 17, 20, and 30 m at both water levels) as well as results from both solvers (quadric – purple, parabolic – yellow). Unrealistic and failed simulations were excluded. 138
Figure 4.8 Conceptual sketch cross section Crater Lake through the Whangaehu outlet and central vent and an approximate location of the east vent. A: The glaciated Crater Lake at maximum fill with (1) Paretetaitonga and (2) the Dome in the background, with active vent locations indicated by (3) sulfur rafts. The (4) outlet is on the far left side. B: Disturbances through a full lake with a (5) shallow depth class explosion forming a parabolic bore, and a (6) quadric bore formed after a (7) deep depth class explosion reaches the surface. C: Disturbances through the Crater Lake with a (8) lowered water level resulting in change in depth class and increase in wave generation efficacy. (9) Approximate initial cavity sizes tested were 10m and 30m, with varying energy inputs required with changing depth, and a comparative upper size limit of explosive cavities in the 1995-1996 eruptive sequence. 140
Figure 5.1 Jittered graph of lahar events recorded from analogue volcanoes: Cotopaxi, Kelud, Mayon, Merapi, Nevado del Ruiz, Pinatubo, Ruapehu, and Villarrica. Triggers are represented as colours and magnitudes as sizes of individual events. Of note are paucity of mass wasting triggered events and increasing completeness of event identification, in addition to trigger variety and predominance across volcanoes 168

List of Tables

Table 1.2 Characteristics of deposits associated with debris flows and hyperconcentrated flows. Modified from Pierson (2005a) and Pierson et al. (2025), with additional information from Costa (1988); Cronin et al., (2000); Manville et al. (2005), Pierson (2005b); and Smith (1986). 11
Table 2.1 Onetapu Formation lithostratigraphic assemblages, naming correlations, volumes, estimated ages, notable characteristics, and interpreted trigger mechanism. Rows are shaded based on common assemblages. Modified from Hodgson et al., 2007 45
Table 2.2 Grainsize characteristics of Onetapu deposits by distance (Appendix A2 & A3). Units are listed by site, bottom to top. Distances are in kilometers from the catchment source, where Whangaehu is default and Wahianoa derived deposits are noted with [A]. Units are subdivided into members where known, and left blank if undifferentiated. Units with unknown associations were left blank. SP indicates stratigraphic position of the sample within the unit: Base, Middle, Top, or Entire. 58
Table 3.1 Sample locations and naming conventions 90
Table 3.2 Total Major element analyses. Oxides are expressed as weight percentages. Sample locations are given in Table 3.1 95
Table 3.3 Spectral similarity clusters, including individual members and group numbers for identification. 108
Table 4.1 Mt. Ruapehu Crater Lake vent locations use for wave simulations in NZTM coordinates with approximate depth below current lake level. 132
Table 5.1 Record of lahars from Ruapehu volcano that have primarily affected the Whangaehu River (after Mead et al., 2021). 150
Table 5.2 Condensed summary of documented lahar events at selected volcanoes, organized by period, trigger, and flow type. Events of similar magnitude, trigger, and character occurring within the same year or over extended decades have been merged for brevity. Full event listings, including all individual occurrences and source details, are provided in the appendix (Appendix D1). 159
Table 5.3 Total recorded lahars per trigger at each analogue volcano. 163

Table 5.4 Representative magnitude divisions for lahar events at selected volcanoes, following divisions in Mead et al. (2021) for Ruapehu to facilitate inter-volcano comparison. Magnitude thresholds and measurement methods vary among volcanoes and are based on published quantitative values assigned to qualitative records where available. Values represent approximate ranges of event size. 165

1 Introduction

1.1 Summary

Lahars, volcanic flows of mixed water and sediment, are among the most frequent, destructive, and globally widespread volcanic hazards (Manville et al., 2013; Pierson et al., 2025; Vallance, 2005). Their impacts range from localized flooding to valley-filling debris flows capable of burying towns, destroying roads and bridges, and causing large loss of life, as exemplified by historic disasters at Nevado del Ruiz (Pierson et al., 1990), Pinatubo (Newhall and Punongbayan, 1996), and Mount St. Helens (Janda et al., 1981).

Lahar formation requires water, unconsolidated debris, sufficient gradients, and a triggering mechanism (Vallance and Iverson, 2015). These flows occupy a spectrum from dilute, turbulent hyperconcentrated flows to concentrated, non-Newtonian debris flows, reflecting contrasts in sediment concentration, rheology, and depositional processes (Beverage and Culbertson, 1964; Pierson and Costa, 1987).

At Mount Ruapehu, lahars are particularly frequent due to the presence of a warm, acidic Crater Lake above the active vent, a feature that makes Ruapehu one of the most lahar-prone volcanoes in the world (Hodgson, 1993; Hodgson et al., 2007; Lecointre et al., 2004). Over the last ~2 ky, Crater Lake related processes have dominated lahar generation, producing a rich and remarkably continuous lahar record that is preserved in the Onetapu Formation. This stratigraphic archive contains dozens of flow units produced by diverse triggers, including eruptive lake water ejection, crater-rim failure, snow/ice melt, rainfall remobilisation, and possible flank collapse (Cronin et al., 1997b; Donoghue and Neall, 2001; Hodgson et al., 2007; Lecointre et al., 2004).

Despite extensive research, major gaps remain in understanding the mechanics, triggering processes, sedimentology, provenance, and hazard implications of Ruapehu lahars. These gaps are particularly important because the prehistoric record contains events far larger than those observed historically (Lecointre et al., 2004; Procter et al., 2021). Modern hazard assessments and monitoring systems still rely heavily on short (≤150 yr) historical windows and qualitative scenario modelling, often ignoring such crucial longer-term records.

This thesis addresses these gaps by integrating sedimentology, stratigraphy, geochemistry, and spectral analysis with hazard modelling to refine the understanding of the 2 ky lahar history of Ruapehu. This chapter provides the necessary conceptual and contextual foundation by reviewing lahar mechanics, hazards, sedimentology, fingerprinting techniques, Ruapehu's geological and eruptive setting, and the historical and contemporary lahar hazard landscape.

1.2 Literature review

1.2.1 Lahars

Lahar is a Javanese term for the fast-moving flows of water-mobilised volcanic debris which differs from normal streamflow (Smith & Fritz, 1989), and while prior definitions were vague, it has generally implied a flow large enough to pose a hazard (Scott, 1988). Lahar genesis requires an adequate water source, abundant unconsolidated debris, steep slopes, and a triggering mechanism (Vallance & Iverson, 2015). The terminology used to describe these hazardous flows is not clear and often misleading mainly due to the multidisciplinary intersection of different fields, e.g., volcanology, hydrology, sedimentology (Pierson & Costa, 1987; Procter et al., 2021). Indeed, volcanoes produce a variety of mass flows, including pyroclastic density currents, lahars, and debris avalanches, all of which are dominantly gravity-driven and involve components of water and rock fragments, yet exhibit a wide variability in the ratio of those components, rheology, and volume (Pierson, 1998).

There is a spectrum of different types of mass flow (Fig. 1.1) on hillslopes with increasing water content (irrespective of sediment origin) that encompass rockfalls, debris avalanches, debris flows, hyperconcentrated flows, and normal stream flow but in modern usage, lahars encompass two types of flow, debris flow and hyperconcentrated flow. The term hyperconcentrated flow was introduced in the engineering literature by Beverage & Culbertson (1964) to describe subaerial flows intermediate between mudflows and common streamflow, and brought into geological usage by Wasson (1977), supplanting the less precise "intermediate-type flow/deposit" (Nemec, 2009). Hyperconcentrated flows might also be referred to in the literature as debris floods or mud floods, and debris flows as mudflows, however modern usage draws a distinction between these terms (Pierson, 2005b), and are analogous to subaqueous turbidity currents (Lowe, 1982). Scott et al. (1995) and Vallance and Scott (1997) defined cohesive (>3% clay by total deposit weight or >5% clay by matrix weight) and noncohesive (<3% clay by total deposit weight or <5% clay by matrix weight) debris flows, where cohesive debris flows preserve high clay percentage over the length of the flow and noncohesive debris flows are more likely to change flow rheology.

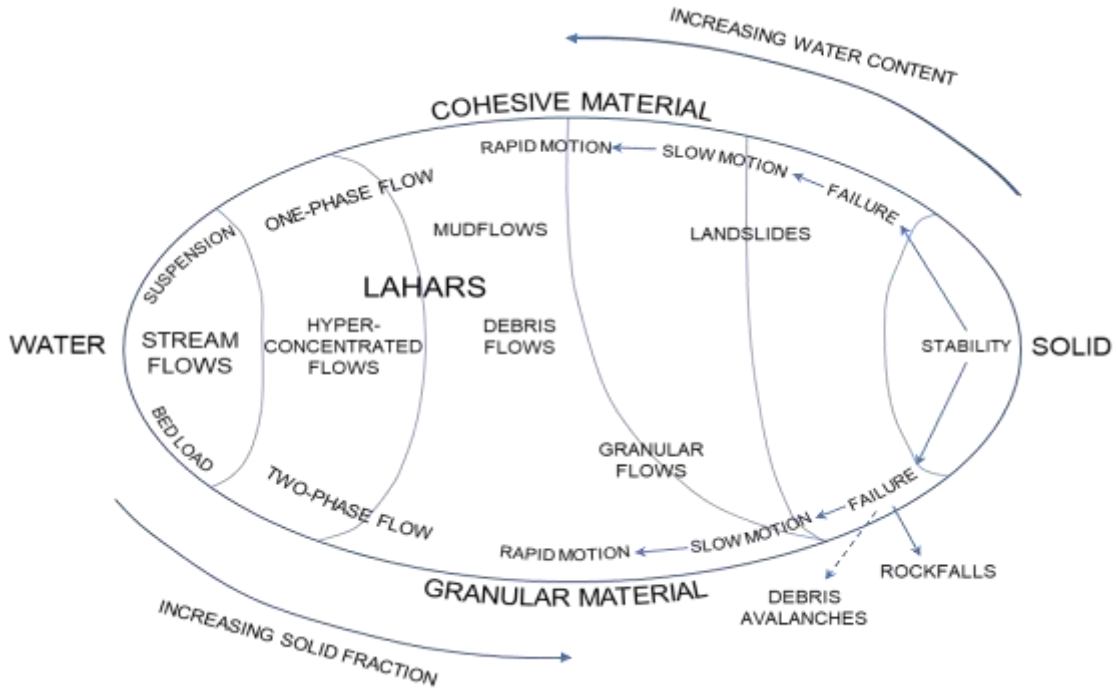


Figure 1.1 Classification of mass movements on steep slopes as a function of solid fraction and material type. After Coussot and Meunier (1996).

1.2.2 Triggering mechanisms

Lahar events can have a number of different triggers, which can often be inferred by studying their deposits, and these can generally be divided into either resulting from direct eruptive activity or not (Neall, 1976; Scott, 1988; Smith & Lowe, 1991). Direct triggers include eruption-induced snow and ice melt (Major & Newhall, 1989; Pierson et al., 1990) including subglacial eruptions forming jökulhlaups (Björnsson, 2009; Gudmundsson et al., 1997) and the eruptive mobilization of crater lake water (Scrivenor, 1929; Suryo & Clarke, 1985), while indirect triggers include, most commonly, rainfall mobilizing volcaniclastics (Arguden & Rodolfo, 1990; Rodolfo, 1989; Scott et al., 2005), the liquefaction of debris avalanches, and the mixing of volcaniclastic materials with water (Crandell, 1971; George et al., 2022; Scott, 1988).

While many lahar triggers have amplifying factors, which can be difficult to separate from the base trigger, most triggers can be simplified to five or six categories, including eruption-induced ice melt, eruption-crater lake interactions, mass-wasting, lake breakout events, rainfall

(Dittmer, 2008; Lecointre et al., 2004a; Pierson et al., 2025) as well as jökulhlaups (Pierson et al., 2025).

1.2.3 Lahar Rheology

Lahars exhibit a variety of flow behaviours, which are generally grouped into two categories: hyperconcentrated flows, where particle concentrations greater than normal streamflow conditions are commonly transported as suspended load and bedload, and debris flows, where high sediment concentrations lead to grain interactions and mass flow (Vallance, 2000). It is recognized that there is a continuum (Fig. 1.2) from floods to hyperconcentrated flows to debris flows, where floods (normal water flow) generally have less than 4% volume or 10% weight of sediment, to debris flows that can contain ~50-80% sediment by volume or 80% by weight (Hampton, 1972; Pierson, 2005b). The rheological changes introduced by the fluid-particle and particle-particle interactions make lahars different from Newtonian streamflow, fundamentally change the way sediment is transported, and are the basis for the quantitative classification of hyperconcentrated flows and debris flows (Pierson, 2005b; Pierson & Costa, 1987). Water floods with little sediment behave as Newtonian fluids, and have little to no shear strength. Shear strength increases slowly with increasing sediment loads, until a critical concentration, dependent on particle size, composition, sorting, and texture, is reached with shear strength increasing rapidly (Costa, 1984, 1988; Manville et al., 2013) along with a measurable static yield stress (Coussot and Meunier, 1996). As relative sediment percentage increases further, the flow is dominated by intergranular collisions which generate dispersive stress, dampen turbulent flow, causing the flow to behave as a non-Newtonian fluid (Manville et al., 2013; Pierson & Costa, 1987; Takahashi, 1980). Additionally, reduced turbulent flow, greater bulk density, and modification of stream channel morphology can lead to velocities twice that of comparable water floods (Manville et al., 2013).

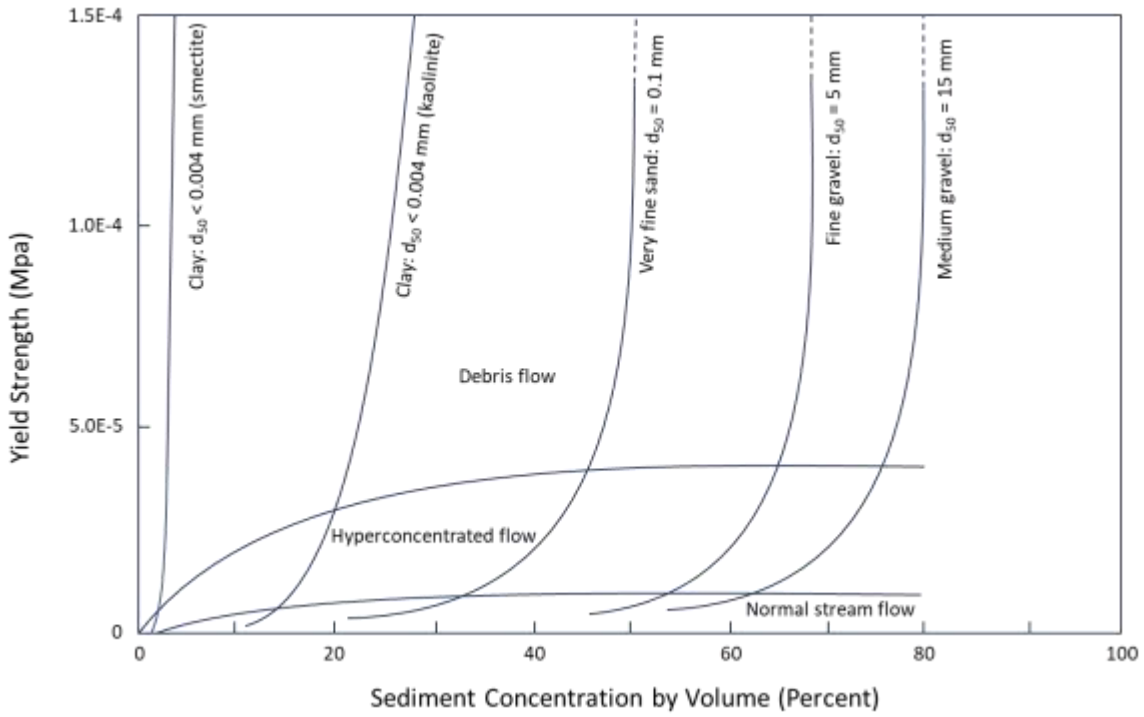


Figure 1.2 Classification of sediment-laden flows based on shear strength and sediment concentration. After Costa (1988).

Dispersive stresses increase with relative sediment percentage, while interstitial pore fluids support solids through buoyancy and increasing fluid pressure while simultaneously reducing intergranular friction. Larger particles migrate to the flow margins, particularly the surface and flow front which behaves as a moving boulder dam (Maizels, 1989; Major & Iverson, 1999; Manville et al., 2013). Competence (largest supported grain size) and cohesion (relative immiscibility with streamflow) of a debris flow are both strongly influenced by clay size particle concentrations, where non-cohesive flows are typically better sorted with fewer fines, and thus more prone to bulking and debulking (Hampton, 1975; Pierson & Scott, 1985; Procter et al., 2009; Scott, 1988). However, clay-rich sediment is relatively uncommon on active volcanoes, so lahars triggered by sudden water release are generally clay-poor, <5% clay/ (sand+silt+clay) by dry weight (Vallance & Iverson, 2015).

Clay size refers strictly to the particle diameter (<0.004 mm), whereas clay minerals are specific layer-lattice silicates that make up a large proportion of this size fraction (Pierson et al., 2025; Scott et al., 1995)(e.g. the Osceola Mudflow had 75% clay species in the clay-size fraction, (Crandell, 1971)). While clay-size particles may consist merely of volcanic ash or glass fragments (Arguden and Rodolfo, 1990; Pirrung et al., 2008), the presence of true clay minerals (such as smectite and kaolinite) is critical because their powerful surface forces provide cohesion and strength to the entire flow, drastically increasing fluid viscosity and decreasing permeability (Lecointre et al., 2002; Pierson et al., 2025; Scott et al., 1995).

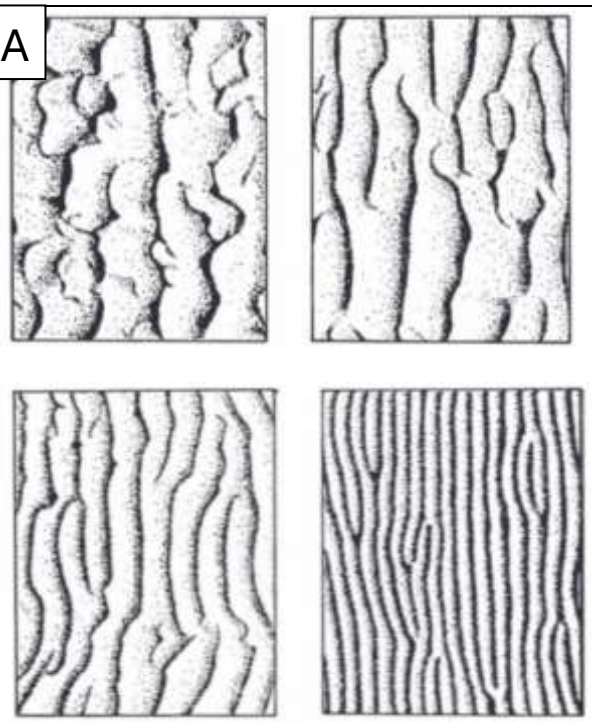
1.2.4 Flow Indicators and Sedimentological Signatures

Sediment concentration and flow rheology can only be determined via direct measurements yet flow conditions and triggering mechanisms can also be inferred by examining deposits (Smith & Lowe, 1991). While textural plots of grain size deviation seem to differentiate between flood and debris flow sediments, sedimentologic categorization of different flows from depositional records is primarily based on sorting and sedimentary structures (Costa, 1988), and triggering mechanisms have been inferred from stratigraphic relationships and grain size analyses (Janda et al., 1981; Ponomareva et al., 1998; Smith, 1988). Previous work to assign triggers to prehistoric Ruapehu lahars has identified uncertainty due to missing evidence (Donoghue and Neall, 2001; Palmer et al.,1993) and several prominent lahar units worldwide have been subsequently reassessed based on new evidence (Crandell, 1971; Pierson et al., 2025; Scott et al., 1995; Siebert, 1984; Vallance and Scott, 1997).

Sedimentary features that can be used to distinguish normal streamflow from lahar deposits (Figure 1.3) include dunes and ripples, cross-bedding, longitudinal bars, and imbricated clasts, while deposits are commonly terraced by receding flows (Pierson, 2005a; Pierson et al., 2025). Pierson (2005a) also notes that vegetation is less damaged and low-density flotsam is left at the flow margins of normal streamflow events, while debris flow deposits, by contrast, have

extremely poor sorting, no clast imbrication, debris levees, and often leave a muddy coating or outright destroy vegetation.

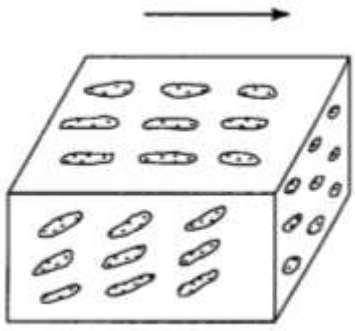
A



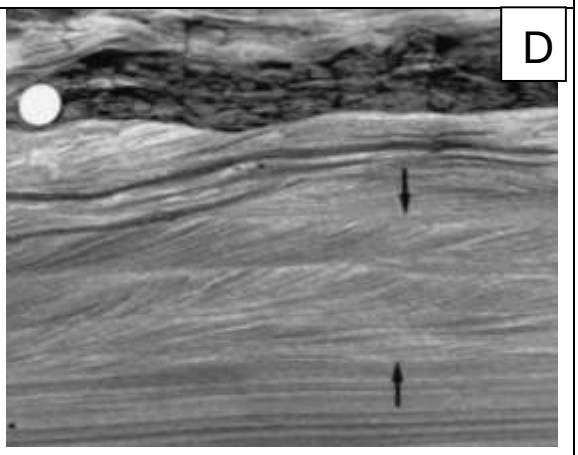
B



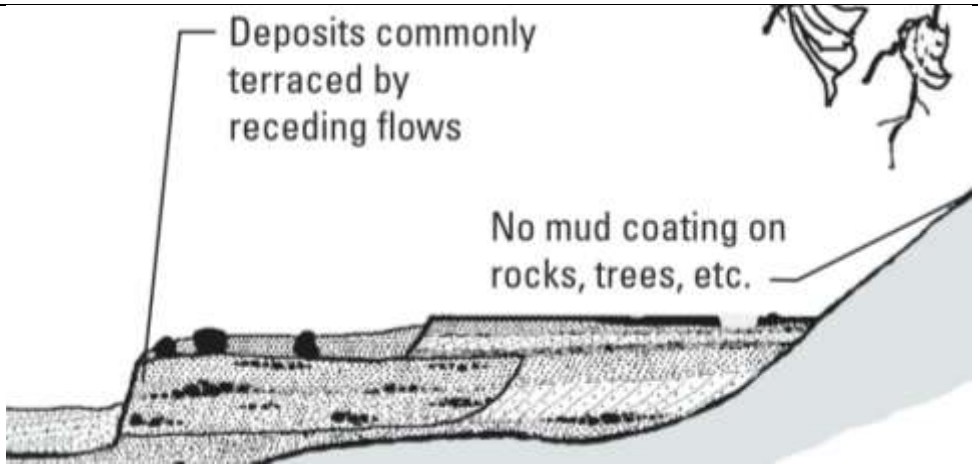
C



D



E


Deposits commonly
terraced by
receding flows
No mud coating on
rocks, trees, etc.

F



G



H



I



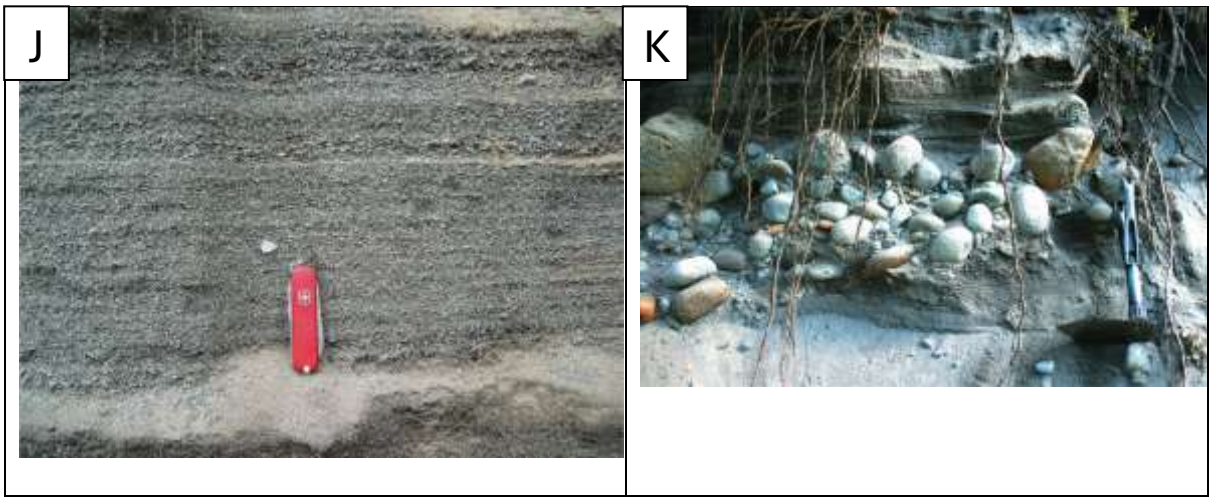


Figure 1.3 Examples of flow indicators and representative outcrop photos. A: Four common ripple mark textures (Boggs, 2009), B: longitudinal bars on the Whangaehu River, C: schematic of imbricated clasts (Boggs, 2009), D : cross bedding in sandstone with coin for scale (Boggs, 2009), E: terracing (Pierson, 2005a) F: Rain-triggered volcanic debris flow deposit (Pierson et al., 2025), G: Clay-poor volcanic debris flow deposit with trenching tool for scale (Pierson et al. 2025), H: Lower gray volcanic hyperconcentrated flow deposit and upper brown volcanic debris flow deposit (Pierson et al. 2025), I: Progressively coarsening volcanic hyperconcentrated flow deposit (Pierson et al., 2025), J: Plane-parallel-bedded channel facies volcanic water flood deposit with pocket knife for scale (Pierson et al., 2025), K: Channel facies volcanic water flood deposit with trenching tool for scale (Pierson et al., 2025).

Lobate flow fronts, lateral levees composed of coarse, angular clasts, and massive, very poorly sorted and ungraded deposits all directly reflect the transport mechanisms seen within a debris flow. However changes in flow rheology, channel morphology, and flow discharge rate can selectively deposit coarser clasts, incrementally deposit sediment, or even completely lock a flow in place (Major, 1997; Major & Iverson, 1999; Manville et al., 2013; Pierson, 2005b; Smith & Lowe, 1991). Hyperconcentrated flow deposits, by contrast, tend to be better sorted than debris flow deposits (Table 1.1), displaying weakly stratified, massive, non-graded or normal graded, clast-supported deposits, reflecting clasts settling through the flow and progressive basal accretion (Smith, 1986).

Table 1.1 Characteristics of deposits associated with debris flows and hyperconcentrated flows. Modified from Pierson (2005a) and Pierson et al. (2025), with additional information from Costa (1988); Cronin et al., (2000); Manville et al. (2005), Pierson (2005b); and Smith (1986).

Deposit Characteristics	**Debris flow**	**Hyperconcentrated flow**
Particle angularity	Boulder-size dense clasts more likely to be pitted/crudely rounded	Boulder-size dense clasts occasionally angular
Sorting	Extremely poorly sorted	Poor to very poor; textural changes usually not abrupt
Grading	Normal and/or inverse grading common in vertical sections	Normal grading common in upper portions of deposit, rare inverse grading more common in pumice-rich flows
Framework	Matrix filling all voids	Clast supported
Deposit Coherence	Coherent, semi-indurated consistency; difficult to dig	Semi-indurated yet friable
Stratification	No stratification, massive	Diffuse stratification to massive
Clast distribution	Coarse-clasts concentrated at deposit margins, coarse-clasts fairly randomly distributed elsewhere	Outsized individual gravel clasts and lenses
Clast orientation	Clasts oriented randomly except at flow margins (openwork)	Some imbrication of coarse gravel clasts

1.2.5 Edifice Alteration, Mass Wasting Transformations, and Lahars

Hydrothermally altered volcanoes have previously been implicated for lahar hazards (Carrasco-Núñez et al., 1993; Crandell, 1971; Finn et al., 2007; John et al., 2008; Vallance and Scott, 1997) as early as 1926 (Tada and Tsyua, 1926, as referenced in Crandell, 1971). This has also been a subject of interest at Ruapehu, aerial hyperspectral imagery supplemented with laboratory

analysis (Douglas et al., 2022; Kereszturi et al., 2020; Miller et al., 2020; Schaefer et al., 2023) has revealed that approximately 7 km^2 of the summit area (out of ~54 km^2) shows some degree of argillic alteration, most of it within a kilometre of the Crater Lake.

Although voluminous, clay-rich (cohesive) lahars are often primarily associated with large-scale edifice collapses and liquefaction of hydrothermally weakened volcano flanks, such as Mount Rainier's Osceola Mudflow (Crowley and Zimbelman, 1997; Vallance and Scott, 1997) or the 18 May 1980 North Fork Toutle River lahar (Crandell, 1987; Janda et al., 1981; Pierson and Scott, 1985), there can be amplifying factors that contribute to mobilizing hydrothermally altered regions, as seen in records from Japan. The 1888 eruption of Bandai volcano, for instance, involved an initial landslide that transformed into a debris flow, followed by phreatic eruptions (Siebert et al., 1987; Yamamoto et al., 1999). The lahar deposit was described as extremely poorly sorted and very clayey (10 to 17 wt.%) (Yamamoto et al., 1999). While hydrothermal alteration is the most common source of cohesive lahars (Pierson et al., 2025) trigger mechanisms can vary. Research following the 2014 small-scale phreatic eruption at Ontake Volcano showed that a subsequent cohesive debris flow with high clay contents (10–20 wt% in the matrix) was rain-triggered, reaching at least 11 km downstream (Kataoka et al., 2018). While at Mt. Taranaki, debris avalanches have transformed into cohesive, long-runout debris flows (Neall, 1976; Alloway, 1989; Palmer and Neall, 1991a; Zernack et al., 2009; Zernack, 2021) which generally exhibit a low proportion of hydrothermally altered clasts, suggesting a lack of pervasive hydrothermal alteration of the past edifices (Zernack et al., 2009; Cronin et al., 2021). Instead the high mobility of these flows is largely attributed to the incorporation of allophane-rich, water-saturated andic soils (Zernack et al., 2009; Zernack, 2021).

The identification of clay species and their abundance in lahar deposits can inform models of flow rheology (Costa, 1988, p. 88; Hampton, 1972; Scott et al., 1995), and when combined with bulk composition data can potentially reveal trigger mechanisms, source material and source

weathering processes (Inoue, 1995). Clay species and abundance have to date been used as the main proxy for "fingerprinting" lahar units to allow correlations between deposits and infer source and trigger mechanisms (Cook, 2002; Crandell, 1971; Detienne et al., 2017; Frank, 1995, 1985; Hodgson, 1993; Hodgson et al., 2007; Mullineaux, 1974; Thouret et al., 1998).

The distinctive mineralogical composition of cohesive lahar deposits also provides insights into the hydrothermal alteration conditions at source. The 2014 Ontake lahar deposits were rich in sulfide and sulfate minerals, as well as pyrophyllite (Kataoka et al., 2018), with a mineral assemblage reflecting intermediate to advanced argillic alteration at 1-2 km depth (Kataoka et al., 2018; Schaefer et al., 2023). This alteration assemblage is tied directly to rock strength as the breakdown of primary minerals to clay minerals and other alteration products results in overall mechanical weakening (Kereszturi et al., 2021; Schaefer et al., 2023) and increased water retention capacity (Detienne et al., 2017). While typical cohesive lahars generally maintain viscosity and resist dilution due to high clay contents (Kataoka et al., 2018; Minami, 2024), the flow behaviour is sensitive to the specific mineral assemblage within the flow, e.g., altered material with a high proportion of silica polymorphs exhibiting greater flow transformation and dilution (Minami, 2024).

1.3 Geological background

1.3.1 Regional geology

The basement rock under Mt. Ruapehu is primarily meta-greywacke and meta-argillite of the Cretaceous Torlesse Composite Terrane sourced from an East Gondwanaland quartzo-feldspathic basement (Adams et al., 2002, 2007; Mortimer et al., 1997; Roser & Korsch, 1999), which is sutured to Mt. Ruapehu's west to the litharenite dominated Jurassic Waipapa Terrane, composed of intermediate volcanic arc sediments (Adams et al., 2007; Beetham & Watters, 1985; Price et al., 2012).

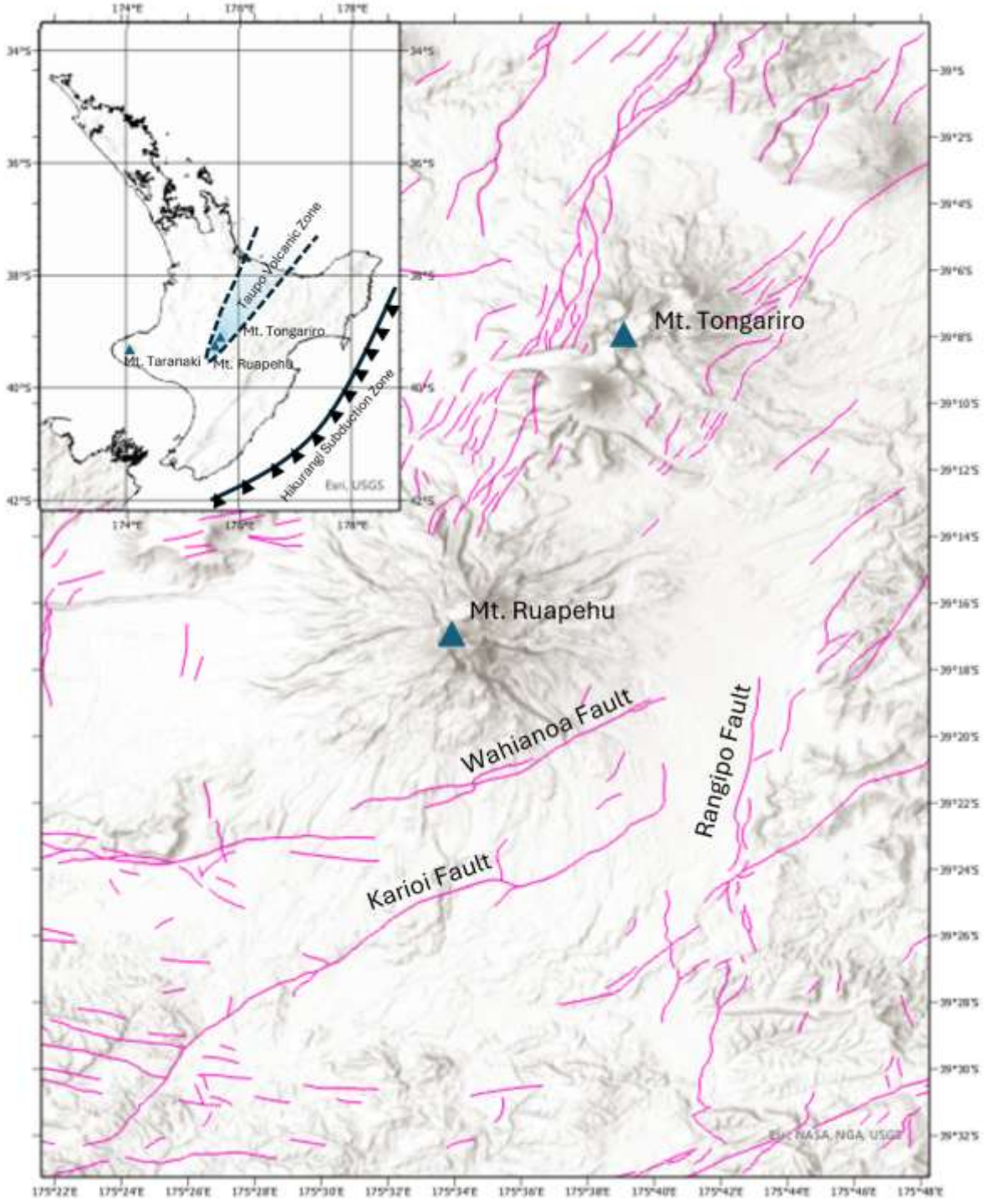


Figure 1.4 Location of Mt. Ruapehu (center) with fault lines from Earth Science New Zealand (Langridge et al., 2016), with inset showing Hikurangi-Kermadec subduction zone, Taupo Volcanic Zone, and major andesitic volcanoes.

North Island volcanism arises from the subduction of the Pacific Plate under the Australian Plate along the Hikurangi-Kermadec trench system. The northern Kermadec Trench segment subducts under oceanic crust, forming a chain of volcanic seamounts and islands, while the southern Hikurangi Trough segment subducts under continental crust, forming the 250 km NE-SW Taupo Volcanic Zone (Cole, 1990; Reyners et al., 2006; Stern et al., 2006). The Taupo Volcanic Zone is considered a back arc rift, which volumetrically is currently the most productive volcanic area in the world (Wilson et al., 2009). This zone of rifting is characterised by large caldera forming volcanism in central regions with thin crust while andesitic volcanism dominates at the northern and southern tip of the zone, marked by the Tongariro Volcanic Center (Rowland et al., 2010).

The Tongariro Volcanic Center (TgVC), comprised of Kakaramea-Tihia, Pihanga, Tongariro, and Ruapehu, marks the southwestern end of the TVZ. Mt. Ruapehu is located in the Mount Ruapehu graben, bounded to the east by the Rangipo fault and by the Raurimu fault to the west (Reyners, 2010; Stern et al., 2006; Villamor & Berryman, 2006; Villamor et al., 2007). The oldest recorded volcanic material from the TgVC dates to ~933 ka and is associated with Hauhungatahi, an eroded andesitic volcano 12 km west of Mount Ruapehu (Cameron et al., 2010), followed by the Otamatereinga (~512 ka) and Tupuna formations (previously Tama) (~304 ka) on Tongariro and the Te Herenga formation (~200 ka) on Ruapehu (Gamble et al., 2003; Pure, 2020).

From ~25 ka to 14 ka the Rangipo fault (also known as Desert Road fault and Whangaehu (river) fault) had a slip rate of 2-9 mm/yr, versus ~0.2 mm/yr since 14 ka. The continuing fault motion after 14 ka changed the course of the Whangaehu River to the southwest after it had previously drained southeast along the Moawhango River (Donoghue, 1991; Villamor et al., 2007). Additionally, a brief increase in rifting along the TgVC from ~11.3 - 11.1 ka coincides with a surge of eruptive episodes (Heinrich et al., 2020).

1.3.2 Mount Ruapehu

Previous K-Ar dating had placed the oldest lava flows on Ruapehu at 230 ka and Tongariro at 273 ka (Patterson and Graham 1988; Hobden et al. 1996), however more recent Ar-Ar dates place the oldest rocks at 250 ka (Gamble et al., 2003). Dating of andesitic clasts in mass flow deposits near Whanganui, 100 km southwest of Ruapehu, would possibly extend Ruapehu's eruptive history to 340 ka (Tost et al., 2015), however subsequent mineralogical analysis is more indicative of a Tongariro source, the Tupuna Formation, and the Turakina Formation debris flows would had to have crossed the area Ruapehu currently occupies, which would indicate an age younger than ~309 ka (Pure, 2020).

Four effusive formations are recognised (Section 1.3.2.2) that represent four edifice-building episodes; Ruapehu's eruptive activity has not been marked by any long periods of dormancy (Conway et al., 2016; Pure, 2020). The Te Herenga formation lavas are the oldest preserved on Ruapehu (Section 1.3.2.2.1) located on the northwestern section of the edifice (Gamble et al., 2003; Hackett, 1985; Townsend et al., 2017), followed by the effusive Wahianoa Formation, which forms the current southeast section of the edifice, the Mangawhero Formation which forms the western and northeastern flanks, and, most recently, the Whakapapa Formation on the north flank and the extensive Rangataua Member south flank flow that terminates near State Road 49 (Gamble et al., 2003; Hackett & Houghton, 1989; Townsend et al., 2017). The four effusive formations display two dominant lithofacies associations: central and flank vent, and proximal (cone-forming) sequences (Hackett & Houghton, 1989). Central and flank vent lithofacies include thin lava flows, dome remnants, and welded spatter cones, while proximal lithofacies are block and autobrecciated lava flows.

Collapse-generated debris avalanches have removed significant (>1 km^3) volumes of the Holocene Ruapehu edifice, including the 9.5 ka Murimotu Formation, which forms the Whakapapa 'mounds' on Ruapehu's western ring plain, and the 4.6 ka Mangaio Formation in the

Whangaehu Valley, which consists of hydrothermally altered cone material derived from a predecessor of the modern Crater Lake (Donoghue & Neall, 2001; Palmer & Neall, 1989; Tost et al., 2014). The formation of the Crater Lake (~2 ka) is marked by a shift from dry to phreatomagmatic ash in the Tufa Trig Formation and initiation of large Onetapu Formation lahars (Donoghue et al., 1997; Hodgson et al., 2007; Lecointre et al., 2004; Palmer et al., 1993).

Ruapehu's summit morphology is primarily the result of eruption processes from multiple vent and glacial erosion, with much of the edifice covered by glaciers during the last glacial maximum (Otira) (Christenson & Wood, 1993; Hackett, 1985), simultaneously weathering and removing sediment (Cronin et al., 1996; Cronin & Neall, 1997; Pure, 2020)

1.3.2.1 Ring plain stratigraphy

While the record of effusive volcanism is relatively well-preserved, unwelded tephra deposits are mostly eroded away and not preserved on the modern edifice. However the ring plain record is much more complete (Hackett and Houghton 1989) preserving deposits of tephras (Donoghue et al., 1999; Heinrich et al., 2020; Moebis, 2010; Moebis et al., 2011; Pardo, 2012), lahars, lava flows, debris avalanches, and fluvial and aeolian sediments, interbedded with rhyolitic Taupo and Okataina tephras (Fig. 1.5)(Campbell, 1973; Cronin, Hodgson, et al., 1997; Donoghue, 1991; Donoghue et al., 1995; Hodgson, 1993; Hodgson et al., 2007; Lecointre et al., 2004; Palmer, 1991; Palmer et al., 1993; Palmer & Neall, 1989; Topping, 1973). The Ruapehu and Tongariro ring plains are unique depositional environments because they are coalescing volcaniclastic aprons from the local andesitic volcanoes, interbedded with regional rhyolitic tephras sourced from the Taupo Volcanic Zone calderas to the north, allowing comparative ages to be determined for local and regional eruptions (Hackett and Houghton, 1989; Purves, 1990; Donoghue, 1991; Palmer et al., 1993; Cronin, 1996; Cronin et al., 1997c; Cronin and Neall, 1997; Gamble et al., 2003; Conway et al., 2016; Gómez-Vasconcelos et al., 2017). Ruapehu's

ring plain has a similar volume, 150 km^3, to the source edifice (Hackett and Houghton, 1989; Gamble et al., 2003).

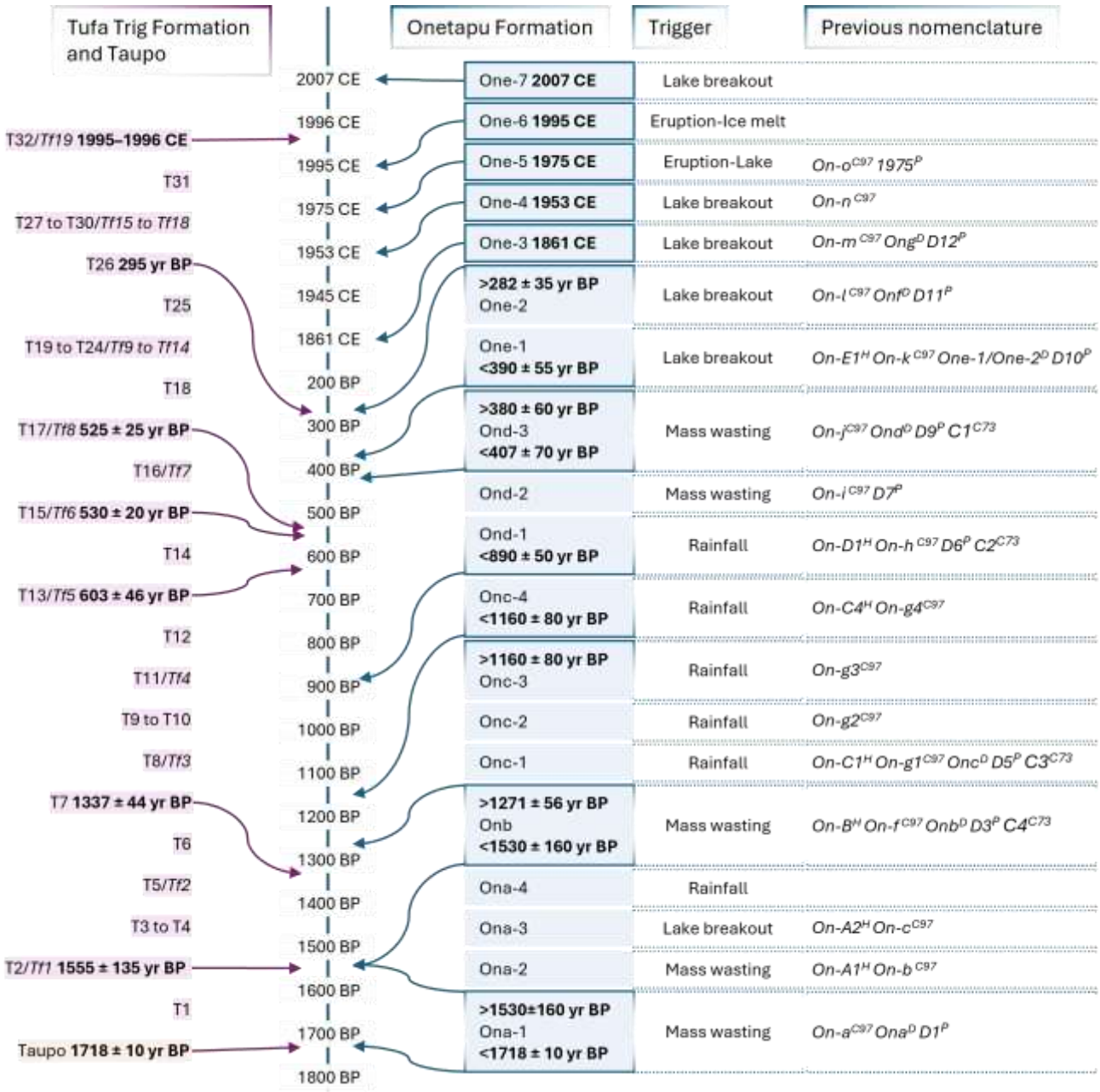


Figure 1.5 Simplified timeline of modern eruptive and lahar units on the eastern Ruapehu ring plain. Tufa Trig nomenclature and dates from Voloschina (2020) with italicized names from Donoghue (1991) and Donoghue & Neall (2001), Onetapu Formation units and dates from Hodgson et al. (2007) with older nomenclature superscripts as cited by Hodgson et al. (2007): H Hodgson (1993), C97 Cronin et al. (1997b), D Donoghue (1991) & Donoghue & Neall (2001), and as cited by Hodgson (1993): C73 Campbell (1973), P Purves (1990). Trigger information simplified (Chapter 5) from Hodgson et al. (2007) and Lecointre et al. (2004).

Tephrostratigraphy indicates that, while the preserved tephra record extends to >70 ka (Cronin, 1996; Cronin, et al. 1997; Hodgson, et al., 1997; Donoghue et al., 1995), eruptive events from 22,600 to present have been dominated by tephra eruptions and lahars, with debris avalanches and pyroclastic flows being uncommon during this period (Donoghue et al., 1999). Ruapehu-sourced tephras are divided into the Bullot Formation (~27 ky to ~10 ky) (Pardo, 2012) and the Tufa Trig Formation (~1.8 ky to present) (Donoghue, 1991) (Section 1.3.2.3), with explosive ash producing eruptions are primarily preserved on the eastern and north-eastern ring plain due to prevailing winds (Donoghue et al., 1995). Lahar sequences are represented by the Te Heuheu Formation (>22.6 ky to 14.7 ky) (Donoghue, 1991), Tangatu Formation (14.7 ky to 5.4 ky) (Donoghue, 1991), Mangaio Formation (~5.2 ky) (Donoghue and Neall, 2001), Manutahi Formation (5,370 to 3,200) (Hodgson, 1993), and Onetapu Formation (Fig. 1.6)(Cronin & Neall, 1997; Donoghue, 1991; Hodgson, 1993).

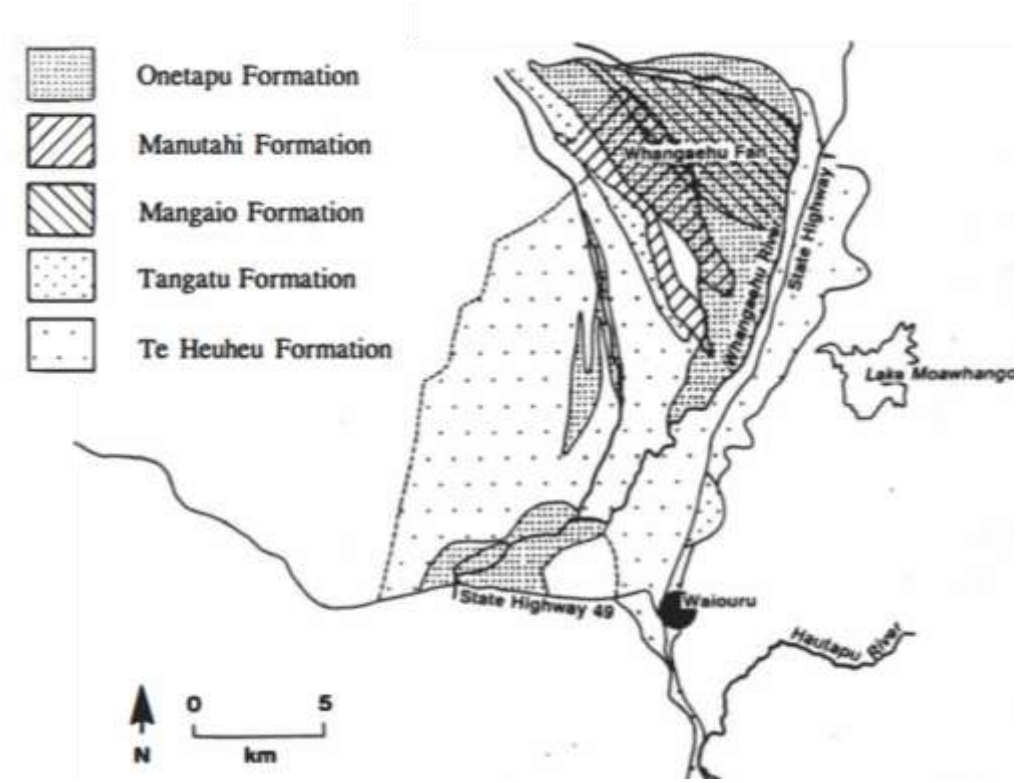


Figure 1.6 Lithostratigraphy of Southeast Mt. Ruapehu ring plain lahar deposits (Hodgson, 1993).

1.3.2.2 Major Effusive Formations

Ruapehu's effusive, edifice building formations (Fig. 1.7) are, in order of age: Te Herenga, Wahianoa, Mangawhero, and the Whakapapa Formations (Auer et al., 2013; Gamble et al., 2003), comprising a total of 22 distinct units (Conway et al., 2016, 2018; Townsend et al., 2017).

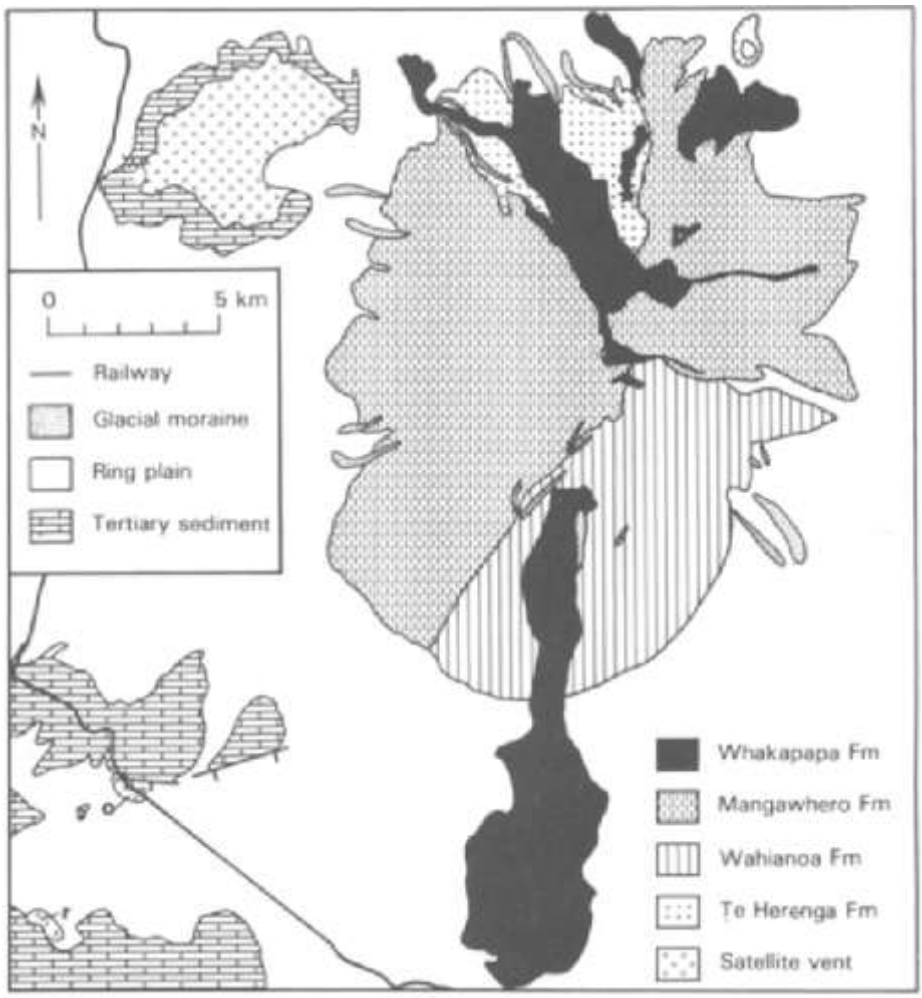


Figure 1.7 Geological sketch map of Mt. Ruapehu's major effusive formations, after Hackett & Houghton, 1989.

1.3.2.2.1 Te Herenga Formation

The Te Herenga Formation is dated to 200 - 150 ka, with a maximum $^{40}Ar/^{39}Ar$ age of 205 ± 27 ka, and an estimated original volume of 65 km^3 (Conway et al., 2016; Gamble et al., 2003; Hackett, 1985; Hackett & Houghton, 1989; Price et al., 2012). The lavas are petrographically distinct due to pyroxene phenocrysts dominating over plagioclase or orthopyroxene (Pure, 2020) as well as distinct $^{87}Sr/^{86}Sr$ to $^{143}Nd/^{144}Nd$ ratios compared to other Ruapehu eruptives. Similar to

Wahianoa Formation, brecciated bases of lava flows are interpreted as magma-water/ice interactions (Conway, 2016).

1.3.2.2.2 Wahianoa Formation

The Wahianoa Formation has an age of 166 - 80 ka, and an estimated original volume of 45 km^3 (Conway et al., 2016; Gamble et al., 2003; Hackett & Houghton, 1989). Similar to the Te Herenga Formation it comprises breccias and ice-confined lava features, indicating subglacial and ice-marginal emplacement (Cole et al., 2020; Townsend et al., 2017).

1.3.2.2.3 Mangawhero Formation

The 50-15 ka Mangawhero Formation has an estimated original volume of 35 km^3 (Conway et al., 2016; Gamble et al., 2003; Hackett & Houghton, 1989) with numerous textures indicating ice interaction during emplacement (Conway et al., 2015). The formation has been subdivided into 11 additional eruptive packages based on age and composition (Conway et al., 2016; Townsend et al., 2017) with compositions ranging from basalt to dacite (Graham & Hackett, 1987).

1.3.2.2.4 Whakapapa Formation

The Whakapapa formation is dated to <15 ka, has an estimated original volume of 2.6 km^3 (Conway et al., 2016; Gamble et al., 2003; Hackett & Houghton, 1989) and has been subdivided into 7 additional eruptive packages based on age and composition (Conway et al., 2016, 2018; Townsend et al., 2017). The Whakapapa formation is characterised by subaerial valley-floor lava flows, indicating a retreat of glaciers around 15 ka (Conway et al., 2015)

1.3.2.3 Tephrostratigraphy and Marker Beds

TgVC tephras are grouped into the 14 ka to present Tongariro Subgroup, and the ~27 ka to ~10 ka Tukino Subgroup, including tephras erupted from Ruapehu, Tongariro, Tama Lakes, and Ngauruhoe (e.g., Donoghue et al., 1995; Grindley, 1960; Topping, 1973; Voloschina, 2020).

1.3.2.3.1 Bullot Formation

The Bullot Formation is a ~27 ka to ~10 ka series of 33 identified beds (Pardo, 2012) of primarily pumice lapilli tephra produced by VEI 4 to VEI 5 eruptions, the largest of which were erupted between ~13.6 ka and ~10 ka (Pardo et al., 2012; Pardo et al., 2012; Pardo, 2012).

1.3.2.3.2 Papakai Formation

The ~11 ka to ~3.5 ka Papakai Formation is commonly found interbedded with rhyolitic Waimihi, Hinemaiaia, and Motutere tephras (Donoghue et al., 1995; Topping, 1973) and is characterized by andesitic tephra and possibly tephric loess, derived principally from the Mt. Tongariro region (Topping, 1974; Donoghue, 1991; Donoghue et al., 1995; Suryaningtyas, 1998).

Mangatawai Formation

The ~2.5 ka to ~1.8 ka Mangatawai Formation is andesitic tephra beds sourced from Mt. Ngauruhoe and Mt. Ruapehu that conformably overlies Papakai Formation and underlies Taupo Tephra (Topping, 1974; Donoghue, 1991; Donoghue et al., 1995; Moebis et al., 2011; Voloschina, 2020).

1.3.2.3.3 Tufa Trig Formation

The ~1.8 ka to present Tufa Trig Formation is a series of at least 19 beds of primarily black sandy ash and lapilli tephras, prominently exposed in the Rangipo desert (Topping, 1973). The most recent member being Tf19/T32 from the 14 October 1995 Mt. Ruapehu eruption (Donoghue, 1991; Voloschina, 2020).

1.3.2.3.4 Ngauruhoe Formation

The Ngauruhoe Formation is andesitic tephra units erupted from Mt. Tongariro and Mt. Ngauruhoe since the Taupo Pumice eruption (~CE 232) (Topping, 1973; Donoghue et al., 1995), the most recent member being the 2012 Te Maari eruption tephra (Voloschina, 2020).

1.3.2.3.5 Taurewa Formation: Pourahu Member

The ~10.5 ka Pourahu Member of the Taurewa Formation is Ruapehu's sole identified pyroclastic flow deposit, generated from a 0.2 to 0.3 km^3 eruption, and preserved in the upper east and west ring plain (Donoghue et al., 1999).

1.3.2.4 Volcaniclastic formations

1.3.2.4.1 Sector collapse formations

Sector collapse-generated volcanic debris avalanche (VDA) deposits have not been identified in the stratigraphic record over the last 2000 years but two older VDA deposits are found in the study area.

1.3.2.4.1.1 Murimotu formation

Previously identified as lahar deposits (Grindley, 1960, Hay, 1967), the 10.6 ka Murimotu Formation is a debris avalanche deposit preserved on the west side of Ruapehu's ring plain as the Whakapapa mounds (Palmer & Neall, 1989).

1.3.2.4.1.2 Mangaio formation

The ~5.2 ka Mangaio Formation is a single debris avalanche lobe covering much of the northeastern Rangipo Desert and sections of the upper Whangaehu Valley, incorporating an estimated volume of 34 x 10^6 m^3 of hydrothermally altered cone deposits (Donoghue & Neall, 2001; Graettinger et al., 2010; Townsend et al., 2017).

1.3.2.4.2 Lahar formations

Lahar deposits represent the volumetrically largest proportion of the volcaniclastic ring plain succession with (Cronin & Neall, 1997; Hodgson, 1993; Lecointre et al., 2004; Purvis, 1990) the following formations encompassing periods of increased laharic activity that have contributed to the construction of the southeastern ring plain.

1.3.2.4.2.1 Te Heuheu

The >22.6-14.7 ka Te Heuheu Formation is largely comprised of Mt. Ruapehu-sourced gravelly diamictons and forms the constructional surface of the Mt. Ruapehu ring plain (Donoghue, 1991). The 14.7 ka Rerewhakaaitu Tephra forms the upper boundary, while the lower boundary is marked by an erosional unconformity (Froggatt and Lowe, 1990; Donoghue, 1991).

1.3.2.4.2.2 Tangatu Formation

The 14.7-5.4 ka Tangatu Formation includes Mt. Ruapehu-sourced gravel and sand-dominated diamictons and is constrained by the 14.7 ka Rerewhakaaitu Tephra and the 5.4 ka Motutere Tephra (Froggatt, 1981; Froggatt & Lowe, 1990; Donoghue, 1991)

1.3.2.4.2.3 Manutahi Formation

The 5,370-3,200 years BP Manutahi Formation is made of weakly bedded sand and gravel hyperconcentrated flow deposits observed at three localities with the type section located in the Rangipo Desert (Hodgson, 1993; Donoghue & Neall, 2001).

1.3.2.4.2.4 The Modern and Historical Onetapu Formation

The Onetapu Formation has been formally divided into five units and 19 members, based on mappable units with distinct lithologies (Hodgson et al., 2007; Manville & Cronin, 2007)(Figure 1.5). Matrix and clast compositions and correlations between mapped units were used to infer triggering mechanisms for prehistoric lahars, specifically:

- **Ona-1** (>1530±160 yr BP) is a medium-large cohesive debris flow deposit that contains hydrothermally altered source rock, lakebed sediments, reworked Taupo Pumice and Mangaio Formation and no juvenile components, indicating a Crater Lake rim collapse. Subsequent **Onetapu A** members are less cohesive, and assumed to have similar (**Ona-2**, **Ona-3**) or unknown triggers (**Ona-4**) (Hodgson, 1993; Hodgson et al., 2007).
- **Onb** (<1530±160 yr BP, >1271 ± 56 yr BP) is a large cohesive debris flow deposit that contains hydrothermally altered source rock, mud-coated scoria, and juvenile eruptive

material, indicating an eruption and Crater Lake rim collapse (Hodgson, 1993; Hodgson et al., 2007).

- **Onc-3** (>1160 ± 80 yr BP) is a hyperconcentrated flow deposit with common lithic clasts and pumice, indicating dry vent conditions and either rain-triggered or glacial melt trigger mechanisms. Prior members (**Onc-1**, **Onc-2**) are of similar composition and thinner, and the later **Onc-4** is thicker and contains primarily unaltered scoria, but all units have similar inferred triggers. The **Onetapu C** members and units are medium- to catastrophic in size (Hodgson, 1993; Hodgson et al., 2007).
- **Ond-2** (>450 ± 55 yr BP) is a very large cohesive debris flow deposit that contains altered and lithic clasts and lake-bed sediments and is interpreted as a Crater Lake barrier collapse. Earlier small hyperconcentrated flow deposit **Ond-1** was possibly rain triggered or represents a bow-wave deposit. Subsequent voluminous cohesive debris flow deposit **Ond-3** comprises abundant juvenile andesitic clasts, lake sediments, and altered clasts, and is interpreted as an eruption-triggered Crater Lake rim collapse (Hodgson, 1993; Hodgson et al., 2007).
- **Onetapu E** units are historic events, the majority of which have been directly observed and recorded: **One-3** in 1861 (e.g., Reverend Richard Taylor, 1861), **One-4** in 1953 (e.g., O'Shea, 1954), **One-5** in 1975 (e.g., Nairn et al., 1979), **One-6** in 1995 (e.g., Cronin et al., 1997b), and **One-7** in 2007 (e.g., Procter et al., 2010a).

1.4 Contemporary Lahar Hazards at Ruapehu

1.4.1 Infrastructure and Downstream Exposure

Contemporary lahar hazards at Ruapehu are principally focused in the Whangaehu River catchment, and lahars, with deposits being volumetrically the largest proportion of volcaniclastic sediments on the ring plain, five historically observed large events (1861, 1953, 1975, 1995, 2007), and one of those (1953, Tangiwai) being New Zealand's worst volcanic

disaster, thusrecognised as Ruapehu's most significant volcanic hazard (Hodgson et al., 2007; Keys et al., 2008; Montgomery et al., 1993; Sherburn & Bryan, 1999). Infrastructure exposure includes three ski fields on Ruapehu's edifice (Kilgour et al., 2010; Montgomery et al., 1993; Sherburn & Bryan, 1999; Voloschina, 2020) and further downstream critical national infrastructure is at risk, including the North Island Main Trunk railway and State Highways (Cronin et al., 1997a; Donoghue, 1991; Hodgson et al., 2007). Hydroelectric power schemes associated with the Tongariro Power Development (THPS) having sustained damage in past eruptions, e.g., the 1975 lahar contaminated the Wahianoa Aqueduct and Mangaio Tunnel (Donoghue, 1991; Montgomery et al., 1993; Paterson, 1980).

1.4.2 Monitoring Systems and Hazard Mitigation

To mitigate these hazards, various monitoring and engineering countermeasures have been implemented, including monitoring by GeoNet (Kilgour et al., 2010; Manville & Cronin, 2007; Whitehead et al., 2022), the Eruption Detection System (EDS) (Sherburn & Bryan, 1999), and the late Eastern Ruapehu Lahar Alarm Warning System (ERLAWS) (Keys et al., 2008; Manville & Cronin, 2007; Manville & Hodgson, 2011; Taig, 2002). Engineered hazard mitigation measures included raising and strengthening the highway bridge at Tangiwai (Keys et al., 2008; Taig, 2002) and constructing a lahar-deflection dike (bund) on the Whangaehu fan specifically to prevent lahars from diverting into the Tongariro catchment (Hodgson et al., 2007; Keys et al., 2008; Procter et al., 2010b; Taig, 2002).

1.4.3 Hazard Assessment and Forecasting Challenges

Hazard assessments and modelling at Ruapehu have been driven largely by the high risk lahars pose to life and infrastructure (Dittmer, 2008; Montgomery et al., 1993), initiated by the 1953 Tangiwai rail disaster, where a lahar destroyed a rail bridge and killed 151 people (New Zealand's worst volcanic disaster). This event prompted immediate and sustained effort in hazard mitigation and assessment (Hodgson et al., 2007; Johnston et al., 2000; Lecointre et al., 2004a;

Manville, 2004; Neall, 1976; Neall et al., 1999; O'Shea, 1954). Ruapehu hazard zones were first mapped and delineated by Hodgson (1993) based on recurrence intervals, which was the foundation for a simplified map by Neall et al. (1999) (Fig. 1.8) that was later expanded by Neall et al. (2004) (Fig. 1.9).

Lahar forecasting was successfully implemented in the aftermath of the 1995/1996 eruptions, when the trigger, magnitude, and timeframe of the 2007 Crater Lake breakout lahar were predicted (Dittmer, 2008; Keys, 2007; Keys et al., 2008; Massey et al., 2010; Procter et al., 2012; Taig, 2002; Webby, 1999). Yet hazard assessments are fundamentally challenged by the complex flow dynamics and rapid rheological variability of lahars (Graettinger et al., 2010; Procter et al., 2021, 2012, 2010b) in addition to the range of diverse trigger mechanisms present at Ruapehu (Graettinger et al., 2010; Hodgson et al., 2007; Lecointre et al., 2004a; Procter et al., 2021).

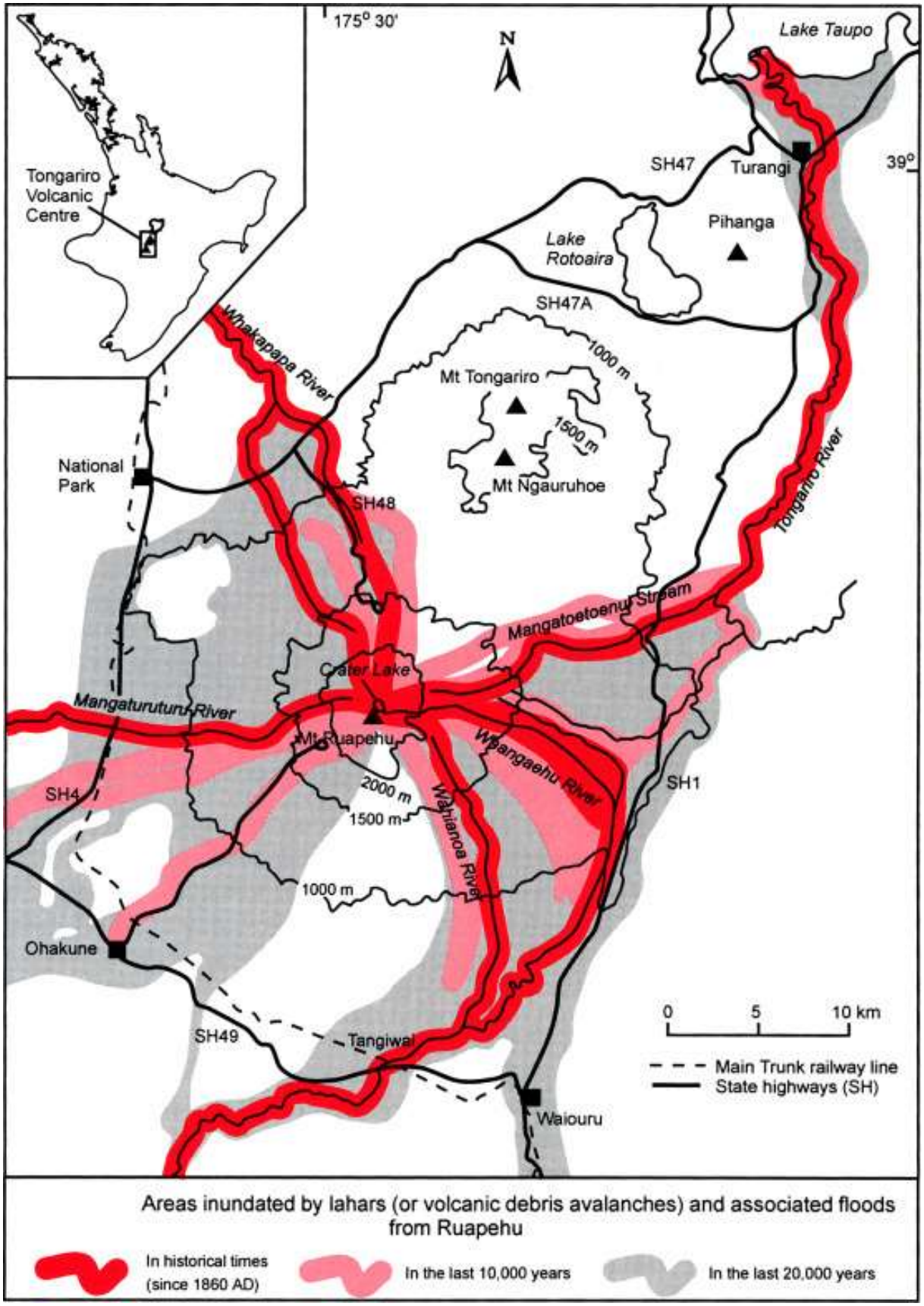


Figure 1.8 Lahar hazard map from Neall et al. (1999).

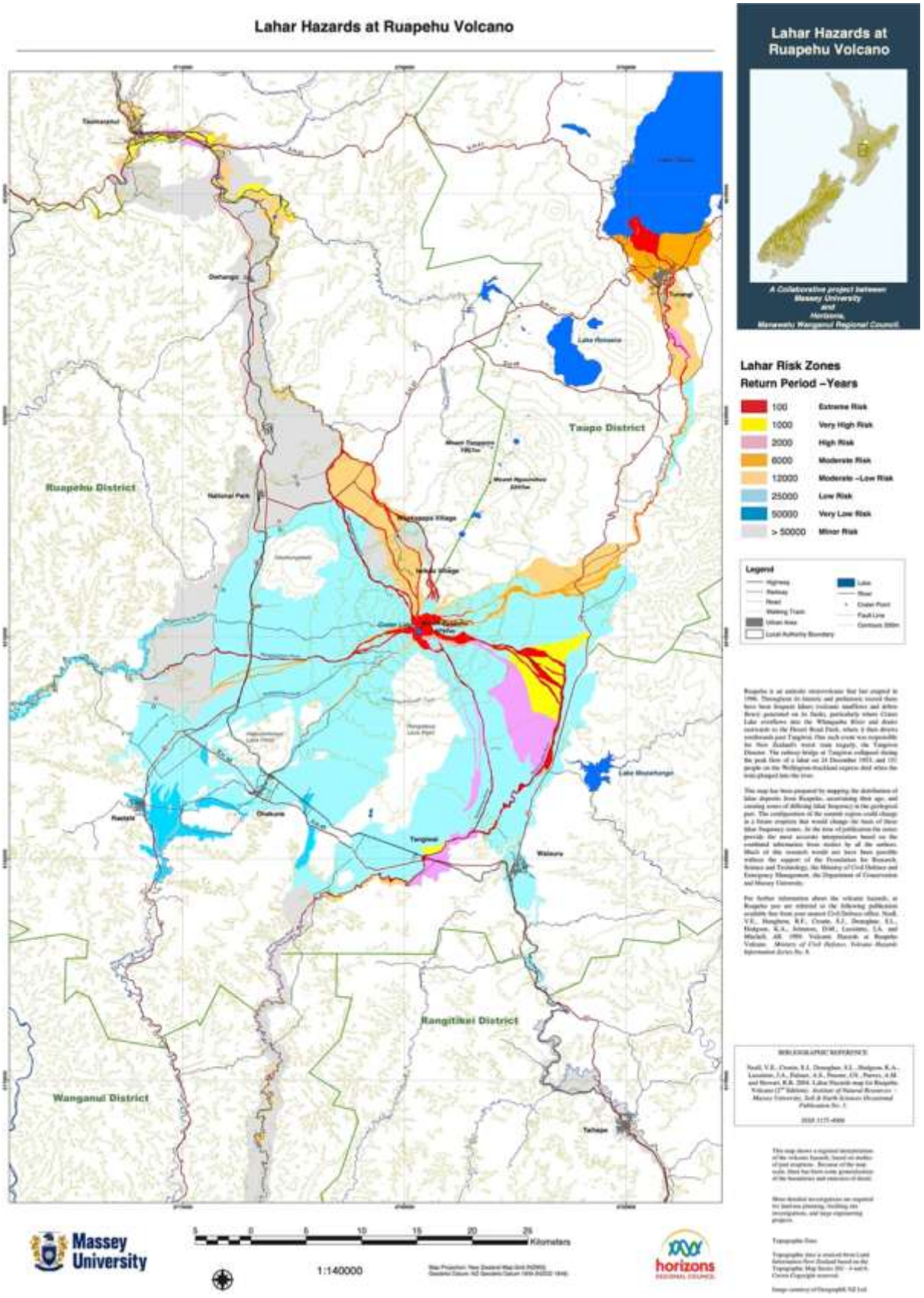


Figure 1.9 Lahar hazard map from Neall et al. (2004).

Numerical models are increasingly being used to assist hazard assessment (Gattuso et al., 2021; Pallister et al., 2019) and various models have been applied on Ruapehu (Mead et al., 2021, 2016; Mead & Magill, 2017; Phillips, 2011; Procter et al., 2012, 2010b). A study using the Titan2D model was run before the 2007 Crater Lake breakout lahar to estimate flow path and inundation area, and demonstrated success in modeling flow dynamics within the upper catchment (Procter et al., 2012, 2010b). Similarly, experiments using the Delft3D numerical model (Carrivick et al., 2010, 2009) were conducted to replicate 2007 conditions with reasonable success (Carrivick et al., 2010; Frimberger et al., 2021; Manville et al., 2013). These models are usually applicable to a single trigger, demanding multiple detailed scenario models (Graettinger et al., 2010; Hodgson et al., 2007; Manville et al., 1998; Procter et al., 2021).

1.4.4 The Importance of the Geological Record for Modern Hazard Planning

The historical record of activity at Ruapehu (post-1861 CE) is heavily biased toward smaller, more frequent events, thus the geological record remains indispensable for robust hazard planning (Cronin et al., 1997a; Donoghue, 1991; Graettinger et al., 2010; Hales, 2000; Lecointre et al., 1999, 2004a; Palmer, 1991; Voloschina, 2020). The Onetapu Formation includes prehistoric lahars that were one to two orders of magnitude larger in volume than the devastating 1953 Tangiwai disaster (Cronin et al., 1997a; Hodgson et al., 2007; Lecointre et al., 2004a), with the potential to overflow into the Tongariro River catchment, threatening larger populations and downstream infrastructure (Keys et al., 2008; Lecointre et al., 2004a; Procter et al., 2021). The geological record provides the essential long-term context, magnitude, and frequency data necessary for constraining computational models, developing mitigation strategies (such as the deflection bund), and ensuring modern plans account for the full

spectrum of potential catastrophic events (Hodgson et al., 2007; Keys et al., 2008; Procter et al., 2021).

1.5 Knowledge Gaps in Lahar Research at Ruapehu

Although Mount Ruapehu is one of the most instrumented and well-studied volcanic systems in New Zealand, significant gaps remain in our understanding of lahar generation, magnitude-frequency behaviour, and long term hazard behaviour which may be relevant in a changing climate. Modern monitoring provides detailed insights into small and moderate flows, but the geological record shows that prehistoric lahars were often substantially larger, more frequent, and more varied in triggering mechanism than those observed historically.

Several key knowledge gaps are identified that provides motivation for this study:

1.5.1 Limited understanding of large-magnitude prehistoric lahars

The depositional records from historical lahars at Ruapehu, such as the 1953, 1975, 1995-96, and 2007 events, are at least an order of magnitude smaller than some of the deposits preserved in the Onetapu Formation. Several prehistoric lahar deposits suggest flow depths several times higher than historic analogues and display cohesive debris-flow sedimentology which has not been observed in any historical lahar flows.

Despite their importance for hazard planning, the timing and triggering of these large events remain poorly constrained.

1.5.2 Poorly resolved trigger mechanisms for prehistoric flows

While historic lahars often have identifiable triggers (lake breakout, eruption-snow interactions, rainfall on tephra), triggering mechanisms for prehistoric flows have to be inferred from deposit characteristics. Better methods of identifying prehistoric triggering mechanisms require more

detailed and integrated sedimentological, geochemical, and stratigraphic assessment to quantify deposit characteristics.

1.5.3 Limited understanding of prehistoric Crater Lake eruptions

Lahars triggered by eruptions through the Crater Lake account for the majority of historical events, however that triggering mechanism is absent or uncertain in prehistoric Onetapu Formation members. The range of magnitudes of historical Crater Lake eruption lahars, as well as behaviour of single events versus Ruapehu's typical syn-eruptive multi-event sequences, as derived from tephra records, would better inform hazard models. In addition typical computational simulation tools ignore the complex source conditions of lahars at stratovolcanoes with crater lakes.

1.5.4 No probabilistic or magnitude-frequency model integrating geological and historical data

Existing hazard assessments rely heavily on the historical record and recurrence intervals of prehistoric Onetapu Formation lahars. They do not incorporate models that account for multiple triggers or changing hazard over the course of multiple eruption or lahar series. This lack of quantitative recurrence modelling restricts the ability to estimate the likelihood and magnitudes of large mass-wasting or multi-event Crater Lake eruption triggered lahars.

1.6 Thesis Objectives

This research aims to refine the record of Onetapu Formation lahars and improve understanding of lahar triggering mechanisms at Mt. Ruapehu with new records to inform new hazard analysis models. Specifically, the objectives are to:

(1) reassess lahar deposits to identify discrete events and revise stratigraphic relationships;

(2) characterise these deposits using grain-size statistics, lithological coding, and geochemical/spectral analytical techniques to identify diagnostic signatures of lahar provenance;

(3) infer provenance and triggering mechanisms for individual events using combined sedimentological, stratigraphic, and spectral evidence;

(4) model typical Crater Lake eruption triggered lahar generation using numerical simulations; and

(5) synthesise these findings into a preliminary multi-trigger probabilistic model that captures how different eruptive and non-eruptive processes modulate lahar hazard over time.

1.7 Thesis structure

This thesis is organised into the following chapters:

Chapter 1: Introduction and Literature Review (this chapter)

The introduction and literature review provides an overview of lahars as a hazard, including foundational research, triggering mechanisms, flow rheology and transformations, flow deposits and field interpretations, and the hydrothermal alteration of edifices that leads to many debris avalanche to debris flow transformations and the detection thereof in deposits. The next section covers Mt. Ruapehu, stratigraphy, lahars, and the previous and current hazard monitoring as well as areas of improvement.

Chapter 2: Deciphering Lahar Stratigraphy and Sedimentology on the Eastern Ring Plain of Mt. Ruapehu, New Zealand: New Insights from the Onetapu Formation

Chapter two reconstructs the detailed stratigraphy, sedimentology, and spatial distribution of Onetapu Formation lahars to refine interpretations of their triggering mechanisms, magnitudes, and flow behaviours. By refining and updating the sequence of prehistoric lahar events, it

strengthens the geological basis for modern hazard forecasts that must account for events much larger than those in the historical record.

Chapter 3: Geochemical and spectral techniques for lahar fingerprinting at Mt. Ruapehu: Improving assessment of triggering mechanisms and provenance

Chapter three develops new geochemical and VNIR-SWIR spectral fingerprinting tools to distinguish lahar units, identify source materials, and separate eruptive versus non-eruptive triggers. These techniques provide an independent way to test and refine stratigraphic correlations, improving the reliability of hazard assessments that rely on understanding lahar origins and pathways.

Chapter 4: Numerical modelling of eruption induced waves in Mt. Ruapehu's Crater Lake: Implications for lahar hazard models

Chapter four uses numerical simulations of eruption-driven waves in the Crater Lake to evaluate how explosive disturbance, vent location, and lake level control the probability and scale of outflow-generated lahars. These results help constrain which eruptive scenarios are capable of producing hazardous lake-breakout lahars, directly informing hazard models and monitoring thresholds.

Chapter 5: Discussion

Chapter five integrates geological, geochemical, spectral, and modelling results into a frequency-magnitude framework to estimate lahar recurrence probabilities through time. By linking physical processes with probabilistic behaviour, it provides an updated basis for lahar hazard planning and synthesises the key implications for monitoring, early warning, and long-term risk management.

Chapter five proposes a method to integrate stratigraphic, sedimentological, and geochemical data as well as numerical modelling to produce the most comprehensive analysis to date of

Ruapehu's late Holocene lahar record, ultimately improving multi-hazard risk assessment for one of New Zealand's most active volcanic systems.

Chapter 6: Conclusions

Conclusions restates the thesis objectives and how those were satisfied, along with how they fit into the greater work. Additionally, a subsection of future work objectives is presented, these are the objectives which have the greatest potential to expand the work already conducted or provide avenues for new research.

2 Deciphering Lahar Stratigraphy and Sedimentology on the Eastern Ring Plain of Mt. Ruapehu, New Zealand: New Insights from the Onetapu Formation

Brian K. Perttu[a*], Jonathan Procter[a], Anke Zernack[a], Stuart Mead[a]

[a]School of Agriculture and the Environment, Massey University, Private Bag 11222, Palmerston North 4442, New Zealand

*Corresponding author: brian.perttu@gmail.com

2.1 Abstract

Mt. Ruapehu, New Zealand, is an active stratovolcano surrounded by an extensive ring plain of mixed volcaniclastic debris. On the eastern ring plain the youngest stratigraphic unit is the Onetapu Formation, a sequence of debris and hyperconcentrated flow units deposited over the last 2000 years. This study focuses on the sedimentology of medial and distal mass-flow deposits from multiple events triggered by different syn-eruptive and non-eruptive processes. Integrating detailed grain size distributions from 19 sections with mapped (existing and new) lithofacies units across 21 logged sections presents new correlations between triggering mechanism, sedimentological features and distribution. Lithostratigraphic packages were identified based on repeated textural and compositional features, allowing for correlation of deposits in the Whangaehu and Wahianoa river catchments. A combined classification approach was used, involving flow type (debris or hyperconcentrated flow), depositional texture (e.g., massive, graded), and lithological composition. The Wahianoa catchment has been found to contribute to the Onetapu Formation, with multiple lahar sequences occurring during and soon after the 232CE emplacement of the Taupo Ignimbrite. Detailed grain size analysis shows variation of sorting within units, but general trends of debulking and increased sorting downstream and in overbank deposits.

Keywords: Ruapehu volcano, lahar stratigraphy, volcanic mass flow, grain size analysis

2.2 Introduction

Lahars are among the most common and deadly volcanic hazards and represent a spectrum of volcanic mass flows, ranging from hyperconcentrated flow to debris flow (Fig. 2.1)(Manville et al., 2013; Vallance, 2005). Lahars have a multitude of triggers and highly variable physical behaviours as a result of sediment concentration (Cronin et al., 1999), interaction with the wider

environment (Procter et al., 2010; Zernack, 2021) and flow rheology (Lube et al., 2012), which can only be determined via direct observation or measurement (Smith and Lowe, 1991). For prehistoric or unobserved lahars the determination of these behaviours can only be elucidated from the sediments and deposits they leave behind (Costa, 1988; Janda et al., 1981; Ponomareva et al., 1998; Smith, 1988; Smith and Lowe, 1991; Zernack et al. 2009).

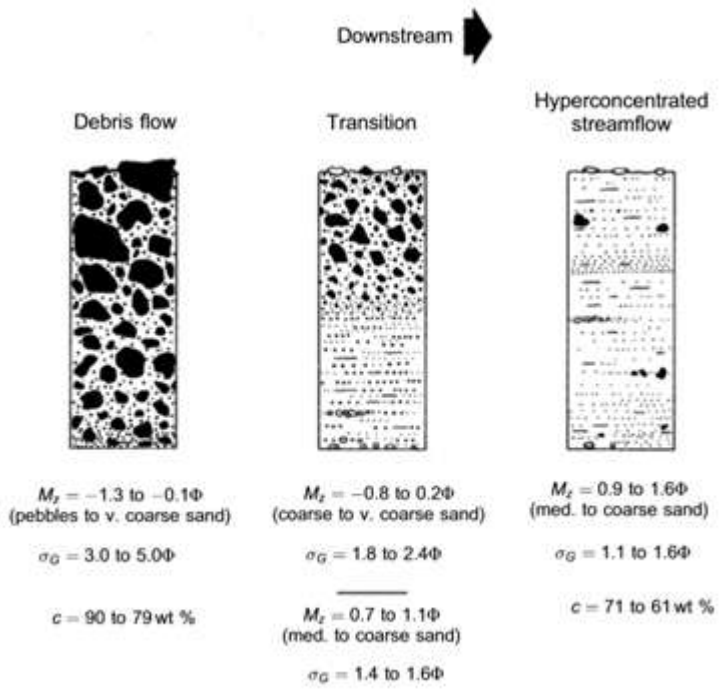


Figure 2.1 Schematic representation of deposit facies resulting from the longitudinal transformation of a lahar. M_Z is mean grain size, σ_G is sorting, and C is concentration of sediment. Size units are in phi scale and categories are calculated after Folk (1965). Manville et al. (2013) after Pierson and Scott (1985).

Complete grain size histograms inform transport dynamics (Costa, 1984; Cronin et al., 2000, 1997b, 1997a; Hodgson, 1993; Lavigne et al., 2000; Pierson et al., 1990; Pierson and Scott, 1985), while identification of clay proportions and species can inform rheological conditions (Fig. 2.2)(Costa, 1988, p. 88; Hampton, 1972; Scott et al., 1995), and, when combined with bulk composition data, the source material and locations can be inferred (Inoue, 1995).

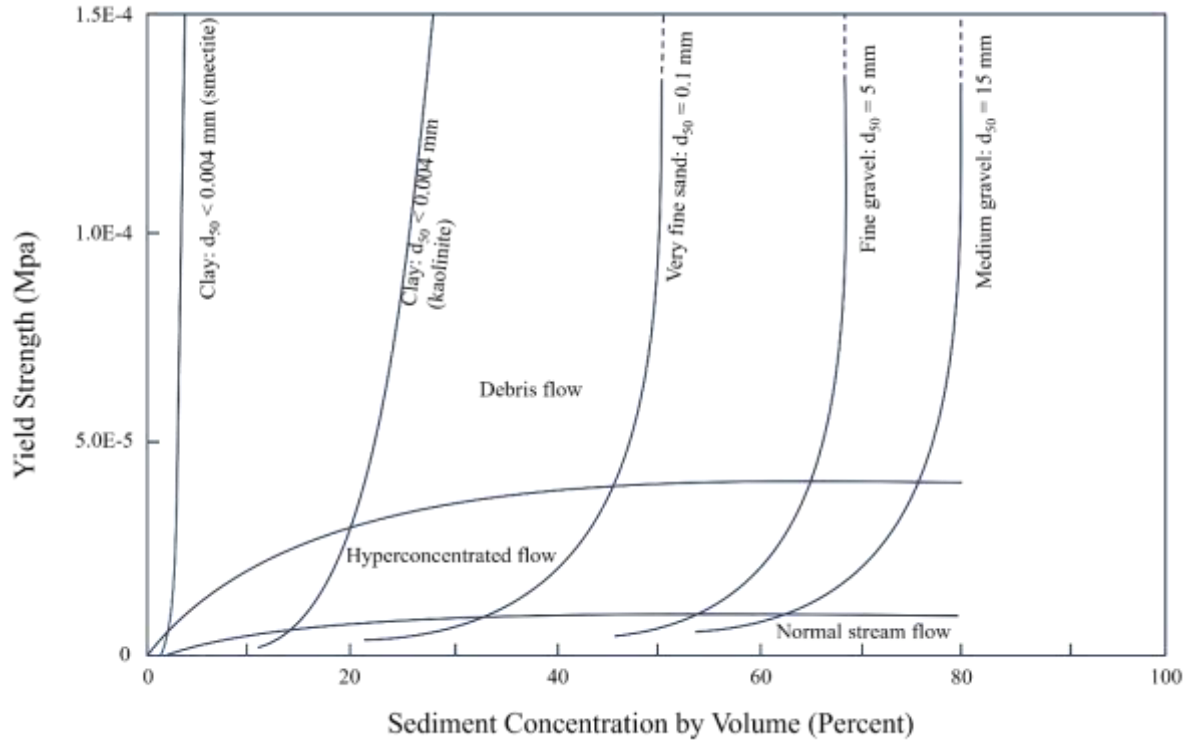


Figure 2.2 Classification of sediment-laden flows based on shear strength and sediment concentration. Increases in smectite (swelling) clay volume have a much more pronounced contribution to rheology changes than similar volumes of kaolinite clays. After Costa (1988).

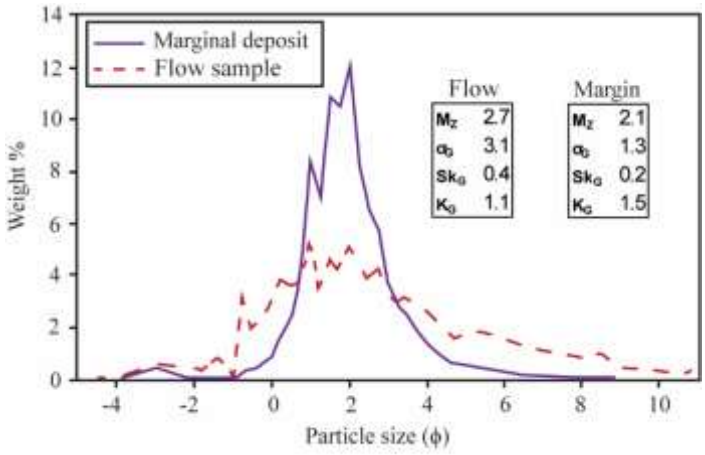


Figure 2.3 Comparison of particle size distributions of the upper 1 meter of the active flow and a marginal sediment deposit taken from an Onetapu e6 lahar 42 km downstream, near site 10 (this study). Size units are in phi scale and categories are calculated after Folk (1980). After Cronin et al. (2000).

Mt. Ruapehu, on the North Island of New Zealand, hosts both glaciers and the Crater Lake and has experienced frequent eruptions over the last 2000 yrs., with most eruptions generating

lahars (Hodgson et al., 2007; Lecointre et al., 2004a). The Whangaehu River and its catchment preserve a sedimentary record that comprises numerous volcaniclastic laharic deposits. Observations in New Zealand began with Māori oral traditions documenting lahar activity (>800 bce) (Gabrielsen et al., 2018), followed by written records from as early as the 1860s (Reverend Richard Taylor, 1861). Studies of lahars on Ruapehu have included direct measurements (Cronin et al., 1999, 1997a, 1997b), and modelling (Carrivick et al., 2010, 2009; Lube et al., 2009; Manville et al., 1998; Mead et al., 2016; Mead and Magill, 2017; Procter et al., 2012, 2010a, 2010b; Vignaux and Weir, 1990). Further detail into trigger and emplacement mechanisms have been postulated predominantly, through field mapping, sedimentological analysis, and stratigraphic measurements (Cronin et al., 1996; Donoghue, 1991; Donoghue and Neall, 2001; Graettinger, 2008; Graettinger et al., 2010; Hodgson, 1993; Hodgson et al., 2007; Hodgson and Manville, 1999; Kastl et al., 2010; Keigler et al., 2011; Kilgour et al., 2010; Lecointre et al., 1998, 2004a; Palmer, 1991; Palmer et al., 1993; Palmer and Neall, 1989; Rosenberg, 2000).

This study provides a new simplified lithostratigraphic framework and classification of lahar sequences derived from direct observations of deposits from the Whangaehu River in New Zealand. The new framework has been developed to accommodate newly discovered sequences and recent sedimentological characterizations and classifications. The use of structural, textural, and lithological codes for assessment of volcanic hazards has been used before (e.g., Palmer and Neall, 1991; Palmer et al., 1993; Zemeny et al., 2021; Purves, 1990) to categorize common sediment sequences and associate these with physical trigger and emplacement parameters. This study intends to create an updated set of sedimentologic and lithologic codes to account for the variations seen in the volcaniclastic (laharic) deposits in the Whangaehu River and Wahianoa catchments on Mt. Ruapehu.

2.2.1 Regional setting

Mt. Ruapehu is an andesitic stratovolcano, as well as the tallest (2,797 m) and only glaciated peak on the North Island of New Zealand. Surrounding Mt. Ruapehu's edifice is an extensive ring plain of volcaniclastic sediments and tephra predominantly derived from Ruapehu.

Volcanic activity at Mt. Ruapehu began between 250 – 309 ka (Gamble et al., 2003; Pure, 2020), and much of the edifice was built during four episodes of effusive activity: Te Herenga Formation (>ca. 120 ka), Wahianoa Formation (ca. 60-120 ka), Mangawhero Formation (ca. 15-60 ka), Whakapapa Formation (0 – ca. 15 ka) (Hackett and Houghton, 1989). However it has experienced no long periods of dormancy (Conway et al., 2016; Pure, 2020) and a more complete record of eruptive activity is preserved in the ring plain succession (Campbell, 1973; Cronin and Neall, 1997; Donoghue, 1991; Donoghue et al., 1995, 1999; Hackett and Houghton, 1989; Hodgson, 1993; Hodgson et al., 2007; Lecointre et al., 2004a; Palmer, 1991; Palmer et al., 1993; Palmer and Neall, 1989; Topping, 1973).

Within the last ~2 ka Mt. Ruapehu's Crater Lake formed and became the primary active vent (Donoghue et al., 1997), draining down the Whangaehu catchment and providing the impetus for the modern Onetapu Formation lahars (Hodgson et al., 2007; Lecointre et al., 2004b).

2.2.2 Background

Eruptions on Mt. Ruapehu have generated both tephra and lahars, yet lahars also occur during inter-eruptive periods (Cronin and Neall, 1997; Hodgson, 1993; Houghton et al., 1996; Lecointre et al., 2004b; Purves, 1990; Scott, 2013), and have caused significant casualties and economic losses, e.g. the 1953 Tangiwai disaster (Johnston et al., 2000; O'Shea, 1954; Stilwell et al., 1954). While the Whangaehu catchment has identifiable deposits from five historically observed Onetapu Formation lahars, other historic lahars have not produced preserved deposits, and some deposits from prehistoric Onetapu Formation members are an order of magnitude larger

than anything observed within the last ~160 years (Cronin et al., 1997a; Donoghue, 1991; Hodgson, 1993; Hodgson et al., 2007; Mead et al., 2021; Procter et al., 2021; Scott, 2013).

The Onetapu Formation units and lahar deposits form a distinctive fan on the eastern Mt. Ruapehu ring plain, and can be found along the entire length of the Whangaehu River (Hodgson, 1993), ranging from clast- or matrix-supported hyperconcentrated flow to clay-rich debris flow deposits with variable lithofacies, and individual formation members varying longitudinally. This is reflected in both the Whangaehu and Wahianoa catchments, where grain size characteristics of deposits reflect downstream transformations in lahar dynamics. Massive matrix-supported bouldery diamictons in the Whangaehu Gorge become matrix-supported pebbly diamictons in the medial zones, and clast-supported sandy hyperconcentrated flow deposits in distal zones and side channels (Graettinger, 2008; Hodgson, 1993; Hodgson et al., 2007; Lecointre et al., 2004a; Palmer et al., 1993). Previous lithofacies analyses have documented changes related to both the channel depositional environment, where coarser mid-channel deposits transition to thinner, lower median grain size overbank deposits (Fig. 2.3)(Cronin et al., 2000; Hodgson, 1993) as well as general clast size trends that follow a progressive decrease in both maximum and modal clast sizes downstream (Hodgson, 1993).

Previous work on categorizing lahar deposits in New Zealand was initially completed on Mt. Taranaki by Palmer and Neall (1991) and Mt. Ruapehu by Purves (1990) and Palmer et al. (1993) using codes derived from Miall (1978) and Schultz (1984). The sedimentological nomenclature and codes created for describing lahar deposits from Mt. Taranaki were later expanded by Zemeny et al. (2021) to account for additional parameters, including separating out categories for lithofacies and depositional environment in addition to flow types.

2.2.3 Onetapu Formation

The Onetapu Formation (Table 2.1, Fig. 2.4), encompassing all lahar deposits in the Whangaehu catchment since the deposition of the Taupo Ignimbrite (Hodgson, 1993), was initially divided

into 7 units (Donoghue, 1991; Hodgson, 1993), revised to 15 units after the 1995 lahars (Cronin et al., 1997b), then further split into 17-18 units (Hodgson et al., 2007; Lecointre et al., 2004b).

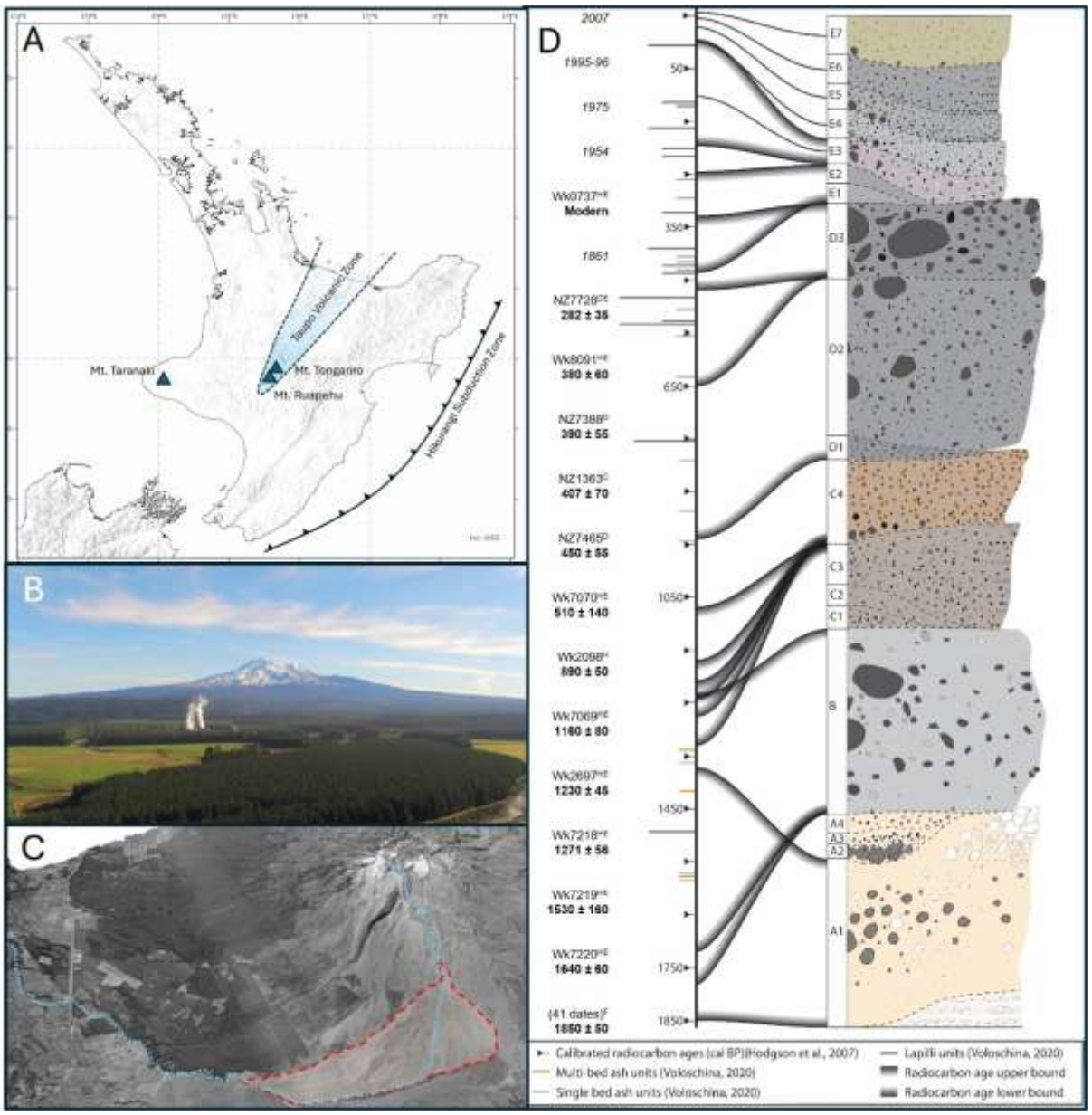


Figure 2.4 A) Overview map of the North Island, New Zealand Mt. Ruapehu shown in relation to the Taupo Volcanic Zone and Hikurangi Subduction Zone. B) View of Mt. Ruapehu from the south, with the Karioi Forest in the foreground, Tangiwai is in the center-right, and the Whangaehu River in the lower right. C) 1969 Crown Survey 2192 (LINZ, 2015) DSM oblique view northwest of Whangaehu River (blue) and Rangipo Desert/fan (red), with Karioi Forest in the lower center and Wahianoa Valley mid-right D) Schematic stratigraphic section of Onetapu Formation units combining descriptions from Hodgson et al. (2007)(Table 2.1) and field relations observed in this study, plotted against eruptive deposits (Voloschina, 2020), with dates of observed deposits and upper and lower bounding radiocarbon dates:

[HE]Hodgson et al. (2007), [DE]Donoghue et al. (1995), [D]Donoghue (1991), [C]Campbell (1973), [H]Hodgson (1993), [F]Froggatt & Lowe (1990).

Deposits within the Onetapu Formation have four identified and one theorized trigger mechanisms, based on the work of Lecointre et al. (2004) and revised from previous triggers (Section 3.5.1), which include:

- Crater Lake rim/tephra dam collapse, producing low-volume, high-peak discharge lahars
- Phreatomagmatic eruption ejecta mobilizing snow and ice, producing low-volume, low discharge lahars
- Eruptive displacement and waves of Crater Lake water, producing low- to high-volume and low- to moderate-discharge lahars
- Rainfall mobilizing unconsolidated tephra beds, producing low-volume, low-discharge lahars
- Crater Lake wall failure and release of all Crater Lake water, producing very high-volume, very high-peak discharge lahars (theorized)

Table 2.1 Onetapu Formation lithostratigraphic assemblages, naming correlations, volumes, estimated ages, notable characteristics, and interpreted trigger mechanism. Rows are shaded based on common assemblages. Modified from Hodgson et al., 2007

Formation-member	Correlations	Volume ($10^6 m^3$)	Est. age	Deposit characteristics	Interpreted trigger
One-7			CE2007		2007; tephra barrier collapse
One-6		1.01	CE1995/1996	Dominantly dark grey juvenile andesite clasts, non-cohesive	1995/96; lahars generated by eruptions through Crater Lake; dry eruptions; rain-triggered lahars
One-5	*On-o* C97 *1975* P	0.92	CE 1975	Rounded to sub-rounded iron-stained boulders (<0.13 m); medium grey aphyric lithics; dominantly dark grey porphyric juvenile andesite clasts; non-cohesive.	1975; eruption through Crater Lake.
One-4	*On-n* C97	<0.5	CE 1953	Sub-rounded boulders (<0.18 m); common grey and black lithic clasts; common hard grey scoria; contains anthropogenic debris from train crash; non-cohesive	1953; no eruption; tephra and ice barrier collapse; abundant juvenile content derived from 1945 eruption products that raised the outlet to Crater Lake following 1945 eruption.
One-3	*On-m* C97 *Ong*D *D12* P	<0.5	CE 1861; radiocarbon dated post-modern (CE 1750-1950)	Angular to subangular boulders (<0.55 m); dark grey vesicular and dark grey glassy juvenile andesite clasts; grey aphyric and purplish altered andesite lithics; cream lake sediment clasts; Taupo Pumice; underlain by thick soil horizon (0.2 m).	1861; reported to contain snow and ice (Taylor 1861); glacier barrier collapse, landslide and/or lake break-out?
One-2	*On-l* C97 *Onf*D *D11* P		250 ya; radiocarbon dated >282 ± 35 yr BP	Not identified in this study	
One-1	*On-E1*H *On-k* C97 *One-1/One-2*D *D10* P		300 ya; radiocarbon dated <390 ± 55 yr BP	Not identified in this study	
Ond-3	On-j C97 OndD	8.4	450 ya; radiocarbon dated 450 ± 55 yr BP,	Iron-stained sub-rounded boulders (<0.74 m); vesiculated dark grey bombs and quenched, joint-fractured glassy dense bombs containing	Abundant coarse juvenile content indicates dome emplacement and destruction; hydrothermally altered source rock indicates Crater Lake rim collapse; deposit

	D9 [P] C1 [C73]		<510 ± 140, <407 ± 70, >380 ± 60 yr BP	inclusions of baked lake sediment; dark grey glassy and porphyric juvenile andesite clasts; non-coated andesitic scoria; grey aphyric and purplish altered andesite; clay-rich matrix; smectite natroalunite, cohesive	extent and dimensions indicate large-scale eruption; eruption driven collapse of Crater Lake rim; entrainment of gravel including few boulders maintained to 137 km from the source by cohesive debris flow; catastrophic event.
Ond-2	*On-i* [C97] *D7* [P]	18.0		Sub-rounded boulders (<0.3 0 m*); dark grey glassy and dark grey vesicular andesite clasts; grey aphyric and purplish altered andesite lithics; cream lake sediment clasts	No distinctive juvenile content but large scale of event indicates possibly generation by Crater Lake barrier collapse (eruption-generated?) preceding dome emplacement (see Ond-3, above); entrainment of gravel >55 km from the source, sand >137 km from the source; catastrophic event.
Ond-1	*On-D1* [H] *On-h* [C97] D6 [P] C2 [C73]	<0.5	Radiocarbon dated <890 ± 50 yr BP	Grey aphyric andesite lithics; dark grey glassy juvenile clasts; overlies buried soil (0.3 m thick), containing tree roots, Tufa Trig Tephra, unconformity.	Small scale event; juvenile lithic content and presence of underlying Tufa Tephra suggest possibly rainfall-triggered remobilisation of tephra on upper slopes of volcano.
Onc-4	On-C4 [H] On-g4 [C97]	3.50	1100 ya; radiocarbon dated <1271 ± 56, <1230 ± 45 <1160 ± 80 yr BP.	Rounded boulders (<0.38 m*); vesiculated bombs of juvenile andesite; abundant pale brown-orange scoria; non-cohesive	Abundant pumice content indicates magma vesiculation at shallow level or dry conditions at an active vent initially not covered by lake waters; lahar most likely triggered by collapse of thick, voluminous pumiceous deposits on upper slopes of volcano during heavy rainfall (see rain-triggered lahars in 1995: Hodgson & Manville 1999); alternative mechanism: lahars generated by hot pyroclastic flows on ice/snow cap (Lowe et al. 1986); pumiceous sand transported >137 km from the source; catastrophic event.
Onc-3	On-g3 [C97]		Radiocarbon dated >1271 ± 56, >1230 ± 45, >1160 ± 80 yr BP	Common grey and black lithic clasts; common grey pumice; non-cohesive.	Common pumices within Onc-1-3 indicate eruption(s), dry vent conditions; heavy rain triggering collapse of thick tephra on upper slopes of volcano (cf. Ruapehu rain-triggered lahars, 1995); Whangaehu channel stripped of loose sediment; sand transported onto ring plain and >55 km from the source; catastrophic events.
Onc-2	On-g2 [C97]			Few to common grey scoria; common yellow-orange pumice; non-cohesive.	
Onc-1	On-C1 [H] On-g1 [C97] Onc [D] D5 [P]		1300 ya	Common grey and few black and red lithic clasts; common grey pumice; non-cohesive.	

	C3 [C73]				
Onb	On-B[H] On-f [C97] Onb[D] D3 [P] C4 [C73]	3.20	1550 ya; radiocarbon dated <1530 ± 160, <1640 ± 60 yr BP, >1271 ± 56 yr BP.	Iron-stained rounded to sub-rounded boulders (<0.56 m); dark grey glassy, vesicular and porphyric juvenile clasts; mud-coated pale grey to pale brown angular, dense andesitic scoria; grey aphyric and purplish altered andesite lithics; clay-rich matrix; halloysite natroalunite smectite; cohesive.	Distinctive mud-coated scoria indicates magmatic eruption through Crater Lake; hydrothermally altered source rock indicates collapse of Crater Lake rim; deposit dimensions and dominant juvenile content indicates large-scale eruption and Crater Lake rim collapse releasing large volumes of stored water; entrainment of boulders maintained by cohesive debris flow >55 km from the source, and gravel >137 km from the source; catastrophic event.
Ona-4		<0.5		Grey, black and red lithic clasts; c. 0.1 m above base of 0.3 m buried soil.	Unclear.
Ona-3	*On-A2*[H] *On-c* [C97]	<0.5	1700 ya	Abundant grey and common black lithic clasts; overlain by 0.09 m buried soil containing Taupo Pumice	Smaller Crater Lake rim collapse? Remobilisation of Ona-1 and/or Mangaio Formation deposits.
Ona-2	*On-A1*[H] *On-b* [C97]	<0.5	1750 ya	Iron-stained rounded to sub-rounded boulders (<0.12 m); grey aphyric, black and few red andesite lithic clasts; abundant Taupo Pumice at top of deposit	Smaller Crater Lake rim collapse.
Ona-1	On-a[C97] Ona[D] D1 [P]	3.00	1800 ya; radiocarbon dated >1530±160 yr BP, overlies c. 1850 Taupo/ ignimbrite.	Iron-stained rounded to sub-rounded boulders (<0.08 m*); dark grey porphyric andesite juvenile clasts; few red altered lithic clasts; creamy fresh lake sediment clasts; common Taupo Pumice; clay-rich matrix; smectite allophane; cohesive	Absence of juvenile component indicates no magmatic eruption; lake bed sediments and hydrothermally altered source rock indicates collapse of Crater Lake rim; iron-stained and altered clasts indicate remobilisation of Mangaio Formation to flow- presence of reworked Taupo Pumice and allophane indicate erosion of Taupo Ignimbrite and soil from channel sides and floodplain

As cited by Hodgson et al. (2007): [H] Hodgson (1993), [C97] Cronin et al. (1997b), [D] Donoghue (1991) & Donoghue & Neall (2001). As cited by Hodgson (1993): [C73] Campbell (1973), [P] Purves (1990). Italicized unit names indicate assumed correlations, where the same sections might not have been visited by different researchers, but units have similar stratigraphic correlations

The Onetapu Formation is grouped into assemblages A to E based on similarities in sedimentology and composition, as well as lacunae in the stratigraphic record, and individual members may be further subdivided into distinct events (Hodgson et al., 2007).

Onetapu A is the oldest assemblage, currently divided into Ona-1 – Ona-4 and has had units logged as Ona (Donoghue, 1991, Donoghue & Neall, 2001), On-a – On-c (Cronin et al., 1997b), and On-A1 & On-A2 (Hodgson, 1993). Onetapu A stratigraphically overlies and incorporates Taupo pumice, and the subunits are interpreted as Crater Lake rim collapses due to lack of juvenile components and presence of lakebed sediments, as well as hydrothermally altered source rock (Hodgson et al., 2007).

Onetapu B has had units logged as Onb (Donoghue, 1991, Donoghue & Neall, 2001), On-f (Cronin et al., 1997b), and On-B (Hodgson, 1993). Onetapu B has been interpreted as an eruption through the Crater Lake and collapse of Crater Lake wall due to predominance of juvenile lithics, mud coated scoria clasts, and hydrothermally altered material (Hodgson et al., 2007).

Onetapu C has had units logged as Onc (Donoghue, 1991, Donoghue & Neall, 2001), On-g1 – On-g4 (Cronin et al., 1997b), and On-C1 & On-C2 (Hodgson, 1993). Onc-3 and Onc-4 are interpreted as rainfall triggered lahars due to similarity to 1995 rainfall triggered deposits, including pumice from dry vents and predominant grey and black non-cohesive lithic fragments, with Onc-4 additionally posited as being a snow/ice melt triggered lahar due to greater volume compared to Onc-3 and 1995 lahars (Hodgson et al., 2007).

Onetapu D has had units logged as Ond (Donoghue, 1991, Donoghue & Neall, 2001), On-h – On-j (Cronin et al., 1997b), and On-D1 (Hodgson, 1993). Ond-1 has been interpreted as a small scale rainfall event due to abundant juvenile lithics; Ond-2 has been interpreted as Crater Lake collapse due to thickness of deposits and lack of juvenile content; Ond-3, correlated to On-j (Cronin et al., 1997b) and Ond (Donoghue, 1991, Donoghue & Neall, 2001) has been interpreted

to be the result of dome emplacement and Crater Lake collapse due to abundant coarse juvenile material as well as hydrothermally altered material (Hodgson et al., 2007)

Onetapu E has had units logged as One-1/One-2, Onf, and Ong (Donoghue, 1991, Donoghue & Neall, 2001), On-k – On-o (Cronin et al., 1997b), and On-E1 (Hodgson, 1993). One-3, possibly correlating to Ong (Donoghue, 1991, Donoghue & Neall, 2001) and On-m (Cronin et al., 1997b) was deposited from a lahar observed in 1861 and contained chunks of ice (Taylor, 1861). One-3 has been interpreted as Crater Lake breakout, possibly due to glacial barrier failure (Hodgson et al., 2007; Taylor, 1861). One-4, possibly correlating to On-n (Cronin et al., 1997b), was deposited in 1953 due to Crater Lake breakout from failure of a tephra/ice barrier from an eruption in 1945. One-5, possibly correlating to On-o (Cronin et al., 1997b), was deposited in 1975 from an eruption through Crater Lake (Nairn et al., 1979). One-6, contemporaneously logged as LH1-LH20 (with associated sub-unit numbers) (Cronin et al., 1997b), was deposited in 1995 as a sequence of lahars from eruptions through Crater Lake as well as subsequent rainfall triggered lahars. One-7 was deposited in 2007 from a lahar caused by Crater Lake breakout/tephra dam failure.

2.3 Methodology

2.3.1 Lithofacies Designations

Sediment from lahar sequences is exposed over the entire length of the Whangaehu river valley/channel, with sections from the source to ~40 km hosting the most recent and complete record of volcanogenic mass flows. The deposits confined and adjacent to the main drainage of the Whangaehu do not present many opportunities to examine transverse profiles and associated physiographic facies, however access to longitudinal profiles and associated sedimentological and textural variations within the same unit elucidate certain mass flow

characteristics. A set of criteria used to assess deposits along the Whangaehu are presented as lithofacies codes (this section), encompassing the various sediment textures and lithologies present in the logged sections.

Lithofacies codes are useful heuristics that have been used in the past to differentiate Mt. Taranaki laharic deposits (Zemeny et al., 2021) and the Whangaehu ring plain fan deposits. Specifically, Palmer et al. (1993) and Purves (1990) used an expanded version of Shultz's (1984) lithofacies codes to describe diamicton types (debris flows and hyperconcentrated flows), and gravel, sand, and mud lithofacies (including hyperconcentrated flow) after Miall (1978). Related studies examining rhyolitic pumice and ash resedimentation after large eruptions have created other schema: *grain size – sediment structure (componentry)* (Manville et al., 2005; Segschneider et al., 2002) for ease of logging three-variable systems. The designations used in this study have been modified to remove non-laharic codes and updated to reflect current nomenclature of lahar processes (Nemec, 2009; Pierson, 2005b).

While there's no codified lahar-specific protocol, grain-size characterization follows standard protocol (Folk and Ward, 1957; Wentworth, 1922), consistent with global practice for clastic sedimentology. Lithofacies designations similarly do not have a standardized scheme for lahar deposits, thus the codes here extend Miall's (1978) widely used clastic facies framework through a lineage of adaptation for volcaniclastic and laharic settings (Palmer et al., 1993; Purves, 1990; Shultz, 1984; Zemeny et al., 2021).

(**Hg**) Graded hyperconcentrated flow deposits in the middle Whangaehu drainage show reverse grading (Donoghue, 1991; Manville et al., 2005) or rare normal grading and are invariably well-indurated. Graded HF deposits often are preceded by a fine to medium sand base layer ranging from 2-10 cm with an abrupt transition to coarser sand and pebbles that gradually grades up into coarser grain sizes, often with an associated color change, and ranges in

thickness from 50 cm to 2 m. The upper sections commonly incorporate more altered clasts or pumice clasts.

(**Hc**) Crudely bedded hyperconcentrated flow deposits range in thickness from 40 cm to 1.5 m, with millimetre- to centimetre-scale silt layers, pumice lenses, or graded (normal or reverse) coarser sand and pebble clasts, with the coarser bands being less apparent on fresh exposures, and silt bands often unnoticeable until a fresh surface is exposed. Coarse banded crudely bedded hyperconcentrated flow deposits can also show reverse grading over the thickness of the deposit.

(**Hm**) Massive hyperconcentrated flow deposits are a single deposit of fine sand to pebble size sediments that range in thickness from 20-50 cm and are often composed of black lithic fragments that are poorly indurated.

(**$D_{M/C}$**) Matrix- and clast-supported debris flow deposits are 60 cm to 3 m thick deposits that are either matrix or clast supported and either lack internal structure or display weak reverse- to normal-grading. Clast sizes range from centimeter-size pebbles to 1.5 meter-size boulders in an indurated to well-indurated deposit.

Additional texture designations have been identified and directly modified from Zemeny et al. (2021) where there is a need to expand on the sedimentary features of a deposit (e.g. debris flows often have an inversely graded, progressively aggradational base that reflects an increasing solids fraction while the majority of the deposit is characteristically massive (Vallance, 2000)).

(**$g_{i/n}$**) Graded/Inversely Graded deposits can be normally or inversely graded throughout the entire unit, graded/inversely graded only for an upper or lower section, or inversely graded at the bottom and normally graded on the top.

(**m**) Massive deposits are often very poorly sorted in the case of debris flow deposits and poorly sorted with a bimodal size distribution for hyperconcentrated flow deposits, with few to no other sedimentary textures.

(**c**) Crudely bedded units are observed solely in hyperconcentrated flow deposits and are identified by millimetre- to centimetre-scale horizontal beds of either finer silt- to clay-size particles, or coarser, coarse sand to pebble-size particles.

A range of clast lithology designations have been investigated for Ruapehu and grouped into scoria, lithics, and pumices (Lecointre et al., 2004a). Later this was expanded to seven categories, including weathered andesite, hydrothermally altered andesite, juvenile andesite lithics, juvenile andesite scoria, mud-coated juvenile andesite scoria, lake sediments, and rhyolitic pumice (Hodgson et al., 2007). These categories have been bridged and simplified, including a category for sandy deposits without readily identifiable clasts. A new and separate category for altered material was introduced based on previous observations that large amounts of altered material in pre-lahar masses is a determining factor for transformation of a debris avalanche to a cohesive debris flow (Vallance and Scott, 1997). While the longitudinal transformation from massive debris flow deposits to bedded/normally graded hyperconcentrated flow deposits identified by Vallance and Scott (1997) is not readily recognizable at field sites in the Whangaehu catchment, the transition of altered rock landslides into clay-rich lahars has been posited as a trigger mechanism (Lecointre et al., 2004a).

(**<**) Sand sections are >50% sand and can contain associated lithic or pumice clasts.

(**A**) Altered lithic dominated deposits are composed of >50% argillic to advanced argillic altered tephra, lava, and breccia clasts. These clasts are identified by changes in colour, texture, luster, density, and competency and are often found as white or red, but predominantly yellow and gold, dull earthy clasts, including brown muddy rinds on otherwise juvenile scoria. Mineralized/muddy rinds on primarily scoriaceous material have been noted previously as

invariably occurring with debris flow deposits (Hodgson, 1993; Hodgson et al., 2007; Lecointre et al., 2004a) and were included into this category when samples were cleaned in the laboratory and found that the rinds did not wash off, while andesitic clasts from the same deposit lack a rind.

(**P**) Pumice-dominated lithology contains >70% pumice and rounded to sub-rounded white, cream or yellow coarse sand to pebble size clasts, associated with a predominantly pumice-derived sandy or silty matrix.

(**L**) Lithic andesite dominated samples are composed of >50% unaltered coarse sand to pebble size clasts, which are dense, dark colour, lustrous or weathered fragments of lava or dome rock.

(**S**) Scoria dominated deposits are composed of >50% clasts of andesite scoria, predominantly black vitric, and occasionally red. Scoria (unaltered) was originally logged under lithic but was designated a separate category following sample cleaning and investigation in the laboratory.

(**O**) Polylithological units are composed of fragments of rock of three different origins (i.e. scoria, pumice, lava, dome, tephra) and are distinguished based on significant proportions of three different colors of rock fragments (e.g. black, gray, red) following Zemeny et al. (2021). Percentages were estimated after sample cleaning and laboratory investigation.

2.3.2 Grain-size analysis

Sediment sequences were described and sampled at nineteen sites along the Whangaehu and Wahianoa catchments (Fig. 2.5) and correlated with previous sampling and mapping where previous sites could be reestablished. Field sites were located based on accessibility due to river stage. The upper boundary of the Taupo tephra, where extant, was the chronostratigraphic base of the measured sections.

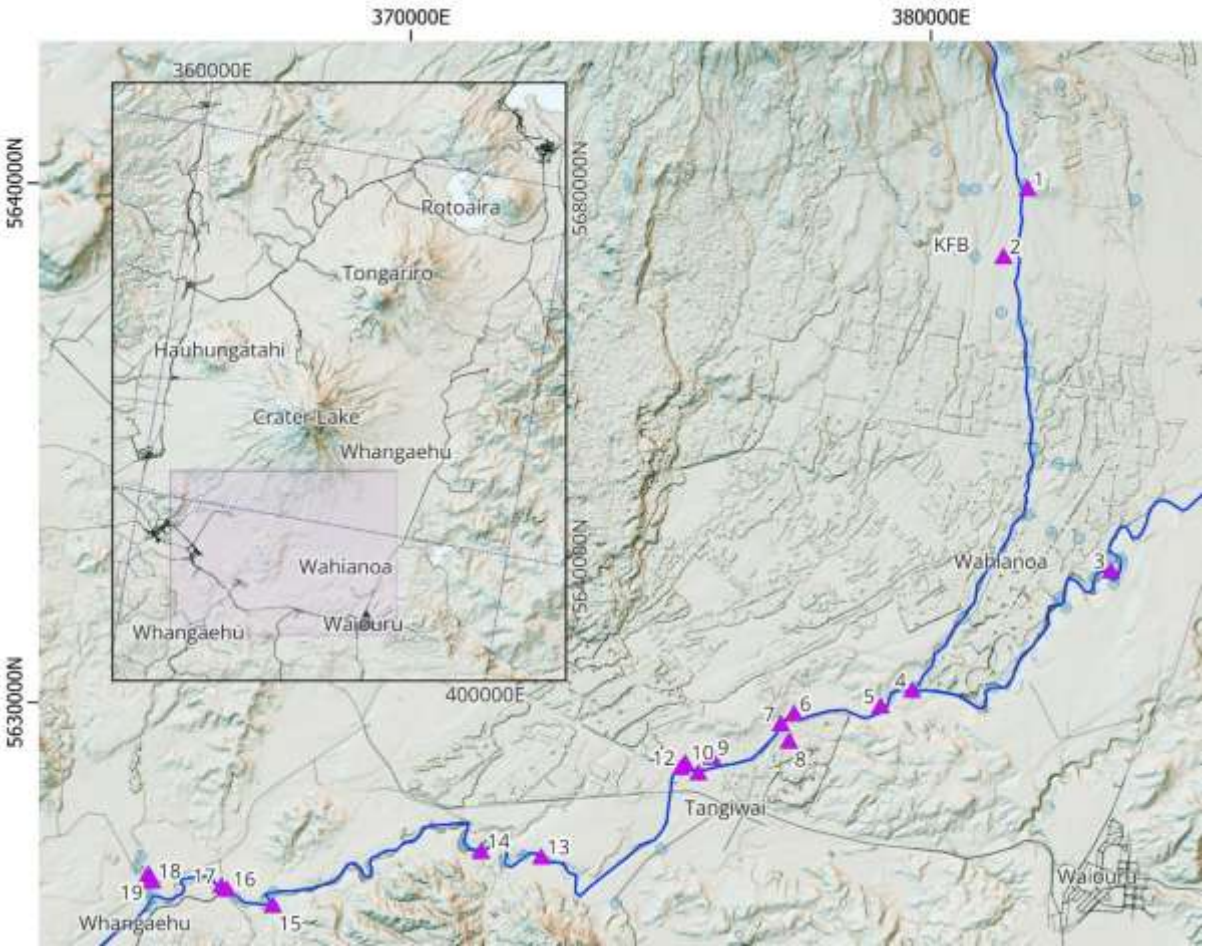


Figure 2.5 Reference sites along the Whangaehu and Wahianoa rivers. Solid colored triangles are where stratigraphic columns were logged and samples were selected, hollow circles are surveyed sites that were visited to check presence of Taupo Ignimbrite and any subsequent deposits. Map projection is New Zealand Transverse Mercator 2000, the regional map is NZ 8m Digital Elevation Model (2012) from LINZ Data Service. Location map is a 1 meter photogrammetric DSM from LINZ historical aerial imagery flown in 2000 and 2003.

Field sites were either excavated or cleared using a spade and soil scraper as needed before being documented and photographed, and then selected sites were sampled. Cobble-to-boulder size clast prevalence was estimated using field and photographic analysis, and sub-cobble size componentry was estimated by dry sieving in the laboratory. Using a modified method based on Hodgson et al. (2007) and Cronin et al. (1997b) a representative sample was extracted from selected units, dried for 24 hours in a 50° C furnace, manually disaggregated, and passed through a set of sieves (Boggs, 2009; Wentworth, 1922) ranging from 1.5 – 4 ϕ in half

ϕ increments. The >1.5 ϕ size fraction clasts were characterized based on lithological code sets, modified from a previously used -1 ϕ category (Cronin et al., 1997a; Hodgson et al., 2007) to account for lack of larger size category clasts at some deposits.

Samples were collected and oven dried in a Carbolite drying furnace (48 hours at 60 °C or until no more condensation is observed), dry hand sieved in half-ϕ steps between 1.5-4 ϕ after Hodgson et al. (2007) and weighed on a Mettler PE 1600 balance (0.00 g). >1.5 ϕ sediment was washed to remove clay and mud coatings for componentry analysis, dried (48 hours at 60 °C), and sieved in whole ϕ steps. Dry sieving was used due to number of samples and time constraints, however a subset of >1.5 ϕ samples were re-sampled via wet-sieving to provide a better control for representative wet vs dry sieving.

<4 ϕ sediment was analyzed via HORIBA Partica LA-950V2 laser particle size analyzer. Samples obtained or processed during the second field season (Fig. 2.5, sites: 14, 9, 7, 5, 4, 3, 2) were dried, dry sieved through 1.5 ϕ mesh, and a <1.5 ϕ sample was taken for laser particle analysis. Sieved sample data was then combined with laser particle size analyzer fractions and used as input for Gradistat (Blott and Pye, 2001) analysis to obtain mean, mode, sorting, and skewness via graphical methods (Folk and Ward, 1957)(Table 2.2) for direct comparison with previous studies.

2.4 Results and Findings

2.4.1 Stratigraphy and Unit Correlation

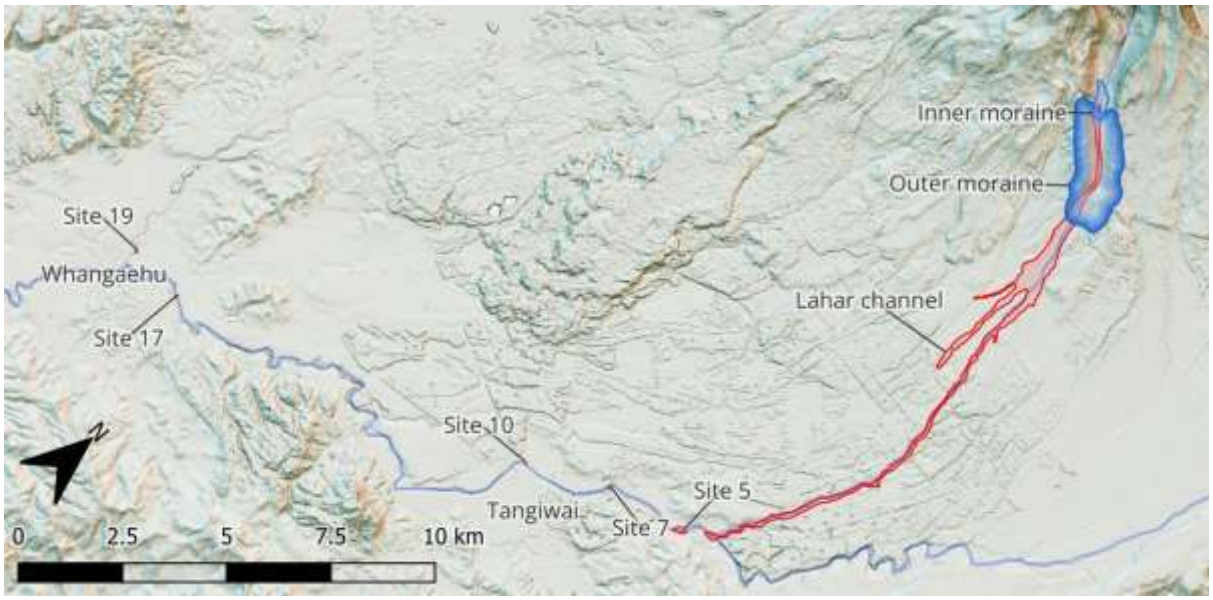


Figure 2.6 Mapped extent of Onetapu lahar deposits associated with the Wahianoa catchment. Lahar extents were observed from current stream exposures and Karioi Forest road sediment traps and inferred from satellite imagery. Moraine extents are generalized from field observations. Map projection is New Zealand Transverse Mercator 2000, the regional map is NZ 8m Digital Elevation Model (2012) from LINZ Data Service. Location map is a 1 meter photogrammetric DSM from LINZ historical aerial imagery flown in 2000 and 2003.

Stratigraphic columns, field photos, and samples (Appendix A1) were logged at 19 field sites and compiled into a composite stratigraphy (Figs. 2.6–2.7) to compare and correlate lahar deposits across the Whangaehu and Wahianoa catchments. The basal contact of each stratigraphic section varied depending on local controls and at some sites (1, 2, 4, 5, 10a, 13a, 17, and 19), it was defined by the presence of the Taupo Ignimbrite or an older underlying rhyolitic tephra. At other sites (3, 6, 7, 8, 9, 10, 11, 12, 14, 15), it coincided with the modern water level of the Whangaehu, Wahianoa, or their tributaries. And at remaining sites (13, 16, 19), excavation terminated at the depth where clast sizes or deposit induration prevented further digging by hand tools, which also influenced site selection.

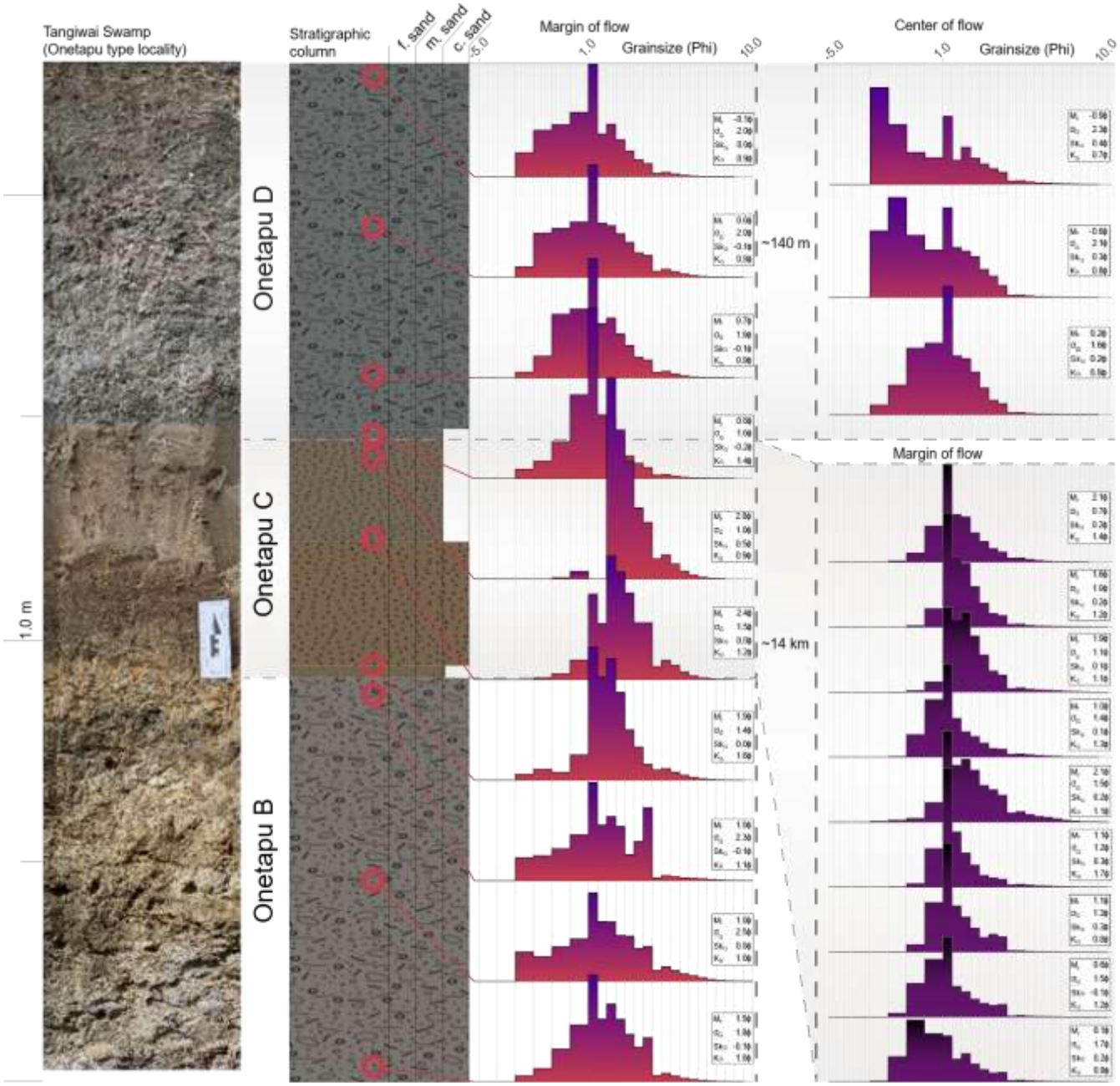


Figure 2.7 Example stratigraphic column with grain sizes, composition, field observations, and sieving results of sampled sections. Field grain size estimates were divided into <fine sand, fine sand, medium sand, coarse sand, and gravel with no upper size limit. Composition was noted based on lith code analysis of clasts and matrix where applicable. Samples were sieved in full ϕ increments from maximum grain size to 1.5 ϕ, in 0.5 ϕ increments from 1.5ϕ to 4.0ϕ, inclusive, and sizes smaller than 4.0ϕ were determined by laser particle grain sizing.

Table 2.2 Grainsize characteristics of Onetapu deposits by distance (Appendix A2 & A3). Units are listed by site, bottom to top. Distances are in kilometers from the catchment source, where Whangaehu is default and Wahianoa derived deposits are noted with [A]. Units are subdivided into members where known, and left blank if undifferentiated. Units with unknown associations were left blank. SP indicates stratigraphic position of the sample within the unit: Base, Middle, Top, or Entire.

Site	Dist	Name	Unit		SP	M_z	σ_G	Sk_G	K_G
1	7.5[A]	*Wai09*	**Ona**		E	-0.61	2.23	-0.27	0.74
		Wai06	**Ona**		E	2.62	1.72	-0.27	1.14
		WB	**On**		M	-1.53	2.26	0.81	0.27
		Wai05	**On**		E	2.45	1.28	-0.04	1.38
2	10[A]	*MPL*	**Ona**	**a1**	M	0.08	2.52	0.11	1.32
		MPU	**Ona**	**a1**	M	0.85	2.5	0.01	1.11
3	29.5	*Lower95*	**One**	**e6**	B	1.27	1.54	0.41	2.11
		L95m	**One**	**e6**	M	1.8	1.23	0.36	1.27
		L07u	**One**	**e7**	E	0.18	1.7	0.28	1.01
4	18.5[A]	*WC*	**Ona**	**a1**	M	-3.17	2.82	1.05	0.53
5	19[A]	*POnaO*	**Ona**	**a1**	E	0.2	2.63	0.24	0.99
		POnaM	**Ona**	**a2**	M	0.81	1.12	0.11	3.2
		POnaT	**Ona**	**a2**	T	2.02	1.37	0.02	1.06
	36.5	*POndB*	**Ond**	**d1**	B	1.93	1.39	0.46	1.06
		POndM	**Ond**	**d1**	M	0.28	2.42	0.3	0.86
6	38.5	*RR6*	**Onc**	**c4**	M	1.43	0.91	0.58	1.5
		RR5	**Onc**	**c4**	T	2.11	1.39	0.21	1.32
		RR4	**Ond**	**d2**	B	-0.16	2.04	0.01	0.92
		RR3	**Ond**	**d2**	M	-0.2	2.08	0	0.77
		RR2	**Ond**	**d2**	T	1.42	1.75	-0.13	1.73
		RR1	**Ond**	**d3**	M	-0.74	2.66	-0.18	0.63
7	22[A]	*RRW1*	**Ona**	**a1**	M	0.08	1.59	0.35	1.21
	39.5	*RRW2*	**Onc**	**c4**	B	1.29	1.7	0.29	1.01
		RRW3	**Onc**	**c4**	T	-1.74	3.49	0.35	0.65
8	22.5[A]	*rp0*	**Ona**	**a1**	T	1.67	1.65	-0.17	1.07
	40	*rp1*	**Onb**		B	1.87	1.98	-0.02	1.09
		rp2	**Onb**		T	1.94	1.43	-0.14	1.65
		rp3	**Onc**	**c4**	B	2.15	1.01	0.19	1.5
		rp4	**Onc**	**c4**	M	2.04	1.06	0.31	0.66
		rp5	**Ond**	**d2**	B	0.41	2	-0.23	0.77
		rp6	**Ond**	**d2**	M	-0.1	1.96	0.01	0.78
14	48.5	*SBSand*	**One**	**e3**	T	2.59	1.52	0.38	1.31
		SBSilt	**One**	**e3**	E	5.77	1.56	-0.15	0.79
15	54.5	*PB10*	**Onb**		T	3.13	0.82	0.25	2.46
		PB09	**One**	**e3**	M	0.54	2.39	-0.21	0.78
		PB08	**One**	**e3**	T	1.73	1.83	-0.21	1.36
		PB04	**One**	**e4**	T	-0.33	2.66	-0.07	0.69
		PB05	**One**	**e4**	M	0.04	2.17	0.13	0.96
		PB03	**One**	**e6**	B	2.43	0.97	0.1	1.25
		PB02	**One**	**e6**	M	1.66	0.84	0.4	0.87
		PB01	**One**	**e7**	M	1.05	1.64	-0.09	1.38
16	55.9	*A_mbq*	**Onc**	**c3**	B	0.11	1.69	0.23	0.86
		B_mbq	**Onc**	**c3**	M	0.59	1.5	-0.12	1.18
		C_mbq	**Onc**	**c3**	M	1.1	1.26	0.28	0.84
		D_mbq	**Onc**	**c3**	M	1.09	1.24	0.27	1.71
		E_mbq	**Onc**	**c3**	T	2.08	1.47	0.24	1.12
		F_mbq	**Onc**	**c4**	B	1.04	1.42	0.14	1.27
		G_mbq	**Onc**	**c4**	M	1.94	1.12	0.07	1.13
		H_mbq	**Onc**	**c4**	M	1.64	1	0.22	1.15
		MQ1	**Onc**	**c4**	T	1.27	1.51	0.21	1.02
		MQ2	**Ond**	**d2**	M	-0.39	2.61	-0.09	0.8
		MQ21	**Ond**	**d2**	M	-1.59	2.7	0.43	0.63
		MQ3			E	1.21	2.29	-0.2	1.2
		MQ4	**Ond**	**d3**	E	-0.33	2.42	-0.01	0.62
		MQ5			E	2.25	1.39	-0.06	1.38
		MQ6	**On**		M	1.62	0.93	0.16	1.45
17	38.5[A]	*MB_1*			M	2.1	0.7	0.2	1.39
	56	*MB_2*	**Onb**		E	-0.32	2.58	-0.11	0.63
		MB_3	**Onc**	**c4**	B	1.95	1.35	0	1.17
		MB_4	**Onc**	**c4**	M	1.27	1.26	0.01	1.58
		MB_6	**Ond**	**d2**	M	-0.29	2.39	0	0.73
18	58.5	*M7_2*			M	0.02	2.36	0.17	1.13

9	40.5	*DRC*	**Ond**	**d1**	E	1.79	1.3	0.42	1.4
10	41	*TS2SDB*	**Onb**		B	1.53	1.79	-0.06	0.96
		TS2SDM	**Onb**		M	0.97	2.46	-0.02	0.95
		TS2SDT	**Onb**		T	1.01	2.27	-0.08	1.09
		TS2BSB	**Onc**	**c4**	B	1.9	1.43	-0.01	1.63
		TS2BSM	**Onc**	**c4**	M	2.41	1.5	0.02	1.16
		TS2BSU	**Onc**	**c4**	T	2.75	0.99	0.51	0.91
		TS2_B	**Ond**	**d1**	B	0.58	1.61	-0.24	1.36
		TS2_1	**Ond**	**d2**	M	0.69	1.85	-0.1	0.86
		TS2_2	**Ond**	**d2**	M	0.64	1.96	-0.13	0.84
		TS2_3	**Ond**	**d2**	T	-0.1	2.02	0.03	0.94
11	41	*rpS2U*	**One**	**e3**	M	-0.21	1.7	0.04	0.95
12	41	*TPBL*	**Ond**	**d2**	B	0.17	1.64	0.18	0.83
		TPBM	**Ond**	**d2**	M	-0.57	2.06	0.34	0.79
		TPBU	**Ond**	**d2**	T	-0.91	2.31	0.35	0.68
13	46.5	*Q1*	**Onb**		T	0.05	1.97	0.1	0.69
		Q2	**Onc**	**c3**	M	1.95	0.94	0.21	1.22
		Q3	**One**	**e3**	E	2.58	0.73	0.2	1.58
		Q4	**One**	**e3**	M	1.92	0.87	0.15	1.01
		Q5	**One**	**e3**	E	2.28	1.3	-0.16	1.07
		Q6	**One**	**e4**	B	1.76	0.77	0.04	0.73
		Q7	**One**	**e4**	M	1.08	1.35	0.07	0.96
		Q8	**One**	**e4**	T	1.6	0.94	0.2	1.43
		M6_2			M	1.26	1.49	-0.26	0.9
		M5_2			E	1.97	0.97	0.21	0.85
		M5			E	1	2.66	-0.48	0.8
		M4			E	1.12	1.17	0.24	1.49
		M3			E	0.93	0.91	0.02	1.15
		M2			E	0.93	1.07	0.15	0.77
		M1			E	-0.22	1.99	-0.01	0.83
19	41.1[A]	*MR1*	**Ona**		M	1.14	1.19	0.24	1.41
		MR2	**Ona**	**a1**	M	2.54	0.82	0.1	1.08
		MR3	**Ona**	**a1**	M	1.92	1.05	-0.02	0.97
		MR4	**Ona**	**a1**	M	1.72	1.63	-0.17	1.02
	58.6	*MR5*	**Onb**		E	-0.09	3.2	-0.39	0.69

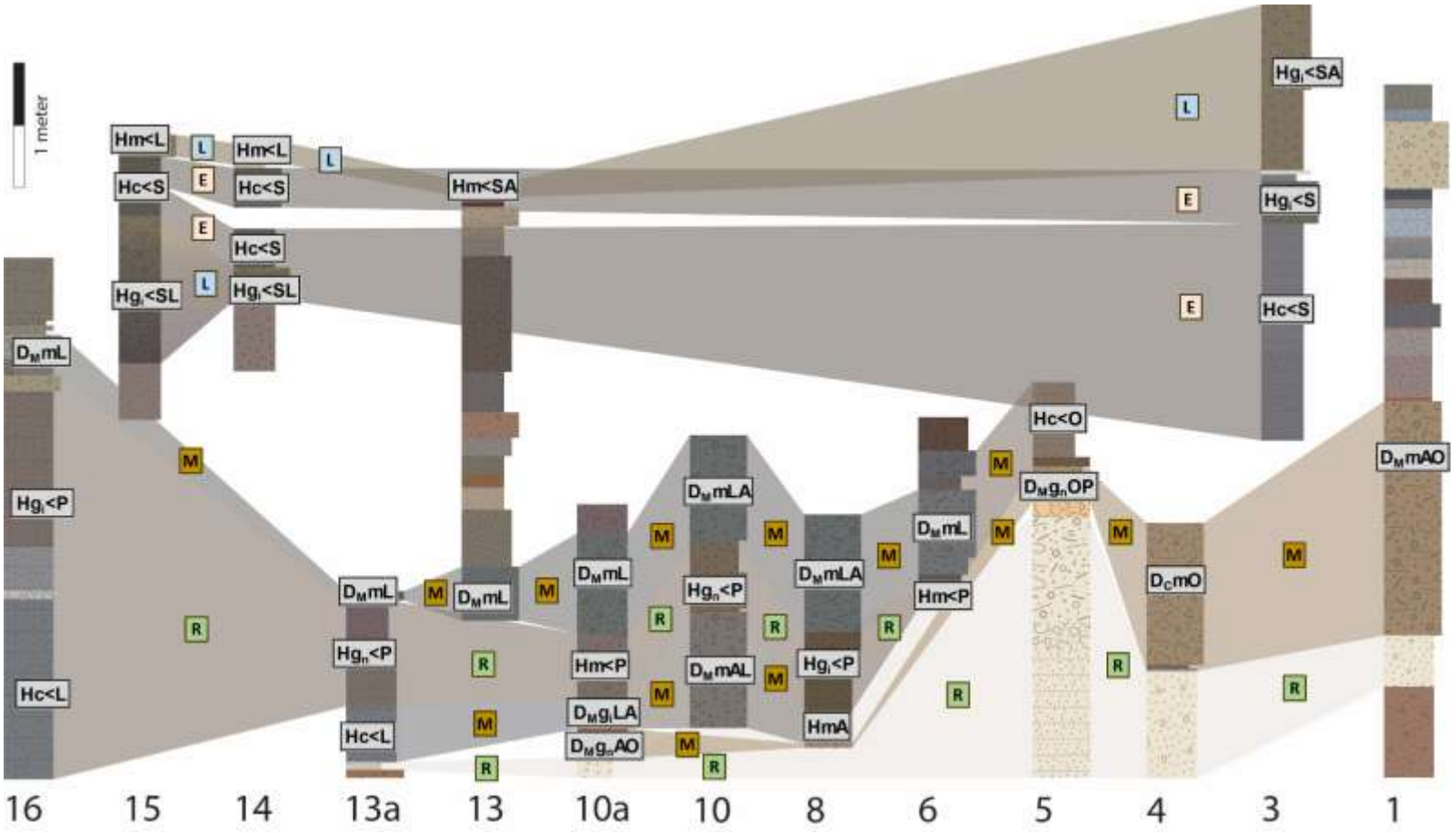


Figure 2.8 Stratigraphy at reference sites along the Whangaehu and Wahianoa catchments. Unit colors are derived from field photos, diagnostic textures are approximated using USGS swatches (U.S. Geological Survey, 2006) for reproducibility, inferred trigger mechanisms are indicated by L: Lake Outbreak, E: Eruption-Crater Lake, R: Remobilised, M: Mass-wasting. Links between columns are shaded where units are readily identifiable via stratigraphic correlations or past studies. Sites 10a and 13a were not sampled, but stratigraphic correlations were logged. Site 10a (Fig. 2.10c) is the Whangaehu cut bank closest to site 10. Site 13a is an exposed track cutting next to an access road ~400 m downstream from site 13.

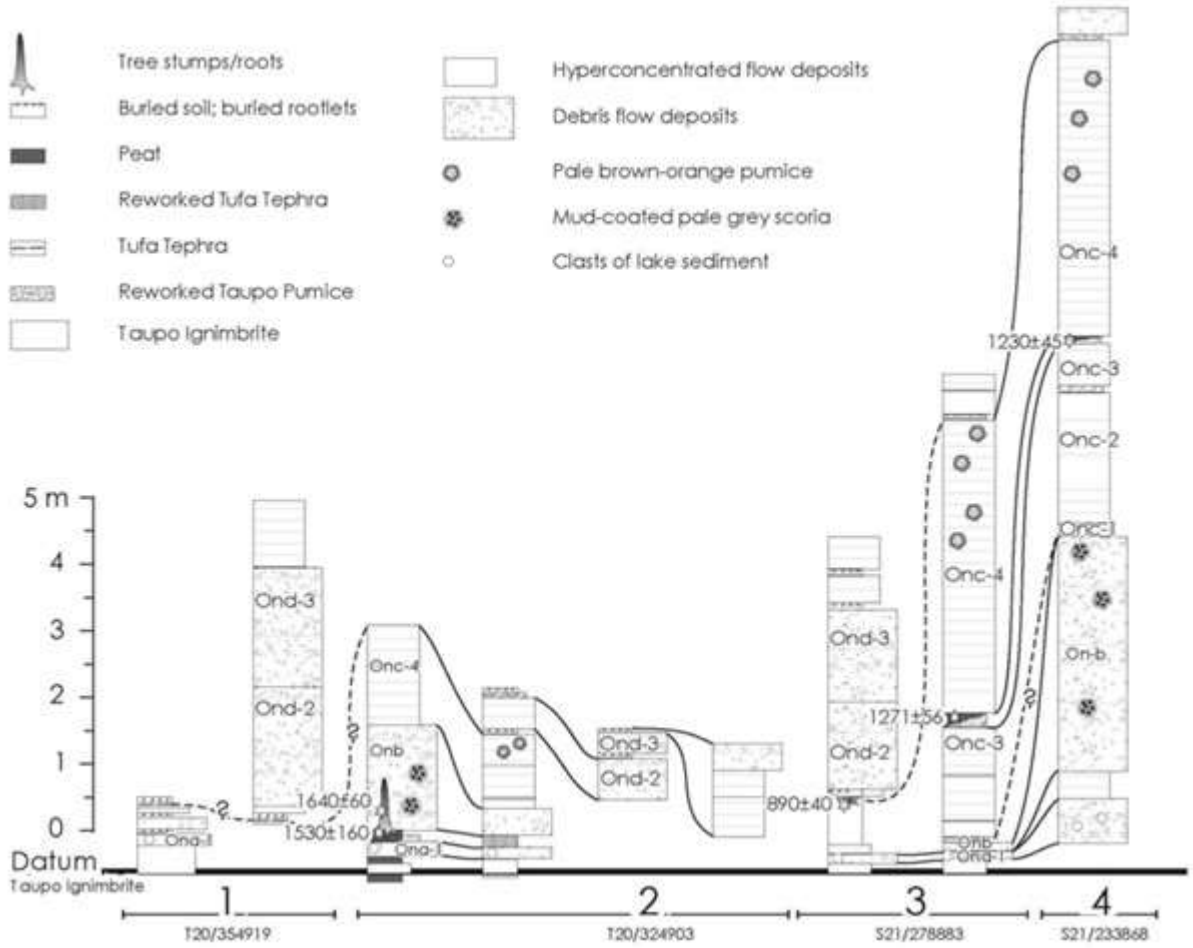


Figure 2.9 Onetapu Formation stratigraphy and radiocarbon dates from Hodgson et al. (2007). Stars mark radiocarbon date localities. Solid lines mark confident correlations between units; dashed lines mark tentative correlations. Column 1 was near site 5 (Fig. 2.5), column 2 was from river exposures between sites 8 and 10 (Fig. 2.5), column 3 was from exposures near site 14 (Fig. 2.5), column 4 is site 16 (Fig. 2.5)



Figure 2.10 Selected representative site photos with code descriptors for logged units. Thicknesses are the same as marked sites from Fig. 2.8. (A) Site 16 (Fig. 2.5) has sequence of Onetapu C hyperconcentrated flow deposits with a sequence of Onetapu D debris flow and hyperconcentrated flow deposits on top. (B) Site 15 (fig. 2.4) has Onetapu E3 hyperconcentrated flow deposits that underwent soft sediment deformation with the underlying soil layer, Onetapu E4 inversely graded hyperconcentrated flow deposits, and Onetapu E6 & E7 hyperconcentrated flow deposits. (C) Site 10a (fig. 2.4) has deposits of Onetapu A, B, C, and D over a thin layer of Taupo, approximately 4 meters above current river level. (D) Site 8 (fig. 2.4) has thin deposits of Onetapu A and B, and thicker layers of Onetapu C and D. (E) Site 4 (fig. 2.4) ~2 meters above current river level rounded to sub-angular clast supported boulders in Onetapu A overlie Taupo deposits. (F) Site 2 (fig. 2.4) Onetapu deposits overlie sequences of tephra and older lahar units. (G) KFB (fig. 2.4) a similar sequence to site 2 with older lahar units under pre-Taupo and Taupo deposits. (H) Site 19 (Fig. 2.5) Onetapu hyperconcentrated flow units (~1.6 m) and reworked Taupo ash and pumice (~5 m) overlie Taupo deposits 300 m up a tributary from the Whangaehu.

The sedimentary deposit types and dominant lithology percentages at selected sites were plotted together for comparison of different selected sites (Fig. 2.12). Figure 2.12 highlights that despite a simplified stratigraphy being presented by past researchers (e.g. Donoghue, 1991; Hodgson, 1993; Palmer, 1991; Purves, 1990) limited by a small number of datable units, the complexity that exists in the grainsize and componentry within the variety of sedimentological units presents a more detailed reconstruction of lahar activity with a greater variety of transformations. In many ways the detail contained in the sedimentological classifications and correlations, parallels the numbers of observed events in the historic record.

Onetapu A subunits could only be reliably identified at Site 1 and at other sites undifferentiated Onetapu A units were referred to as Ona. The pumice clasts in Onetapu A deposits are a mixture of white and yellow, rhyolitic and andesitic, respectively. No field relationships between Wahianoa and Whangaehu catchment Onetapu A units were observed, and with the exception of Sites 5 and 19, all Whangaehu Onetapu A units had a reddish-brown matrix matching descriptions of upper Whangaehu Onetapu A units (Hodgson, 1993; Hodgson et al., 2007).

Onetapu B is readily identified at three middle Whangaehu river sites above Tangiwai (e.g. 8, 10, and 10a), and is a well-indurated grey debris flow deposit with distinctive mud coating/rinds on scoria and pumice pebbles.

Onetapu C deposits are predominantly Onetapu C4 pumice/scoria hyperconcentrated flow deposits and one identified Onetapu C3 lithic/pumice hyperconcentrated flow deposit, located at sites along the Whangaehu river (e.g. 6, 8, 10, 13a, and 16). Onetapu C units at site 6 are thin (Fig. 2.5), and do not display the textures observed at other sites and are recognized solely by composition and stratigraphic relationships. Where inverse grading is present, it is due to larger pumice clasts (similar to deposits mentioned in Manville (2005) and Donoghue (1991)) (site 16).

Onetapu D is found at sites along the Whangaehu river (e.g. 6, 8, 10, 10a, 13a, and 16), and composed of a well-indurated mix of lithic, scoria, and altered clasts, including mud-coated/rind clasts of scoria and pumice similar to those in Onetapu B. Onetapu D1 is a finer-grained hyperconcentrated flow deposit associated with Onetapu D2, and visually Onetapu D2 and D3 are indistinguishable except being separated by a compositionally similar hyperconcentrated flow layer at site 9.

Onetapu E units are located along the Whangaehu river and are mostly valley confined in contrast to probable overbank deposits of e.g. Onetapu C and D at sites 8, 10, and 10a. Onetapu E1 and E2 were not reliably identified in this study. Onetapu E3 is a massive hyperconcentrated flow deposit that shows soft sediment deformation features where it overlies a purple-grey pumice sand layer at sites 14 and 15 (Fig. 2.5). Onetapu E4 is a massive hyperconcentrated flow deposit that primarily contains dark scoria and lithic sands. Onetapu E 5 was not reliably identified in this study. Onetapu E6 is a crudely bedded/inversely graded hyperconcentrated flow deposit composed predominantly of dark scoria and lithic at sites 3, 14, and possibly 15. Onetapu E7 is a dark yellow massive scoria, lithic, and altered component-rich hyperconcentrated flow deposit at sites 3, 13, 14, and possibly 15.

The most complete records of the Onetapu Formation for this study are the Tangiwai Swamp type locality (Donoghue, 1991; Hodgson, 1993) and associated cut bank (Sites 10 & 10a) that record overbank deposits of Ona-1, Onb, Onc-4, and Ond-2, and the Marae Bridge roadcut (Site 17) which records the same units.

A previous survey of the upper Wahianoa catchment noted two lahar units under a tephra layer with an 830 B.P. minimum age (Donoghue, 1991). Those units were identified near Site 13 (Fig. 2.5) in the upper Wahianoa valley (Fig. 2.11) and expanded. The sequence consists of two lahar diamicts over a sequence of phreatomagmatic and reworked deposits interbedded with Taupo Ignimbrite and remobilized Taupo Ignimbrite. The stratigraphic sequence from Figure 2.10

shows Taupo Ignimbrite deposition, erosion, two lahars incorporating distinct phreatomagmatic deposits (units 1 & 2), and intermittent reworked lahar (units 4 & 6) and streamflow (unit 5) deposits, separated by a soil layer (unit 7) from two overlying Wahianoa-Onetapu units. Tephra and Taupo Ignimbrite layers provide the bounding ages ~830 to 1850 B.P. (Table 2.1, Fig. 2.4).



Figure 2.11Reference site 1 on the upper Wahianoa, showing a sequence of events from the Taupo ash to several subsequent lahars. Pre-Taupo deposit, Taupo deposit, and Onetapu lahar are labelled, and the intermediate sequence is numbered based on interpreted order of events.

2.4.2 Sedimentary Characteristics and Facies Analysis

Grain size distributions and statistical parameters (Table 2.2) reveal inter-unit and stratigraphic position variations at all locations across all samples. Higher mean sorting values occur in units with a debris flow subunit. Onetapu A (1.77σ_G), Onetapu B (2.06σ_G), and Onetapu D (2.06σ_G), have higher mean sorting values (poorly sorted to very poorly sorted) than grouped

Onetapu E (1.46σ_G) and Onetapu C (1.3σ_G) (poorly sorted) and higher sorting values tend to correspond to finer mean sizes when units are grouped. Additionally within unit, skewness was highest in the Onetapu C (0.20Sk_G, Fine skewed) unit and lowest in the Onetapu B (-0.05Sk_G, Near symmetrical) and Onetapu D (0.07Sk_G, Near symmetrical) units, with Onetapu E and Onetapu A being equal (0.10Sk_G, Fine skewed) Combined stratigraphic position statistics give greatest mean size, greatest positive skewness, and lowest kurtosis for the middle of a sampled deposit (0.73M_Z, 0.14σ_G, 1.07Sk_G) vs base (1.26M_Z, 0.09σ_G, 1.16Sk_G) or top (1.24M_Z, 0.11σ_G, 1.18Sk_G), and a general increase in sorting with stratigraphic position 1.52K_G, 1.68K_G, 1.74K_G.

At the Tangiwai Swamp type locality (Sites 10 & 12; Table 2.2, Fig. 2.7), lateral changes away from the thalweg can also be observed within the Onetapu D unit. Leptokurtosis increases laterally from the thalweg, and ~100 m from the main channel, the Onetapu D overbank deposit has a coarser-skewed, greater mean size basal layer with high kurtosis, transitioning upward into finer, more mesokurtic sediments. While at site 12, representing a whaleback bar deposition from the same flow, shows increasing leptokurtosis, poorer sorting, and finer skew upward in the sequence, along with greater silt and clay content than overbank counterparts.

Sedimentary textures fall into three main categories: Graded/inversely graded, Massive, and Crudely bedded. Debris flow deposits typically display a massive texture throughout or an inversely graded base grading into a massive matrix. In contrast, hyperconcentrated flows often exhibit inverse grading or crude bedding, sometimes with horizontal bands or lenses of coarser material. Crude bedding was best observed on exposed faces as continuous horizontal bands of slightly coarser material, or semi-continuous horizontal bands and lenses of silt.

Lithological composition was classified into five categories: Sand-size undifferentiated grains, pumice-dominated, polylithologic, lithic-dominated, and altered lithic-dominated (chalky white/yellow argillic clasts). Sand designation was used where grain sizes were too minute to

make an accurate field assessment of grain lithology percentages and were instead estimated using magnification in the laboratory.

Pumice was rare except in the Taupo Ignimbrite layer and some hyperconcentrated flow units, where it appeared in semi-discrete lenses or as inversely graded tops. Altered lithics were more frequent in debris flows and were identified in the field by pervasive chalky white or yellow clasts.

Lithofacies code assignment is a field categorization to allow correlation between units, such as at site 16, where Onetapu C units have **Hc<L** (crudely bedded sandy hyperconcentrated flow*)* and **Hg_i<P** (crudely bedded and inversely graded sandy and pumice hyperconcentrated flow*)*, and Onetapu D units have **D_MmL** (massive matrix-supported lithic debris flow*)* (Figs. 2.6, 2.10a) which both correlate with Onetapu C or Onetapu D sequences at Sites 13a, 10a, 10, 8, and 6 (Fig. 2.7).

When channel and longitudinal flow variations are accounted for a correlation of triggering mechanisms over time is exhibited through grainsize and sedimentological classification. Poorly sorted, massive diamictons (e.g. Onetapu B & D) are most consistent with debris flows generated by landslides, where the incorporation of cohesive, lithic and altered lithic material dominates the deposit and there are comparatively lower sorting values and platykurtic distribution. In contrast, single-sequence, hyperconcentrated flows (e.g. Onetapu E4 & E7) are more typical of large, sudden releases of water, such as tephra-dam collapses. These events are characterized in the stratigraphy by thick deposits intermediate between typical debris flow and hyperconcentrated flow structure, with inverse grading from base to middle/top of the deposit which is also reflected compositionally in Onetapu E7, and overall reflects source material.

Other deposits show evidence of eruptive lake water expulsion, particularly where multi-sequence hyperconcentrated flows incorporate fresh eruptive products with or without crater

lake sediments or dewatering silt layers (e.g. Onetapu E6). Stratigraphic divisions might not be observable in field observations, and the absence was noted soon after deposition (Cronin et al., 1997b) however these units display compositionally uniform scoria deposits without significant grain size or composition variations like what is seen in single-sequence units.

Finally, deposits dominated by remobilized rainfall or glacial melt remobilized tephra (e.g. Onetapu C & Karioi-Onetapu A respectively) show variation based on triggering mechanism and catchments. Karioi-Onetapu A has pale rhyolitic ashy matrix, evident at site 2 and site 4, and sub-rounded polylithic stream cobbles at site 4, which indicates sudden outflow with bulking material sourced from the Wahianoa stream channel. This is in stark contrast to the Onetapu C hyperconcentrated flow units, which primarily exhibit crudely bedded and inversely graded scoria sands along with common andesitic pumices, indicating dry vent conditions and remobilization of a more homogenous source material.

2.5 Discussion

Lahar deposits are often discontinuous both longitudinally and laterally (Costa, 1984; Pierson, 2005a), which is complicated by deposit preservation and exposure. Sites 9, 10, and 12 represent the only cross section sequence perpendicular to flow direction located for this study (Table 2.1) displaying a systematic improvement in sorting and decrease in grain size away from the thalweg. Thus assessment of prehistoric lahar histories are complicated by the temporal and spatial variability of the depositing flows combined with complex deposition and erosion patterns (Procter et al., 2010a) that make lateral and longitudinal correlations difficult and subsequent preservation of deposits that often results in a patchy sedimentary record.

Previous studies of lahars along the Whangaehu river have applied lithographic codes associated with the sedimentary features of the deposit (Palmer et al., 1993), however the sedimentary codes differ between different sites for the same Onetapu units (Figs. 2.6, 2.7, 2.9-2.13). This led to the collection of more field data that could be used to identify trigger

mechanisms, specifically commonly noted lithological divisions (Hodgson et al., 2007; Lecointre et al., 2004a).

Physiographic codes were not included, as paleo-channel profiles have to be inferred from deposits where the channel bed is unknown due to lack of transverse exposures, instead of being directly observed (Zemeny et al., 2021; Zernack, 2021). And in most cases bed height and paleo-channel position would be an estimation and not first-order observation. Excluding these codes avoids introducing potentially misleading correlations based on uncertain channel morphology, ensuring that subsequent interpretations are grounded in directly observable stratigraphic and sedimentological evidence rather than speculative geomorphic reconstructions.

Including detailed grain size analysis proved valuable for supporting lithofacies assignments (e.g. systemic poorer sorting in Ona/Ond units consistent with debris flow assignment), but also for indicating subtle intra and inter-unit variations that were not always apparent from field descriptions alone. Trends in sorting, skewness, and kurtosis across a stratigraphic unit and between proximal and distal settings provided constraints on lahar rheology and depositional processes. Indeed, trends in downstream fining and sorting were most evident with the Wahianoa sourced Onetapu-Karioi lahars, which were able to be sampled closer to the source, and included the only sampled units with negative ϕ mean sizes and much higher variability in all parameters.

2.5.1 Karioi lahars (interpretation of newly identified units)

The discontinuous nature of lahar deposits is further complicated in catchments influenced by glaciation, where reworked moraine and outwash sediments form part of the lahar stratigraphy and in some cases source material. In the Wahianoa catchment there are ample sediments sourced from glacial erosion (McArthur and Shepherd, 1990), with deposits preserved in the cutbank downstream from the terminus of the lateral moraines and upstream from site 1 (Fig.

2.5). Understanding the interplay between glacially derived and volcanogenic material is critical for reconstructing the origin and relative magnitude of Karioi lahars with respect to the Onetapu Formation. Fresh volcanogenic sediment in the Wahianoa catchment is limited by current vent dynamics, with the last lahars composed of fresh lithics and scoria being limited to small hyperconcentrated flows occurring sometime soon after Taupo Ignimbrite emplacement. Later Karioi-Onetapu units are covered by Tufa Trig layer with an 830 B.P. minimum age (Donoghue, 1991) and are polylithic massive diamicts composed of lahar remobilized glacial till separated by a mottled gray and purple mud layer emplaced soon after the earlier diamict, possibly indicative of breakout of a dammed section of moraine, drainage, and subsequent remobilization of lake mud. A smaller polylithic diamict above this layer is the last Onetapu-Karioi lahar recorded at this location.

There are abundant rounded boulders exposed at site 2 (Fig. 2.10f) showing energetic mobilization associated with Taupo Ignimbrite lahars, but also thicker pre-Taupo Ignimbrite lahars, which were likely a significant but waning component of the southeastern ring plain, which the Whangaehu dissects at the southeastern bounds of the Karioi Forest.

2.5.2 Interplay with large rhyolitic eruptions and ignimbrites from neighbouring calderas

An exposed section of the upper Wahianoa catchment (Fig. 2.12) shows multiple episodes of volcanism and reworking of Taupo pyroclastic deposits below the first previously recorded Onetapu-Karioi lahar. A section of the Taupo ignimbrite situated on andesitic tephra has been eroded and infilled by coarse black vitric tephra mixed with andesitic tephra (Fig. 2.12: 1), overlain by a coarse black vitric tephra (Fig. 2.12: 2), polylithological lahar deposits (Fig. 2.12: 3, 4), black vitric sand fluvial deposits (Fig. 2.12: 5), further polylithological hyperconcentrated flow deposits (Fig. 2.12: 6), and paleosol (Fig. 2.12: 7) that underlies the Karioi B unit. Manville et al. (2005) note that pumiceous hyperconcentrated flows in the Rangitaiki catchment were

modelled to occur within the first three years post-eruption, although the Whangaehu and Wahianoa catchments received less Taupo pyroclastic deposits than the Rangitaiki (Walker et al., 1981; Wilson and Walker, 1985).

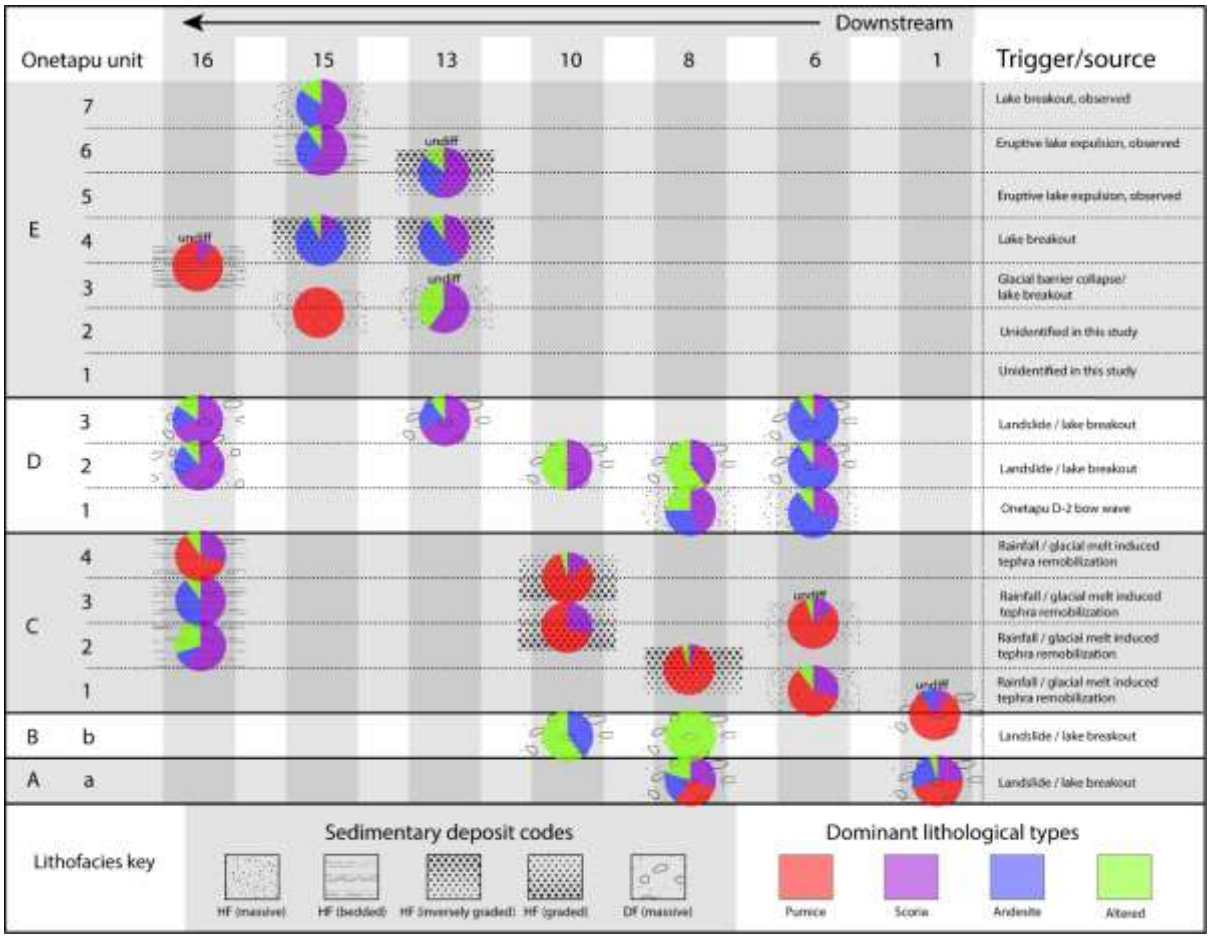


Figure 2.12 Sedimentary deposit codes and dominant lithological types at selected sites. Lithological componentry was estimated (Terry & Chilingar, 1955) based on gravel size fractions, where available, or the coarsest sand fractions otherwise. Units of indeterminate age were assigned ''undiff'' as undifferentiated and plotted across the age ranges inferred from their stratigraphic relationships, sedimentary deposit types, and lithological componentry. Trigger mechanisms have been assigned after Hodgson et al. (2007).

On the Wahianoa fan, Taupo Ignimbrite has been erosionally removed up to 500 meters on either side of the primary and overbank channels and has accumulated at the Wahianoa confluence (Fig. 2.5, Site 4 & 5). Taupo Ignimbrite deposits have been removed from sites on the Wahianoa fan up to 7 meters above current stream bed while preserving Onetapu-Karioi

deposits, which would indicate the flows from the Wahianoa catchment were much more voluminous in the past.

Rounded and sub-angular gravel and cobble clasts (Fig. 2.10e) in the ~2m Onetapu-Karioi A diamicton overlying Taupo pyroclastic deposits at Site 4 are possibly indicative of incorporation of fluvially transported material from the Wahianoa catchment. The clasts display weak imbrication in the direction towards the Wahianoa river, an indication of upstream direction in debris flows (Vallance, 2005, 2000; Vallance and Scott, 1997). The pale deposit matrix, lack of juvenile clasts (Hodgson et al., 2007; Lecointre et al., 2004a), as well as the immediate superposition above Taupo Ignimbrite is likely indicative of Taupo Ignimbrite induced glacial melting.

The most recent lahar is a small debris flow (Onetapu-Karioi C) preserved in the cut bank, separated from the Onetapu-Karioi B deposit by sections of a mottled maroon and grey muddy/silty layer that resembles lake sediment (Dr. Peter Almond, Pers comm.) or loam (Donoghue, 1991) which conformably overlies the Karioi B diamict.

The contribution of the Wahianoa catchment to the lahar record is significant, though waning over time. While the current focus for lahar hazards is still the Whangaehu catchment, the Wahianoa contributed to downstream sedimentation and represented, with or without contemporaneous contribution from the Whangaehu, the path for the first post-Taupo lahar, Onetapu-Karioi A.

2.5.3 Deposit sedimentology and lithology

Lahar genesis, with or without an eruption, is a complex process that can span days to months (Cronin et al., 1997b; Gran and Montgomery, 2005; Umbal and Rodolfo, 1996). Lithographic codes have been modified from tools to describe braided river sequences (Miall, 1977) for use in volcaniclastic analysis (E.g.: (Manville, 2002; Palmer et al., 1993; Palmer and Neall, 1991b; Purves,

1990; Segschneider et al., 2002)) to help with logging and comparing multiple units. The set of lithofacies codes used herein for logging the Onetapu Formation was modified as described for identifying trigger mechanisms of the deposits encountered in the Whangaehu and Wahianoa catchments (Fig. 2.12), which vary based on where in the transverse and longitudinal profiles the deposits can be identified and logged but is then strengthened through being correlated with logs of similar stratigraphic profiles at different sites.

Lake breakout/tephra barrier collapse lahar composition is largely dependent on composition of the tephra dam deposited from previous open vent periods, however the record of these single events (One-3, One-4, One-7) in the Whangaehu sites surveyed produce a massive or inversely graded hyperconcentrated flow. This is with the caveat that lahars can bulk and incorporate new material as well as debulk, using sedimentary deposit types and dominant lithologies together, trigger mechanisms for other deposits can also be inferred.

Onetapu C hyperconcentrated flow deposits contain large amounts of poorly indurated yellow/brown andesitic pumice and scoria and occur in several distinct episodes. Uniformity of componentry suggests that these were all sourced from similar Ruapehu andesitic pumice deposits, likely deposited on snow or glaciers and causing melt and remobilisation.

Lahar deposits from units Onetapu A, B, and C have been documented near the current river level, indicating stable bed height near sites 16 and 14 (Cronin et al., 1997a; Hodgson, 1993) and current hazard models are run on the assumption that the bed height has not changed significantly. For areas where the current bed is lava or Tertiary mudstone the bed has not been lower, similarly in areas where the bed is pre-Onetapu lahar units. However, lahar hazard following the 1991 Pinatubo eruption was exacerbated by riverbed aggradation as well as debris flow dams at constriction points, causing backflow upstream (Umbal and Rodolfo, 1996) with gradual erosion and removal (Gran and Montgomery, 2005; Kataoka, 2005). Cronin et al. (1997a) did not identify similar controls on Onetapu D units, so it is unknown if aggraded Onetapu C was

still present, which would have lowered the size of subsequent lahars needed to inundate the same area, a hazard identified by Campbell (1973).

The hyperconcentrated flow unit that occurs stratigraphically above Onetapu D (Hodgson et al., 2007: Fig. 2.9, Fig. 2.8; Lecointre et al., 2004: Fig. 2.10) logged at Site 16 (Figs. 2.9 & 2.7) has only been preserved at sites that also comprise Onetapu D units, and logging at site 16 shows a depositional contact with the underlying pumice cap of the thin Onetapu D3 deposits. One explanation for lack of widespread identification of this deposit despite it being up to 12 meters above current water level is its deposition on aggraded Onetapu D2/3 sediments, or a trailing pulse (Pierson, 2005b; Scott et al., 1995) from Onetapu D3.

The thick Taupo pumice cap above the Onetapu A sheet deposit (Costa, 1984) at site 19 (Figs. 2.4, 2.10h) is notable for being a lahar composed of mostly Taupo material. The deposition and preservation of this deposit is likely due to the local and paleo-channel morphology, as site 19 is preserved up a canyon-confined tributary stream. These settings are known for preserving thick sequences of sediment (Baker et al., 1983; Kochel and Baker, 1982). Early remobilization of Taupo pumice is most clearly seen at Site 5, which has a sequence of ignimbrite valley-fill (Walker et al., 1981; Wilson and Walker, 1985) Taupo deposits with an erosional upper contact with a Taupo-pumice enriched Onetapu A unit.

Grain size characteristics of deposits reflect downstream transformations in lahar dynamics. Massive matrix-supported bouldery diamictons in the Whangaehu gorge become matrix-supported pebbly diamictons in the medial zones, and clast-supported sandy hyperconcentrated flow deposits in distal zones and side channels (Graettinger, 2008; Hodgson, 1993; Hodgson et al., 2007; Lecointre et al., 2004a; Palmer et al., 1993). Previous lithofacies analysis have revealed changes associated both with the channel depositional environment, where coarser mid-channel deposits transition to thinner, lower median grain size overbank deposits (Hodgson, 1993) which also contain > 65% less silt- and clay-size fraction

than the parent flow (Fig. 2.3)(Cronin et al., 2000) as well as general clast size trends that follow a progressive decrease in both maximum and modal clast sizes downstream (Hodgson, 1993). For comparable sections of deposits (e.g. top, base) this general reduction in coarse and fine particles and thus reduction in kurtosis occurs as all deposits progress downstream (Table 2.1).

Assignment of lithofacies codes along with detailed grain size analysis revealed trends of sorting and transformation within, along, and across units, as well as inter-unit differences, supporting and expanding previous detailed sedimentology studies both at Ruapehu (e.g. Hodgson, 1993) and other volcanoes (Castruccio et al., 2010; Lavigne et al., 2000; Scott, 1988). Of particular interest is the possibility of reconstructing original flow states using grain size analysis and what we know of depositional processes, such as the silt cap that is part of One-6 at Site 14 (Fig. 2.5, 2.7, Table 2.1). Silty layers above lahar deposits have been documented previously, particularly in marginal settings where lower energy conditions and post-depositional dewatering of coarse material lead to silt and clay sediment segregation (Cronin et al., 2000, 1997b; Pierson and Scott, 1985). Detailed grain size analysis and proportional combination of these separate features could provide additional insights into lahar flow and deposition mechanisms.

2.5.4 Trigger mechanisms

Triggering mechanisms have been observed and correlated to deposits for Onetapu E4 – E7 (Cronin et al., 2000, 1999, 1997a, 1996; Graettinger et al., 2010; Manville et al., 1998; Nairn et al., 1979; O'Shea, 1954; Procter et al., 2018; Scott, 2013) and inferred from records for Onetapu E3 (Reverend Richard Taylor, 1861), all of which have been non-cohesive. Clay mineral contents in cohesive Onetapu units have been determined in previous studies (Hodgson et al., 2007; Lecointre et al., 2004a) as abundant smectite, kaolin-smectite, and natroalunite: products of hydrothermal alteration on Mt. Ruapehu's flanks (Kereszturi et al., 2020; Lecointre et al., 2002;

Miller et al., 2020). All extensive cohesive lahars have been assumed to have a landslide/flank failure trigger (Lecointre et al., 2004a) and this remains the current criteria.

Defining trigger mechanisms using sedimentological codes, grainsize analysis, and componentry isn't as definitive as mineralogical evidence for triggers, however previous work (Donoghue and Neall, 2001) has posited that Onetapu lahar units were either result of eruptive activity or lake outbreak (categorized based on presence of immediate overlying tephra units vs. paleosols or aeolian sediment on the alluvial fan), grouping Onetapu debris flow units together with historical lake breakout events (prior to the 2007 lahar: Onetapu E7). Onetapu E3, E4, and E7 lake breakout deposits from these study sites are all massive to inversely graded hyperconcentrated flow units with predominantly higher grain sorting than any of the diamict units. This further supports the hypothesis (Hodgson, 1993; Hodgson et al., 2007; Lecointre et al., 2004a) that the diamicts are the result of a different process.

However determination of triggering mechanisms need to account for downstream variations of the flow and the resulting deposits as previous observers have noted changes in clast size and composition when sampling the same active lahar at different points, coinciding with changing sedimentary features downstream (Cronin et al., 1997b) or lateral transition from debris flow to hyperconcentrated flow deposits (Donoghue, 1991). Additionally, different phases of the same flow at a given location have different rheological characteristics and different sedimentary codes for the associated deposits (Pierson and Scott, 1985; Vallance, 2005, 2000).

Notable in Onetapu sites the componentry analysis and the increasing pumice segregation with increasing distance downstream, which has been recorded in the literature in flows transitioning from debris flow to hyperconcentrated flows (Dolan, 2004; Vallance, 2005) provides an indication that flows may be increasing in volume over time and becoming more erosive. Onetapu C deposits change from a soft brown pumice sand at sites 8, 10, and 10a to a semi-indurated grey scoria sand with an increasing pumice content towards the top of the deposit

downstream at site 16. Notable is site 19 (Fig. 2.5: site 19, Fig. 2.10h), where Onetapu A overlays primary Taupo ignimbrite as a ~1.5 meter crudely bedded hyperconcentrated flow deposit capped by a ~3-meter-thick reworked Taupo pumice and ash deposit. This could represent a case where eruption generated lahars are moving into a regime of rain-triggered events that are remobilising the surrounding material.

2.6 Conclusions

This study highlights the complexity of lahar deposits in the Whangaehu and Wahianoa catchments, emphasizing the importance of both longitudinal and transverse perspectives in reconstructing lahar history. While lateral exposures are rare, especially in the Wahianoa valley, the pseudo-transverse sequence observed at Sites 9, 10, and 12 shows distinct trends of fining and improved sorting with distance from the thalweg. The preserved lahar record is limited to sites that offer some exposure while simultaneously being less susceptible to subsequent erosion, suggesting an inherent preservation bias that must be considered when reconstructing volcanic histories and developing hazard models (Section 6.5.1).

This study identified four main lahar triggering mechanisms at Ruapehu, with much of the deposit variability arising from downstream rheological changes. The four identified triggers and identifying characteristics are summarized as follows:

Landslides and Flank Failures: While this is the sole lahar type represented in the Whangaehu record without supporting historical observations, analogous observations indicate that extensive cohesive debris flows in the Whangaehu are most likely triggered by landslides or flank failures, variably incorporating unconsolidated material. These lahars form massive diamictons.

Lake Breakouts/Tephra Barrier Collapses: Historical observations correlated to the Onetapu Formation indicate lahars triggered by lake breakouts or tephra barrier

collapses tend to produce large, single event hyperconcentrated flows, largely reflecting the composition of the tephra dam in more proximal deposits, and incorporating catchment derived bulking products in more distal deposits.

Eruptive lake water expulsion: Lahars triggered by eruptive lake water expulsion have been historically observed as hyperconcentrated flows that vary in size, have multiple events, and have incorporated varying amounts of fresh eruptive products and crater lake sediments. Onetapu Formation multi-sequence hyperconcentrated flow deposits or deposits with fresh eruptive products and crater lake sediments are most likely triggered by eruptions through the crater lake.

Rainfall/glacial melt induced tephra mobilization: These are hyperconcentrated flows incorporating products indicative of strombolian/subplinian dry vent eruptive conditions (I.e. pumice, ash, scoria), mobilized either through rainfall or direct glacial interaction. These lahars vary in size and tend to produce discrete events with proximal deposits that are massive or graded while distal deposits can be crudely bedded or inversely graded.

New observations from the upper Wahianoa catchment provide a more nuanced view of early Onetapu events and indicate that lahar remobilization of Taupo ash occurred during and soon after the Taupo eruption. This includes evidence for multiple lahar pulses prior to the previously identified Onetapu A lahar, suggesting abundant sediment supply and remobilization during and immediately following the Taupo eruption. The stratigraphy and sedimentary characteristics at Site 4, incorporating rounded streambed gravels with no juvenile lithic input but with a rhyolitic ashy matrix, point to remobilization of existing deposits and potential Taupo-induced Wahianoa glacial melting as a trigger rather than a Ruapehu eruption, adding complexity to the classification of lahar types in this region.

Finally, the use of modified lithofacies codes, adapted from fluvial environments, proved useful for capturing the diversity of lahar sedimentation styles. This was particularly important for identifying and categorizing the main depositional features of each unit, which may otherwise be lost in minutiae. These were useful for determining the new stratigraphy of the Onetapu-Karioi lahars and how they fit into the existing stratigraphy.

By refining the stratigraphic record and mapping the sedimentology of the Onetapu Formation, this chapter shows the diversity of lahar deposits, but also the limitations inherent in using solely visual field characteristics for lithologically similar deposits. In order to overcome this and more accurately infer trigger mechanisms, the next chapter introduces geochemical fingerprinting techniques to group deposits and link them to several distinct source (trigger) mechanisms.

3 Geochemical and spectral techniques for lahar fingerprinting at Mt. Ruapehu: Improving assessment of triggering mechanisms and provenance

3.1 Abstract

Distinguishing between individual lahar events and determining their triggering mechanisms within Mt. Ruapehu's Onetapu Formation is challenging due to the deposits' lithologically similar nature and extensive reworking. Lahar provenance (source material) and trigger mechanisms (e.g., eruption, landslide, rainfall) are fundamental inputs required for building robust hazard assessments.

This study introduced a multi-criteria analytical approach to fingerprint these lahar deposits, integrating X-ray fluorescence (XRF), X-ray diffraction (XRD), and visible to Short-Wave Infrared Reflectance (SWIR) spectroscopy. While bulk XRF/XRD analysis showed that matrices generally converged around typical andesitic compositions, the key methodological advantage was found in the SWIR technique. SWIR successfully resolved subtle hydrothermal alteration signatures, specifically phyllosilicates such as smectite and kaolinite, at abundances as low as 1–5 weight percent. These low-abundance minerals are typically below the reliable detection limits of bulk XRD analysis.

The spectral clustering results demonstrated the ability to discriminate reliably between relatively unaltered hyperconcentrated flows (e.g., Onetapu C) and highly altered, clay-rich cohesive debris flows (e.g., Onetapu B and D). Elevated Loss on Ignition (LOI) values further corresponded consistently with cohesive debris flows, reinforcing the link between high clay

content, hydrothermal alteration, and flow rheology. This integrated methodology provides a sensitive and globally applicable forensic toolset for tracing lahar provenance, strengthening the link between summit hydrothermal processes and downstream lahar hazards.

3.2 Introduction

Lahar is a generic term for a range of volcanic debris flows (Smith and Lowe, 1991) that are fast-moving mixtures of water, volcanic material, and other debris that differs from normal streamflow (Smith and Fritz, 1989). Lahars have the potential to devastate downstream areas (Scott, 1988) and can impact areas far from the volcano edifice. Lahar formation requires water, unconsolidated debris, and a triggering mechanism (Vallance & Iverson, 2015) for the flow to propagate downslope primarily under the influence of gravity (Crandell, 1971). There are several processes that can trigger lahars that can be more generally divided into either eruption triggered or non-eruptive. (Neall, 1976; Scott, 1988; Smith and Lowe, 1991). Non eruptive triggers primarily occur post an eruptive sequence. Examples of eruption triggered events include the melting of snow and ice from contact with hot eruptive material (Hodgson et al., 2007; Major and Newhall, 1989; Pierson, 1980) and the eruptive expulsion of crater lake water (Hodgson et al., 2007; Scrivenor, 1929; Suryo and Clarke, 1985) while post-eruptive triggers include the remobilisation of deposited eruptive material through heavy rainfall (Arguden and Rodolfo, 1990; Hodgson et al., 2007; Rodolfo, 1989; Scott et al., 2005), liquefaction of debris avalanche deposits, the collapse of small volumes near vent deposits, the collapse of crater lake dams, and the mixing or entrainment of volcaniclastic materials with flood waters (Crandell, 1971; George et al., 2022; Hodgson et al., 2007; Scott, 1988).

Ruapehu volcano is a stratovolcano at the propagating tip of the Taupo Volcanic Zone within the Tongariro Volcanic Centre. The primarily andesite, subduction related stratovolcano was formed ~230k years ago and subsequent laharic, fluvio-glacial and mass wasting processes have contributed to building a corelative ringplain. In the last 2000 yrs with the formation of the

southern vent and the development of the Crater Lake small (>3 VEI) eruptions and lahars have dominated volcanic activity. Lahars at Ruapehu can have multiple triggers (Cronin et al., 1997a; Hodgson et al., 2007; Lecointre et al., 2004a) including some that haven't yet been observed in recent records (Hodgson et al., 2007; Lecointre et al., 2004a).

The identification of single lahar events from past deposits isn't straightforward due to source material being lithologically similar, bulking and debulking processes cannibalising material as well as eroding older surfaces and lateral and longitudinal variations in their sedimentology limit the ability to accurately fingerprint events. This is also an issue for the Onetapu Formation deposits at Ruapehu Volcano were correlations cannot be made solely via outcrop/hand specimen (Hodgson et al., 2007) so identifying distinct "fingerprints" would need improvements to be made in correlation techniques and methods. Being able to identify the triggers, origins, and changing conditions of these flows is crucial for building hazard assessments and designing mitigation.

Hydrothermally altered volcanoes have previously been implicated for lahar hazards (Carrasco-Núñez et al., 1993; Crandell, 1971; Finn et al., 2007; John et al., 2008; Vallance and Scott, 1997) and as early as 1926 (Tada and Tsyua, 1926, as referenced in Crandell, 1971), and has also been a subject of interest at Ruapehu, as the summit has been characterized via use of aerial hyperspectral imagery supplemented with laboratory analysis (Douglas et al., 2022; Kereszturi et al., 2020; Miller et al., 2020; Schaefer et al., 2023) with approximately 7 km^2 of the summit area (out of ~54km^2) having some degree of argillic alteration, most of it within a kilometer of the crater lake.

The identification of clay species and their abundance can inform models of flow rheology (Costa, 1988, p. 88; Hampton, 1972; Scott et al., 1995), and when combined with bulk composition data can potentially inform trigger mechanisms, source material and source weathering processes (Inoue, 1995). The identification of clay species and relative abundance

have to date been the main tool applied to act as a proxy for "fingerprinting" correlations between deposits and infer source and trigger mechanisms (Cook, 2002; Crandell, 1971; Detienne et al., 2017; Frank, 1995, 1985; Hodgson, 1993; Hodgson et al., 2007; Mullineaux, 1974; Thouret et al., 1998).

In this study we present a multi-criteria analytical approach to fingerprint lahars to determine source triggering mechanisms. The laharic deposits of Ruapehu Volcano over the last 2000 yrs (the Onetapu Formation; Hodgson et al, 2007) provide an ideal set of deposits that have been emplaced through well constrained eruptive and Crater Lake processes, providing examples of eruption triggered glacial melting, eruptive lake water ejection, Crater Lake breaching, rain-triggered events, and flank failure events (Christenson et al., 2010; Cronin et al., 1997a; Donoghue, 1991; Graettinger et al., 2010; Hodgson, 1993; Hodgson et al., 2007; Lecointre et al., 2004a; Nairn et al., 1979).

Correlation of individual deposits (and trigger mechanisms) remains a significant challenge at Mt. Ruapehu, lahar deposits often share similar bulk lithologies and experience extensive reworking, so assigning units has relied heavily on stratigraphic correlations: yet previous trends have been noticed in matrix mineralogy and some units have been identified based on altered clasts and variable bulk content (Hodgson, 1993; Hodgson et al., 2007; Lecointre et al., 2004a). The combination of syn- and post-eruptive triggers offers an ideal sequence for testing high-resolution fingerprinting methods. This study applies a combined geochemical and spectral analysis approach to characterize the clay mineralogy and alteration fingerprints of lahar matrix with the objective of developing diagnostic criteria for source provenance and inferring trigger mechanisms. Bulk X-ray diffraction and X-ray fluorescence of silt-clay size fraction shows the primary mineral assemblages and whole geochemistry, while complementary visible to shortwave infrared (VNIR-SWIR: 350-2500nm) reflectance spectroscopy quantifies structural phyllosilicate water and hydroxyl absorption features diagnostic of alteration minerals,

exploiting their sensitivity for low abundance phases (<1-5 wt%) (Zhang et al., 2001) not resolvable by XRD (Maghsoudi Moud et al., 2021). 1400, 1900, 2200, and 2350 nm absorption bands (Bishop, 2019) are used to detect variations in clay species and crystallinity, and as a proxy for alteration intensity.

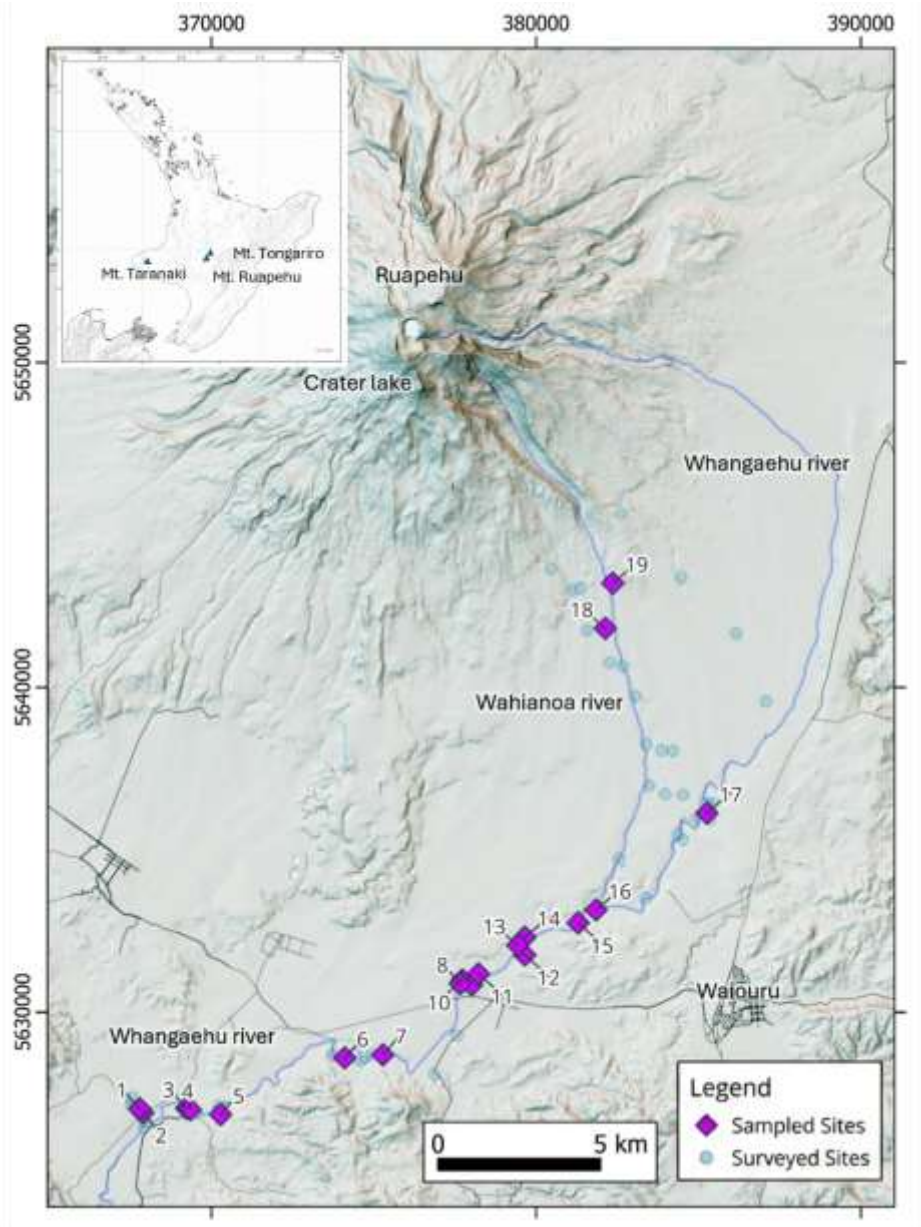


Figure 3.1 Location map of samples and logged sections along Whangaehu and Wahianoa river drainages off Mt. Ruapehu.

3.2.1 Geological setting

Mt. Ruapehu (2797m) is a glaciated, andesitic composite strato-volcano with an active summit vent filled with a warm, acidic Crater Lake (Johnston et al., 2000) located at the southern end of the Taupo Volcanic Zone (TVZ) (Graham and Hackett, 1987; Hackett and Houghton, 1989) in the North Island, New Zealand. Volcanism in the TVZ is primarily from the Pacific Plate subducting under the Australian Plate at the Hikurangi Subduction Zone (Stern et al., 2006; Wallace, 2004). The southern tip of the TVZ is dominated by andesitic volcanism, specifically the Tongariro Volcanic Center (TgVC) (Rowland et al., 2010).

The oldest eruptive deposits associated with the TgVC is the ~933 ka Hauhungatahi (Cameron et al., 2010), followed by the ~512 ka Otamatereinga Formation and the ~304 ka Tupuna formations on Tongariro and the ~200-150 ka Te Herenga Formation on Ruapehu (Gamble et al., 2003; Pure, 2020). Ruapehu has had four edifice-building episodes (Hackett and Houghton, 1989): the Te Herenga Formation, the ~180-160 Wahianoa Formation, the ~50-15 ka Mangawhero Formation and the <15 ka Whakapapa Formation (Gamble et al., 2003; Hackett & Houghton, 1989; Townsend et al., 2017). Ongoing mass wasting processes have removed parts of the edifice, including >1 km^3 of material in the Murimotu Formation and hydrothermally altered Mangaio Formation debris avalanche deposits (Donoghue & Neall, 2001; Palmer & Neall, 1989; Tost et al., 2014). The Crater Lake is estimated to have formed ~2 ka, along with the initiation of large modern Onetapu Formation lahars in the Whangaehu catchment (Donoghue et al., 1997; Hodgson et al., 2007; Lecointre et al., 2004; Palmer et al., 1993).

Phreatic and phreatomagmatic events producing unwelded tephras are poorly preserved on the edifice, however the ring plain preserves much more of this record (Hackett and Houghton, 1989) and is roughly volumetrically equivalent, 150 km^3, to the source edifice (Conway et al., 2016). On the eastern portion of the ring plain, where the Whangaehu River empties off the edifice is the Whangaehu Fan, a ~36km2 alluvial fan with lahars being the most significant

source of sedimentation (Palmer et al., 1993), and Onetapu Formation lahars being the majority of those identified (Hodgson et al., 2007; Palmer et al., 1993). The Onetapu Formation has been formally divided into five units and 18 members, based on mappable units with distinct lithology (Hodgson et al., 2007; Manville and Cronin, 2007). Matrix and clast compositions and correlations between mapped units were used to infer triggering mechanisms for prehistoric lahars, specifically:

- **Ona-1** (>1530±160 yr BP) is a medium-large cohesive debris flow deposit that contains hydrothermally altered source rock, lake bed sediments, reworked Taupo Pumice, with reworked earlier Mangaio Formation and no juvenile components, indicating a Crater Lake rim collapse. Subsequent **Onetapu A** members are less cohesive, and assumed to have similar (**Ona-2**, **Ona-3**) or unknown triggers (**Ona-4**) (Hodgson, 1993; Hodgson et al., 2007).
- **Onb** (<1530±160 yr BP, >1271 ± 56 yr BP) is a large cohesive debris flow deposit that contains hydrothermally altered source rock, mud-coated scoria, and juvenile eruptive material, indicating an eruption and Crater Lake rim collapse (Hodgson, 1993; Hodgson et al., 2007).
- **Onc-3** (>1160 ± 80 yr BP) is a hyperconcentrated flow deposit with common lithic clasts and pumice, indicating dry vent conditions and either rain-triggered or glacial melt trigger mechanisms. Prior members (**Onc-1**, **Onc-2**) are similar composition and thinner, and the latter **Onc-4** is thicker and is primarily unaltered scoria, all with similar inferred trigger. The **Onetapu C** members and unit are medium- to catastrophic in size (Hodgson, 1993; Hodgson et al., 2007).
- **Ond-2** (>450 ± 55 yr BP) is a catastrophic cohesive debris flow with altered and lithic clasts and lake-bed sediments, interpreted as a Crater Lake barrier collapse. Prior, small hyperconcentrated flow **Ond-1** is possibly rain triggered or a bow-wave deposit, and subsequent catastrophic cohesive debris flow **Ond-3** has abundant juvenile andesitic

clasts, lake sediments, and altered clasts, interpreted as an eruption triggered Crater Lake rim collapse (Hodgson, 1993; Hodgson et al., 2007).

- **Onetapu E** units are post **Onetapu D**, the majority of which have been directly observed and recorded (**One-3**: 1861 (e.g. (Reverend Richard Taylor, 1861), **One-4**: 1953 (e.g. (O'Shea, 1954), **One-5**: 1975 (e.g. (Nairn et al., 1979), **One-6**: 1995 (e.g. (Cronin et al., 1997b), **One-7**: 2007 (e.g. (Procter et al., 2010a)).

3.2.2 Mineralogical and Spectral Techniques on Lahars

XRD (X-Ray Diffraction) has been used extensively for analysis of lahar deposits, specifically matrix samples in order to determine the origins and composition of the sediments of lahars after they have been emplaced XRD analysis has been carried out on the Onetapu Formation (Cronin et al., 1997b; Graettinger, 2008; Hodgson et al., 2007; Lecointre et al., 2004a) and other lahar deposits worldwide (Ban et al., 2022; Cook, 2002; Crandell, 1971; Detienne et al., 2017; Kataoka et al., 2018; Minami, 2024; Rasmussen et al., 2007) in an attempt to characterise the sediments and make some inferences on flow rheology (e.g. (Crandell, 1971)).

While some clay-rich lahars form due to reworking clay-rich volcanic materials (Kataoka et al., 2018; Minami et al., 2019, 2015) most clay-rich lahars are assumed to derive from flank collapses of hydrothermally altered volcanic edifices (Carrasco-Núñez et al., 1993; Vallance, 2005; Vallance and Iverson, 2015; Vallance and Scott, 1997) which has become a diagnostic criteria to infer source conditions and trigger mechanism of past deposits. This diagnostic tool has never been analysed in a quantitative manner across a sequence of lahar events over time.

Other spectral techniques to examine the clay alteration from hydrothermal activity on stratovocanoes has primarily been applied using airborne sensors for the identification and delineation of alteration zones on edifices (Crowley and Zimbelman, 1997; Douglas et al., 2022; Kereszturi et al., 2020; Mars et al., 2015; Miller et al., 2020; Schaefer et al., 2023; Williams and Ramsey, 2024) and has been used in conjunction with XRD to characterize alteration

assemblages (Abdale et al., 2023; Deon et al., 2022; Irwin, 2016; John et al., 2019, 2008) as VNIR & SWIR can detect clay minerals at abundances as low as 1 wt% in single-clay mineral samples and at <5 wt% in mixed clay samples (Zhang et al., 2001). In contrast, bulk XRD analysis does not reliably detect clay content below 5 wt% (Lipman, 1976).

The use of spectral techniques to identify alteration materials relies on absorption features in the light spectrum, for the case of this study the VNIR-SWIR 350 – 2500 nm spectra (Section 2.4) were examined, and of particular interest are the OH^- and H_2O bands seen in the 900 -2500 nm range resulting from incorporating hydroxyl and water in alteration minerals (Clark et al., 1990; Hunt, 1977). Band position and depth is a result of a combination of attachment sites and mineral reflectance and scattering, while apparent depth relative to the continuum is also dependent on mineral properties, grain sizes, and abundance relative to abundance of other materials in the sample, so water and hydroxyl bands have different positions and depths depending on the mineral and surrounding materials (Clark, 1981; Clark and Lucey, 1984; Clark and Roush, 1984). These are prominent in the clay minerals formed by argillic alteration associated with volcanic environments, specifically kaolinite, smectite and alunite (John et al., 2008), although it has been noted alunite is uncommon on Ruapehu's summit (Douglas et al., 2022; Kereszturi et al., 2020).

Clay minerals have different absorption wavelengths that occasionally overlap and form hybrid absorption features (Clark, 1999; Hunt, 1977; Mulder et al., 2013; Waiser et al., 2007; Zhang et al., 2001) the overall spectrum produced by an assemblage of different clay minerals, such as kaolinite, smectite, and other phyllosilicates characteristic of argillic alteration (John et al., 2008; Regassa et al., 2014; Schaefer et al., 2023), results in a characteristic composite spectral curve (Bishop, 2019; Mulder et al., 2013). This resultant spectrum, defined by the specific positions, intensities, and shapes of combined absorption bands, provides a unique "spectral fingerprint" of the lahar matrix (Bishop et al., 2008; Thompson et al., 1999). This methodology is

a direct application of techniques employed in forensic geoscience, where the overall spectral signature of a deposit sample, which provides an integrated measure of its chemical and mineralogical composition (including clay mineralogy) (Rossel and Chen, 2011; Tighe et al., 2018), is used for matching geolocation and determining provenance (Pirrie et al., 2017; Tighe et al., 2018). Forensic science uses a variety of similarity algorithms on spectral attributes to correlate unknown samples to a reference library (Zeng et al., 2023), the distinctive spectral signature of a lahar containing a mixture of hydrothermally derived clay minerals can serve as a diagnostic criterion to suggest similar volcaniclastic flows. Because phyllosilicate spectral features reflect variations in chemical composition and crystal structure (Bishop et al., 2008; Savitri et al., 2021), the unique alteration mineralogy detected (e.g., the presence or dominance of kaolinite, smectite, halloysite, or sulfates in the lahar matrix) can be effectively employed to identify the flow's origin, linking it back to a distinct alteration style or source region on the volcanic edifice, as well as linking flow units (Crowley and Zimbelman, 1997; Detienne et al., 2017; John et al., 2008).

3.3 Methods

Establishing diagnostic fingerprints of lahar deposits requires methods that can resolve both bulk characteristics and subtle mineralogical variations. The Onetapu Formation presents a particular challenge: its deposits are lithologically similar, widely reworked, and laterally variable, which makes traditional field and stratigraphic approaches non-ideal for distinguishing between individual events (Chapter 2). These complexities demand an integrated analytical strategy capable of capturing both broad compositional trends and fine-scale alteration signals.

Our workflow (Fig. 3.2) combines field logging (Table 3.1) and targeted sampling with bulk chemical (XRF) and mineralogical (XRD & VNIR–SWIR) analyses. XRF provides quantitative data on major oxides that are sensitive to hydrothermal alteration (e.g., K_2O, CaO, MgO), XRD identifies dominant mineral phases and assemblages, and reflectance spectroscopy resolves

low-abundance clays and phyllosilicates below XRD detection limits. Together, these complementary techniques allow us to characterize both the coarse mineral framework and the subtle alteration fingerprints that can indicate provenance and trigger conditions.

Applying this workflow to the Onetapu Formation is particularly valuable because its sequence of lahars over the past ~2000 years is well constrained stratigraphically and includes examples of multiple trigger types (eruption-driven, lake breach, rainfall-induced, and flank collapse). This provides an ideal testbed for evaluating whether integrated mineralogical and spectral fingerprints can reliably discriminate between trigger mechanisms. In doing so, we test the central hypothesis of this study: that combined geochemical, mineralogical, and spectral datasets can be used to fingerprint lahar deposits and link them back to their source processes.

3.3.1 Field sampling

Field investigations were conducted based on examining sites from previous field studies (e.g.Cronin et al., 1997a, 1997a; Donoghue, 1991; Hodgson, 1993) as well as sites identified during reconnaissance of the Whangaehu and Wahianoa catchments (see chapter 2). Accessible exposures were logged stratigraphically, described and photographed, and representative sites were sampled. 108 samples were collected from 18 field sites (Fig. 3.1, Table 3.1). A range lithologies were sampled, including multiple samples from different stratigraphic sections of the same unit, and tephra layers and paleosols associated with lahar units. Table 3.1 provides locations, site descriptions, and sample naming conventions and is ordered in increasing proximity to Ruapehu.

Table 3.1 Sample locations and naming conventions

Site	Location Description	Samples	Latitude	Longitude
1	Exposed bluff above Mangaehuehu stream gauge on north side of Oruakukuru Rd before Mangaehuehu bridge	MR	-39.49610575	175.4623329
2	Quarry site on north side adjacent to Oruakukuru Rd before Mangaehuehu bridge	MOTTS	-39.49732183	175.4633858

3	Exposed roadcut on north side of Whangaehu Valley Road bridge adjacent to Tirorangi Marae	MB	-39.49619503	175.4790892
4	Quarry wall ~100 m east of Whangaehu Valley Road bridge adjacent to Tirorangi Marae	MQ	-39.49665332	175.4805517
5	Whangaehu right bank tip of a point bar ~1 km upstream of Tirorangi Marae	PB	-39.49826436	175.4913746
6	Whangaehu river right bank ~500 upstream from Strachan's bridge	SB	-39.48306178	175.536092
7	Whangaehu river right bank ~600 m upstream from Blackburn's quarry (Carriage site)	Q	-39.48273028	175.5503668
8	Tangiwai swamp, Karioi forest drainage canal ~80 m north of Whangaehu river	TS2	-39.46199995	175.5786868
9	Whangaehu river left bank adjacent to Tangiwai swamp, ~20 m downstream from Karioi forest water pipe	S2	-39.46320039	175.5827572
10	~60 m west of Karioi forest Dump Road/K11 Midtrack intersection	DRC	-39.4602788	175.5840667
11	~250 m north on Karioi forest Access 019e from Access 019e/Access 019 intersection	RP	-39.45571584	175.6009946
12	Whangaehu river right bank ~230 m south of Karioi forest Rock Road/Whangaehu Road intersection	RRW	-39.45258728	175.5987323
13	~50 m north of Karioi forest Whangaehu Road on drainage canal ~200 m east of Rock Road/Whangaehu Road intersection	RR	-39.45044895	175.6013003
14	Karioi forest Pumice pit Whangaehu Road ~1 km downstream from Wahianoa river crossing	PON	-39.44666478	175.6203882
15	Whangaehu river right bank directly south of Karioi forest Wahianoa river crossing	WC	-39.44307071	175.6269248
16	Whangaehu river right bank ~100 m southeast of Karioi forest Pumice Mine Road/Whangaehu Road intersection	L	-39.41672534	175.6671087
17	East side of Karioi forest metal pit, ~70 m north of Extreme Road/Campion Road intersection	MP	-39.36511392	175.6318251
18	Wahianoa river left bank, ~150 m upstream from Karioi forest Doubtful Road/Wahianoa river crossing	W	-39.35254568	175.6345908

3.3.2 X-ray fluorescence

Major oxides as well as Sr and Ba concentrations were analyzed for all samples via X-ray fluorescence (XRF) spectroscopy using a Bruker S8 TIGER wavelength dispersive X-ray fluorescence spectrometer at Massey University, Palmerston North. Samples were weighed on a Mettler PE 1600 balance and powdered using an alumina mortar and pestle and ~2 grams or less (depending on amount of sample available) was added to glazed ceramic crucibles, heated in a Carbolite furnace to 110° for 2.5 hours and transferred overnight to a desiccator, the crucible and crucible + sample were weighed on a Mettler Toledo ML204 balance, then heated in a Thermo Scientific Thermolyne muffle furnace at 900° for 8 hours and left to cool to 110° overnight, transferred to a desiccator while still >100° and weighed using a Mettler Toledo ML204 balance within 10 minutes to calculate LOI (Eq. 1).

Eq. 1:

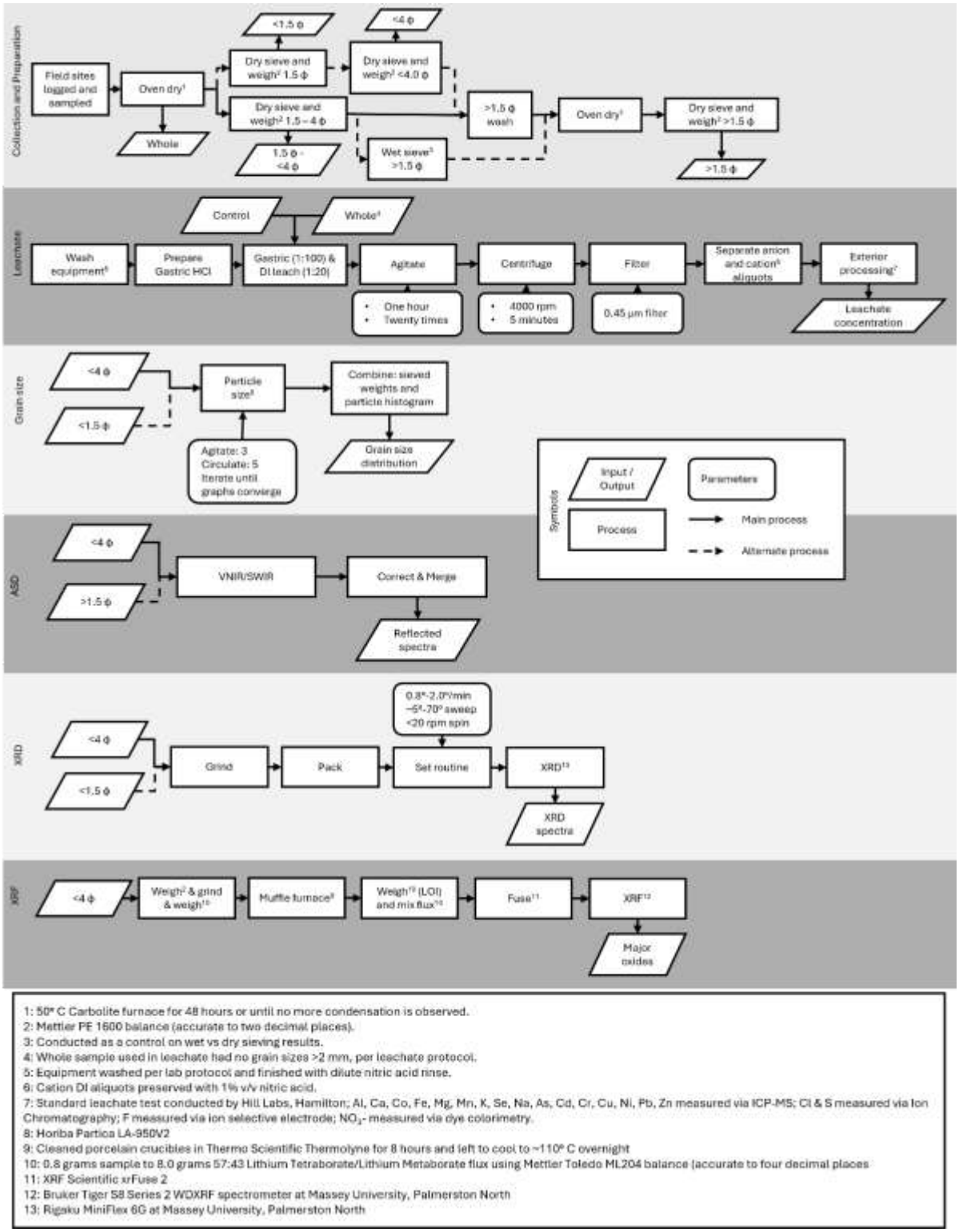
$$L.O.I._{Weight\%} = \frac{(n_2 - n_3)}{(n_2 - n_1)}$$

$n_1 = empty\ crucible$

$n_2 = ceramic\ crucible + sample\ powder$

$n_3 = total\ mass\ crucible + sample\ after\ furnace$

0.8 grams of dessicated sample was then added to 8.0 grams of 57:43 Lithium Tetraborate/Lithium Metaborate flux on a ML204 balance, manually agitated to achieve homogeneity, and fused using platinum crucibles in an XRF Scientific xrFuse 2. Standards Oreas 24b or Oreas 24c were included in each processing and XRF group as a control on analytical precision.



1: 50° C Carbolite furnace for 48 hours or until no more condensation is observed.
2: Mettler PE 1600 balance (accurate to two decimal places).
3: Conducted as a control on wet vs dry sieving results.
4: Whole sample used in leachate had no grain sizes >2 mm, per leachate protocol.
5: Equipment washed per lab protocol and finished with dilute nitric acid rinse.
6: Cation DI aliquots preserved with 1% v/v nitric acid.
7: Standard leachate test conducted by Hill Labs, Hamilton; Al, Ca, Co, Fe, Mg, Mn, K, Se, Na, As, Cd, Cr, Cu, Ni, Pb, Zn measured via ICP-MS; Cl & S measured via Ion Chromatography; F measured via ion selective electrode; NO_3- measured via dye colorimetry.
8: Horiba Partica LA-950V2
9: Cleaned porcelain crucibles in Thermo Scientific Thermolyne for 8 hours and left to cool to ~110° C overnight
10: 0.8 grams sample to 8.0 grams 57:43 Lithium Tetraborate/Lithium Metaborate flux using Mettler Toledo ML204 balance (accurate to four decimal places
11: XRF Scientific xrFuse 2
12: Bruker Tiger S8 Series 2 WDXRF spectrometer at Massey University, Palmerston North
13: Rigaku MiniFlex 6G at Massey University, Palmerston North

Figure 3.2 Flow chart of methods applied.

3.3.3 VNIR & SWIR

Air dried <4.0 ϕ samples and washed and oven dried >1.5 ϕ samples (and >-1.0 ϕ, gravel size fraction where applicable (Folk and Ward, 1957)) were analyzed in the laboratory following a

modified method of Kereszturi et al. (2020) using an ASD FieldSpec 4 Hi Res spectroradiometer. Spectral readings were calibrated every 5 minutes of elapsed sampling time against a white reflectance standard, and 10 readings were taken from each homogenized sample (or individual clast). Spectral measurements were imported, splice corrected and averaged using asdreader (Roudier, 2015) and prospectr (Stevens and Ramirez-Lopez, 2013) R packages. Averaged spectral reflectance was processed via continuum removal (Clark & Roush, 1984) and matched using spectral angle mapper R toolbox (Müller et al., 2025) against United States Geological Survey (USGS) Spectral Library Version 7 (Kokaly et al., 2017). Additionally, spectral angles and principal component analyses distances were computed between each averaged spectral reflectance and different size categories within the same sample were plotted against each other.

3.3.4 XRD

XRD analysis was conducted on selected samples to directly compare with ASD results. Samples were analyzed with a Rigaku MiniFlex 6G at Massey University following a modified version of the multi-sample powder diffraction analysis outlined in the WWU AMSEC Standard Operating Procedures (Cite: https://amsec.wwu.edu/files/2020-08/Rigaku_SOPs.pdf). <4ϕ matrix analysis was conducted to determine composition of silt+clay fractions.

3.4 Results and interpretations

3.4.1 X-ray fluorescence and x-ray diffraction

Major element analysis (Table 3.2) shows little variation in major element percentages and initial analysis indicates all matrix compositions are within the general trend of Ruapehu lavas (Conway et al., 2016), with the exception of predominantly rhyolitic tephra units (W7, W8). However, previous studies have noted variance of 1 – 3 wt% K_2O and 2 – 8 wt% MgO (Conway et al., 2016), while analyzed samples are on the lower end of this range. High LOI percent samples

are present at most sampling sites, and when LOI is plotted against major elements (Fig. 3.8) weak to strong positive relationships (0.26 – 0.51 r-squared values) (Fig. 3.9) can be seen.

Table 3.2 Total Major element analyses. Oxides are expressed as weight percentages. Sample locations are given in Table 3.1

Oxide	MQA	MQB	MQC	MQD	MQE	MQF	MQF	MQG	MQH	MB1	MB2	MB3	MB4	MB6	M1	M2
SiO2	59.96	59.49	60.16	60.22	57.82	58.80	58.96	57.20	58.92	50.07	58.69	58.67	58.64	57.65	53.40	51.40
Al2O3	18.06	18.03	17.78	18.04	18.48	19.07	18.86	18.08	18.35	21.25	17.54	17.69	18.50	18.40	21.83	19.42
TiO2	0.70	0.71	0.74	0.71	0.69	0.67	0.67	0.71	0.74	0.83	0.74	0.77	0.75	0.68	0.78	0.77
MnO	0.08	0.08	0.09	0.08	0.07	0.07	0.08	0.08	0.09	0.08	0.09	0.08	0.09	0.09	0.10	0.10
Fe2O3	6.20	6.64	6.44	5.60	5.09	5.18	5.24	6.39	6.79	7.93	5.96	6.44	6.51	6.10	7.28	7.43
MgO	3.00	3.00	3.53	3.01	2.78	2.97	2.99	2.76	2.96	2.04	3.41	2.68	2.85	3.38	2.97	3.17
CaO	4.75	4.59	4.93	4.83	4.39	4.92	4.94	4.51	4.82	2.30	5.13	4.29	5.02	5.39	4.92	5.37
Na2O	2.68	2.63	2.73	2.78	2.56	2.82	2.78	2.63	2.83	1.83	2.91	2.70	3.12	2.93	2.51	2.51
K2O	1.41	1.41	1.41	1.47	1.36	1.47	1.45	1.40	1.47	1.11	1.56	1.50	1.62	1.51	1.16	1.05
P2O5	0.15	0.14	0.12	0.14	0.12	0.15	0.15	0.14	0.15	0.11	0.14	0.15	0.16	0.14	0.17	0.15
SO3	0.01	0.01	0.01	0.01	0.01	0.01	0.01	0.01	0.01	0.01	0.01	0.01	0.01	0.01	0.00	0.00
LOI	3.84	4.02	3.24	3.83	7.16	4.92	4.71	6.05	3.82	12.48	3.60	6.15	3.98	4.92	5.99	9.05
Total	100.83	100.75	101.18	100.73	100.54	101.06	100.83	99.97	100.95	100.04	99.77	101.13	101.25	101.19	101.10	100.40
Oxide	M3	MS4	MS5	M52	M62	M72	MR1	MR2	MR3	MR4	MR5	MPL	MPU	MQ1	MQ2	MQ21
SiO2	53.36	52.22	50.76	46.49	54.84	50.70	52.49	52.02	55.30	47.76	58.52	53.87	50.10	51.32	59.00	57.62
Al2O3	17.91	19.11	19.88	17.51	19.54	19.05	18.85	21.13	17.38	16.60	18.16	22.02	23.75	17.57	18.22	18.24
TiO2	1.16	0.77	0.84	0.60	0.91	0.75	0.71	0.78	0.79	0.58	0.72	0.77	0.88	0.61	0.67	0.67
MnO	0.14	0.09	0.10	0.07	0.11	0.09	0.08	0.08	0.07	0.05	0.07	0.09	0.10	0.07	0.09	0.09
Fe2O3	10.68	7.33	7.61	5.88	8.23	6.90	6.28	6.22	5.30	5.10	5.51	7.00	7.16	6.14	5.86	6.19
MgO	5.12	3.16	2.94	2.66	3.39	2.92	2.99	3.05	2.80	1.11	2.81	2.96	2.33	2.52	3.40	3.31
CaO	6.74	5.49	5.12	4.19	5.93	5.64	5.06	4.79	4.02	1.44	4.65	4.85	4.38	4.34	5.56	5.41
Na2O	2.61	2.60	2.47	2.35	2.87	2.51	2.66	2.70	2.40	1.87	2.74	2.56	2.46	2.53	3.02	2.95
K2O	0.95	1.09	1.09	1.13	1.21	1.07	1.36	1.16	1.13	1.42	1.61	1.17	1.15	1.30	1.55	1.51
P2O5	0.12	0.15	0.16	0.19	0.17	0.15	0.21	0.11	0.11	0.08	0.14	0.18	0.20	0.14	0.14	0.14
SO3	0.00	0.01	0.01	0.01	0.01	0.00	0.02	0.02	0.11	0.02	0.01	0.01	0.01	0.01	0.01	0.01
LOI	2.33	8.09	9.97	19.73	3.56	9.75	9.75	8.31	10.88	24.67	5.46	5.85	8.37	14.34	3.88	4.96
Total	101.11	100.12	100.95	100.81	100.75	99.54	100.46	100.38	100.28	100.68	100.40	101.33	100.88	100.90	101.38	101.09
Oxide	MQ3	MQ4	MQ5	MQ6	PB01	PB02	PB03	PB04	PB05	PB06	PB07	PB08	PB09	PB10	POAO	POAM
SiO2	55.52	54.88	56.30	58.83	59.28	61.73	63.92	58.98	61.03	59.44	56.23	55.93	58.61	59.08	58.08	57.34
Al2O3	16.98	17.07	16.41	17.51	16.16	15.39	14.84	16.25	17.05	16.19	15.28	16.17	16.90	16.76	19.30	18.77
TiO2	0.66	0.67	0.67	0.69	0.71	0.70	0.71	0.69	0.71	0.71	0.69	0.68	0.70	0.72	0.61	0.73
MnO	0.07	0.08	0.07	0.09	0.08	0.08	0.08	0.08	0.08	0.09	0.09	0.10	0.11	0.11	0.06	0.08
Fe2O3	6.29	6.17	5.77	6.53	7.26	6.06	5.30	7.70	6.20	7.21	10.38	8.18	7.33	7.32	6.54	7.56
MgO	2.77	3.12	2.85	3.40	3.24	3.28	3.54	2.97	3.19	3.49	3.57	3.76	4.76	4.56	1.57	2.96
CaO	4.50	4.90	4.43	5.41	4.72	4.82	4.70	4.84	5.33	5.55	5.33	5.68	6.66	6.46	2.35	4.80
Na2O	2.51	2.61	2.44	2.85	2.49	2.63	2.56	2.67	2.85	2.79	2.73	2.80	3.04	3.01	2.25	2.77
K2O	1.36	1.47	1.32	1.43	1.32	1.44	1.33	1.40	1.41	1.36	1.44	1.27	1.37	1.28	1.50	1.50
P2O5	0.16	0.16	0.16	0.15	0.15	0.13	0.10	0.17	0.14	0.14	0.16	0.16	0.13	0.11	0.16	0.20
SO3	0.02	0.02	0.02	0.01	0.02	0.03	0.03	0.02	0.02	0.02	0.02	0.01	0.01	0.01	0.02	0.01
LOI	10.38	7.72	10.70	4.35	4.96	4.64	3.99	5.27	3.28	3.19	4.91	6.54	1.99	1.99	8.57	4.64
Total	101.23	98.86	101.13	101.24	100.38	100.93	101.10	101.03	101.28	100.17	100.81	101.27	101.60	101.41	101.00	101.36
Oxide	POAT	PODB	PODM	Q1	Q2	Q3	Q4	Q5	Q6	Q7	Q8	RP0	RP1	RP2	RP3	RP4
SiO2	57.21	56.88	59.61	59.07	58.55	57.35	59.13	57.23	59.20	59.10	58.55	59.92	56.52	57.78	55.22	58.96
Al2O3	18.60	18.55	18.52	17.14	17.07	16.25	15.26	16.29	17.24	17.50	16.63	17.16	17.55	17.56	17.81	18.43
TiO2	0.67	0.70	0.76	0.77	0.70	0.69	0.76	0.70	0.71	0.69	0.71	0.67	0.71	0.73	0.69	0.71
MnO	0.09	0.09	0.08	0.10	0.10	0.10	0.11	0.11	0.10	0.10	0.09	0.07	0.08	0.09	0.08	0.09
Fe2O3	6.45	6.94	6.67	6.81	6.51	6.12	7.67	7.41	7.20	6.93	6.86	6.71	5.81	6.15	5.89	6.07
MgO	2.74	3.04	2.85	3.25	4.19	4.06	4.51	4.62	4.32	4.17	3.66	2.16	2.78	2.93	2.95	3.73
CaO	4.45	4.70	5.24	5.79	6.44	5.70	5.88	6.35	6.43	6.49	5.61	2.92	4.43	5.26	4.94	6.26
Na2O	2.90	2.87	3.20	3.29	3.13	2.78	2.74	2.94	3.06	3.10	2.81	2.39	2.71	3.14	2.89	3.26
K2O	1.47	1.42	1.65	1.61	1.39	1.22	1.28	1.27	1.38	1.38	1.34	1.57	1.56	1.64	1.46	1.54
P2O5	0.16	0.17	0.16	0.15	0.14	0.17	0.13	0.12	0.13	0.13	0.14	0.17	0.20	0.16	0.22	0.18
SO3	0.01	0.01	0.01	0.01	0.01	0.01	0.01	0.01	0.01	0.01	0.01	0.02	0.01	0.01	0.01	0.01
LOI	6.57	6.02	3.17	2.10	2.75	6.45	3.12	3.97	2.12	2.01	4.02	7.24	8.68	5.59	8.88	5.50
Total	101.32	101.38	101.91	100.10	100.98	100.89	100.59	101.02	101.90	101.61	100.42	100.99	101.03	101.03	101.04	104.75
Oxide	RP5	RP6	RR1	RR2	RR3	RR4	RR5	RR6	RRW3	RRW2	RRW1	S2U	S2L	Sbsand	Sbsilt	TPBU
SiO2	57.82	58.26	57.58	53.96	57.85	58.01	54.50	56.96	50.56	50.91	53.66	58.94	55.46	62.96	61.79	59.49
Al2O3	17.60	17.52	17.07	17.41	17.49	17.51	17.78	17.41	24.46	23.30	19.35	18.35	17.74	14.95	16.01	16.78
TiO2	0.67	0.70	0.71	0.65	0.68	0.68	0.66	0.72	0.69	0.66	0.70	0.66	0.70	0.72	0.71	0.69
MnO	0.09	0.10	0.09	0.08	0.09	0.09	0.09	0.09	0.04	0.06	0.06	0.09	0.07	0.08	0.06	0.08
Fe2O3	5.77	6.58	6.08	5.49	5.87	6.20	5.68	6.40	8.81	6.48	6.75	6.25	7.58	5.67	4.83	6.44
MgO	3.41	3.72	3.56	3.21	3.39	3.57	3.27	2.80	1.82	1.77	2.09	3.67	2.02	3.20	2.34	3.05
CaO	5.52	5.75	5.49	5.27	5.62	6.00	5.87	5.34	1.39	2.80	3.47	5.46	2.52	4.45	3.61	5.06
Na2O	2.98	3.02	2.87	2.72	2.94	3.02	3.01	3.14	0.92	1.74	2.04	2.89	2.01	2.49	2.33	2.68
K2O	1.53	1.52	1.53	1.38	1.51	1.51	1.45	1.61	0.77	0.95	1.14	1.48	1.22	1.40	1.49	1.39
P2O5	0.13	0.14	0.14	0.17	0.15	0.14	0.20	0.18	0.13	0.20	0.22	0.15	0.13	0.12	0.13	0.16
SO3	0.01	0.01	0.02	0.01	0.01	0.01	0.01	0.01	0.02	0.02	0.04	0.01	0.01	0.03	0.04	0.02
LOI	5.76	3.67	4.12	7.74	3.85	3.01	8.41	4.86	11.18	11.49	11.34	3.61	10.92	5.02	7.67	5.48
Total	101.28	100.99	99.26	98.08	99.45	99.74	100.92	99.52	100.79	100.38	100.86	101.56	100.39	101.08	101.02	101.31
Oxide	TPBM	TPBL	TS2BU	TS2 3	TS2 2	TS2 1	TS2B	TS2BSU	TS2 BSM	TS2BSB	TS2SDT	TS2SDM	TS2SDB	W01	W02	W03
SiO2	59.86	60.39	50.31	58.52	58.44	55.43	58.69	53.68	57.17	59.09	58.67	54.98	59.59	53.91	56.65	57.94
Al2O3	16.53	16.85	15.85	18.24	18.94	18.74	18.01	17.87	18.48	17.72	18.71	16.07	18.13	17.56	17.83	17.95
TiO2	0.71	0.73	0.60	0.69	0.70	0.68	0.69	0.68	0.72	0.73	0.77	0.64	0.69	0.72	0.70	0.72
MnO	0.09	0.09	0.07	0.09	0.09	0.08	0.09	0.08	0.08	0.09	0.07	0.07	0.07	0.08	0.10	0.09
Fe2O3	6.75	6.86	4.96	5.45	5.43	5.33	5.57	4.92	4.95	5.66	5.53	5.26	5.52	6.30	6.36	6.11
MgO	3.34	3.83	2.95	3.54	3.41	3.27	3.64	3.11	2.99	3.31	2.80	2.50	2.79	2.62	3.41	3.12
CaO	5.40	5.88	4.60	5.77	5.50	5.29	5.97	5.25	4.87	5.03	4.56	4.19	4.35	4.44	6.31	6.44

Na2O	2.80	2.91	2.41	3.06	2.97	2.86	3.10	2.85	2.87	2.86	2.62	2.50	2.52	2.64	3.29	3.43
K2O	1.39	1.38	1.27	1.55	1.54	1.47	1.54	1.38	1.46	1.46	1.41	1.46	1.45	1.44	1.57	1.65
P2O5	0.15	0.13	0.21	0.15	0.16	0.18	0.15	0.23	0.22	0.17	0.12	0.13	0.15	0.14	0.15	0.15
SO3	0.02	0.01	0.01	0.01	0.01	0.01	0.01	0.01	0.01	0.01	0.01	0.01	0.01	0.02	0.01	0.01
LOI	3.29	2.31	17.70	4.12	5.27	7.74	3.80	10.33	7.18	4.73	5.15	13.10	4.64	11.21	5.00	3.50
Total	100.31	101.36	100.94	101.19	102.46	101.08	101.25	100.39	100.99	100.84	100.42	100.89	99.91	101.09	101.36	101.12

Oxide	W04	W05	W06	W07	W08	W09	W10	WB	WC	L07	L95M	DRC
SiO2	56.34	53.30	58.20	71.19	70.55	57.35	47.48	56.34	57.82	58.87	58.00	56.26
Al2O3	18.07	17.60	16.97	13.58	13.60	16.40	18.61	18.25	18.24	15.81	16.90	17.69
TiO2	0.68	0.69	0.55	0.30	0.31	0.69	0.68	0.75	0.73	0.68	0.69	0.69
MnO	0.11	0.09	0.09	0.09	0.09	0.12	0.07	0.09	0.07	0.07	0.10	0.08
Fe2O3	6.51	5.19	5.14	2.39	2.55	7.79	8.02	6.96	6.34	7.02	7.24	5.82
MgO	3.72	3.59	1.87	0.49	0.55	5.06	3.16	3.42	2.69	3.22	3.91	3.43
CaO	6.28	5.21	2.97	1.72	1.79	6.19	3.38	5.68	4.44	4.77	6.11	5.21
Na2O	3.22	2.81	2.91	4.29	4.26	2.90	1.81	2.85	2.65	2.55	2.97	2.66
K2O	1.48	1.31	1.66	2.64	2.61	1.36	0.83	1.37	1.52	1.30	1.33	1.29
P2O5	0.15	0.15	0.12	0.06	0.07	0.13	0.17	0.15	0.16	0.13	0.14	0.20
SO3	0.01	0.01	0.01	0.00	0.00	0.01	0.02	0.01	0.01	0.03	0.01	0.01
LOI	4.05	11.00	10.50	4.00	4.00	2.57	16.50	5.49	6.85	6.35	3.77	7.32
Total	100.62	100.94	100.98	100.75	100.38	100.57	100.73	101.36	101.52	100.81	101.17	100.66

When samples with ≥ 5% LOI are removed, following Regassa et al. (2014), SiO_2, Na_2O, and K_2O now only show a negligible relationship to LOI (Fig. 3.9, Saura, 2018) as would be expected (Lipman, 1965) and remaining samples can be graphed on plots incorporating those major oxides (Fig. 3.11) and compared to previous studies (Fig. 3.12). After excluding ≥ 5% LOI samples, CaO, MgO, and MnO still display a weak/moderate positive relationship, and graphs including those major oxides are not possible.

Plotting the low LOI samples on a TAS diagram (Fig. 3.11) shows most units plotting within andesite and basaltic andesite domains, with the exception of two samples of rhyolitic Taupo airfall (Table 3.2: W7, W8), and a single hyperconcentrated flow unit (Table 3.2: PB03). Perhaps unsurprisingly, most well-indurated debris flow unit samples have an LOI% above the cutoff.

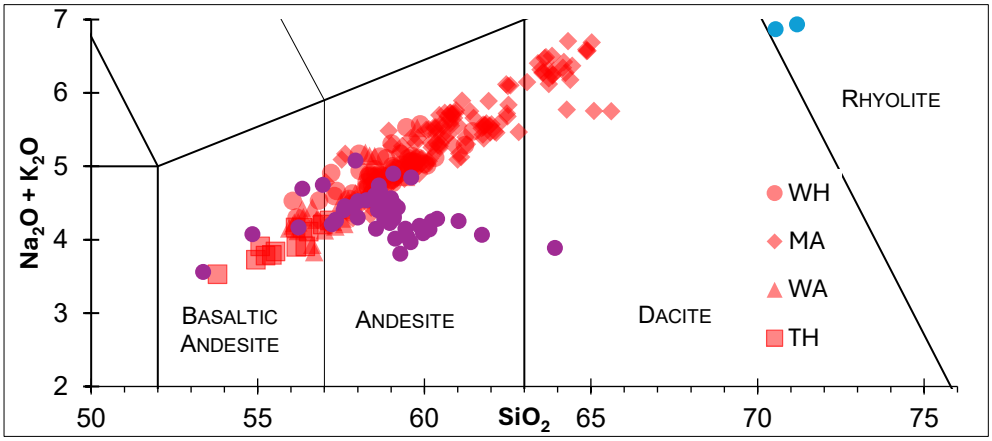


Figure 3.3 TAS diagram of composition of samples (purple) excluding ≥5% LOI, Taupo pumice layers plotted as light blue. Plotted against whole rock major element data from Conway et al. (2016) WH: Whakapapa Formation, MA: Mangawhero Formation, WA: Wahianoa Formation, TH: Te Herenga Formation.

When LOI is controlled for and SiO_2 vs K_2O oxide weight percents are plotted against trends of major lava flows on Ruapehu (Conway et al., 2018) (Fig. 3.12) there is a trend of lower wt% K_2O, however this trend is similar across all formations for alkaline elements vs. averaged whole rock oxides from Conway et al. (2018) with 11-22% less K_2O, 7-16% less Na_2O, and 6-20% less CaO. All MnO wt% and most MgO wt% values are also lower than averaged flow values.

Examination of the prehistorical lahars reveals some trends and interesting relationships. Exclusion of high LOI values reduces Onetapu A to just two useable SiO_2 values which are from different distinct Onetapu A subunits. Onetapu B units have the widest distribution, however the 56.4 wt% and 54.0 wt% SiO_2 values are from separate layers of the same tributary backfill at the distal end of the longitudinal sampling profile. Onetapu C units vary between 59.6 and 62.1 wt% SiO_2 and 1.41 wt% and 1.70 wt% K_2O and at the marae bridge quarry site (Fig. 3.2, site 4) where units C2 and C3 are both exposed have a tighter clustering between 60.6 wt% and 62.1 wt% SiO_2 and 1.43 wt% and 1.52 wt% K_2O across units. Onetapu D has a tight clustering that varies between 59.8 wt% and 60.7 wt% SiO_2 and 1.47 wt% and 1.67 wt% K_2O across all applicable units, where the outlying point is the uppermost Ond-3 hyperconcentrated flow deposit at the marae bridge quarry site.

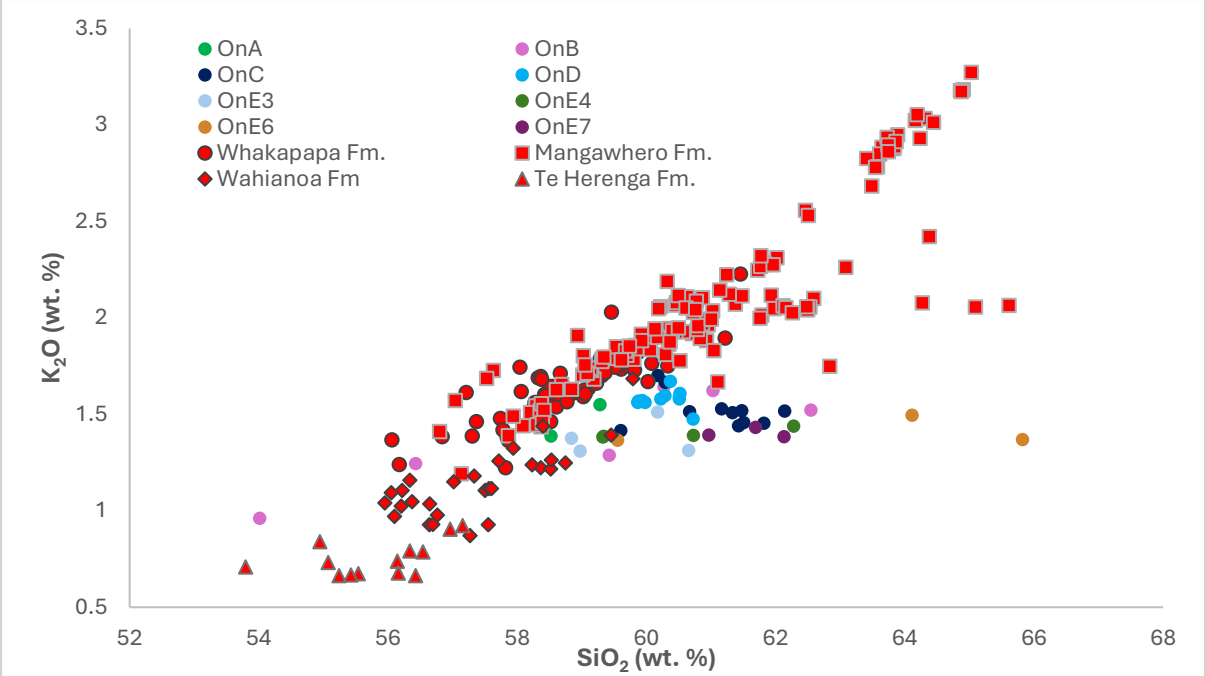


Figure 3.4 SiO_2 vs K_2O of major chronostratigraphic lava formations (Conway et al., 2018) and lahar units (Hodgson et al., 2007). Whakapapa formation (<15 ka) are red circles, Mangawhero formation (50 – 15 ka) are red squares, Wahianoa formation (160-80 ka) are red diamonds, Te Herenga formation (200-150 ka) are red triangles. Onetapu formation members are all represented by circles, with Onetapu A (>1530 ± 160 BP - <1850 BP) light green, Onetapu B (<1640 ± 60 yr BP - >1271 ± 56 yr BP) lavender, Onetapu C (<1271 ± 56 yr BP - >890 ± 50 yr BP) black, Onetapu D (<890 ± 50 yr BP- >380 ± 60 yr BP), and Onetapu E3 as pale blue, E4 as forest green, E6 as ochre, and E7 as violet (1861AD, 1953AD, 1995AD, 2007AD respectively).

The composition of the silt+clay size fraction for certain samples was also examined via X-ray diffraction (XRD) (Fig. 3.13) to detect mineral phases that were not identified via VNIR & SWIR analysis. 38 samples were analyzed (appendix B1) and the dominant mineral phase was plagioclase feldspar, followed by clinopyroxene group minerals, spinel group minerals, ± trace opal, quartz, & cristobalite. Ruapehu's lavas are predominantly moderately to highly porphyritic and all that have been sampled contain plagioclase phenocrysts, followed by orthopyroxene and clinopyroxene and spinels are dominantly magnetite (Conway, 2016).

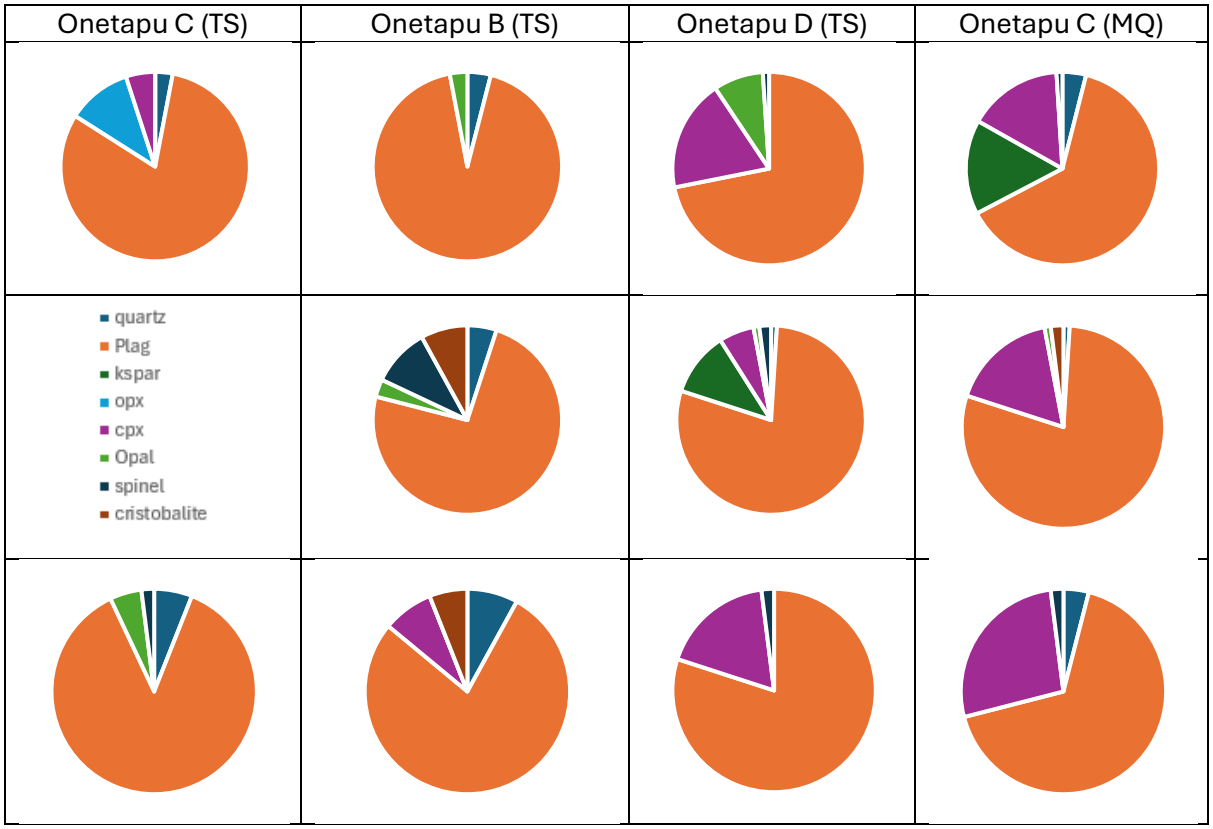


Figure 3.5 XRD mineral phases in lahar matrix samples. Samples are dominated by plagiclase (orange) and clinopyroxene (purple). Other common mineral phases are quartz (dark blue), orthopyroxene (light blue), magnetite/spinel (grey-blue), kspar (dark green), and a broad peak alternatively identified as cristobalite or opal (green and violet, respectively). Onetapu C Tangiwai Swamp samples (TS) are TS2BSU and TS2BSB, Onetapu B Tangiwai Swamp (TS) samples are TS2SDT, TS2SDM, TS2SDB, Onetapu D Tangiwai Swamp (TS) samples are TS23, TS22, TS21, Onetapu C Marae Bridge Quarry (MQ) samples are MQE, MQC, and MQA.

XRD analysis of selected lahar unit silt+clay size fractions has been conducted in the past one selected Onetapu A and B units using clay separation methods (Fig. 3.14, Hodgson et al., 2007) to find matrix compositions, invariably finding compositions consistent with hydrothermal alteration.

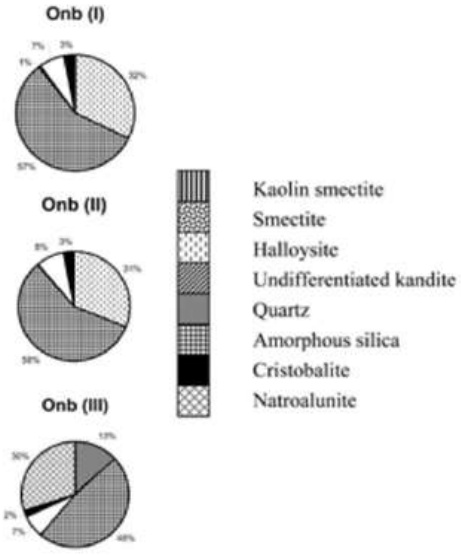


Figure 3.6 Pie charts of clay mineral assemblages progressing upstream. Sites duplicated in this study are: I = MQ, II = TS2, III = PON. After Hodgson et al. (2007)

3.4.2 VNIR & SWIR

Matrix and clasts of 108 lahar samples were measured, including individual outsized clasts where applicable, resulting in 222 averaged spectral reflectance measurements (appendix B2). This study presents selected results of correlation matrices and dendrograms based on spectral angles and principal component analyses, best fit continuum removed matches for selected USGS (Kokaly et al. 2017) reference phyllosilicate library (Clark & Roush, 1984) determined, relative phyllosilicate peaks of lahar clasts and matrix, and intra- vs inter- unit comparisons longitudinally.

LOI values as an indicator of higher degrees of alteration is corroborated by SWIR data of averaged ≥5% and <5% LOI samples (Fig. 3.10) showing greater absorption in the 1410 nm and

1910 nm bands.

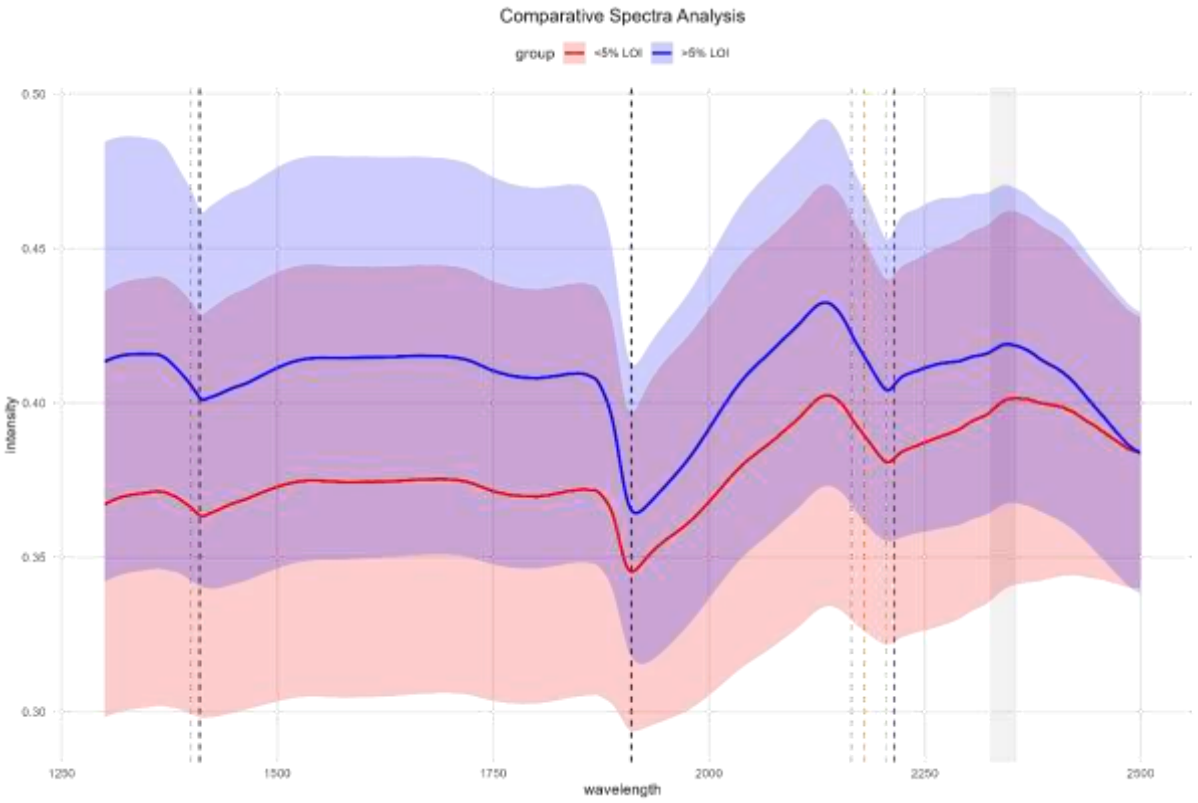


Figure 3.7 Continuum removed SWIR spectra of >5% LOI lahar matrix (blue) vs. <5% LOI lahar matrix (red) showing comparitively greater absorption in the 1410 nm band, and much greater absobption in the 1910 nm band.

Following Schaefer et al. 2023, we used wavelengths between 1410-1450 nm, 1920 nm, and between 2180-2400 nm for indicators of phyllosilicates, primarily kaolinite and montmorillonite. Most samples have an absorption feature around 1900 nm, characteristic of smectite (Bishop et al., 2008; Bishop, 2019). These features are generally more pronounced in the matrix vs clast categories (Fig. 2.4).

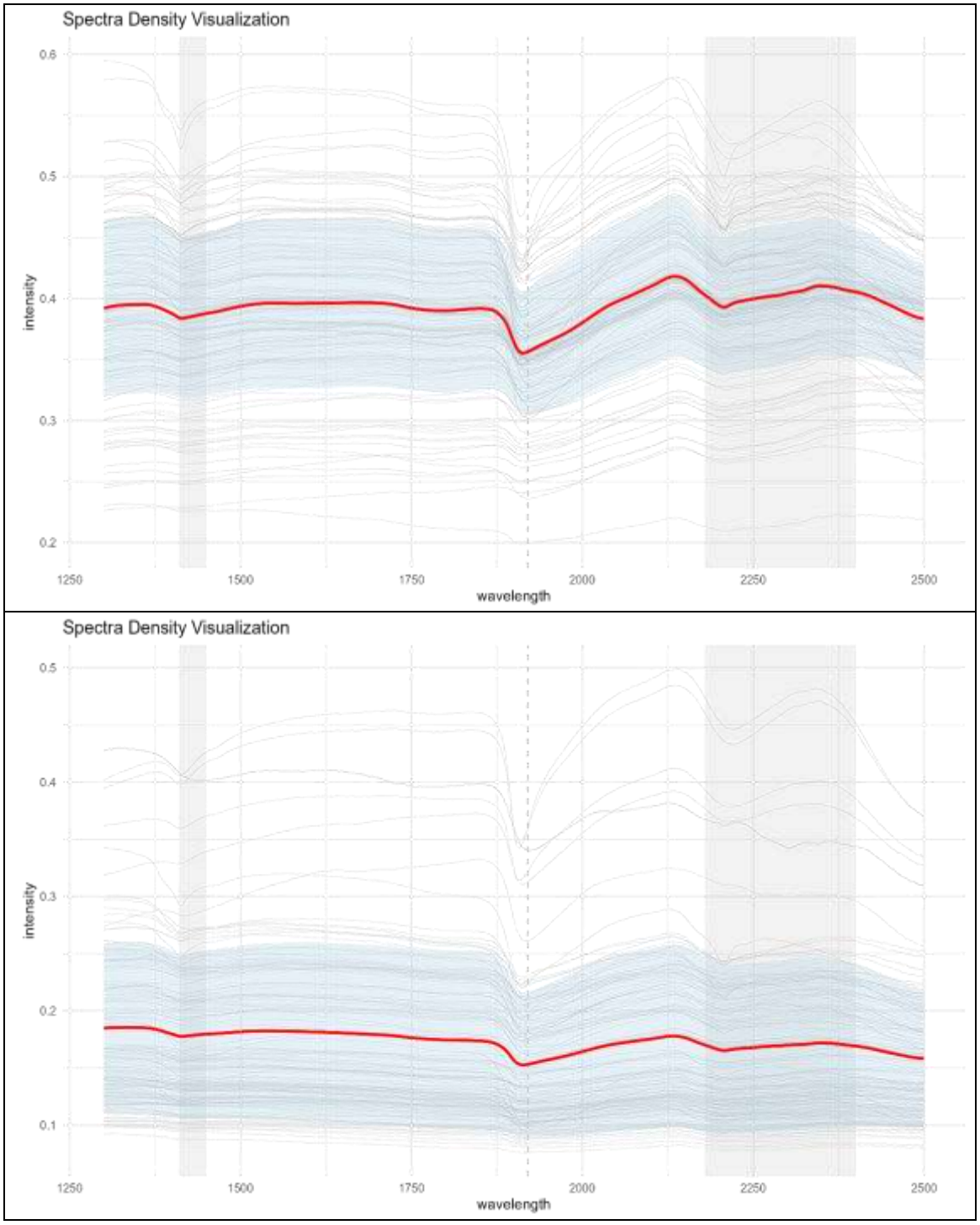


Figure 3.8 Combined continuum removed 1300 – 2500 nm subset spectra of (a) matrix material (<4ϕ) and (b) clast material (>1.5 ϕ) of all samples. Individual spectra are plotted along with a mean line (red) and a blue ribbon representing one standard deviation. Gray bars and dashed lines at 1410 – 1450 nm, 1920 nm, and 2180 – 2400 nm are general absorption features of phyllosilicate minerals.

Matrix vs clast comparisons were plotted to show heterogeneity of the sample and to help track changes in composition within identified lahar units between sampling sites (Fig. 3.2).

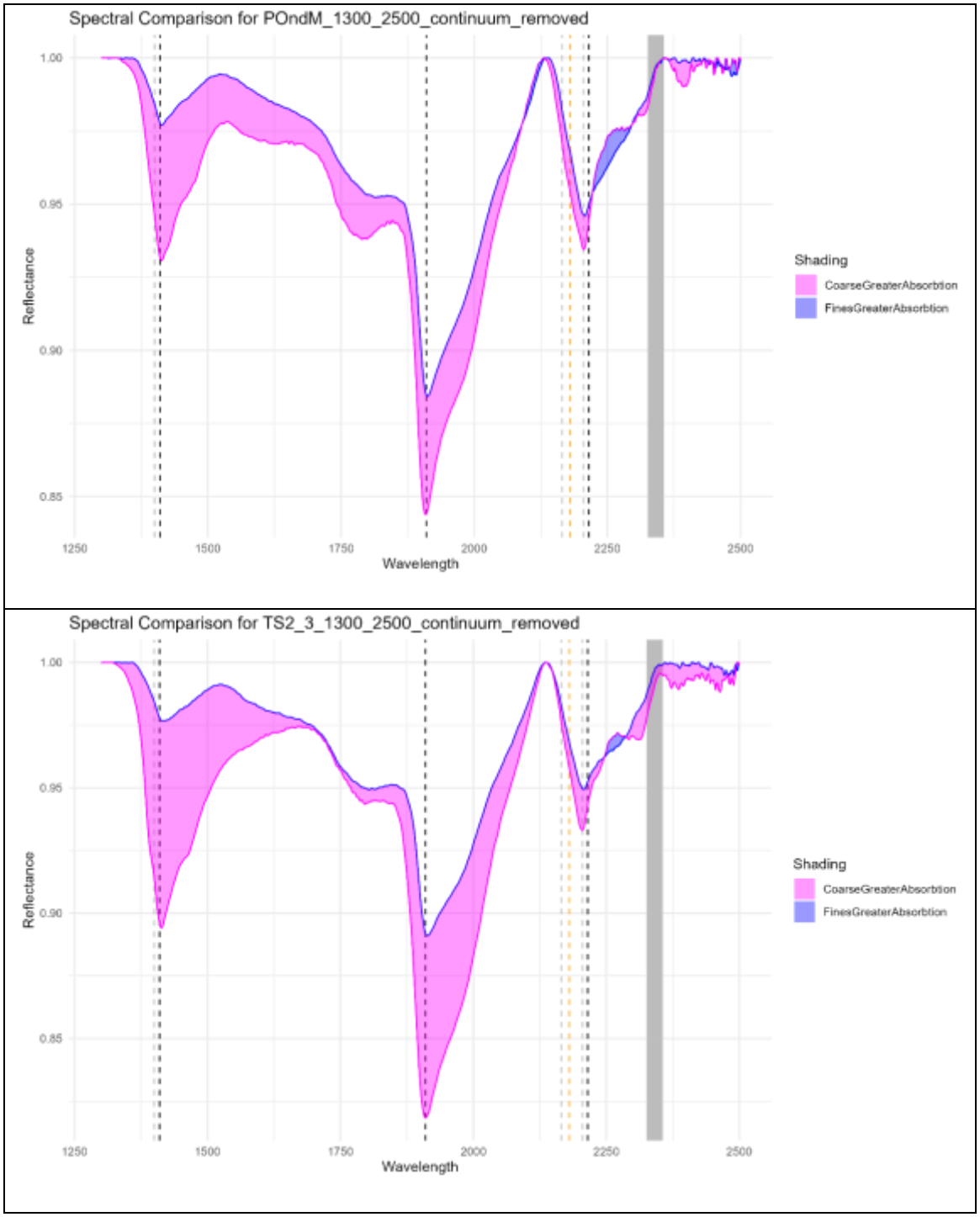
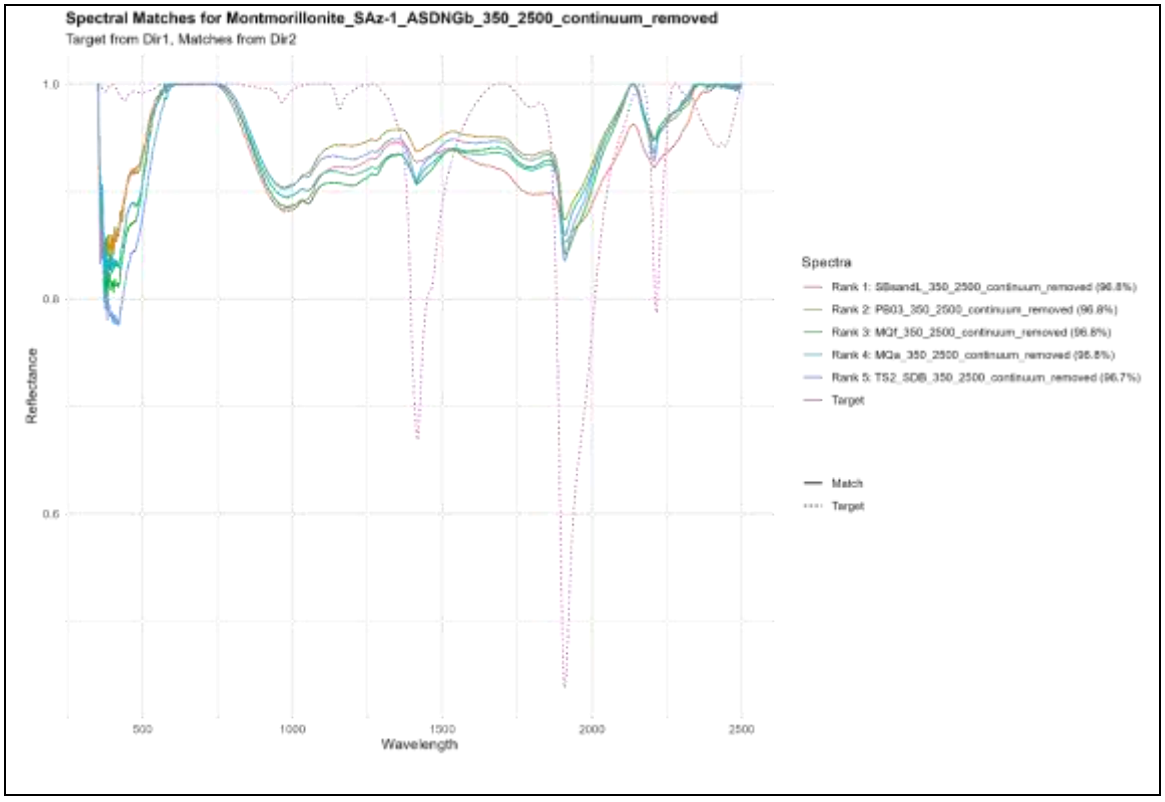
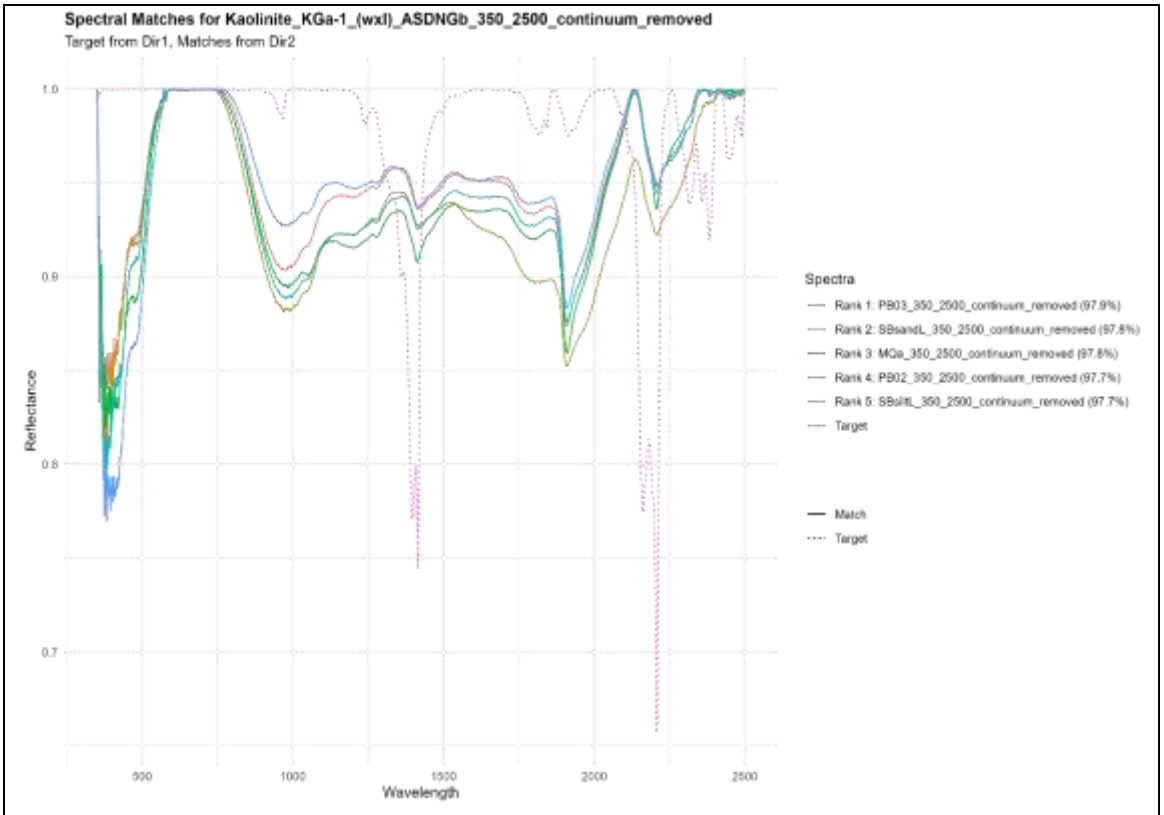
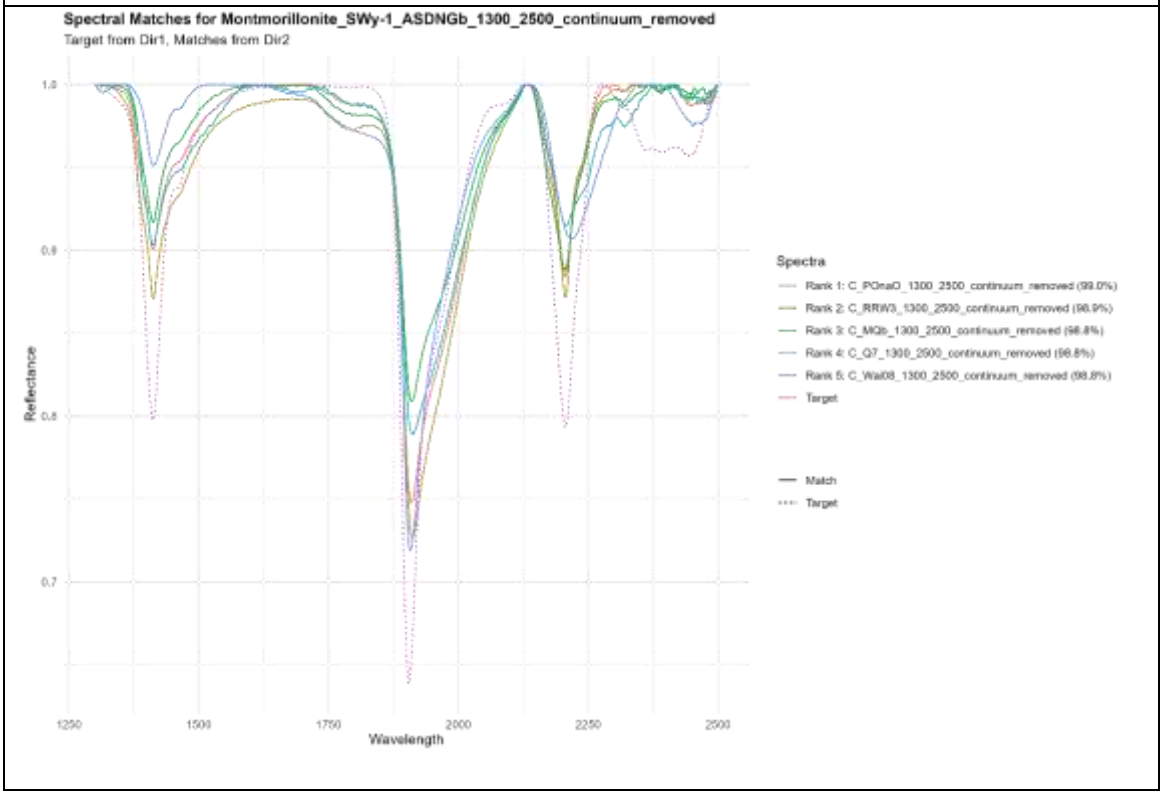


Figure 3.9 Comparison of 1300 nm to 2500 nm subset of continuum removed spectra for clasts vs matrix from the same lahar unit and relative location within the column at two sampling sites. Blue line is matrix reflectance, pink line is clast reflectance, where pink shaded areas indicate where clasts have relatively greater absorption features (greater abundance), and blue shaded areas indicate where matrix has relatively greater absorption features (greater abundance). Black vertical lines are smectite absorption peaks, grey vertical lines and areas are kaolinite absorption peaks, and orange vertical lines are alunite absorption peaks.

Best fit spectral angle matches were generated for selected USGS spectral library minerals and all samples were given a ranking (Fig. 3.6) which serves two purposes, the identification of those samples with best representation of minerals of interest and displaying spectral angle expression in multi-mineral lahar matrix samples. Even among the best matches, there were no fines samples that have the characteristic kaolinite doublet absorptions near 2200 nm and 1400 nm (Fig. 3.6b), which would be partially masked by the presence of montmorillonite and not present in disordered kaolinite or halloysite (Clark et al., 1990). This shoulders towards shorter wavelengths at 2200 nm and 1400 nm which are indicative of kaolinite (Clark et al., 1990). Many clast samples have identifiable doublet absorption features (Fig. 3.6d). Montmorillonite was identifiable (Fig. 3.6a, 3.6c) at various concentrations in all matrix samples, and most clast samples (Fig. 3.4)




Spectral Matches for Kaolinite_KGa-1_(wxl)_ASDNGb_350_2500_continuum_removed
Target from Dir1, Matches from Dir2
Reflectance
Wavelength
1.0
0.9
0.8
0.7
500
1000
1500
2000
2500
Spectra
Rank 1: PB03_350_2500_continuum_removed (97.9%)
Rank 2: SBsandL_350_2500_continuum_removed (97.8%)
Rank 3: MQa_350_2500_continuum_removed (97.8%)
Rank 4: PB02_350_2500_continuum_removed (97.7%)
Rank 5: SBsiltL_350_2500_continuum_removed (97.7%)
Target
Match
Target


Spectral Matches for Montmorillonite_SWy-1_ASDNGb_1300_2500_continuum_removed
Target from Dir1, Matches from Dir2
Reflectance
Wavelength
1.0
0.9
0.8
0.7
1250
1500
1750
2000
2250
2500
Spectra
Rank 1: C_PCnaO_1300_2500_continuum_removed (99.0%)
Rank 2: C_RRW3_1300_2500_continuum_removed (98.9%)
Rank 3: C_MQb_1300_2500_continuum_removed (98.8%)
Rank 4: C_Q7_1300_2500_continuum_removed (98.8%)
Rank 5: C_Wal08_1300_2500_continuum_removed (98.8%)
Target
Match
Target

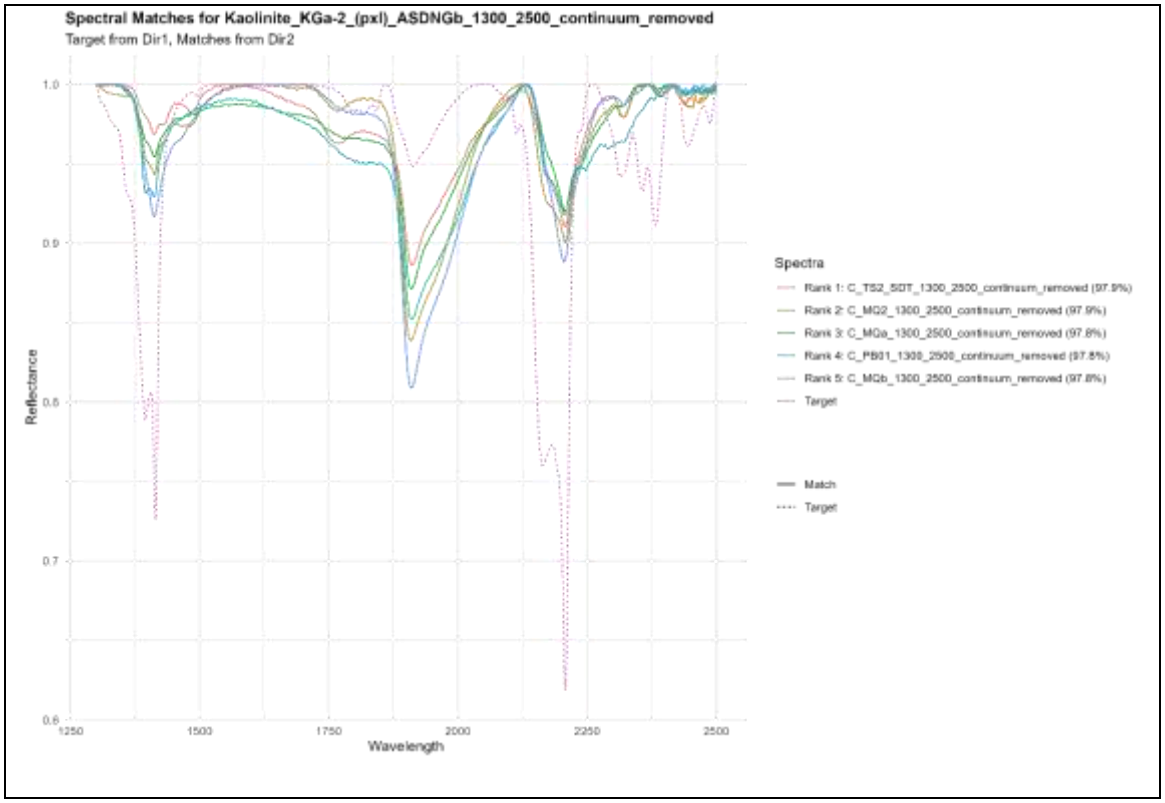


Figure 3.10 Spectral angle mapping matches of matrix and clast samples with spectral database entries for pure samples with top 5 closest matches displayed. Reference samples (Kokaly et al. 2017) for montmorillonite (a & c) and kaolinite (b & d) are graphed against the top five best 350 nm to 2500 nm (fine, a & b) and 1300 nm to 2500 nm (coarse, c & d) continuum removed spectra spectral angle matches.

The <4.0 ϕ (silt-clay) size category and 1300-2500 nm spectral region were examined to see if the lahar matrix could be used for fingerprinting. All samples and sampled sizes were compared against each other via spectral angle mapping, a similar technique to what is used in forensic geology (Tighe et al., 2018; Zeng et al., 2023), hierarchically grouped (Ward, 1963), and plotted against all other samples (Fig. 3.7) to determine degrees of similarity (Farifteh et al., 2007). Dendrogram clusters were ranked by dissimilarity and plotted and then separated into smaller bins between 0.35 – 0.25 percent dissimilarity, resulting in 14 distinct bins.

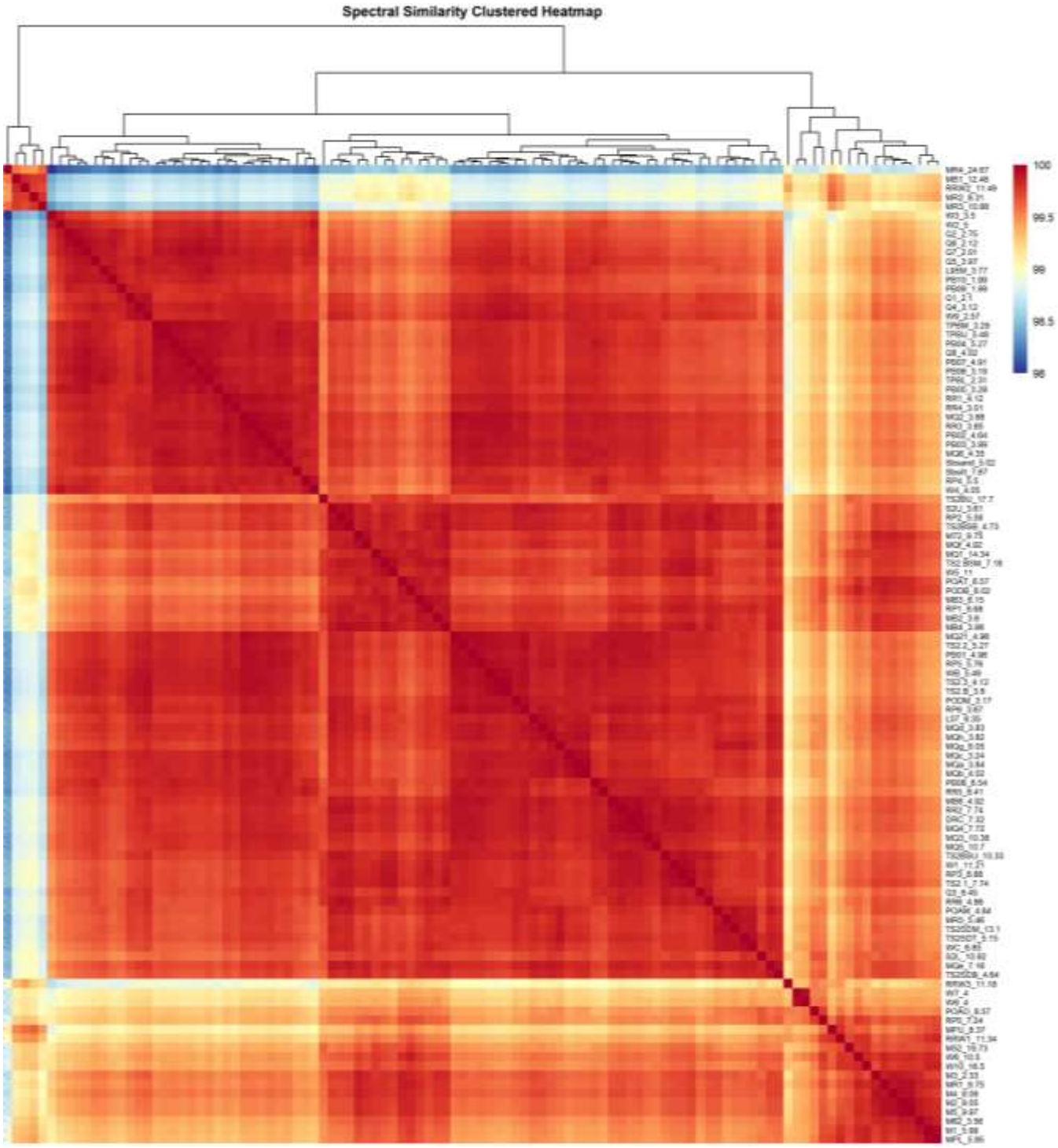
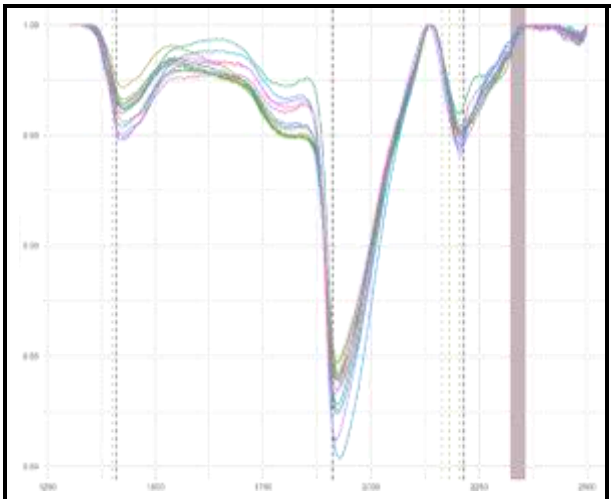
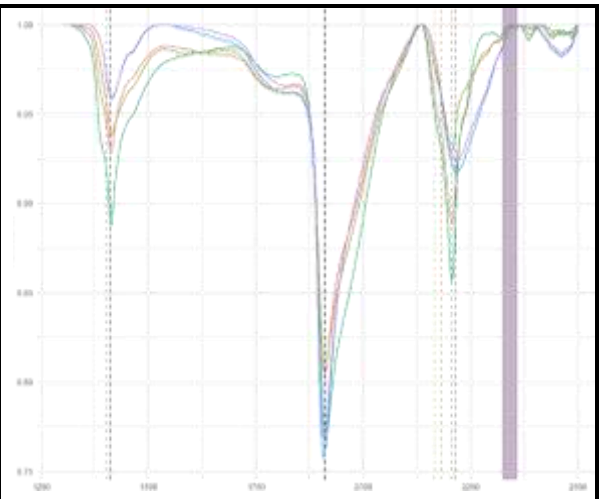
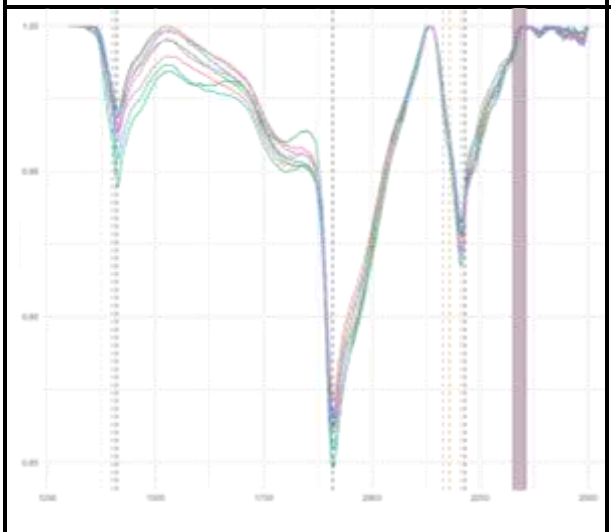
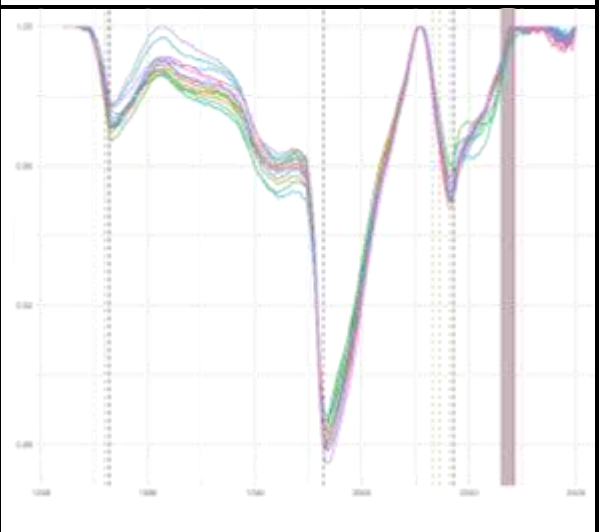


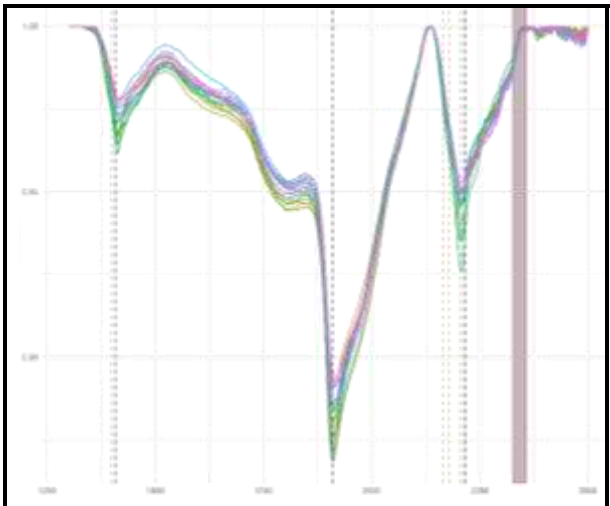
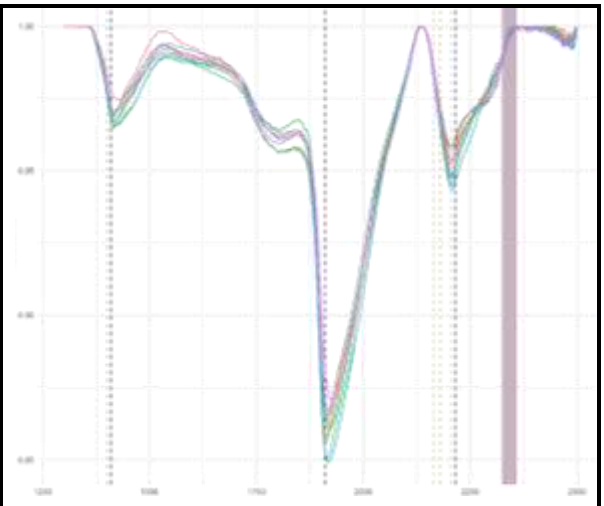
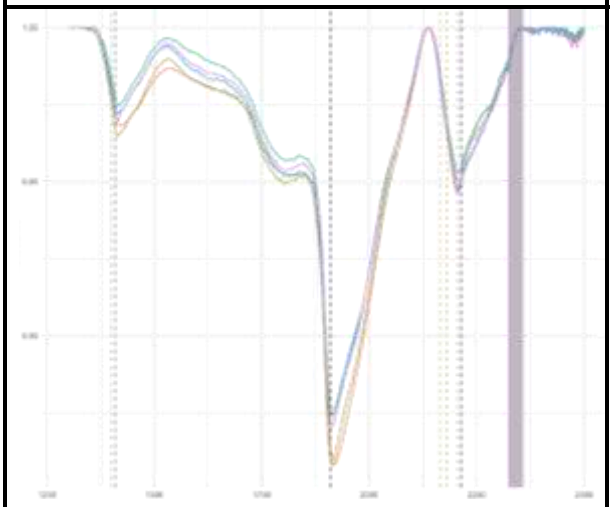
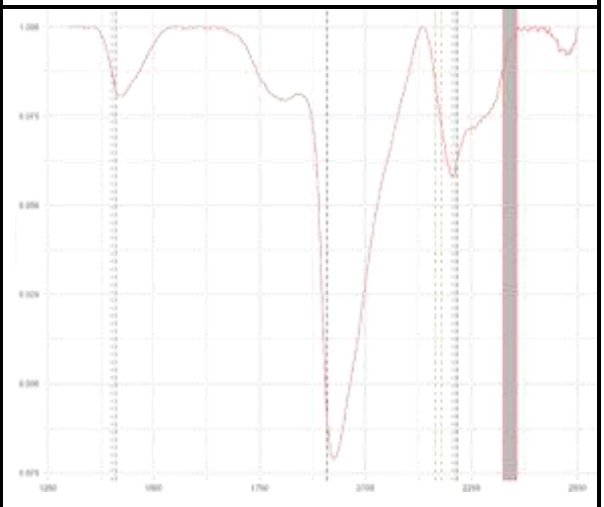
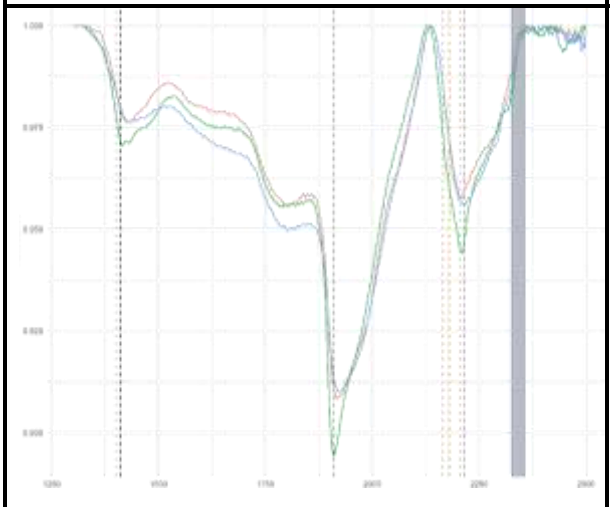
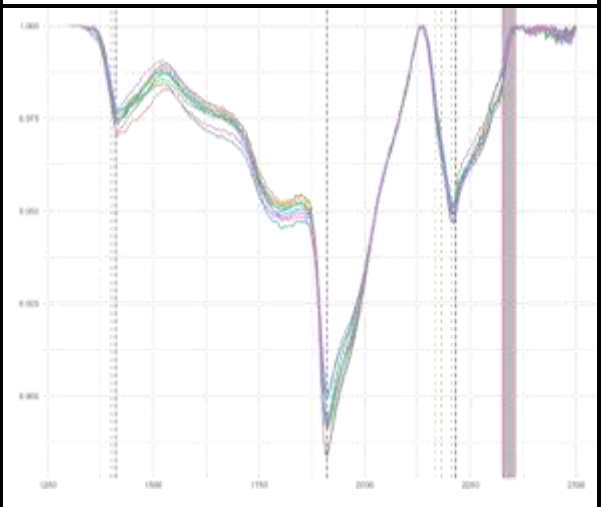
Figure 3.11 Spectral angle similarity distance heatmap, red showing greater similarity. Similarity clusters are denoted by dendrograms.

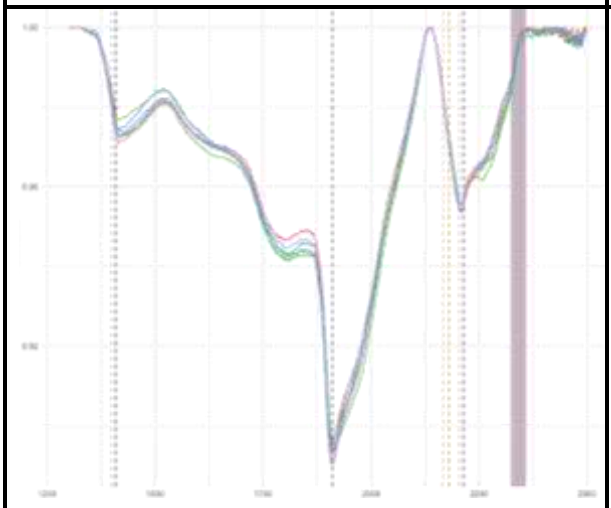
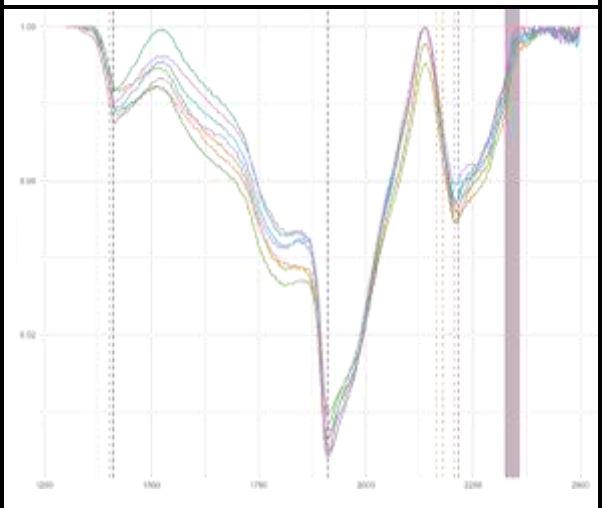
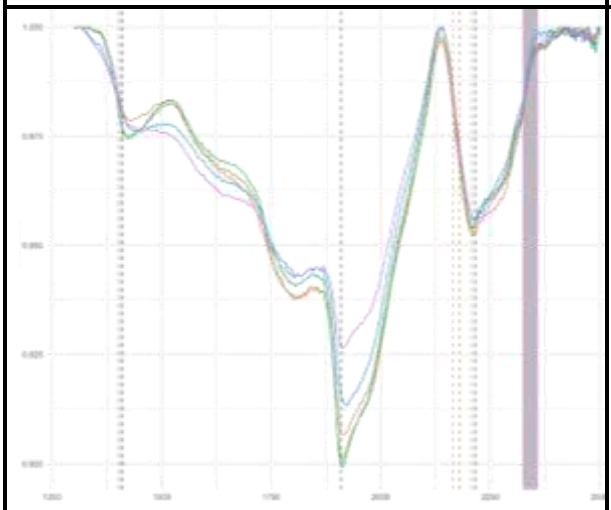
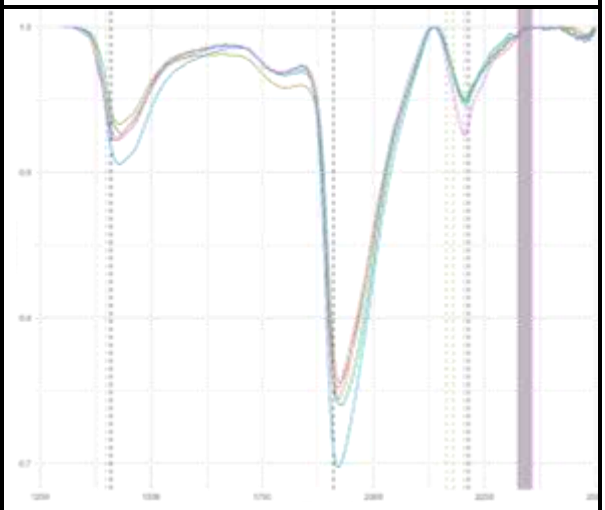
Hierarchical clusters of lahar matrix are identified in Table 3.3 along with spectra of all samples within a cluster. Reflectance is scaled by continuum removal and relative depth of absorption

features, so narrow absorption features are of primary interest and artifacts of processing (e.g. the slope between ~1520 nm and ~1800 nm in groups 9-13) are less significant.

Table 3.3 Spectral similarity clusters, including individual members and group numbers for identification.

	
Group 1 samples: M1, M2, M3, M4, M5, M52, M62, MPL, MPU, MR1, RRW1, W06, W10	Group 2 samples: POnaO, RP0, RRW3, W07, W08
	
Group 3 samples: MQe, MR5, PonaM, S2L, TS2SDB, TS2SDM, TS2SDT, WC	Group 4 samples: DRC, MB6, MQ3, MQ4, MQ5, PB08, Q3, RP3, RP5, RR2, TS21, TS2BSU, W01

	
Group 5 samples: L07, MQ2, MQa, MQb, MQc, MQd, MQg, MQh, PB01, POndM, RP5, RP6, TS22, TS23, TS2B, WB	Group 6 samples: MB2, MB3, MB3, MQ1, POnaT, POndB, RP1, TS2BSM, W05
	
Group 7 samples: M72, MQf, RP2, S2U, TS2BSB	Group 8 samples: TS2BU
	

Group 9 samples: RP4, SBsilt, W04	Group 10 samples: MQ2, MQ6, PB02, PB03, RR1, RR3, RR4, SBsand
	
Group 11 samples: PB04, PB06, PB07, Q8, TPBL, TPBM, TPBU	Group 12 samples: L95m, PB09, PB10, Q1, Q4, Q5, W09
	
Group 13 samples: Q2, Q6, Q7, W02, W03	Group 14 samples: MB1, MR2, MR3, MR4, RRW2

3.5 Discussion

3.5.1 Triggers

Possible trigger mechanisms for Onetapu formation deposits have been suggested based on clast componentry and deposition styles, including rainfall-triggered remobilization (Onc), lake outbreak (One-4, One-7), crater lake water displacement (One-5, One-6), and debris avalanche

(Onb, Ond) (Hodgson et al., 2007; Lecointre et al., 2004a). Componentry and stratigraphic relationships between units are the main tools that have been used previously to determine trigger mechanism. Other methods such as the clay species analysis, geochemistry of components need to be examined to contribute to providing a broad matrix of measures in identifying these triggering mechanisms for areas where componentry might have changed dramatically due to the incorporation of foreign through the erosion of older units or smaller units that are limited in preservation.

Units identified at the Onetapu type locality, the Tangiwai Swamp, were of particular interest. SWIR analysis of clasts shows differing composition/alteration through single units, with sharper absorption bands towards the top of units, while fines exhibit a much less variable distribution. SWIR clast analysis of Tangiwai swamp samples shows a prominent opal shoulder, also present in XRD analysis, in Onb and Ond units which is absent in Onc, indicating clast alteration, which is absent from fluvial andesitic clasts analysed from the Ona unit at the Waihianoa/Whangaehu confluence. The Tangiwai Swamp Ond finer-grained basal unit lacks the opaline shoulder, so is possibly sediment entrained in the bow wave of a larger Ond debris flow.

The matrix and clast SWIR measurements of Onetapu B units at Tangiwai Swamp show relatively close agreement, both between matrix and clasts and between sampled sections, whereas Onetapu D sections sampled at Tangiwai Swamp have small variations in matrix, but larger variations between clast/clast comparisons and clast/matrix, suggesting different magnitudes of triggers, with Ond being a much larger event incorporating disparate clast sources. The most prominent unit at the Marae Bridge Quarry, Onetapu C, exhibits relatively uniform matrix and clast compositions throughout, aside from lenses of remobilized Taupo material. The spectral angles of the matrix composition for these units most closely matches with matrix from One-7 and Tangiwai Swamp Ond units.

Alteration patterns provide further clues to the triggering mechanisms. Relatively deep montmorillonite and kaolinite SWIR absorption features are seen in both matrix and clasts from the Onb unit, which is thought to have been triggered by a landslide associated with the Crater Lake vent rim partially on the basis of no juvenile clasts (Hodgson et al., 2007; Lecointre et al., 2004a). Meanwhile Ond-3 unit members matrix has deeper montmorillonite and kaolinite SWIR absorption features than the clasts, which is thought to have been triggered by landslide associated with dome building partially on the basis of presence of juvenile and altered clasts (Hodgson et al., 2007; Lecointre et al., 2004a). If clasts are altered to a similar high degree as the matrix, it could suggest a non-eruptive landslide trigger, whereas matrix being more altered than clasts might indicate an eruptive triggered landslide or lake breakout as with Ond-3. If all components remain unaltered, an eruptive origin is considered more likely due to the homogeneity of the deposit.

Other deposits exhibit similar trends. Wahianoa/Whangaehu confluence Ona matrix and smaller clasts separated in sieving are similarly altered, but incorporated larger fluvial clasts which are relatively unaltered. Ona deposits at site 18 (Fig. 3.1) have clasts with a relatively greater degree of alteration than fines, while One-3 clasts from site 9 (Fig. 3.1) remain unaltered compared to their matrix. The type of clast mineralization could serve as a useful indicator of hydrothermal triggers, though due to bulking and debulking proximal deposits may also similarly provide insights into lahar dynamics as well. Bulking and debulking has been inferred for all Onetapu debris flows, eventually transforming into hyperconcentrated flows downstream (Hodgson, 1993), so while most flows at the studied sites would be considered at their greatest (bulked) flow volumes (Procter et al., 2018, 2010a), it is unknown how much of the clast componentry is progressively inherited from the catchment.

Comparing relative alteration of One-6 and One-7 units at site 16 (Fig. 3.1) the 1413 nm band is sharper and deeper than both matrix and clasts for One-7 and both have an opal shoulder,

which is absent or minimal in One-6 matrix and clasts. The 1413 nm band is more defined in the matrix of both One-6 and One-7, although to what degree this could be the product of milling vs. inherited at ~22km from the source is uncertain without histograms and composition of initial hyperconcentrated flows.

3.5.2 Fingerprints

The Tangiwai Swamp drainage canal serves as the original type section for Onetapu deposits (Donoghue, 1991) and remains the most accessible and complete of previously identified outcrops. As a result, samples from this location, along with One-6 and One-7 units at site 16 identified independently by Dr. Katy Hodgson and Dr. Anke Zernack (pers. comm.) were extensively utilized in this study to establish correlations and identify common features among different exposures of the same unit.

Spectral angle matching (supplemental data) indicates a lack of self-similarity between clast and matrix samples, except for the andesitic Mangatawai tephra beds, Taupo ash and pumice deposits, and the interiors of large debris flows. The SWIR measurements of the matrix of Onetapu units showed greater similarity compared to clast composition, which changed both longitudinally and within the same deposit.

The question of in-situ weathering vs inherited weathering was a concern, especially for units within the vadose zone, however other studies have indicated a longer time period is necessary for alteration at various surface conditions for the same deposit (Cook, 2002; Rasmussen et al., 2007) and indeed, clay alteration of Taupo Ignimbrite is generally less than 5% (Bakker et al., 1996; Lowe and Percival, 1993), and Ona-1 & Ona-3 are the only deposits with significant remobilized c. 4,600 yr BP Mangaio Formation (Donoghue and Neall, 2001; Hodgson, 1993; Hodgson et al., 2007).

High LOI values for XRF measurements makes direct comparison between units difficult, as the majority of samples of certain Onetapu units (Ona ~90%, Onb ~60%, Ond ~50%) can't be plotted against lava trends, with the caveat that high LOI values also seem to correspond to cohesive debris flows. Samples at the base of Ond deposits (Ond-1) at sites 8 and 14 (Fig. 3.1) don't have LOI issues and SWIR measurements indicate they are slightly less altered, which could indicate a clay-poor bow wave, as it has only been noted as occurring with Ond-2 (Hodgson et al., 2007).

SWIR analysis can be broken down into clusters divided by dissimilarity (Fig. 3.11, Table 3.3), and samples from Onetapu Formation units previously identified via stratigraphy and sedimentology (Refer to chapter 2) tend to plot in the same cluster or in neighbouring clusters, with debris flow units showing tighter clustering than hyperconcentrated flow units (e.g. Group 3 (Table 3.3) Onetapu B units: TS2SDB, TS2SDM, TS2SDT, MR5; Group 5 Onetapu D2 units: TS22, TS23, TS2B, MQ2, PONDM, RP5, RP6; vs Onetapu C3 units in Group 4 (TS2BSU, RP3), Group 5 (MQg, MQh), Group 6 (MQ1, MB3, RP1, TS2BSM), Group 7 (RP2, TS2BSB)).

3.5.3 Refining the lahar record

SWIR matrix data have a distinct grouping that corresponds to the earliest Onetapu flow (Table 3.2: 14), which likely represents a pre-Taupo Ignimbrite flank collapse/remobilization of Mangaio Formation, seen at sites 12, 3, and 1. No sites have been located that show a direct stratigraphic relationship between this and Taupo Ignimbrite/other Onetapu A units.

Results on timing and extent remain inconclusive, however 400 years ago the Wahianoa valley hosted a much more extensive glacier, possibly to the valley mouth (Nolan, 2008), and since all current Ruapehu tephra isopachs extend over the head of the Wahianoa catchment (Voloschina, 2020), sites 18, 17, and 15 likely record a waning contribution by the Wahianoa catchment to the Onetapu lahar record with glacial retreat. Site 18 has distinct andesitic,

possibly Mangatawai, tephra beds, later Taupo ignimbrite airfall tephra, and subsequent lahar units that seem to have both andesitic tephra and Taupo ignimbrite matrix based on field assessment and SWIR clustering. Initial field observation linked this unit to units at sites 17 and 14, and subsequent SWIR clustering indicated similarity to additional unassigned units at sites 12 and 2. While this occurred early in the Onetapu sequence, no stratigraphic relationships between it and Ona-1 have been observed and it has a separate SWIR grouping from Ona-1.

The newly mapped unit at the Wahianoa/Whangaehu confluence (site 15) has a stratigraphic relationship of being above a variably 1-2 cm thick soil layer above a >80 cm unit of charcoal-bearing Taupo ash. This unit is likely the WB unit at site 18 (Table 3.2: WB), however it shares a matrix SWIR cluster with Onb units at sites 9, 8, and 1, while the WB unit's cluster includes mainly Ond-2 units.

The Taupo ignimbrite units and underlying Mangatawai tephra beds are both visually distinct units, and one of the first post Taupo ingnimbrite lahars has been previously logged as a combination of the two units (Refer to chapter 2) which is supported by spectral similarity of both units with the lahar unit along the Wahianoa and Whangaehu catchments (Sites 18, 17, 14, 12, and 2). The upper, matrix supported debris flow unit at the Wahianoa confluence (Site 15) correlates to the same group as Onb units at sites 9, 8 (Tangiwai Swamp), and unit at site 1 that occupies a similar stratigraphic position above remobilized Taupo deposits. No other outcrops that match this spectral group were located further upstream on either the Wahianoa or Whangaehu rivers, although the orientation and roundedness of the cobbles imply it was sourced from the Wahianoa catchment (Refer to chapter 2). This could imply a similar flank source as Onb, affecting both Whangaehu and Wahianoa catchments, or the Onb lahar remobilizing Wahianoa cobbles, and given the similar stratigraphic positions and spectral grouping, some relationship is likely.

The thickest unit at site 18 correlates to Ond units at site 14, 11, 8 (Tangiwai Swamp), and 4, which suggests a possible similar source, however it is stratigraphically lower than a muddy unit that matches the description of redox paleosols found at other locations in the Rangipo Desert (Purves, 1990) and groups loosely with Onc units. The sequence at site 18 ends with the T11 tephra layer (Donoghue, 1991; Voloschina, 2020).

3.5.4 Applicability of methods

Infrared spectroscopy proved especially valuable in this study because it resolved alteration signatures at abundances below the detection limits of bulk XRD methods. VNIR-SWIR spectra captured subtle absorption features of clays and phyllosilicates that differentiated otherwise similar deposits. This sensitivity enabled us to separate relatively unaltered hyperconcentrated flows (e.g., Onc) from the highly altered, clay-rich cohesive debris flows (e.g., Onb and Ond), even where bulk mineralogical and geochemical compositions converged around typical Ruapehu andesite.

These laboratory-based spectral results also directly complement airborne and satellite mapping of hydrothermal alteration on volcanic edifices. Remote sensing surveys at Ruapehu and other stratovolcanoes effectively delineate zones of alteration at the surface, but they cannot by themselves demonstrate how altered materials are entrained into lahars and preserved in downstream deposits. By establishing that alteration fingerprints are detectable and interpretable in the lahar record, our approach bridges edifice-scale mapping with deposit-scale analysis. This creates a transferable framework: edifice alteration zones identified by remote platforms can be tested against spectral fingerprints in lahar deposits, strengthening provenance models and enabling hazard reconstructions at volcanoes worldwide.

3.6 Conclusions

This study demonstrates that a combined geochemical, mineralogical, and spectral approach provides a robust framework for fingerprinting lahar deposits. Bulk XRF and XRD established that Onetapu matrices generally converge around typical andesitic compositions, limiting discrimination between units, however, high LOI values complicated geochemical comparisons: ~90% of Ona, ~60% of Onb, and ~50% of Ond samples could not be reliably plotted against lava trends. Importantly, these elevated LOI values corresponded with cohesive debris flows, reinforcing the link between clay abundance, alteration, and flow rheology. Exceptions occurred at the base of some cohesive debris flow deposits (e.g. Ond-3 at sites 8 and 14), where LOI was lower and SWIR spectra indicated weaker alteration, possibly representing a clay-poor bow wave preceding the main debris flows. This highlights both the limitations of bulk measurements the value of LOI when paired with spectral data.

Infrared spectroscopy proved especially valuable by detecting alteration minerals at concentrations below XRD sensitivity. The ~1.3 to 2.2 µm SWIR spectral region examined in this study, including diagnostic absorption features near 1.4 µm (OH), 1.9 µm (H_2O), and 2.2 µm (Al-OH), resolved different phyllosilicate abundances well-established as indicators of hydrothermal alteration (Douglas et al., 2022; John et al., 2019; Kereszturi et al., 2018; Schaefer et al., 2023). These features allowed us to discriminate between relatively unaltered hyperconcentrated flows (Onc) and highly altered cohesive debris flows (Onb, Ond). Clustering analyses of VNIR-SWIR spectra showed that units form compositional groups consistent with mapped stratigraphy and inferred triggers, while clast vs. matrix comparisons indicates that single origin triggers have more consistent clast-matrix clustering. Moreover, the lahar matrix retains clustering consistency over greater distances than clasts, underscoring its importance for fingerprinting provenance.

The compositional clustering of the Onetapu Formation mirrors regional (Taupo) and local (Ruapehu) processes. Onetapu A units are largely similar to rhyolitic ash and pumice from the 1.8 ka Taupo eruption (similar lahars have been mapped in other catchments, e.g. Wilson and Walker, 1985; Smith, 1991; Segschneider et al., 2002, incorporating a variable amount of underlying andesitic components. Post-crater lake formation, units reflect a spectrum of trigger mechanisms, from eruption-driven and lake-breach events to rainfall-induced flows and flank collapses. Our results show that fingerprinting is most effective where clays are abundant, i.e., in cohesive debris flows, or in comparing stratigraphically similar unknowns. Additionally, the Wahianoa catchment's contribution to Onetapu lahars has largely ceased with the disappearance of its glacier, further constraining sediment sources in the modern system. Future work may refine discrimination by applying XRF and XRD to powdered whole clasts and extending analyses to trace elements in both clasts and matrix.

Finally, this approach establishes a transferable framework for volcanic hazard analysis. Spectral alteration maps from airborne and satellite VSWIR surveys (e.g., ASTER, AVIRIS, HyMap) are widely used to delineate weakened zones on volcanic edifices (Clark et al., 2003; Kereszturi et al., 2018; Mars et al., 2015). By showing that the same alteration fingerprints are preserved in lahar deposits, this study bridges edifice-scale mapping with downstream stratigraphic records, directly linking summit hydrothermal processes to lahar hazards. VNIR-SWIR spectrographic fingerprinting methods, supported by XRF, XRD, and stratigraphic common-sense, provides a sensitive and globally applicable forensic toolset for distinguishing lahar triggers, sequencing flows, and tracing provenance. Demonstrated in the Onetapu Formation, this methodology opens up more quantitative hazard assessment options at lahar-prone volcanoes.

Utilizing geochemical analysis, this chapter successfully developed diagnostic "fingerprints" for triggering mechanisms at Ruapehu as well as sediment provenance. While this helps to

clarify the historical lahar record, it also highlights the underrepresentation of Ruapehu's eruption triggered Crater Lake lahars in the historical record, which requires the CFD modelling in the following chapter to link vent conditions to lahar initiation.

4 Numerical modelling of eruption induced waves in Mt. Ruapehu's Crater Lake: Implications for lahar hazard models

4.1 Abstract

Lahars triggered by explosive activity through Mt. Ruapehu's Crater Lake (Te Wai ā-moe) account for nearly half of its historically recorded events, but the systematic physical linkage between explosive processes and lahar initiation remains poorly quantified. This study uses numerical modelling to simulate the conditions under which explosive waves could produce hazardous outflows, initiating a lahar.

Using the Basilisk computational fluid dynamics program and a non-hydrostatic, multi-layer approach, simulations modeled waves generated by submerged explosions of fixed cavity radii (10 m to 30 m) placed at five different active vents. The results indicate that the resulting outflow volume is highly sensitive to the initial water level in the lake, demonstrating an order-of-magnitude increase in discharge when the lake level was near the outlet crest (-30 cm) compared to lower levels (-1.3 m).

The largest simulated outflows (~3.6×10^3 m^3) are comparable to the water volumes ejected during the first phase of historical events, such as the 2007 eruption (~5.7×10^3 m^3). This work suggests that while an individual, bore-generating eruption produces only limited flow, the repetition within Ruapehu's characteristic multi-phase eruptive sequences can rapidly escalate the lahar hazard through cumulative lake drainage and sediment mobilization. This highlights the necessity of linking physical thresholds directly to eruptive dynamics for hazard forecasting.

4.2 Introduction

Volcanic crater lakes can generate impulse waves during explosive water–magma interactions, with the potential to overtop outlets and initiate lahars. The efficacy of this process depends strongly on cavity dynamics, water depth, and lake morphology, but remains difficult to quantify and simulate. In this study, we attempt to use numerical modelling to simulate the conditions under which Mt. Ruapehu's Crater Lake could produce hazardous explosive wave driven outflows, generating an eruption -triggered lahar while also highlighting the uncertainties and limitations inherent simulating such a process.

At Ruapehu, explosive eruptions and lahars are intimately linked (Healy et al., 1978; Lecointre et al., 2004a; Nairn et al., 1979). Historically, nearly half (35) of the recorded lahars from Ruapehu have been generated by eruptive disturbances to the Crater Lake (Cronin et al., 1997a; Houghton et al., 1987; Scott, 2013). Yet despite individual studies on Ruapehu's eruptions, lahars, and lake/vent dynamics, there has been little work to integrate these processes into a quantifiable hazard model that can be simulated (Leonard et al., 2021). The consequence is that while both the eruptive record and lahar chronologies are relatively well studied as individual hazards they are intrinsically linked and need to be modelled as such. The processes that systematically connects explosive activity to (eruption-triggered) lahar initiation remain incompletely unquantified.

Previous work has shown that Ruapehu's eruptive activity has shifted dramatically in scale and style over time(Pardo et al., 2012b, 2012a), from large Late-Pleistocene, Plinian, VEI 4–5, eruptions) (Pardo et al., 2012a; Pardo, 2012; Voloschina, 2020) to dominantly smaller Holocene phreatomagmatic and phreatic events (typically VEI ≤3) (Leonard et al., 2021; Moebis, 2010; Pardo, 2012). Although more recent eruptions are less voluminous and less explosive (Pardo,

2012; Voloschina, 2020), they pose a disproportionate downstream impact through their ability to disturb and mobilise water from the Crater Lake (Keys et al., 2008; Nolan, 2008; Pardo, 2012; Voloschina, 2020) to produce lahars. Historic examples such as the 1971 (Houghton et al., 1987), 1975 (Nairn et al., 1979), 1995 (Cronin et al., 1997a), and 2007 (Kilgour et al., 2010) eruptions all demonstrate that explosive activity can initiate destructive lahars through the displacement of Crater Lake water. The eruption generated lahars vary widely in magnitude depending on the available lake volume, snow/ice conditions, and sediment entrainment, meaning that eruption magnitude alone doesn't completely correlate with downstream hazard. Recognising and quantifying these linkages is critical, as a lahar-prone catchment such as the Whangaehu River hosts significant infrastructure and agricultural land.

4.2.1 Mt. Ruapehu

Mount Ruapehu is New Zealand's highest volcano at 2792 m with a long history of lahars and other mass wasting events. Its active summit vent hosts a warm, acidic Crater Lake encircled by glacial ice (Johnston et al., 2000)(Fig. 4.1), creating ideal conditions for phreatic and phreatomagmatic eruptions as well as lake breakout/overflow events which have generated hazardous lahars with the most notable events occurring in 1953, 1973, 1995-96, and 2007 (Cronin et al., 1997a; Hayward et al., 2022; Hodgson et al., 2007; Nairn et al., 1979; O'Shea, 1954; Procter et al., 2010a; Stilwell et al., 1954). Stratigraphic records show that over the past 2000 years, lahars and phreatomagmatic eruptions have dominated Ruapehu's eruptive history (Lecointre et al., 2004a, 1998; Palmer et al., 1993; Purves, 1990; Voloschina, 2020). This hazard still persists today, especially as the impacts from lahars increase due to agriculture and infrastructure encroaching on lahar-prone areas.

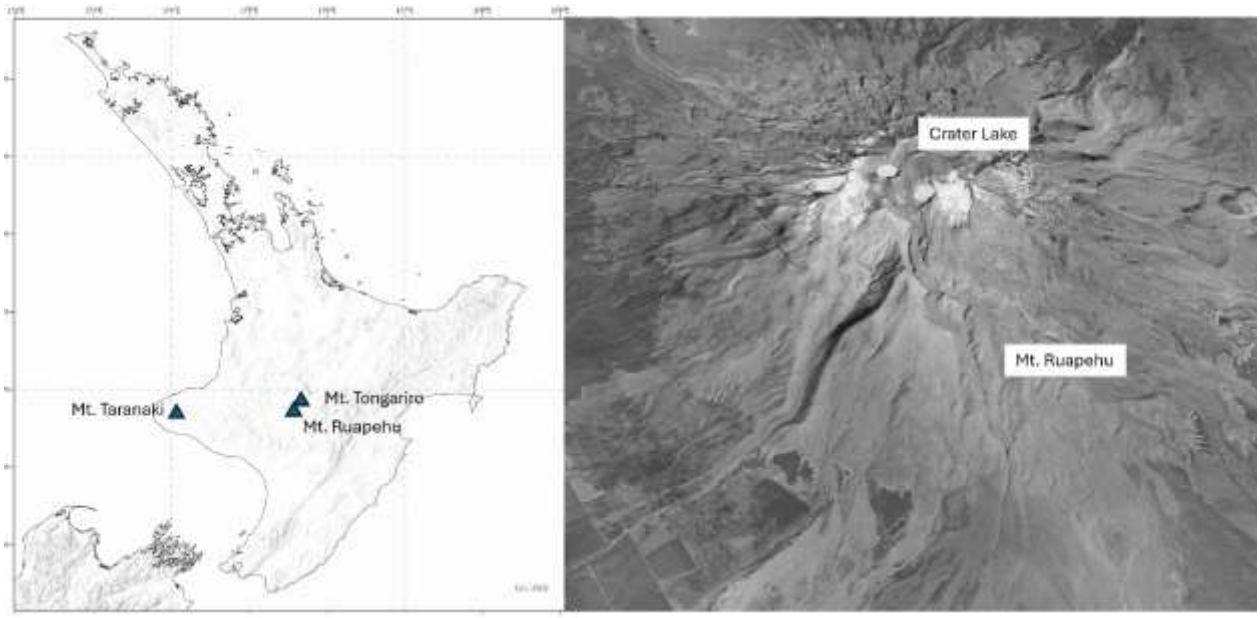


Figure 4.1 Overview map of the location of Mt. Ruapehu in North Island, New Zealand (left), with a 1969 Crown Survey 2192 (LINZ, 2015) DSM oblique view northwest of Mt. Ruapehu edifice (right) with the Crater lake visible in the upper-middle section.

4.2.2 Crater lake eruptions

Globally ~12% of 714 Holocene volcanoes have volcanic lakes (Rowe et al., 1992; Siebert et al., 2011), which is concerning, as volcanic eruptions through water disproportionately increase the range of possible volcanic hazards (Mastin and Witter, 2000) which is specifically noted for volcanic lakes (Pasternack and Varekamp, 1997). Hazardous phenomena include eruption induced tsunami and seiche waves (Freundt et al., 2007) which have been observed at Taal, Philippines (Delos Reyes et al., 2018; Moore et al., 1966; Paris and Ulvrova, 2019), Poás, Costa Rica (Rowe et al., 1992), Karymskoye, Kamchatka (Belousov and Belousova, 2000, 2001; Muravyev et al., 1997; Ulvrová et al., 2014) and other phenomena such as base surges, Surtseyan jets, and gas release (Manville, 2015).

As of 2021 for Mount Rupaehu's Crater Lake, there were five active vents in the crater lake floor, four of which correspond to bathymetric lows (Ching, 2022). The central vent, beneath a >100 meter water column, has historically been the most active, however there is also a north vent

with a ~60 meter water column; an (north)east vent with a ~70 meter water column; a northwest vent with a ~70 meter water column, noted as being the second most active, and a center-north vent with a ~80 meter water column (Christenson, 2012 after Ching, 2022).

Historic eruptions have included a wide range of lake/explosive eruption interactions. The 1975 and September 2007 events produced powerful vertical jets from the central vent, ejecting water and debris >100 m high and up to 800 m horizontally (Kilgour et al., 2010; Nairn et al., 1979) generating surges and lahars. Smaller-scale activity has included episodes of surface doming up to 20 m without lahar generation (Scott, 2013), whereas other phreatic and phreatomagmatic events have driven surges through the outlet and produced lahars (Scott, 2013).

Previous modeling of volcanic explosions disturbing or displacing Crater Lake water has been conducted using the SAGE framework (Morrissey et al., 2010) which simulated a variety of eruption styles through a central vent. The simulation involved applying models derived from the experimental work of Kedrinskii (2005). Of note were the different hazards associated with "deep" and shallow explosions (e.g. Section 2.1), however the two-dimensional model of scenarios based on a cylindrical central conduit does not accurately represent the three-dimensional lake-eruption interaction or the surface topography to more realistically evaluate lake surface disturbances. The previous simulations where focused on generating explosions underwater rather than accurately simulating the displacement of lake water to generate a lahar.

4.3 Methodology

4.3.1 Underwater explosions

In this study inverse methods were used to derive the following relationships from empirical gauge data obtained from field-scale underwater explosive tests conducted at Mono Lake,

California (Mehaute and Wang, 1996; Wallace and Baird, 1968; Whalin et al., 1970). Two simplified equations (Fig. 4.2) can be used to represent the initial surface disturbance from an underwater explosion, a parabolic (Eq. 1) and quadric (Eq. 2) which are noted by Mehaute and Wang (1996) as each closely fitting the experimental data, with a slight overestimate by the parabolic and a slight underestimate by the quadric (Mehaute and Wang, 1996).

The following equations describe an initial free-surface disturbance given a cavity generated by an explosion of known energy at known depth. In the following equations, η_0 is the initial surface disturbance, η_c is the maximum depth of the initial cavity with radius R below the equilibrium water surface, z is the water depth of the initial explosion, h is the total height of the water column, r is the radial distance from ground zero, c is a conversion constant from imperial units to metric (406.2), D is a depth parameter given by equation X, and E is explosive energy released.

Parabolic: $$\eta_0(r) = \begin{cases} \eta_c \left[2\left(\frac{r}{R}\right)^2 - 1\right], & r \le R \\ 0, & r > R \end{cases}$$

Quadric: $$\eta_0(r) = \begin{cases} \eta_c \left[-\frac{1}{3}\left(\frac{r}{R}\right)^4 + \frac{4}{3}\left(\frac{r}{R}\right)^2 - 1\right], & r \le R\sqrt{3} \\ 0, & r > R\sqrt{3} \end{cases}$$

Where the increasing pressure at depth in intermediate and shallow cases is approximated via the cavity parameters:

$$D = \frac{ch}{\sqrt[3]{E}}$$

$$Depth\ parameter = \begin{cases} Deep: D > 14 \\ Intermediate: 1 < D \le 14 \\ Shallow: D \le 1 \end{cases}$$

For the deep and intermediate cases:

$$\eta_c = aE^{\frac{6}{25}}$$

$$R = bE^{\frac{3}{10}}$$

With the constants a and b varying with depth accordingly:

$$a = \begin{cases} 0.02913, 0 < \dfrac{z}{E^{\frac{3}{10}}} \leq 9.965 \times 10^{-4} \\ 0.01433, 9.965 \times 10^{-4} < \dfrac{z}{E^{\frac{3}{10}}} \leq 2.9895 \times 10^{-2} \end{cases}$$

$$b = \begin{cases} 0.03803, 0 < \dfrac{z}{E^{\frac{3}{10}}} \leq 9.965 \times 10^{-4} \\ 0.04293, 9.965 \times 10^{-4} < \dfrac{z}{E^{\frac{3}{10}}} \leq 2.9895 \times 10^{-2} \end{cases}$$

And shallow conditions ($R > h$) generate a cavity extending through the water column and the energy is instead scaled as (Khangaonkar and Mehaute, 1991):

$$R = 0.03608E^{\frac{1}{4}}$$

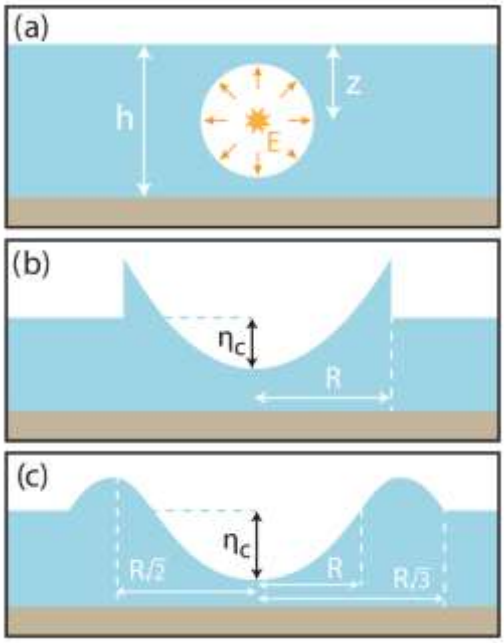


Figure 4.2 Graphical representation of subaqueous explosion parameters. (a) An explosion of yield E at depth z in a water column of depth h. (b) The initial surface elevation given by the parabolic equation. (c) The initial surface elevation given by the quadric equation. After Hayward et al. (2022).

The a and b coefficients are empirically defined for a scaled range of explosive burst depths, and outside these bounds a cavity will experience bathymetry effects (shallow) or might collapse entirely without generating waves of consequence (deep) (Mehaute and Wang, 1996).

At Ruapehu Volcano, a full crater lake depth, h of the shallowest presumed active vent (~60 meters) is approximately twice as deep as typical cavity radii generated by moderate explosive activity. During progressive lake water expulsion events (e.g. 1995-1996 eruption sequence) there will be a reduction in h values and potential increase in efficiency of surface disturbance.

A first-order estimate of explosion energy can be expressed as:

$$E = \frac{4\pi R^3 P_\infty}{3(\gamma - 1)}$$

where P_∞ is hydrostatic pressure and γ is the adiabatic index of gas (1.3–1.4). Using conservative γ values, a 30 m cavity at 100 m depth yields E ≈ 1.4×10^{11} Joules. These are order-of-magnitude estimates only; TNT (trinitrotoluene) equivalence scaling does not fully account for depth-pressure effects, and coefficients remain poorly constrained for moderate cavities at moderate depths.

In our simulations (appendix C1), as in Morrissey et al. (2010), cavity radii were fixed at representative values (10m, 15m, 17m, 20m, and 30m) across a range of depths. Physically, adiabatic scaling indicates that these radii would require different energy inputs at different depths, but here the emphasis is on exploring plausible scenarios rather than prescribing exact energetics. This approach is consistent with other scenario-based studies, such as modelling of Anak Krakatau (Grilli et al., 2019) and Campi Flegrei, where large cavities of fixed radii (200m, 650m, and 900m) were placed at multiple depths but assigned the same nominal input energy (Paris et al., 2019). In the case of Ruapehu, adopting this setup is necessary because the α and β constants that describe cavity scaling become unreliable under the intermediate conditions relevant to the crater lake (Section 2.2).

4.4 Modeling

Other papers that have modeled subaqueous explosions (Morrissey et al., 2010; Muravyev et al., 1997; Paris et al., 2019; Paris and Ulvrova, 2019; Ulvrová et al., 2014) used solvers such as COMCOT (Cornell multi-grid coupled tsunami model), FUNWAVE-TVD and SAGE however the models have limitations for nearshore hydrodynamics (Paris and Ulvrova, 2019). While inundation of a generated surface wave impacting a shore or specifically the propagation of a wave over the shallow outlet was the explicit desired output of this study alternative solvers were applied more suited to the complex terrain interactions controlling wave.

4.4.1 Numerical Model Setup

The underwater explosion-generated waves were simulated using Basilisk, a free, open-source computational fluid dynamics program (Popinet, 2018). Basilisk was selected for its ability to handle multi-layer shallow water equations with complex bathymetry and its adaptive mesh refinement (AMR) capabilities implemented via a quadtree Cartesian grid (Popinet, 2011), which enables efficient resolution of localized, rapidly varying phenomena, such as cavity propagation, while limiting computation across the broader domain. Simulations were parallelized using an OpenMP framework to allow scaling to larger grids and longer simulation times. Basilisk has also been successfully applied to other tsunami simulations (Grilli et al., 2007; King et al., 2023; Lane et al., 2017, p. 201; Lee et al., 2021, 2020; Popinet, 2012) underwater explosions (Hayward, 2023) PDC generated tsunamis (Battershill et al., 2021), and applied for future eruptions under Lake Taupo (Hayward, 2023; Hayward et al., 2022).

The governing equations for these simulations are multi-layer and non-hydrostatic, which account for vertical acceleration and better captures wave dispersion and bathymetric effects compared to depth-averaged hydrostatic approximations. The governing equations can be expressed as:

$$\partial_t h_k + \nabla \cdot (hu)_k = 0,$$

$$\partial_t (hu)_k + \nabla \cdot (huu)_k = -g h_k \nabla(\eta) - \nabla(h\phi)_k + [\phi \nabla \mathrm{z}]_k,$$

$$\partial_t (hw)_k + \nabla \cdot (hwu)_k = -[\phi]_k,$$

$$\nabla \cdot (hu)_k + [w - u \cdot \nabla \mathrm{z}]_k = 0,$$

where h_k is the layer thickness, u the horizontal velocity vector, w the vertical velocity, η the free-surface elevation, z the bathymetric depth, and ϕ the non-hydrostatic pressure correction.

4.4.2 Model Domain and Resolution

The computational domain was established as an 800 m × 800 m area centred on Ruapehu's Crater Lake, consistent across all scenarios. The origin was positioned at the lower left corner using modified NZTM coordinates + Moturiki elevation coordinates adjusted to local grid coordinates for computational efficiency and reduce significant figure handling issues in Basilisk. The grid resolution was controlled through an adaptive quadtree grid, with refinement levels tailored to each batch of simulations. For example, all second run simulations used levels 9-13, and all third run simulations were tested at a lower resolution band (levels 5-11) with additional boundary dampening around the western, eastern, and northern lake perimeter. Adaptive refinement enabled higher spatial resolution near vents and the outlet channel, while conserving computational resources in other parts of the simulation.

Numerical stability was controlled with a Courant–Friedrichs–Lewy (CFL) condition of 0.5. Five vertical layers (nl=5) were applied in all cases to provide sufficient vertical structure without introducing numerical instabilities and excessive processing times. Breaking wave thresholds were tuned (breaking=0.35) to better approximate eruption-driven waves, allowing steeper growth before dissipation.

4.4.3 Bathymetry and Initial Conditions

Crater Lake bathymetry was digitized from Ching (2022) (Fig. 4.3, Table 4.1), who reproduced unpublished Earth Sciences New Zealand survey data (~2012), and merged with a 0.6 m resolution 2016 DSM provided by Horizons Regional Council. This dataset was processed in ArcGIS, exported to XYZ format with GDAL, and converted into Basilisk's Octree k–d tree input via the xyz2kdt utility. To comply with Basilisk's six significant figure limit, coordinate offsets were applied (X reduced by 1,819,000, Y by 5,640,000, Z by 2416 m), and decimal precision was truncated (X, Y: two digits; Z: three digits).

For computational efficiency and to prevent numerical instabilities outside the crater, exterior cells were raised to ~2524.9 m (approximately 2 meters below the outlet crest). DEM smoothing (5-cell Gaussian) and gap filling were applied to prevent artifacts from interpolation and reduce numerical instabilities. In some scenarios, boundary absorption zones were added to prevent wave migration through the crater margins, implemented through exponential damping of velocities near the crater edges

Initial conditions were set by filling the lake to target levels below the scoured outlet (−1.275 m for the first series, −0.275 m for the second). Cavities representing explosive eruptions were modeled as water column displacement using either the quadric or parabolic Mehaute & Wang (1996) formulae.

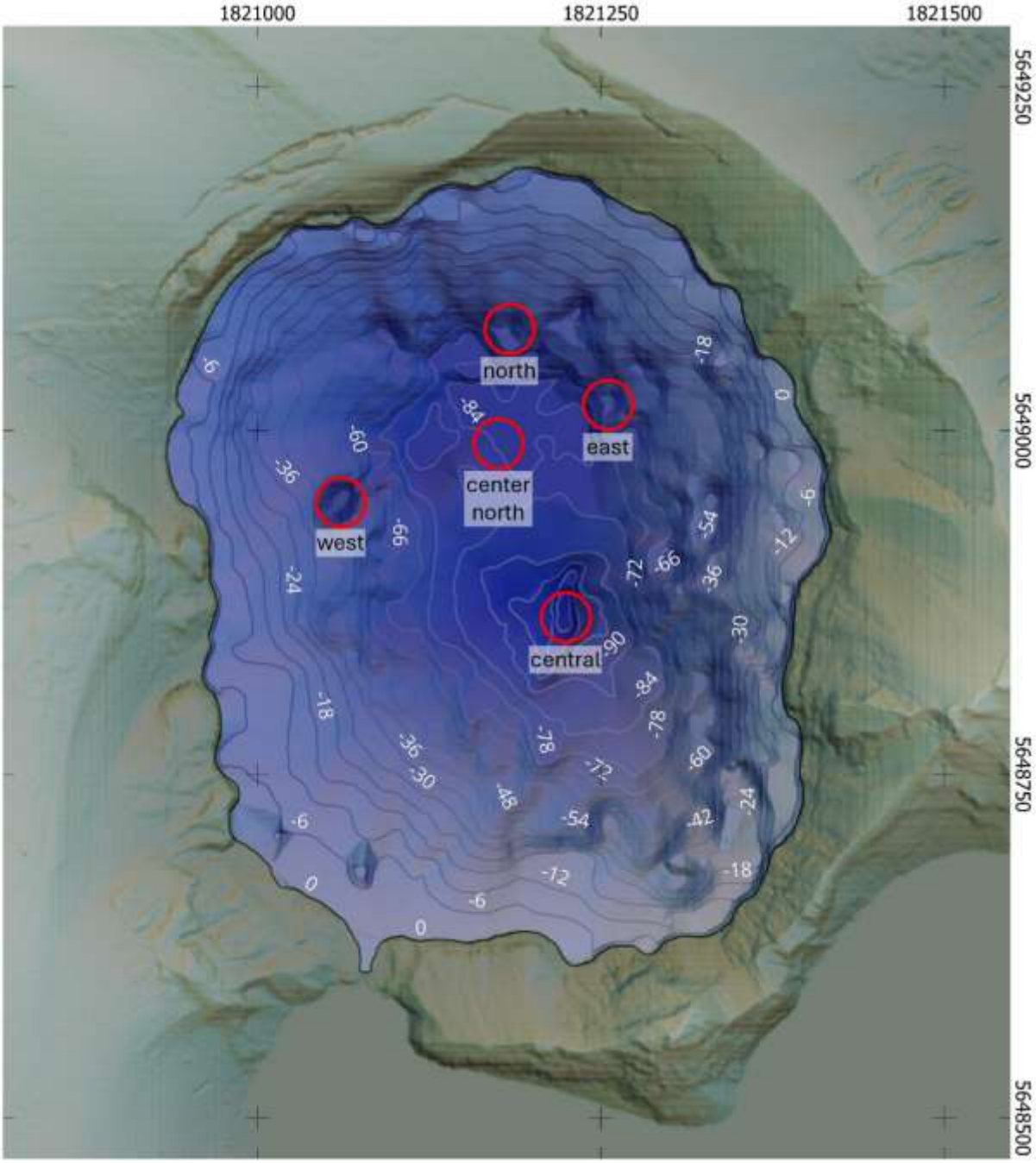


Figure 4.3 Bathymetry and hillshade topopgraphy of Mt. Ruapehu's summit Crater Lake that was the basis for numerical simulations. Bathymetry contours are displayed in 6 meter increments with the outlet on the southern edge. Hillshade DEM is modified from Horizons LIDAR imagery, with raised topography on areas outside the Crater Lake basin to reduce computational load and numerical instabilities due to water level effects. Crater Lake bathymetry was unpublished data from Christenson (2012) as cited in, and digitized from, Ching (2022).

Table 4.1 Mt. Ruapehu Crater Lake vent locations use for wave simulations in NZTM coordinates with approximate depth below current lake level.

Vent	Approximate Location	Current Depth (m)
West	5648947,1821060	~70.0
East	5649019,1821256	~70.0
Center-north	5648997,1821174	~80.0
North	5649073,1821181	~60.0
Central	5648862,1821224	~100.0

4.4.4 Explosion Parameter Definition

Two cavity formulations based on Mehaute and Wang (1996) empirically derived equations for shallow underwater explosions were tested using both the parabolic and quadric equations (Section 2.1) noting that they tended to respectively slightly over- and under-estimate wave sizes. Eruptions were placed at identified vent sites; Center, Center North, North, East, and West and assigned cavity radii of 10, 15, 17, 20, and 30 meters across depths of ~60-100 meters, which were chosen to capture a representative range of possible vent/depth interactions while remaining at or below VEI 3 equivalent energy (Hayward, 2023; Hayward et al., 2022).

This approach follows a scenario-based approach rather than strict energy scaling, and is consistent with previous event tree simulations (Hayward, 2023; Hayward et al., 2022; Paris et al., 2019; Paris and Ulvrova, 2019) where cavity radii and depths varied systematically with fixed input energies to explore hazard implications.

4.4.5 Data Collection and Analysis

Wave propagation was recorded using a network of virtual gauges defined within Basilisk, positioned in a grid pattern across the outlet channel (Figs. 4.4, 4.5) and at locations around the Crater Lake rim. These gauges recorded time series data (dt≤0.1) of the free-surface elevation throughout the simulation. Other outputs include:

- Separate spatial field files recording maximum free-surface elevation (Fig. 4.5) (etamax), etamin, and time of first wavefront arrival (etamax time) across the full domain.
- Separate movie files of topography + water surface, etamax, and etamax time for quality control and diagnosis of numerical instabilities.
- Each simulation also had an end state CSV subdomain (2048 x 2048 grid) file of etamax, water depth (h), and bed elevation (z_b) encompassing the outlet channel to assess wave runup relative to topography.

Flux across the outlet was quantified using two complementary approaches. First, by summing gauge time series along transects, integrating overtopping depth (h) through time:

$$V = \int_{t_0}^{t_1} h(t) \cdot A \, dt$$

$$V \approx A \cdot \sum_{i=0}^{n-1} \frac{h_i + h_{i+1}}{2} \cdot (t_{i+1} - t_i)$$

where V is overtopped volume and A the cross-sectional area. This enabled direct comparison of overtopping potential between scenarios with different cavity sizes and vent locations. Second, a weir formulation was used as a physically based estimate of discharge across the outlet:

$$Q = CLH^{3/2}$$

where Q is discharge (m3/s), C is the weir coefficient for broad-crested instances (here 1.7 $m^{1/2}/s$ (Chow, 1959)), L is the weir length, and H is the hydraulic head. The broad-crested weir is a common approach when considering outflow from volcanic lakes (Carrivick et al., 2009; Manville, 2001; O'Connor et al., 2022).

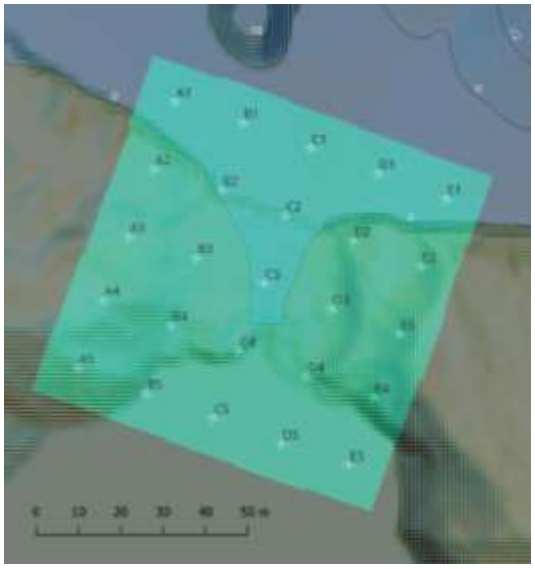


Figure 4.4 Numerical model gauge locations on Crater Lake outlet.

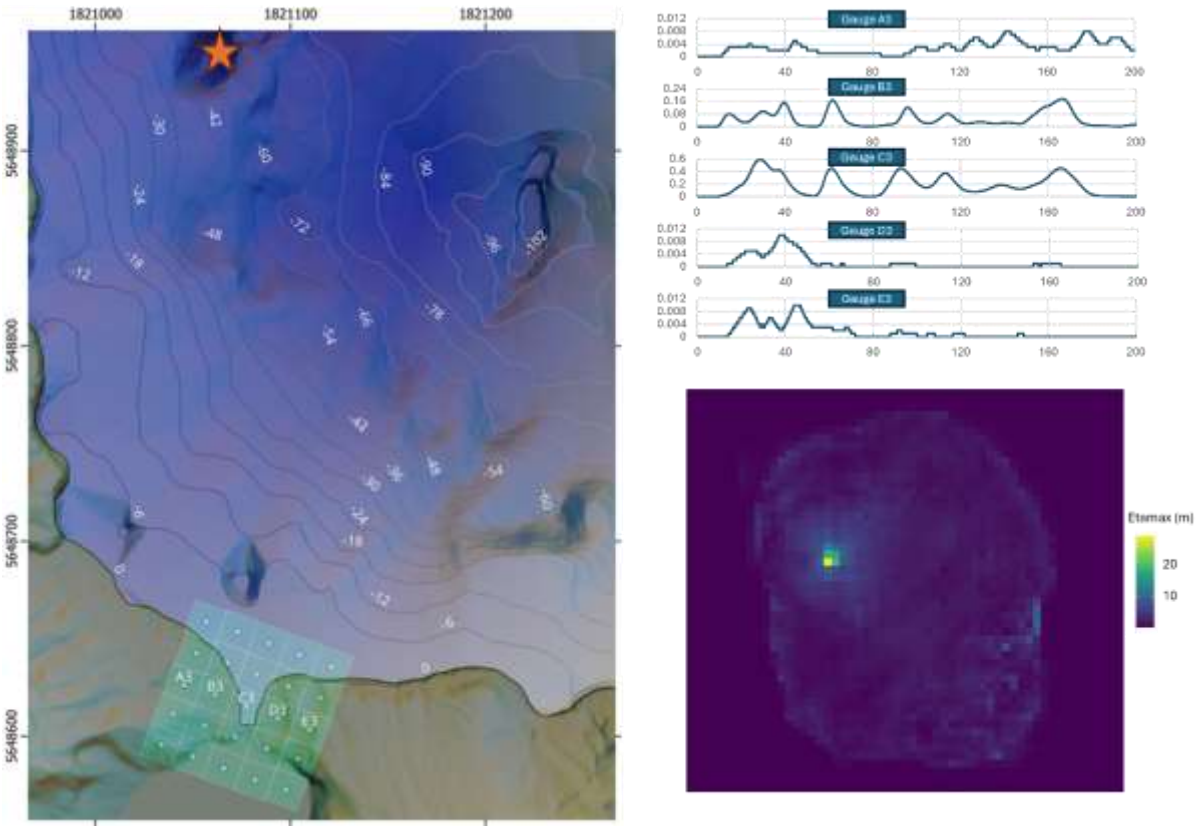


Figure 4.5 Mid-saddle gauges used for calculations from an example 30 meter cavity from an explosion from the west vent (star), 70 meters depth, water height 30 cm below outflow level, using a parabolic solver, along with gauge timeseries from gauges A3-E3, top to bottom, and a maximum height free surface plot (etamax).

4.5 Results and Findings

Simulated outflow volumes were highly variable, and some either failed due to numerical instability, producing zero discharge, or generated unrealistic values of an order of magnitude greater than comparable simulations. These cases were excluded from the analysis, though some high outflow outliers were retained where results appeared physically plausible. The results should be interpreted as an approximation of possible outcomes.

Over a 200-second runtime, most outflow was associated with first or second wave arrival due to cavity collapse (Fig. 4.6). Volumes ranged from tens to thousands of cubic meters (Fig. 4.7),

depending on initial conditions. Initial water level was the strongest variable: simulations initiated at 110 m water depth produced relatively small discharges (median approximately 35 m^3), vs. 111 m which produce an order of magnitude larger values (median approximately 340 m^3, with maximum >3000 m^3).



Figure 4.6 Time series comparison of waves arriving at gauge C1 located on the crater lake surface near the outlet channel. Vent locations are organized by row (Center, Center North, North, West, East from top to bottom) and initial cavity radii are organized by column (10, 15, 17, 20, 30 meters) with colors corresponding to initial water level and solver (Red - -1.3m, parabolic, Green - -30cm, parabolic, Blue - -1.3m quadric, Purple - -30cm quadric).

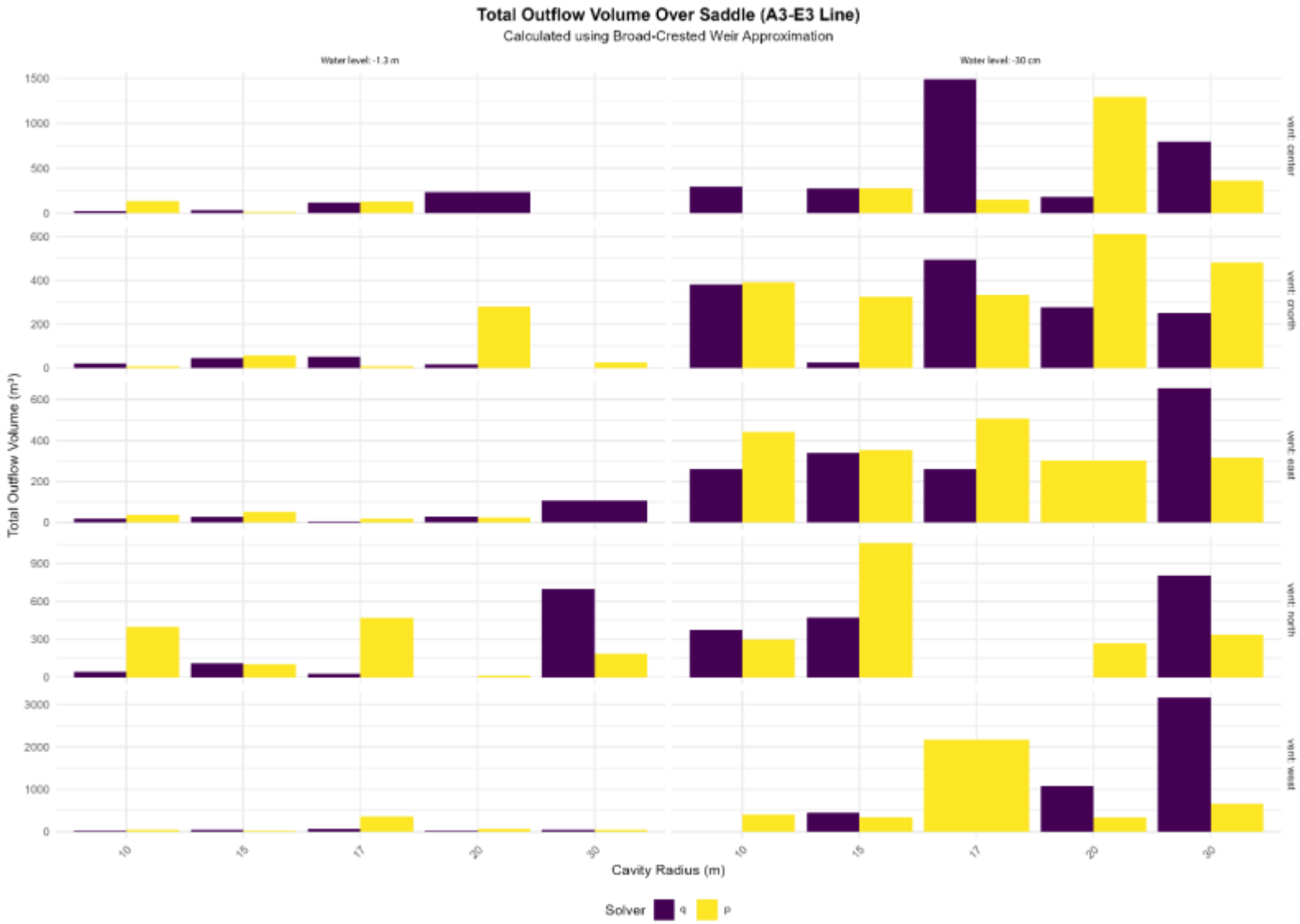


Figure 4.7 Cumulative outflow volume through the outflow channel of crater lake calculated from a simulated gauge transect across the scoured outlet and using a broad crested weir approximation. Water levels were 1.3 meters below the outflow (left half of the figure) and 30 cm below the outflow (right half of the figure), with each line corresponding to modelled vent location (Center, Center North, East, North, West) from top to bottom, and progressively greater cavity radii (10, 15, 17, 20, and 30 m at both water levels) as well as results from both solvers (quadric – purple, parabolic – yellow). Unrealistic and failed simulations were excluded.

Initial cavity radius was the second largest contributor to outflow. Larger cavities tended to produce higher outflow volumes, with the median increasing from ~87 m^3 at 10 m radius to ~316 m^3 at 30 m radius. Yet, larger cavities also displayed greater variability, including the highest outliers in the dataset, indicating a strong sensitivity to both cavity geometry and numerical stability. Additionally, using a quadric solver generally returning smaller medians but occasional extreme outliers, while the parabolic solver gave higher median values but fewer outliers, with volume estimates following the expected variations noted by Mehaute and Wang (1996)(Section 2.1). These variations also have implications for how eruption sequences of differing scale may transition between multistage and single-stage behaviour (see Discussion 4.1).

Taken as a whole, the simulations suggest that moderate cavity collapses at lower lake levels are unlikely to generate significant lahars, as most runs produced only minor discharges. When lake levels are elevated, small to moderate lahars are most likely, especially given a large cavity or eruptions through the western vent.

4.6 Discussion

At Ruapehu Volcano, where multiple active vents lie between water depths of 60–100 m (Ching, 2022), the interaction between cavity size, depth, and basin geometry exerts strong control on the magnitude and distribution of wave energy (Fig. 4.8). Consistent with prior experimental and field observations (Morrissey et al., 2010; Scott, 2013), nearly all explosions at intermediate depths will displace enough water to overtop the outlet, however the same nominal energy release at greater depths becomes markedly less efficient due to hydrostatic damping (Mehaute and Wang, 1996) which, while still increasing outflow when the lake is full, is likely on

creating a hazardous impact at the outlet (Scott, 2013). Conversely, a similar energy contribution at a shallower vent will produce a larger cavity and more water expulsion (Fig. 4.8).

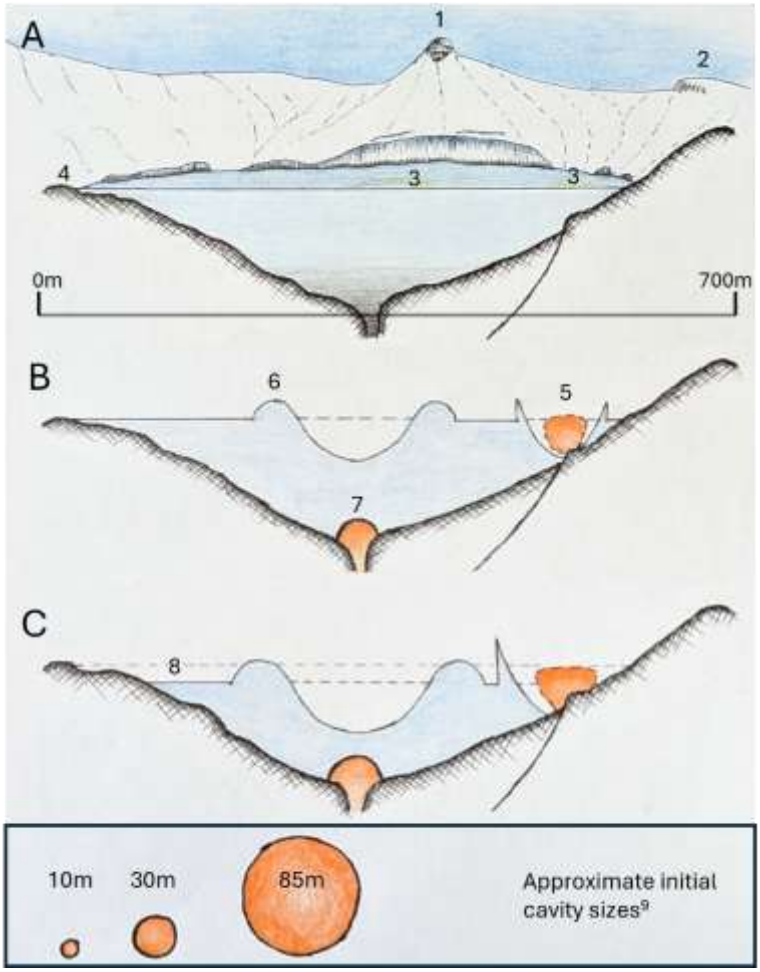


Figure 4.8 Conceptual sketch cross section Crater Lake through the Whangaehu outlet and central vent and an approximate location of the east vent. A: The glaciated Crater Lake at maximum fill with (1) Paretetaitonga and (2) the Dome in the background, with active vent locations indicated by (3) sulfur rafts. The (4) outlet is on the far left side. B: Disturbances through a full lake with a (5) shallow depth class explosion forming a parabolic bore, and a (6) quadric bore formed after a (7) deep depth class explosion reaches the surface. C: Disturbances through the Crater Lake with a (8) lowered water level resulting in change in depth class and increase in wave generation efficacy. (9) Approximate initial cavity sizes tested were 10m and 30m, with varying energy inputs required with changing depth, and a comparative upper size limit of explosive cavities in the 1995-1996 eruptive sequence.

The uncertainty around eruption sizes and energy partitioning makes direct comparison between modelled parameters, empirically derived equations, and historical activity a loose

approximation. A semi-quantitative eruption scale has been incrementally developed for Ruapehu's historical activity (Houghton et al., 1987; Hurst, 1981; Scott, 2013; Sherburn et al., 1999; Wilson et al., 2009) which classifies eruptions from 0 (Crater Lake steaming) to 5 (large-scale explosive eruption displacing moderate lake volumes, lahars in most major valleys, and ashfall off the cone, or very tall eruption columns >10,000 ft when no lake is present)(Scott, 2013). While this framework provides a practical way to assess the scale of historical events, comparison with other volcanic systems and underlying energy equivalences remains poorly constrained.

It has previously been noted that there is only a weak correlation between lahar magnitude and eruption size, with available water, sediment, and trigger mechanisms having a much stronger control (Mastin and Witter, 2000). On Ruapehu this may be accentuated, with eruptions up to a certain size producing larger waves until the system becomes dominated by jetting and explosive expulsion. For example, the 1975 eruption that mobilized half the crater lake released an estimated 20–30 kT TNT (1.0×10^{14} J) (Kilgour et al., 2010; Nairn et al., 1979) , while the gas-driven surtseyan jetting on 25 September 2007 was estimated at 1.54 kT TNT (6.45×10^{12} J) (Kilgour et al., 2010). While the approximate upper limit of the energy used in our simulations was ~1.4×10^{11} J. The largest simulated wave outflow in this study (~3.6×10^3 m^3) is roughly comparable to volume of lake water ejected by the 2007 eruption (~5.7×10^3 m^3 ; Cole, 2011) which produced lahars with total volume 9.0 – 28×10^3 m^3 (Kilgour et al., 2010). As Whangaehu lahars typically increase in volume by 2.5 times through entrainment of volcanic debris (Procter et al., 2010) , relatively small eruptions may still produce lahars of comparable size. Multiple closely spaced explosions could further enhance this effect by generating compound lahar waves, as observed in the 1995 sequence (Cronin et al., 1997a).

Historical eruptive sequences at Ruapehu illustrate these dynamics. In both 1971 and 1995, the initial eruption generated smaller lahars than those that followed, with later flows waning in size

(Cronin et al., 1997a; Houghton et al., 1987) Notably, the smallest lahar from either sequence was triggered by a 1.5 km-high phreatomagmatic eruption on 8 May 1971 (~4.1×10^4 m^3; Houghton et al., 1987), which would be comparable to the upper limits of a lahar formed by the largest outflow from this study, confirming the modelling application.

From a modelling standpoint, these simulations should be regarded as a set of general scenarios rather than predictive. While Basilisk's non-hydrostatic multilayer approach provides higher fidelity than shallow-water or Boussinesq approximations, as well as much faster processing than Navier-Stokes fluid volume calculations (Hayward, 2023; Hayward et al., 2022; Popinet, 2018), there are limitations. Primarily, phreatic eruptions seldom consist of a singular cavity-forming explosion, and previous field observations have noted that eruptive energy partitions into vertical jets, ballistics, and cavity formation during phreatic eruptions (Kilgour et al., 2010), and a majority of the expelled water can fall back into the lake, changing free surface conditions in ways that are difficult to parameterize. Our use of a singular set of fixed cavity radii across depths, while necessary for efficiency, simplifies these dynamics. Similarly, solver-based assumptions (parabolic vs. quadric) about cavity shape and propagation introduce differences in predicted wave heights.

Another challenge in modelling underwater eruptions is reconciling different approaches and energy scaling. The framework used in this study (Mehaute and Wang, 1996) was developed from nuclear and chemical explosion tests, and classifies cavities formed through underwater explosions according to a dimensionless depth parameter, D. While this framework covers a broad transition from shallow to deep regimes, the scaling coefficients work best with very large explosions (cavity radii >100 m) and corresponding shallow to intermediate depths. The Ruapehu simulations, ranging from 10 to 30 meter cavities at 60 to 100 meters depth, mostly fall outside the previous modelling space, the required ratios of depth to scaled energy ($z/E^{3/10}$ in Section 2.2) exceed the ranges for which coefficients are defined, and the energy estimates

either fail to converge or yield physically implausible values. Other modelling conducted on Ruapehu (Morrissey et al., 2010) presented the cavity as a rapidly expanding gas phase, with resulting cavity sizes on the scale of the scenarios modelled in this paper. Applications of both approaches (Hayward, 2023; Hayward et al., 2022; Morrissey et al., 2010) also acknowledge that energy transfer during magma-water interactions only converts a fraction of thermal energy into mechanical cavity growth. By prescribing cavity sizes and depths we are avoiding uncertainty around energy partitioning, while still examining the resulting wave generation and outflow.

Compared to other observed and modelled volcanic eruption induced tsunamis, there are variable results. At Karymskoye (Kamchatka), the 1996 eruption generated runup of ~30 m from water depths similar to Ruapehu (Belousov and Belousova, 2000, 2001; Ulvrová et al., 2014). At Taal (Philippines), multiple historical eruptions displaced large water volumes, producing waves several meters high with extensive runup (Delos Reyes et al., 2018; Moore et al., 1966; Paris and Ulvrova, 2019). In both cases, explosive mechanisms dominated over other processes such as surges or surface jets. Other mechanisms, including pyroclastic density current entry, and flank collapse, have also produced significant tsunamis (Freundt, 2003; Freundt et al., 2007; Grilli et al., 2021, 2019; Paris et al., 2020) however, Ruapehu's crater morphology along with previous analysis (Phillips, 2011) and eruption frequency suggest that explosive cavity formation remains the most probable tsunami trigger.

Although the simulations here suggest that even relatively modest underwater explosions can generate outflows capable of triggering lahars, the long-term stratigraphic retention of such events is likely very limited. Graettinger et al. (2010) noted that only a fraction of Ruapehu's historic lahars can be found in proximal deposits, with preservation strongly biased toward either the largest or the most recent flows. Eruption triggered hyperconcentrated flow deposits, such as all 1995 deposits other than LH4c (Cronin et al., 1997a) and 25 September 2007

eruption triggered lahars W1a, W1b, and W2 (Kilgour et al., 2010) tend to be finer-grained, confined to active channels, and rapidly overprinted by subsequent larger events (Cronin et al., 1997a; Graettinger et al., 2010; Kilgour et al., 2010), giving them virtually zero preservation potential or preserved downstream as a single unit with little observable difference in deposits texture to suggest multiple eruption triggers. Thus, while the crater lake frequently produces small lahars following minor explosive outflows, their contribution to the preserved geologic record is likely very under-represented, and recurrence intervals based solely on deposits are likely to miss their true frequency.

Overall, Ruapehu's crater lake represents a known and credible source of lahars, with hazard frequency (if not magnitude) dominated by intermediate-depth explosive cavity formation rather than passive overflows or structural failures. Our modeling demonstrates that outlet overtopping is likely under almost all plausible scenarios, but uncertainties in cavity geometry, energy partitioning, and bathymetric controls caution against overinterpretation of absolute wave heights.

4.6.1 Predictive hazard application of model

The simulations in this study reproduce an initial, small-scale water displacement associated with single phreatomagmatic or phreatic explosions at Mt. Ruapehu, generating outflow volumes up to ~3.6×10^3 m^3. These results align closely with the first phase of typical low-to-moderate intensity eruptive activity (VEI < 3) in the post-Crater Lake eruptive record (Scott, 2013; Voloschina, 2020). ~55% of Ruapehu's preserved eruptions are multi-phase sequences, transitioning from phreatic to phreatomagmatic to Strombolian/subplinian eruption styles. These multi-phase sequences, rather than single discrete eruptions (e.g. 1975 ~VEI 2, (Nairn et al., 1979)), account for most eruption-triggered lahars in the stratigraphic record, with the 1995-1996 sequence providing the most well-documented case (Cronin et al., 1997a, 1997b).

The modelling presented here can therefore be regarded as representing the first phase of a multi-phase sequence. While an individual moderate-energy explosion ($E \approx 1.4 \times 10^{11}$ J) may produce only a small lahar, typical multi-phase sequences will involve cumulative displacement of lake volumes with potential to generate larger lahar sequences as with the 1995 eruption, where frequent eruptions ejected increasing amounts of lake water, triggering larger, and shorter repose lahars. Only the largest of these (LH4c) was widely preserved, emphasizing the strong preservation bias threshold (Cronin et al., 1997b; Graettinger, 2008). The comparatively smaller volume of modelled lahars would indicate a limited hazard potential if not for the probability of a multi-phase eruptive sequence.

The model also helps constrain the physical thresholds governing eruption style and associated lahar hazard. Voloschina (2020) demonstrated that eruptions initiating through a water-filled vent produce phreatomagmatic fragmentation and wet, lahar-generating conditions, but that sustained activity progressively lowers the lake, ultimately leading to a transition into “dry” magmatic phases once the explosion cavities exceed the residual water depth. This transition was also observed during the 1995 sequence, where repeated sub-VEI 3 events displaced enough of the Crater Lake for the eruption style to shift to dry Strombolian activity. In terms of modelling, this transition occurs when the cavity diameter and water height are within the shallow depth parameter.

From a predictive lahar hazard perspective, the Crater Lake explosion models presented here should be regarded as representing the initial stages of a progressive eruptive sequence. As single, high-magnitude eruptions at Ruapehu are less common than multi-phase eruptions, explosive wave generation should be cautiously viewed as the initial hazard, with subsequent and progressive lake drainage and increasing lahar hazard through declining hydrostatic pressure and closely spaced lahar generation. Furthermore, the multi-phase eruptions preserved in the geological record are typically at least an order of magnitude larger than the

1995-1996 sequence (Voloschina, 2020), approaching the inferred threshold for prehistoric structural failure of the Crater Lake wall (Hodgson et al., 2007; Lecointre et al., 2004a).

4.7 Conclusions

This study applied a broad-crested weir approximation to explore the potential for wave generated outflow lahars from explosive eruptions in Mt. Ruapehu's crater lake, which led to identification of several key points. The outflow volume is highly sensitive to water level in the lake. The high water level for the simulations was still 30 cm below the scoured channel, given current full volume conditions, any of the modelled cavity radii will result in an increase in outflow, which increased an order of magnitude between -1.3 m and -30 cm water depths.

Larger cavities generally produced higher outflow, but also greater variability and numerical instabilities, resulting in outflow that ranged from negligible to several thousand cubic meters. This also highlights limitations of modelling on the scale of the Crater Lake vs. Lake Taupo (Hayward, 2023; Hayward et al., 2022), as the model encountered difficulties with the smaller scale in relation to cavity sizes and water depth.

The results of all simulations indicate that at lower lake levels, waves from explosive eruptions are unlikely to be significant (however with likely greater hazard from jetting and shallow water explosions). Collectively, these results suggest that while individual bore-generating eruptions may produce only limited outflows, their repetition within Ruapehu's characteristic multi-phase eruptive sequences can rapidly escalate hazard through cumulative lake drainage and lahar generation, linking the modelled physical thresholds directly to the eruptive dynamics and stratigraphic record that define Ruapehu's most frequent and credible future lahar scenarios.

Numerical modeling in this chapter demonstrates the sensitivity of lahar triggers to multiple conditions including water depth and multi-phase eruptions. This and previous chapters have identified multiple triggering mechanisms, all of which depend on the physical state of the

volcano rather than fixed intervals, leading to the final chapter which uses this new understanding to propose a new state-dependent probabilistic hazard framework.

5 A new approach to lahar hazard assessment

This chapter presents a new conceptual state-dependent probabilistic hazard framework for lahar hazard analysis, using variables identified in previous chapters. Creation of a model through statistical testing and validation of this framework is a one of the primary identified directions of future work (Chapter 6.5.4).

5.1 Introduction

Lahar hazard assessments depend fundamentally on the quantity and quality of data available (Loughlin et al., 2015; Mead et al., 2016). From recognizing hazard extent to defining recurrence intervals, successive steps rely on sufficient event records to constrain uncertainty. Traditional approaches have often treated lahars as a homogeneous class of hazard (Chapter 1.4.3), but at Mount Ruapehu this assumption breaks down because multiple, interacting trigger mechanisms (e.g. eruptions through the lake, ashfall melting snow/ice, rainfall remobilising unconsolidated material, lake breakouts, and mass wasting) produce events of different magnitudes, modifies the recurrence interval, and can change the associated risk (Cole, 2011). While earlier hazard models have noted and addressed spatial dependencies between covariates such as watersheds, slope angles, and source alteration (e.g., Iverson et al., 1998), the challenge at Ruapehu lies in delineating the magnitudes and recurrence that arise from its varied triggers (Graettinger, 2008; Mothes et al., 1998).

Sequences of lahars are not independent events. Crater Lake tephra barrier breakouts and Crater Lake eruptive sequences can trigger lahars that deplete available sediment or water, respectively, reducing the occurrence of subsequent lahars until the system is replenished. However deposits from previous lahars are often cannibalised and remobilized, in effect increasing the likelihood of lahars from other triggers (i.e. rainfall) (Flores, 2022; Graettinger,

2008; Mothes and Vallance, 2015). These dependencies mean that the lahar probability varies over time between eruptive activity, crater lake state, and rainfall/climate regime rather than following a steady recurrence pattern.

Following the 1995-96 eruption sequence, hazard assessments at Ruapehu increasingly focused on the evolving state of the Crater Lake and its outlet (Dittmer, 2008; Fagents and Baloga, 2006; Hancox et al., 1995; Leonard et al., 2021; Manville et al., 2007; Massey et al., 2010). The Eastern Ruapehu Lahar Alert and Warning System (ERLAWS), which was installed to detect and warn of possible lake dam failure, proved effective during the 18 March 2007 lake breakout and continued operation until 2022 (Tongariro District Office, 2023). Today, the Volcanic Alert Network (VAN) within Tongariro National Park provides continuous monitoring of volcanic unrest through GeoNet's seismic and acoustic sensors. This system operates under the assumption that secondary lahars occur within given post-eruption timeframes, typically within ~5 years for rain-remobilized flows (Graettinger, 2008; Umbal and Rodolfo, 1996) and within ~10 years for lake breakouts (Dittmer, 2008; Graettinger, 2008; Keys and Green, 2010; Massey et al., 2010), thus syn-eruptive lahars should be the monitoring focus.

Despite these operational practices, most previous hazard recurrence estimates at Ruapehu have relied on empirical frequency (Hodgson, 1993; Neall et al., 2004, 1999), without incorporating the influence of trigger-specific covariates such as crater lake volume, outlet stability, and snow or ice cover. Given Ruapehu's diversity of lahar-generating processes, a re-examination of recurrence intervals and associated hazards by trigger is warranted. Here, we compile and analyze a comprehensive record of lahar events at Ruapehu to explore relationships among trigger mechanisms, magnitudes, and recurrence patterns. Comparisons with global analogues selected for data richness and scope (ie. Cotopaxi, Kelud, Mayon, Merapi, Nevado del Ruiz, Pinatubo, and Villarrica; Section 4) help contextualize Ruapehu's lahar behaviour within a broader probabilistic framework.

5.2 Lahar Frequency and Probability

Building on the framework of Mead et al. (2021), a revised dataset of 75 lahar events from Mount Ruapehu (Table 5.1) has been compiled, together with events from global analogues such as Cotopaxi, Kelud, Mayon, Merapi, Nevado del Ruiz, Pinatubo, and Villarrica (Appendix D1; Table 5.3). These records enable examination of how lahar triggers, magnitudes (Table 5.2), and recurrence intervals interact within and across volcanoes.

At Ruapehu, record completeness varies by both event size and age, consistent with other volcanic hazard datasets (Rougier et al., 2016). Following the completeness assumptions of Mead et al. (2021), small and medium lahars are considered well documented over the last~160 years, while large and extreme events are assumed complete across the ~1800-years since the modern crater lake formed. This distinction allows frequency-magnitude relationships to be corrected for different observation windows and interpreted meaningfully across size classes.

Table 5.1 Record of lahars from Ruapehu volcano that have primarily affected the Whangaehu River (after Mead et al., 2021).

Event date	Years B.P.	Radiocarbon dating	Significant events	Onetapu formation	Trigger	Classification	Catchment affected	Volume (m^3)	Discharge (m^3/s) Calculated	Deposits preserved	Hazard (scenario) classification
25-Sep-2007	18		1		Eruption triggered lake expulsion/glacial melting	HF	WE, WP	$3.4x10^{5M}$	$800-1200^{M}$	Y	Medium
18-Mar-2007	18		1	One-7	Lake breakout	DF	WE	$1.9-3.8 x 10^{6K}$	$990-1200^{K}$	Y	Extreme
28-Oct-1999	26		1		Rainfall triggered	HF	WE			Y	Small
17-Jun-1996	29		1		Eruption triggered lake expulsion/glacial melting	DF					Small
21-Apr-1996	29		1		Crater rim collapse	DF					Small
17-Dec-1995	30		1		Rainfall triggered/seasonal glacial melting	HF					Small
25-Nov-1995	30		1		Rainfall triggered/seasonal glacial melting	HF					Small
1-Nov-1995	30		1		Rainfall triggered/seasonal glacial melting	HF					Small

30-Oct-1995	30		1		Rainfall triggered/seasonal glacial melting	HF					Small
29-Oct-1995	30		1		Rainfall triggered/seasonal glacial melting	HF					Small
28-Oct-1995	30		1		Rainfall triggered/seasonal glacial melting	HF				Y	Large
20-Oct-1995	30		1		Rainfall triggered/seasonal glacial melting	HF					Small
19-Oct-1995	30		1		Rainfall triggered/seasonal glacial melting	HF					Small
18-Oct-1995	30		1		Rainfall triggered/seasonal glacial melting	HF					Small
11-Oct-1995	30		2		Eruption triggered lake expulsion/glacial melting	DF					Small
7-Oct-1995	30		2		Eruption triggered lake expulsion/glacial melting	DF					Small
6-Oct-1995	30		1		Eruption triggered lake expulsion/glacial melting	DF					Small
29-Sep-1995	30		1		Eruption triggered lake expulsion/glacial melting	DF					Medium
29-Sep-1995	30		2		Eruption triggered lake expulsion/glacial melting	DF					Large
27-Sep-1995	30		3		Eruption triggered lake expulsion/glacial melting	DF					Small
27-Sep-1995	30		1		Eruption triggered lake expulsion/glacial melting	DF					Medium
26-Sep-1995	30		3		Eruption triggered lake expulsion/glacial melting	DF					Small
25-Sep-1995	30		3		Eruption triggered lake expulsion	HF					Small
25-Sep-1995	30		≥4	One-6	Eruption triggered lake expulsion	HF	WE, TR, MN	$4.8x10^{6K}$, $1.01x10^{6H}$	360^{K}	Y	Large
24-Sep-1995	30		4		Eruption triggered lake expulsion/glacial melting	HF					Small
23-Sep-1995	30		1		Eruption triggered lake expulsion/glacial melting	HF					Small
20-Sep-1995	30		1		Eruption triggered lake expulsion/glacial melting	HF					Small
18-Sep-1995	30		2		Eruption triggered lake expulsion/glacial melting	HF					Small
8-Dec-1988	37		1		Eruption triggered lake expulsion/glacial melting	HF	WE				Small
16-Jul-1977	48		1		Eruption triggered lake expulsion/glacial melting	HF	WP	$1.3x10^{5M}$			Small
27-Apr-1975	50		1		Eruption triggered lake expulsion/glacial melting	HF					Small

24-Apr-1975	50		2		Eruption triggered lake expulsion/glacial melting	HF					Small
24-Apr-1975	50		3	One-5	Eruption triggered lake expulsion/glacial melting	HF	WE, WP	$1.8x10^{6K}$, $0.92x10^{6H}$	500^{K}	Y	Large
4-Jul-1971	54		1		Eruption triggered lake expulsion/glacial melting	HF					Small
3-Jul-1971	54		1		Eruption triggered lake expulsion/glacial melting	HF					Small
21-May-1971	54		1		Eruption triggered lake expulsion/glacial melting	HF					Small
19-May-1971	54		1		Eruption triggered lake expulsion/glacial melting	HF					Small
16-May-1971	54		2		Eruption triggered lake expulsion/glacial melting	HF					Small
8-May-1971	54		1		Eruption triggered glacial melting	HF	WE, WP, MT	$1.8\text{-}7.2x10^{4M}$			Small
22-Jun-1969	56		1		Eruption triggered glacial melting	HF	WE	67000			
22-Jun-1969	56		1		Eruption triggered glacial melting	HF	WP	117000			
22-Jun-1969	56		1		Eruption triggered glacial melting	HF	MT	24000			
6-Apr-1968	57		1		Eruption triggered glacial melting	HF	WP	0.67 & $7.3x10^{5M}$			Large
24-Jul-1966	59		1		Eruption triggered glacial melting	HF	WE	$1x10^{3M}$			Small
1964	61		1		Eruption triggered glacial melting	HF	WE				Medium
24-Dec-1953	72		1	One-4	Lake breakout	DF	WE	$1.65x10^{6K}$, $0.5x10^{6H}$	600^{K}	Y	Large
8-Mar-1945	80		1		Eruption triggered glacial melting	HF	WE, WA				Small
1940	85		1		Eruption triggered glacial melting	HF	WA				Medium
3-Feb-1925	100		1		Lake breakout	HF	WE				Medium
23-Jan-1925	100		1		Lake breakout	HF	WE	1 & $3x10^{5M}$	430		Large
Apr-1907	118		1		Eruption triggered lake breakout/glacial melting	HF	MW				Medium
1-Mar-1903	122		1		Eruption triggered lake breakout/glacial melting	HF	WE, MA, MN				Medium
10-Mar-1895	130		1		Eruption triggered lake breakout/glacial melting	HF	WN	$6.7x10^{4M}$			Medium
Dec-1889	136		1		Eruption triggered lake breakout/glacial melting	HF					Small

Aug-1889	136		1		Eruption triggered lake breakout/glacial melting	HF					Small
30-Apr-1889	136		1		Eruption triggered lake breakout/glacial melting	HF					Small
22-Apr-1889	136		1		Eruption triggered lake breakout/glacial melting	HF	WE				Small
Jul-1886	139		1		Eruption triggered lake breakout/glacial melting	HF	TR				Medium
Jan-1869	156		1		Eruption triggered lake breakout/glacial melting	HF	WE	$3x10^{5M}$			Medium
13-Feb-1861	164	Post-modern (AD 1750-1950)	1	One-3	Lake breakout	DF	WE	$6x10^{6K}$, $0.5x10^{6H}$	2000^{K}	Y	Extreme
13-Dec-1859	166		1		Lake breakout	HF	WE				Medium
	250^{L}		1	One-2	Lake breakout	HF	WE		2100^{M}	Y	Small
	300^{L}	<390 ± 55, >282 ± 35 yr BP	1	One-1	Lake breakout	HF	WE		1100^{M}	Y	Medium
	450^{L}	450 ± 55 yr BP, <510 ± 140, <407 ± 70, >380 ± 60 yr BP	1	Ond-3	Crater rim collapse/Lake breakout	DF	WE	$8.4x10^{6H}$		Y	Extreme
	500^{L}		1	Ond-2	Crater rim collapse/Lake breakout	DF	WE	$18x10^{6H}$	$1700\text{-}1800^{M}$	Y	Extreme
	550^{L}	<890 ± 50 yr BP	1	Ond-1	Rainfall triggered	DF	WE	$0.5x10^{6M}$		Y	Medium
	1100^{L}	<1271 ± 56, <1230 ± 45 <1160 ± 80 yr BP	1	Onc-4	Rainfall triggered	HF	WE			Y	Large
		>1271 ± 56, >1230 ± 45, >1160 ± 80 yr BP	1	Onc-3	Rainfall triggered	HF	WE	$3.5x10^{6H}$		Y	Large
			1	Onc-2	Rainfall triggered	HF	WE			Y	Large
	1300^{L}		1	Onc-1	Rainfall triggered	HF	WE			Y	Large
	1550^{L}	<1530 ± 160, <1640 ± 60 yr BP, >1271 ± 56 yr BP	1	Onb	Crater rim collapse/Lake breakout	DF	WE	$3.2x10^{6H}$		Y	Extreme
	1650^{L}		1	Ona-4	Crater rim collapse/Lake breakout	DF	WE	$0.5x10^{6H}$		Y	Small
	1700^{L}		1	Ona-3	Crater rim collapse/Lake breakout	DF	WE	$0.5x10^{6H}$		Y	Small

	1750[L]		1	Ona-2	Crater rim collapse/Lake breakout	DF	WE	0.5x10^{6H}		Y	Small
	1800[L]	>1530±160 yr BP, <c. 1850 Taupo ignimbrite	1	Ona-1	Crater rim collapse/Lake breakout	DF	WE	3.0x10^{6H}		Y	Extreme

L: approximate dates from Lecointre et al. (2004), K: volumes and peak discharge at Tangiwai from Keys et al. (2008), H: volumes based on deposits from Hodgson et al. (2007), G: volumes and peak discharges at Round the Mountain Track footbridge from Graettinger et al. (2010), Hazard classification derived from Mead et al. (2021) & Taig (2002). WE: Whangaehu catchment, WP: Whakapapa catchment, TR: Tongariro catchment, MN: Mangatoetoenui catchment, MT: Mangaturuturu catchment, WA: Wahianoa catchment, MW: Mangawhero catchment, MA: Manganui Te Ao catchment, WN: Whanganui catchment.

Recurrence interval RI is defined as the observation period T divided by the number of events N. Annual probability is approximated as $p = \frac{1}{RI}$. When adjusted for observation bias and classified using the magnitude divisions of Mead et al. (2021) and Taig (2002), the updated recurrence characteristics for Ruapehu are as follows:

- Small lahars (<3x10^5 m^3): 44 events; recurrence ~3.9 years (annual probability ~0.26)
- Medium lahars (3x10^5 - 5x10^5 m^3): 14 events; recurrence ~11 years (annual probability ~0.09)
- Large lahars (5x10^5 - 3x10^6 m^3): 11 events; recurrence ~160 years (annual probability ~0.006)
- Extreme lahars (>3x10^6 m^3): 6 events; recurrence ~300 years (annual probability ~0.003)

When plotted on log-log axes, the frequency-magnitude relationship for Ruapehu lahars approximates a power-law decay, consistent with other mass-movement systems (e.g., Iverson, 1998; Mead et al., 2021), though deviations at the largest magnitudes likely reflect limited data completeness or physical boundaries of the system.

Nearly all historical eruptions at Ruapehu have generated at least one syn-eruptive lahar (Hodgson and Manville, 1999; Mead et al., 2021), implying that the conditional probability of lahar occurrence during eruption approaches unity. In contrast, Ruapehu's non-eruptive triggers such as rainfall, lake breakout, and mass wasting require additional, state-dependent conditions to be met (Baumann et al., 2018; Dittmer, 2008; Graettinger, 2008; Hodgson and Manville, 1999; Mead et al., 2021, 2016). As a result, average recurrence intervals provide only limited predictive power: they are descriptive of long-term behaviours but cannot account for eruptive clustering, inter-event dependence, or evolving system states between eruptions.

This recognition motivates a shift from purely empirical recurrence models toward conditional, process-based approaches. Understanding how lahar frequency and magnitude varies with

trigger type and antecedent conditions is therefore central to refining hazard forecasts at Ruapehu and contextualizing its activity within broader global analogues.

5.3 Ruapehu Trigger Mechanisms and Dependencies

The likelihood and magnitude of lahars at Mount Ruapehu are closely linked to both morphology and trigger type. The steep, deeply incised Whangaehu channel promotes rapid flow bulking, enabling even dilute Crater Lake outflows to evolve into debris flows (Cronin et al., 1997a; Graettinger, 2008; Graettinger et al., 2010; Manville and Hodgson, 2011; Massey et al., 2010; Procter et al., 2010b; Taig, 2002). Post-2007 surveys indicate that the current lake outlet, reinforced by dense lava breccia, is more stable than its pre-2007 tephra dam configuration but remains somewhat vulnerable to mechanical or hydrothermal weakening (Schaefer et al., 2018). Under these conditions, Ruapehu's lahar hazard is best characterized as bipartite, including syn-eruptive lahars (associated with lake expulsion or ice melt) and inter/post-eruptive lahars (triggered by rainfall, lake breakout, or mass wasting).

The latter group, especially lake-breakout and mass-wasting events, represents the largest and most destructive flows in both the historical and prehistoric record. The 1861, 1953, and 2007 dam-break lahars exemplify these low-frequency, high-hazard events. Syn-eruptive lahars can generally be anticipated through monitoring of eruptive precursors (Kilgour et al., 2010; Mead et al., 2021; Tongariro District Office, 2023), while post-eruptive lahars require continuous hydrological and environmental observation integrated into real-time hazard management (Cronin et al., 1997a; Keys and Green, 2010; Massey et al., 2010; Mead et al., 2021).

Distinguishing between syn- and post-eruptive lahars is not always straightforward. During prolonged eruptive phases, individual lahar events may or may not coincide precisely with eruptive pulses (Cronin et al., 1997b). For prehistoric lahars, synchronicity is often inferred from stratigraphic context, specifically tephra beds immediately above or below Onetapu Formation

deposits have been used as indicators of syn-eruptive origin (Donoghue, 1991; Donoghue and Neall, 2001).

There is more complexity when determining triggering mechanisms, as reports often include amplifying factors, such as Crater Lake expulsion generating glacial meltwater or seasonal rainfall generating glacial meltwater (e.g. 1995 lahars; Cronin et al., 1997b), however a primary trigger can be identified in most cases. Trigger mechanisms (Table 5.1) were simplified to capture key processes while maintaining comparability with prior trigger assignments (Compare with Lecointre et al. (2004), Dittmer (2008), Pierson et al. (2025)), as well as comparability with international analogues (Section 4). For the 75 catalogued events at Ruapehu, triggering mechanisms can be simplified to include:

- Eruption-lake interactions **(35 events)** dominate, encompassing all variations of lahars generated from eruptions mobilizing lake water outside the Crater Lake basin, often including ice melting.
- Rainfall-triggered lahars **(15 events)** represent the second most frequent category, forming through remobilization of fresh tephra under high-intensity precipitation, often including ice melting.
- Eruption-ice melt events **(9)** occur mainly during eruptions that have already depleted the Crater Lake.
- Lake breakout events **(8)** result from tephra or ice dam breaches, often post-eruptive at Ruapehu.
- Mass-wasting **(8)** involve sector or rim collapses, often enhanced by incorporation of much of the Crater Lake.

Mass-wasting triggered (e.g. flank collapse, debris avalanche/flow) lahars tend to be the largest lahars preserved in the stratigraphic record both at Ruapehu and globally (Pierson et al., 2025; Vallance and Scott, 1997) with exceptions (e.g. Chillos Valley Lahar, Hall and Mothes, 2008;

Mothes et al., 1998; April 1996 Ruapehu rockfall generated lahar, Scott and Sherburn, 2003). The large magnitudes correlate with low frequencies (long recurrence intervals) and few recorded events, yet with good stratigraphic preservation in contrast to smaller, more frequent events (Mead et al., 2021).

Rainfall triggered lahars are the second most common and is dependent on presence of tephra on a steep enough slope to be mobilized as a lahar. Rainfall triggered lahars tend to decrease in magnitude and frequency after an eruption (e.g. Ruapehu, Cronin et al., 1997b; Pinatubo, Tuñgol, 2002; Mayon, Paguican et al., 2009; Merapi, Lavigne et al., 2000) and be associated with seasonal precipitation. Modelling by Mead et al. (2016) calculated rain-triggered lahar susceptibility as probability of occurrence of a particular initial lahar volume given surface models and probabilistic rainfall data as Intensity-Frequency-Duration (IFD) curves which need to be calibrated for different climatic regions.

In terms of frequency and magnitude, lake breakout lahars are potentially the most hazardous (Neall, 1976). Lake breakout events are strongly linked to lake level (and presence of an ice or tephra dam), which, at Ruapehu, refills 8-11 years following a larger volume tephra producing event (Graettinger, 2008), and also allows the hazard to be anticipated and managed (Manville et al., 2007; Taig, 2002). However, lake outbreak lahars resulting from lahar dammed river tributaries can occur weeks to hours after the emplacement of the dam (Umbal and Rodolfo, 1996).

Glacial and snowmelt processes also contribute to Ruapehu's lahar events (Cronin et al., 1996; Graettinger, 2008; Manville et al., 2000; Rosenberg, 2000), though their influence varies with ice cover extent (Graettinger, 2008; Moebis, 2010). As noted by Major and Newhall (1989), classification of eruption triggered ice melt lahars are often complex, similar complications are noted in triggers at Ruapehu, however it should be noted "eruption-lake" triggered lahars at Ruapehu (which require the presence of a crater lake) almost invariably have an ice melt

component (Cronin et al., 1997a; Dittmer, 2008), while ice melt lahars can also occur when the lake is absent.

Understanding these interacting mechanisms highlights the importance of volcano-specific, state-dependent hazard models (Flores, 2022; Graettinger, 2008; Manville et al., 2000; Mead et al., 2021; Pallister et al., 2019). The next section explores how these triggers and their associated magnitudes compare across global analogues, and how frequency-magnitude relationships can inform probabilistic assessments of lahar recurrence.

5.4 Magnitude-Frequency and Global Analog Comparisons

To quantify lahar recurrence and magnitude relationships, Ruapehu's event record was compared with well-documented global analogues (Table 5.2) (similar to previous ash studies, Hurst and Smith, 2010) representing a spectrum of lahar-generating environments comparable to Ruapehu's different lahar triggers (Table 5.3). This comparison helps contextualize Ruapehu's multi-trigger lahar regime and, by adding strength to hazard models through additional data, refine estimates of conditional hazard probabilities.

Analogues were selected to include presence/absence of either glaciers or a crater lake and including trigger mechanisms present at Ruapehu. The availability of monitoring data or post-event studies for magnitude comparisons was also included. A selection of seven analogues is by no means exhaustive but is relatable to Mt Ruapehu and this limited set of analogues allowed fora more complete event catalogue for each analogue.

Table 5.2 Condensed summary of documented lahar events at selected volcanoes, organized by period, trigger, and flow type. Events of similar magnitude, trigger, and character occurring within the same year or over extended decades have been merged for brevity. Full event listings, including all individual occurrences and source details, are provided in the appendix (Appendix D1).

Cotopaxi, Ecuador	*Lithology: Andesite / Basaltic Andesite;Dacite;Rhyolite*
Köppen-Geiger Climate classes: (Peak: Polar, tundra; Flank: Temperate, no dry season, cold summer)	

Period/Year	Events	Magnitude	Trigger	Type of flow	**Source**
2024	3	Medium	Rainfall	Hyperconcentrated flow	GVP
2023 (Jun-Jul)	4	Small	Eruption-glacial melt		**GVP**
2023 (Apr-May)	4	Small	Rainfall	hyperconcentrated flow	**GVP**
2022	>1	Small	Eruption-glacial melt	non-cohesive debris flow	**GVP**
2015-2016	59	Small	Rainfall	hyperconcentrated flow	**GVP**
2016	1	Medium	Eruption-glacial melt	hyperconcentrated flow	**GVP**
2015	4	Small	Eruption-glacial melt	hyperconcentrated flow	**GVP**
1880-1904	>36	Small	Eruption-glacial melt	non-cohesive debris flow	**GVP, HM08**
1877	6	Large	Eruption-glacial melt	non-cohesive debris flow	**GVP, HM08**
1877	1	Extreme	Eruption-glacial melt	non-cohesive debris flow	**GVP, HM08**
1532-1863	126	Small	Eruption-glacial melt	non-cohesive debris flow	**GVP, HM08**
2220 BCE ± 100 - 1350CE	23	Medium	Eruption-glacial melt	non-cohesive debris flow	**GVP, HM08**
2640 BCE ± 200 years	1	Extreme	Eruption-snowmelt/avalanche	cohesive debris flow	**HM08**
3280 BCE ± 500 years	1	Medium	Eruption-glacial melt	cohesive debris flow	**GVP**
3880 BCE ± 75 years	1	Medium	Eruption-glacial melt	non-cohesive debris flow	**GVP**
Villarrica, Los Ríos, Chile			*Lithology: Basalt / Picro-Basalt;Andesite / Basaltic Andesite;Rhyolite*		
Köppen-Geiger Climate classes: (Peak: Polar, tundra; Flank: Temperate, no dry season, cold summer/Cold, no dry season, cold summer)					
2015-03-03	>1	Small	Eruption-glacial melt	hyperconcentrated flows	**GVP**
1984-1991	3	Small	Eruption-glacial melt	hyperconcentrated flows	**GVP, PB94, VD14**
1971-1976	9	Small	Rainfall	hyperconcentrated flows	**GVP, PB94, VD14, NM04**
1971	5	Medium	Eruption-glacial melt	non-cohesive debris flow	**GVP, NM04, VD14**
1971	5	Extreme	Eruption-glacial melt	non-cohesive debris flow	**GVP, NM04, VD14**
1904-1964	5	Extreme	Eruption-glacial melt	non-cohesive debris flow	**GVP, NM04, VD14**
1904-1964	18	Medium	Eruption-glacial melt	non-cohesive debris flow	**GVP, PB94, VD14, NM04**
1904-1964	>36	Small	Eruption-glacial melt	non-cohesive debris flow	**GVP, NM04, VD14**
1948	6	Large	Eruption-glacial melt	non-cohesive debris flow	**GVP, NM04, VD14**
1410-1897	37	Medium	Eruption-glacial melt	non-cohesive debris flow	**GVP, PB94, VD14, POVI**
Pinatubo, Zambales, Philippines			*Lithology: Dacite;Andesite / Basaltic Andesite;Basalt / Picro-Basalt*		
Köppen-Geiger Climate classes: (Peak: Tropical, monsoon; Flank: Tropical, monsoon)					
1997	1	Large	Rainfall	hyperconcentrated flows	**TU02**
1996	3	Medium	Rainfall	hyperconcentrated flows	**TU02**
1995	2	Extreme	Rainfall	hyperconcentrated flows	**BGVN, TU02**
1995	7	Large	Rainfall	hyperconcentrated flows	**BGVN, TU02**

1995	7	Medium	Rainfall	debris flows	**TU02**
1995	36	Medium	Rainfall	hyperconcentrated flows	**BGVN, TU02**
1995	1	Small	Rainfall	hyperconcentrated flows	**TU02**
1994	2	Extreme	Rainfall	hyperconcentrated flows	**TU02**
1994	1	Extreme	Rainfall	debris flows	**TU02**
1994	5	Large	Rainfall	debris flows	**TU02**
1994	1	Large	Lake breakout	debris flows	**BGVN, TU02**
1994	1	Medium	Lake breakout	hyperconcentrated flows	**TU02**
1994	6	Large	Rainfall	hyperconcentrated flows	**TU02**
1994	28	Medium	Rainfall	hyperconcentrated flows	**TU02**
1994	>90	Small	Lake breakout	hyperconcentrated flows	**BGVN**
1994	>5	Small	Rainfall	hyperconcentrated flows	**BGVN**
1993	2	Extreme	Rainfall	debris flows	**BGVN, TU02**
1993	2	Large	Rainfall	debris flows	**BGVN**
1993	138	Medium	Rainfall	debris flows	**BGVN**
1993	6	Small	Rainfall	hyperconcentrated flows	**BGVN**
1992	1	Extreme	Rainfall	hyperconcentrated flows	**TU02**
1992	8	Large	Lake breakout	debris flows	**RU96**
1992	>249	Medium	Rainfall	debris flows	**PD96, RU96**
1991	19	Large	Lake breakout	hyperconcentrated flows	**RU96**
1991	288	Medium	Rainfall	hyperconcentrated flows	**PD96, RU96**
1450	1	Extreme	Rainfall	debris flows	**ND96**
1050	1	Extreme	Rainfall	debris flows	**GVP**
3550 BCE	1	Extreme	Rainfall	debris flows	**GVP**
Nevado del Ruiz, Caldas, Colombia			*Lithology: Andesite / Basaltic Andesite;Dacite*		
Köppen-Geiger Climate classes: (Peak:Polar, frost/Polar, tundra; Flank:Temperate, no dry season, warm summer)					
1989	1	Medium	Eruption-snowmelt/avalanche	debris flow	**SEAN**
1985	9	Medium	Eruption-snowmelt/avalanche	debris flow	**SEAN**
1985	1	Medium	Lake breakout	debris flow	**HE86**
1985	4	Extreme	Eruption-snowmelt/avalanche	cohesive debris flow	**PJ90, LW86**
1985	1	Small	Collapse/avalanche	debris flow	**HE86**
1985	1	Medium	Slope collapse	debris flow	**PJ90**
1985	1	Medium	Eruption-snowmelt/avalanche	debris flow	**SEAN**
1845	1	Extreme	Collapse/avalanche	debris flow	**TC90**

1595	1	Extreme	Slope collapse	debris flow	**TC90**
~850 BCE - 1400 CE	4	Medium	Eruption-snowmelt/avalanche	debris flow	**GVP, HE86, TC90**
1245 BCE ± 150 years	1	Large	Collapse/avalanche	debris flow	**TC90**
6660 BCE (in or before)	1	Medium	Eruption-snowmelt/avalanche	debris flow	**GVP**
Merapi, Central Java, Indonesia			*Lithology: Andesite / Basaltic Andesite;Trachyandesite / Basaltic Trachyandesite*		
Köppen-Geiger Climate classes: (Peak:Temperate, no dry season, warm summer; Flank:Tropical, monsoon)					
2001-2016	17	Large	Rainfall		**GVP**
2001-2016	>7	Medium	Rainfall		**GVP**
2001-2016	>2	Small	Rainfall		**GVP**
1970-1999	8	Extreme	Rainfall		**GVP, LT00**
1970-1999	>25	Large	Rainfall		**GVP, LT00**
1970-1999	199	Medium	Rainfall		**GVP, LT00**
1970-1999	61	Small	Rainfall		**GVP, LT00**
1920-1969	16	Large	Rainfall		**GVP, LT00, SC34**
1920-1969	>234	Medium	Rainfall		**GVP, LT00, SC34**
0020-1888	1	Extreme	Rainfall		**GVP, LT00**
0020-1888	8	Medium	Rainfall		**GVP, LT00**
Mayon, Albay, Philippines			*Lithology: Andesite / Basaltic Andesite;Basalt / Picro-Basalt*		
Köppen-Geiger Climate classes: (Peak:Temperate, no dry season, warm summer; Flank:Tropical, rainforest)					
2000-2018	3	Extreme	Rainfall	debris flow	**PHIVOLCS, PL09**
2000-2018	2	Large	Rainfall	debris flow	**PHIVOLCS, PL09**
2000-2018	3	Medium	Rainfall	hyperconcentrated flows	**PHIVOLCS, PL09**
2000-2018	>2	Small	Rainfall	hyperconcentrated flows	**PHIVOLCS, PL09**
1981-1993	3	Large	Rainfall	hyperconcentrated flows	**PHIVOLCS, AR90, GVP**
1981-1993	35	Medium	Rainfall	hyperconcentrated flows	**PHIVOLCS, AR90, GVP**
1981-1993	6	Small	Rainfall	hyperconcentrated flows	**PHIVOLCS, AR90, GVP**
1900-1972	14	Medium	Rainfall	hyperconcentrated flows	**PHIVOLCS, AR90, GVP**
1616-1897	2	Extreme	Rainfall	hyperconcentrated flows	**GVP, AR90, MA02**
1616-1897	19	Medium	Rainfall	hyperconcentrated flows	**GVP, AR90, MA02**
Kelud, East Java, Indonesia			*Lithology: Andesite / Basaltic Andesite;Basalt / Picro-Basalt*		
Köppen-Geiger Climate classes: (Peak: Tropical, monsoon; Flank: Tropical, monsoon)					
2014	1	Medium	Rainfall	hyperconcentrated flows	**GVP**
1966-1991	>11	Large	Eruption-lake breakout	hyperconcentrated flows	**BGVN, GVP, TA98**
1966-1991	≥6	Large	Rainfall	debris flow	**BGVN, GVP, TA98**

1966-1991	>29	Medium	Rainfall	hyperconcentrated flows	**BGVN, GVP, TA98**
1966-1991	>1	Small	Rainfall	hyperconcentrated flows	**BGVN, GVP, TA98**
1901-1951	>15	Extreme	Eruption-lake breakout	debris flow	**GVP, TA98**
1901-1951	>11	Medium	Eruption-lake breakout	hyperconcentrated flows	**GVP, TA98**
1901-1951	3	Medium	Rainfall	hyperconcentrated flows	**GVP, TA98**
1716-1875	>15	Extreme	Eruption-lake breakout	debris flow	**GVP, TA98**
1716-1875	>1	Extreme	Lake breakout	debris flow	**GVP, TA98**
1716-1875	>3	Large	Eruption-lake breakout	hyperconcentrated flows	**GVP, TA98**
1716-1875	>6	Medium	Eruption-lake breakout	hyperconcentrated flows	**GVP, TA98**
1716-1875	≥2	Medium	Rainfall	hyperconcentrated flows	**GVP, TA98**
1000-1641	>12	Extreme	Lake breakout	debris flow	**GVP, TA98**
1000-1641	>2	Large	Eruption-lake breakout	hyperconcentrated flows	**GVP, TA98**
1000-1641	>8	Medium	Eruption-lake breakout	hyperconcentrated flows	**GVP, TA98**

Source tags: GVP: Global Volcanism Program, BGVN: Bulletin of the Global Volcanism Network, PHIVOLCS: The Phillippine Institute of Volcanology, SEAN: Scientific Event Alert Network Bulletin, POVI: Proyecto de Observacion Villarrica, TU02: Tungol (2002), HM08:Hall and Mothes (2008), M98: Mothes et al. (1998), PB94: Petit-Breuilh, Ma. E. (1994), VD14: Van Daele et al. (2014), NM04: Naranjo y Moreno Roa (2004), LT00: Lavigne et al. (2000), LW86: Lowe et al. (1986), RU96: Rodolfo et al. (1996), PD96: Pierson et al. (1996), HE86: Herd (1986), TC90: Thouret et al. (1990), TA98: Thouret et al. (1998), AR90: Arguden & Rodolfo (1990), PL09: Paguican et al. (2009), SC34: Schmidt (1934), PJ90: Pierson et al. (1990), ND96: Newhall et al. (1996), M02: Maso (1902)

Table 5.3 Total recorded lahars per trigger at each analogue volcano.

Volcano	Eruption-Ice Melt	Eruption-lake	Lake breakout	Rainfall	Mass wasting
Cotopaxi	207				
Kelud		78	15	45	
Mayon				92	
Merapi				587	
Nevado del Ruiz	20		1		5
Pinatubo			120	795	
Ruapehu	8	55	11	14	5
Villarrica	133			4	

When compared with other volcanoes (Tables 5.1&5.2), Ruapehu occupies an indeterminant position between crater-lake, ice melt, and rainfall triggered systems. Its persistent lake, seasonal precipitation, and pervasive ice cover allow multiple trigger mechanisms to operate, making its lahar system unusually diverse.

At Kelud, prior to installation of mitigation measures (Suryo and Clarke, 1985) catastrophic crater-lake breakout lahars of 10^6-10^8 m^3 occurred roughly every 100-150 years (Table 5.2) with frequent medium to extreme magnitude lake-eruption triggered lahars. The larger lake volume and intense tropical rainfall allow for higher maximum magnitudes and slightly shorter recurrence intervals than seen at Ruapehu.

At Pinatubo, post-1991 lahar activity was dominated by rainfall-triggered hyperconcentrated and debris flows, often enhanced by tropical cyclones (Janda et al., 1996; Pierson et al., 1996; Umbal and Rodolfo, 1996), with some long-duration, low-peak discharge flows exceeding 10^7 m^3. These high recurrence rates reflect the extraordinary sediment supply following the 1991 eruption rather than a fundamentally different meteorological regime (Gran and Montgomery, 2005; Newhall and Punongbayan, 1996; Tuñgol, 2002).

Villarrica and Cotopaxi are characterized primarily by eruption-ice melt triggered lahars. Villarrica typically generates medium to large lahars (10^5-10^6 m^3) associated with effusive eruptions (Castruccio et al., 2010; Clavero and Roa, 2004; Naranjo and Moreno Roa, 2004) on decadal timescales, while Cotopaxi produces flows exceeding 10^7 m^3 roughly once per century (Andrade et al., 2005; Frimberger et al., 2021), commonly during VEI 4-5 eruptions (Andrade et al., 2005). In contrast, rainfall-dominated volcanoes such as Merapi and Mayon experience lahars seasonally, sustained by monsoonal precipitation acting on young and recently deposited tephra mantles (Bautista et al., 2023; Jumadi et al., 2018; Lavigne et al., 2000; Paguican et al., 2009).

Intra-volcano comparisons necessitated the construction of a relative magnitude scale (Table 5.4). Although magnitude classification schemes exist (e.g., Jakob, 2005), most quantitative approaches are difficult to apply consistently across systems because historical lahar records, similar to other volcanic hazards, are often incomplete or qualitative (Coles and Sparks, 2006; Deligne et al., 2010; Dzierma and Wehrmann, 2010; Mead et al., 2016; Mead and Magill, 2017; Rougier et al., 2016). Many authors classify events simply as *small, medium, large,* or *very large/extreme* (Andrade et al., 2005; Mead et al., 2021; Newhall and Punongbayan, 1996; Taig, 2002; Van Daele et al., 2014), based on local qualitative experience rather than measured characteristics (e.g. volume, stage height at a known location or discharge) , or applying reference scales from other volcanoes to a new system (e.g., Nevado del Ruiz 10^7-10^8 m^3 volumes “moderately large” as cited in Pierson et al., 1990). As a result, inter-volcano comparisons rely primarily on the few events with measured or reconstructed event magnitudes.

Table 5.4 Representative magnitude divisions for lahar events at selected volcanoes, following divisions in Mead et al. (2021) for Ruapehu to facilitate inter-volcano comparison. Magnitude thresholds and measurement methods vary among volcanoes and are based on published quantitative values assigned to qualitative records where available. Values represent approximate ranges of event size.

Volcano	Event magnitude	Total volume (m^3)	Discharge (m^3 s^{-1})	Flow height (m)	Deposit thickness (m)	Notes
Ruapehu	Small	$<3x10^5$	$\sim10^2$	—	—	
	Medium	$3x10^5$ - $5x10^5$	$<10^3$	—	—	"Small/Medium"
	Large	$5x10^5$ - $3x10^6$	$\sim1x10^3$-$2x10^3$	—	—	"Medium/Large"
	Extreme	$>3x10^6$	$>2x10^3$	—	—	"Very Large/Extreme" Values based off Mead et al., 2021 and Taig, 2002
Cotopaxi	Small	$<10^4$	$\sim10^2$	—	—	Evento pequeño VEI 1-2[A]
	Medium	10^4-10^5	—	—	—	Evento moderado VEI 2-3[A]
	Large	10^5-10^6	—	—	—	Evento grande VEI 4[A]
	Extreme	$\geq10^6$	—	—	—	Evento muy grande VEI 4-5[A]
Villarrica	Small	$<10^4$	—	—	—	Records of Van Daele et al. 2014 that show flows not reaching the lakes[V]
	Medium	10^4-10^5	—	—	—	Records of Van Daele et al. 2014 that show flows reaching the lakes[V]
	Large	10^5-10^6	—	—	—	Mapped large flows[V]
	Extreme	$\geq10^6$	$\geq4\times10^3$	1-3	—	Mapped "major" flows.[V] Lahar channels at Villarrica end within 15-20 km at Lago Villarrica and Lago Calafquen

Pinatubo	Small		$<2x10^2$	—	—	
	Medium	$1x10^6$ - $1x10^7$	$2x10^2$ - $5x10^2$	—	—	AFM cutoff amplitude[TU]
	Large	$>1x10^7$ - $<5x10^7$	$5x10^2$ - $1x10^3$	—	—	
	Extreme	$>5x10^7$	$>1x10^3$	—	—	
Nevado del Ruiz	Small	$<1x10^6$	—	—	—	
	Medium	$1x10^6$ - $1x10^7$	—	—	—	
	Large	$>1x10^7$ - $<5x10^7$	—	—	—	
	Extreme	$>5x10^7$	—	—	—	
Merapi	Small		$<0.5x10^3$		<1	
	Medium		$0.5\text{-}1x10^3$	~2	1 - 3	"Moderate"[L]
	Large	10^5	$1\text{-}2x10^3$		3 - 10	"Large"[L] + "Very Large"[L]
	Extreme	10^6	$>2x10^3$	$7m^2$ ~15-	$15m^1$ $10m^2$	[1]~0-15km: Sisir, Kali Senawa [2]~15-30km: Salam, Kali Krasak) "Catastrophical"[L]
Kelud	Small	$<10^5$	—	—	—	
	Medium	10^5	—	—	—	
	Large	10^6	—	—	—	
	Extreme	$>10^6$	—	—	—	
Mayon	Small		Flow rate $(ms^{-1})^P$			
	Medium		~2 - 3			
	Large	10^5	~3 - 4			
	Extreme	10^6	~ >4			

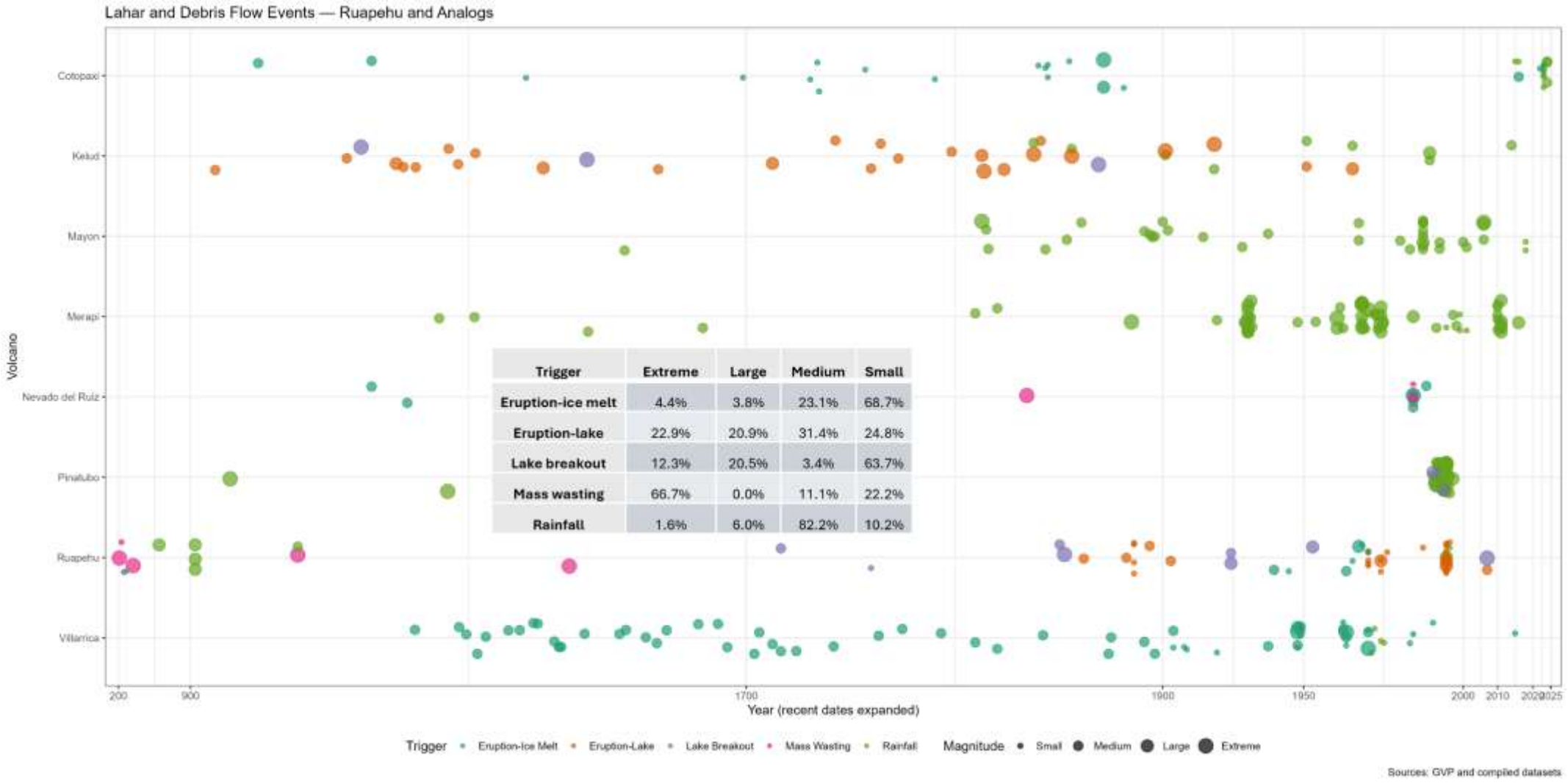
Magnitude divisions follow Mead et al. (2021) for Ruapehu to facilitate inter-volcano comparison. Magnitude thresholds and measurement methods vary among volcanoes and are based on published volume, discharge, or qualitative magnitude descriptions of qualitative records where available. Values represent approximate ranges of event size. Sources include Mead et al. (2021), [A]Andrade et al. (2005), [V]Van Daele et al. (2014), Newhall et al. (1997), Pierson (1985), [L] Lavigne et al. (2000, 2011), Arguden & Rodolfo (1990), [P]Paguican et al. (2009), Thouret et al. (1998), [TU]Tungol (2002), Hall & Mothes (2008).

Even where measurements exist, large uncertainties persist (Fig. 5.1). Lahar volumes span nine orders of magnitude, from ~10^2 to 10^9 m^3 (Manville et al., 2013; Mothes et al., 1998; Pierson et al., 2025; Vallance and Scott, 1997), and field-based estimates are often highly uncertain (Andaru et al., 2022). This uncertainty leads to a bias toward recording and analyzing the largest

events, while small or moderate lahars remain underrepresented due to limited impacts and low preservation potential (Cronin et al., 1997a; Graettinger, 2008).

Monitoring limitations also influence magnitude-frequency interpretations. Acoustic Flow Monitors (AFMs), for example, have detection thresholds that balance missing small events against false alarms (Tuñgol, 2002; Tuñgol and Regalado, 1996). At Mount Pinatubo in the years after the 1991 eruption, AFMs were calibrated and able to distinguish lahars by order-of-magnitude discharge (Table 5.4)(Janda et al., 1996; Pierson et al., 1996). Similar challenges apply to other automated monitoring networks (Cole, 2011; Walsh et al., 2023).

Magnitude-frequency comparisons remain approximate because classification methods and measurement thresholds vary among volcanoes. Applying the qualitative volume framework (Table 5.4) to Ruapehu's lahar volumes (ie. Small ($<3x10^5$ m^3), Medium ($3x10^5$ - $5x10^5$ m^3), Large ($5x10^5$ - $3x10^6$ m^3), and Extreme ($>3x10^6$ m^3)) Ruapehu has produced relatively few *Extreme* events but several *Large* ones comparable to Villarrica. Its hazard curve (Fig. 5.1) is consequently steeper (event frequency drops off quickly as magnitude increases) than that of Pinatubo or Nevado del Ruiz, where extreme ($>10^7$ m^3) lahars dominate.



Trigger	Extreme	Large	Medium	Small
Eruption-ice melt	4.4%	3.8%	23.1%	68.7%
Eruption-lake	22.9%	20.9%	31.4%	24.8%
Lake breakout	12.3%	20.5%	3.4%	63.7%
Mass wasting	66.7%	0.0%	11.1%	22.2%
Rainfall	1.6%	6.0%	82.2%	10.2%

Figure 5.1 Jittered graph of lahar events recorded from analogue volcanoes: Cotopaxi, Kelud, Mayon, Merapi, Nevado del Ruiz, Pinatubo, Ruapehu, and Villarrica. Triggers are represented as colours and magnitudes as sizes of individual events. Of note are paucity of mass wasting triggered events and increasing completeness of event identification, in addition to trigger variety and predominance across volcanoes

5.5 Hazard Implications

The revised lahar dataset shows through trigger patterns (e.g. Clustering after eruptions, quiescent periods before lake breakouts) (Table 5.1, Appendix D1) that Ruapehu's lahars cannot be interpreted as arising from a fixed recurrence rate; instead, their likelihood varies sharply with the volcanic and hydrologic state of the system. One method for accounting for this type of system is a proportional hazard modelling framework (Green et al., 2013) which incorporates the physical processes that affect the different triggers as covariates for hazard assessments. In a proportional hazards formulation, lahar occurrence is treated as a point process whose instantaneous hazard rate depends on variables evaluated at the beginning of each repose interval.

Initial variables proposed for a relevant Ruapehu framework include time since last eruption and last eruption magnitude (and changes in tephra supply), time since last lahar and last lahar magnitude, and cumulative number of lahars since last eruption. Additional covariates for the modelling framework would have to account for individual triggers and the physical states that control their likelihood as well as functions for how to covariates change with time. Such a framework would be able to account for the multi-event sequences of syn-eruptive lahars, semi-linked patterns of post-eruption lahars, and independent triggers such as mass-wasting.

Thus a more appropriate model for lahar recurrence at Ruapehu would be a state dependent proportional hazards model (Green et al., 2013), in which variables such as eruptive state, lake level, rainfall, and time since the last lahar changes the likelihood of the next lahar. This would allow the hazard rate to vary with changing physical conditions, rather than assuming a fixed recurrence interval. The trigger patterns identified above (Table 5.1; Appendix D1) motivate the conceptual formulation below, which is presented to define the covariate structure and

functional form that such a model would require rather than as a fitted or validated statistical model.

In a proportional hazards formulation, lahar occurrence is treated as a point process whose instantaneous hazard rate depends on variables evaluated at the beginning of each repose interval. If s is the time of the previous lahar and T is the start time of the most recent eruption, then the time since the last event is $r = t - s$. Syn-eruptive lahars may be represented as a point mass at eruption onset via the term $\delta(T - t)$, while all other lahars follow a Weibull-type hazard modified by covariates. The resulting intensity is

$$\lambda(t) = \delta(T - t)f(y) + \exp(w \cdot z)\alpha\beta^{\alpha}u^{\alpha-1}$$

where $u = min(r, t - T)$ and z is a covariate vector describing the volcanic state. For Ruapehu, the relevant variables include last-eruption magnitude M, time since the last eruption $(t - T)$, time since the last lahar r, number of lahars since the previous eruption N, lake fullness L, and rainfall state R. Together these capture the dominant controls on lahar likelihood: water availability, rapid changes in tephra supply, and progressive removal of sediment and lake volume during multi-event sequences.

Set up this way, the model is a conceptual framework rather than a working forecasting tool. The functional form and covariates are qualitatively known, as well as their qualitative effects on the hazard rate from the physical relationships established in Section 5.3. However weighting parameters, as well as relative weighting between syn-eruptive point-mass and Weibull-type background hazard remain unconstrained by the current dataset. Fitting, testing, and validation requires a greater and more consistently resolved covariate history than is presently available at Ruapehu alone (Section 5.2).

The model explicitly predicts elevated hazard immediately following eruptions, consistent with Ruapehu's historical record of syn-eruptive and post-eruptive lahar clusters. It also allows lake

conditions amplify lahar probability: when $L = 1$, the hazard is shifted upward by $\exp(w_L)$, which is historically consistent with the presence of a full Crater Lake. Third, seasonal rainfall effects can be included through a wet/dry state R, which adjusts the hazard multiplicatively. Because the covariates change on different timescales, hours during eruptions, months for rainfall changes, and years for long-term crater lake refilling, the model can reproduce the semi-linked hazard patterns consistent with the triggers. Importantly, this approach avoids assuming that lahars follow independent, identically distributed waiting times, and instead captures the way in which system state modifies time and controls lahar triggering. These qualitative relationships support the model's plausibility as a conceptual framework, but are not statistical validation, which would require formal parameter estimation and testing against the compiled event record.

Lahar magnitude can be treated within a parallel but separate structure following the model for a distribution across four points (Bebbington, 2014). Under this model, magnitude categories s for $s \in (small, medium, large, extreme)$ may follow a distribution of the form

$$P(S = s) \propto s^c(4 - s)^d$$

with c and d functions that vary with R, N, M, and L. This acknowledges that large lahars at Ruapehu typically require both sediment availability and a substantial water source. Under this formulation, the probability of large and extreme events increases when the lake is full or when there are large eruptions inducing ice melt, whereas events late in repose periods are more likely to be smaller and rainfall-limited. Such a model would allow hazard assessments to specify not only when lahars are likely, but also the expected *size distribution* under different covariate states, an essential requirement for operational risk management. Similarly to the hazard rate framework previously, this magnitude model is conceptual, as it states a framework for event size based on covariate state without estimating c and d from data. Fitting both

components and the previous formulation against an expanded Ruapehu and global analog record is proposed as the next stage of this work.

5.6 Conclusions

Cursory analysis of Ruapehu's lahar records indicates that lahar occurrence reflects the interaction of multiple trigger mechanisms, evolving system states, and variable sediment and water availability rather than a fixed recurrence pattern. When contrasted with global analogues, Ruapehu's record demonstrates a frequency-magnitude relationship with a greater relative ratio of large vs extreme events. These different frequency-magnitude relationships emphasize that lahar magnitude-probability is conditioned by eruptive activity, Crater Lake level, ice presence, rainfall, and sediment supply, and that meaningful hazard assessment must therefore incorporate state-dependent controls rather than rely on long-term empirical recurrence alone. Section 5.5 presents conceptual proportional-hazards and magnitude-distribution formulation frameworks built to capture these controls, while fitting and validating the framework against a high-resolution combined Ruapehu and global analog event record is identified as the immediate next step for Ruapehu lahar hazard forecasting. Additionally, there are likely other state-dependent variables that haven't been identified in this framework or even recorded, as the global lahar records contain disparate size estimates and sporadic trigger information.

Improving these assessments will require both better physical characterization of lahar deposits, detection of active flows, and closer coupling between source conditions and flow modelling. Higher-resolution mapping, targeted outcrop sedimentology, and spectral methods capable of identifying provenance and trigger signatures would provide stronger constraints on event classification and magnitude reconstruction. Combining these data with geophysical flow models and statistical models that explicitly incorporate lake volume, eruptive state, rainfall,

and sediment availability would allow more accurate evaluations of expected flow size, runout, and downstream impact under different triggering scenarios.

Finally, this work highlights the need for a more systematic and internationally consistent database of lahar events that includes sedimentology, trigger mechanisms, and quantitative flow characteristics. Such a resource, paired with statistical approaches that can accommodate multi-criteria datasets and incomplete records, would allow for more robust cross-volcano comparisons and more reliable hazard models incorporating both frequency and magnitude. Together, improved mapping, increased field work and deposit analysis, advanced flow models, and unified datasets offer the clearest route to advancing lahar hazard forecasting by enabling consistent trigger classification, improved magnitude estimates, and providing covariate information for more detailed statistical models.

6 Conclusion

This research achieved its primary aim of refining the Onetapu Formation lahar record for Mt. Ruapehu and enhancing the understanding of lahar triggering mechanisms at Mt. Ruapehu through the following objectives:

6.1 Objective (1) reassessing lahar deposits and revising stratigraphic relationships

This objective was fulfilled through detailed field analysis of the lahar deposits in the Whangaehu and Wahianoa catchments, identifying new field sites and adding additional information on units with respect to grain size and componentry across the units. The reassessment incorporated a new lithostratigraphic framework for the eastern ring plain and, crucially, provided new observations identifying that the Wahianoa catchment contributed multiple lahar sequences to the Onetapu Formation during and immediately following the 232 CE Taupo Ignimbrite emplacement. This new record contributed to building a new lahar event new record for Mt. Ruapehu that could be applied to robustly undertake hazard analysis. Deposits described were also additionally cateogorised further based on trigger mechanism. This new multicriteria classification is needed to inform new hazard analytical methods to account for non-eruptive events.

6.2 Objectives (2 & 3) characterising these deposits and inferring triggering mechanisms

Deposit characterisation and trigger mechanism identification were achieved using a novel multi-criteria analytical approach combining grain-size statistics, lithological coding, X-ray fluorescence (XRF), X-ray diffraction (XRD), and visible to Short-Wave Infrared Reflectance (SWIR) spectroscopy. Bulk XRF and XRD showed most Onetapu Formation lahar matrices

generally converged around typical andesitic compositions, with indiscernible variation across units, the SWIR analysis provided additional information about the deposits highlighting that distinct correlations of deposits and clusters of spectra allow for the creation of diagnostic spectral fingerprints of lahar triggering mechanisms. This technique was sensitive enough to resolve low-abundance hydrothermal alteration signatures (e.g., smectite and kaolinite), allowing for the separation of relatively unaltered hyperconcentrated flows (e.g., Onetapu C units) from highly altered, clay-rich cohesive debris flows (e.g., Onetapu B and D2). Additionally, high Loss on Ignition (LOI) values corresponded consistently with cohesive debris flows, reinforcing the spectral link between hydrothermal alteration and flow rheology. Furthermore, spectral clustering analysis provided groupings largely consistent with the mapped stratigraphy and inferred triggering mechanisms: landslides/flank failures for massive cohesive debris flows (Onb, Ond-2) and eruption-lake expulsion or rainfall for multi-sequence hyperconcentrated flows (Onc units, One-6).

6.3 Objective (4) modelling typical Crater Lake eruption triggered lahar generation

Modelling Crater Lake eruption triggered waves/lahar generation was accomplished through numerical simulations using the Basilisk computational fluid dynamics program. The modelling demonstrated that the outflow volume generated by underwater explosions is highly sensitive to the initial water level in the Crater Lake, increasing by an order of magnitude between low and high water depths. The simulated outflow volumes (~3.6x103 m3) represent the initial phase of typical low-to-moderate intensity eruptive activity (VEI < 3) in the post-Crater Lake record. Crucially, the results indicate that the repetition of these outflows within Ruapehu's characteristic multi-phase eruptive sequences (e.g., 1995-1996) can rapidly escalate the lahar hazard through cumulative lake drainage, even if individual events produce only limited flows.

6.4 Objective (5) synthesising these findings into a preliminary multi-trigger probabilistic model

Synthesising the findings of previous chapters into a preliminary multi-trigger model addressed the limitations of relying solely on empirical recurrence rates. The research established that lahar occurrence at Ruapehu reflects the complex interaction of multiple trigger mechanisms (eruption-lake, rainfall, mass wasting, lake breakout) and evolving system states, confirming that lahars are not independent events. This synthesis strongly motivates a shift toward conditional, process-based hazard approaches. The derived frequency-magnitude data and trigger-dependency patterns underscore the necessity of a state-dependent proportional hazards model, explicitly incorporating time-varying covariates such as Crater Lake level, eruptive state, rainfall, and available sediment supply to modulate the instantaneous hazard rate and provide more accurate evaluations of expected flow sizes and impacts.

6.5 Future work

6.5.1 Opportunistic field mapping to address preservation bias:

The excavation of a swamp drainage canal above Tangiwai in the Karioi Forest provided the type locality for the Onetapu Formation, a site now overgrown and covered. Future fieldwork should quickly document ephemeral exposures in sites less susceptible to erosion to overcome the inherent preservation bias in the current lahar record. This involves seeking rare transverse profiles outside the main Whangaehu river channel, particularly within the Rangipo Desert, to accurately reconstruct paleo-channel positions and flow dynamics.

6.5.2 Quantify low abundance clay minerals using SWIR:

The development of quantitative calibration techniques is required to create more robust correlation and provenance methods and to estimate the percentage of low-abundance clay

minerals (e.g., smectite and kaolinite) detected by SWIR spectroscopy. The goal is to generalize this sensitive fingerprinting methodology for provenance tracing and trigger classification worldwide, as well as doing more work to constrain exact provenance of large debris flows from the Ruapehu edifice.

6.5.3 Link Crater Lake outflow to downstream lahar dynamics:

Integrate the numerical wave generation outputs from the *Basilisk* computational fluid dynamics program directly into established downstream lahar propagation models (such as Titan2D, used in previous hazard assessments). This integration would translate the water volume predicted during explosive lake events into realistic predictions of flow size and runout velocity on the ring plain, considering sediment mobilization potential.

6.5.4 Develop and validate multi-trigger probabilistic model:

Formalize and test the proposed multi-trigger probabilistic model. This involves constructing statistical frameworks that treat lahar recurrence as conditional upon time-varying covariates, such as the state of volcanic activity (eruptive state), Crater Lake volume, recent rainfall measurements, and available unconsolidated sediment supply. Furthermore, define data necessary to construct an internationally consistent database of lahar events which will, in turn, enable more robust cross-volcano hazard comparisons, integrating frequency, magnitude, and multi-criteria datasets

7 References

Abdale, L., Leiter, S., Wilson, S., Russell, K., Groat, L., 2023. Characterization of Hydrothermal Alteration in Palagonitized Deposits Using Short-Wave Infrared Spectroscopy and X-Ray Diffraction Methods. The Canadian Journal of Mineralogy and Petrology 61, 365–385. https://doi.org/10.3749/2200056

Alloway, B.V., 1989. The late quaternary cover bed stratigraphy and tephrochronology of north-eastern and central Taranaki, New Zealand: a thesis presented in partial fulfullment of the requirements for the degree of Doctor of philosophy in soil science at Massey University, Palmerston North, New Zealand.

Andaru, R., Rau, J.-Y., Setya Prayoga, A., 2022. Determination of potential secondary lahar hazard areas based on pre-and post-eruption UAV DEMs: Automatic identification of initial lahar starting points and supplied lahar volume. International Journal of Applied Earth Observation and Geoinformation 115, 103096. https://doi.org/10.1016/j.jag.2022.103096

Andrade, D., Escuela Politécnica Nacional (Quito, Ecuador), Institut de recherche pour le développement (France) (Eds.), 2005. Los peligros volcánicos asociados con el Cotopaxi, Peligros volcánicos en el Ecuador. Corporación Editora Nacional, Quito.

Arguden, A.T., Rodolfo, K.S., 1990. Sedimentologic and dynamic differences between hot and cold laharic debris flows of Mayon Volcano, Philippines. Geological Society of America Bulletin 102, 865–876. https://doi.org/10.1130/0016-7606(1990)102%3C0865:SADDBH%3E2.3.CO;2

Baker, V.R., Kochel, R.C., Patton, P.C., Pickup, G., 1983. Palaeohydrologic Analysis of Holocene Flood Slack-Water Sediments, in: Collinson, J.D., Lewin, J. (Eds.), Modern and Ancient Fluvial Systems. Wiley, pp. 229–239. https://doi.org/10.1002/9781444303773.ch18

Bakker, L., Lowe, D.J., Jongmans, A.G., 1996. A micromorphological study of pedogenic processes in an evolutionary soil sequence formed on Late Quaternary rhyolitic tephra deposits, North Island, New Zealand. Quaternary International 34–36, 249–261. https://doi.org/10.1016/1040-6182(95)00090-9

Ban, M., Kawashima, K., Tsunematsu, K., Imura, T., Kataoka, K.S., Yamanoi, T., Faculty of Science, Yamagata University 1-4-12 Kojirakawa-machi, Yamagata, Yamagata 990-8560, Japan, Graduate School of Science and Technology, Yamagata University, Yamagata, Japan, Research Institute for Natural Hazards and Disaster Recovery, Niigata University, Niigata, Japan, 2022. Geologic and Petrologic Characteristics of the Lahar Deposits at the Western Foot of Zao Volcano. JDR 17, 736–744. https://doi.org/10.20965/jdr.2022.p0736

Battershill, L., Whittaker, C.N., Lane, E.M., Popinet, S., White, J.D.L., Power, W.L., Nomikou, P., 2021. Numerical Simulations of a Fluidized Granular Flow Entry Into Water: Insights Into Modeling Tsunami Generation by Pyroclastic Density Currents. JGR Solid Earth 126, e2021JB022855. https://doi.org/10.1029/2021JB022855

Baumann, V., Bonadonna, C., Cuomo, S., Moscariello, M., Manzella, I., 2018. Slope stability models for rainfall-induced lahars during long-lasting eruptions. Journal of Volcanology and Geothermal Research 359, 78–94. https://doi.org/10.1016/j.jvolgeores.2018.06.018

Bautista, M.L.P., Delos Reyes, P.J., Santos, E.R.U., Gaurino, W.A., Olfindo, V.S.V., Rivera, D.A.V., Dizon, M.P., Maximo, R.P.R., Ativo, S.C.J., Degones, M.F., Cabaluna, S.B., Babon, L.G.O., Bautista, B.C., Jenkins, S.F., Solidum, R.U., 2023. Quantitative impact assessment of the 2019 tropical cyclone Kammuri lahars: Mayon volcano, Philippines. International Journal of Disaster Risk Reduction 94, 103779. https://doi.org/10.1016/j.ijdrr.2023.103779

Bebbington, M.S., 2014. Long-term forecasting of volcanic explosivity. Geophysical Journal International 197, 1500–1515. https://doi.org/10.1093/gji/ggu078

Belousov, A., Belousova, B.V., M., 2000. Tsunamis Generated by Subaquatic Volcanic Explosions: Unique Data from 1996 Eruption in Karymskoye Lake, Kamchatka, Russia. Pure and Applied Geophysics 157, 1135–1143. https://doi.org/10.1007/s000240050021

Belousov, A., Belousova, M., 2001. Eruptive Process, Effects and Deposits of the 1996 and the Ancient Basaltic Phreatomagmatic Eruptions in Karymskoye Lake, Kamchatka, Russia, in: White, J.D.L., Riggs, N.R. (Eds.), Volcaniclastic Sedimentation in Lacustrine Settings. Wiley, pp. 35–60. https://doi.org/10.1002/9781444304251.ch3

Bishop, J., Lane, M., Dyar, M., Brown, A., 2008. Reflectance and emission spectroscopy study of four groups of phyllosilicates: Smectites, kaolinite-serpentines, chlorites and micas. Clay minerals 43, 35–54.

Bishop, J.L., 2019. Visible and Near-Infrared Reflectance Spectroscopy: Laboratory Spectra of Geologic Materials, in: Bishop, J.L., Bell Iii, J.F., Moersch, J.E. (Eds.), Remote Compositional Analysis. Cambridge University Press, pp. 68–101. https://doi.org/10.1017/9781316888872.006

Blott, S.J., Pye, K., 2001. GRADISTAT: a grain size distribution and statistics package for the analysis of unconsolidated sediments. Earth Surf Processes Landf 26, 1237–1248. https://doi.org/10.1002/esp.261

Boggs, S., 2009. Petrology of sedimentary rocks, 2nd ed. ed. Cambridge University Press, Cambridge.

Campbell, I.B., 1973. Recent aggradation in Whangaehu Valley, Central North Island, New Zealand. New Zealand J. Geol. Geophys. 16.

Carrasco-Núñez, G., Vallance, J.W., Rose, W.I., 1993. A voluminous avalanche-induced lahar from Citlaltépetl volcano, Mexico: Implications for hazard assessment. Journal of Volcanology and Geothermal Research 59, 35–46. https://doi.org/10.1016/0377-0273(93)90076-4

Carrivick, J.L., Manville, V., Graettinger, A., Cronin, S.J., 2010. Coupled fluid dynamics-sediment transport modelling of a Crater Lake break-out lahar: Mt. Ruapehu, New Zealand. Journal of Hydrology 388, 399–413. https://doi.org/10.1016/j.jhydrol.2010.05.023

Carrivick, J.L., Manville, V.R., Cronin, S.J., 2009. A fluid dynamics approach to modelling the 18th March 2007 lahar at Mt. Ruapehu, New Zealand. Bulletin of Volcanology 71, 153–169. https://doi.org/10.1007/s00445-008-0213-2

Castruccio, A., Clavero, J., Rivera, A., 2010. Comparative study of lahars generated by the 1961 and 1971 eruptions of Calbuco and Villarrica volcanoes, Southern Andes of Chile. Journal of Volcanology and Geothermal Research 190, 297–311. https://doi.org/10.1016/j.jvolgeores.2009.12.005

Ching, C., 2022. Observations of Ruapehu Crater Lake (Te Wai ā-moe) and implications for lake dynamics and volcano monitoring. https://doi.org/10.26021/13107

Chow, V., 1959. Open channel hydraulics. MacGraw-Hill Book Co. Inc., New York, NY.

Christenson, B.W., Reyes, A.G., Young, R., Moebis, A., Sherburn, S., Cole-Baker, J., Britten, K., 2010. Cyclic processes and factors leading to phreatic eruption events: Insights from the 25 September 2007 eruption through Ruapehu Crater Lake, New Zealand. Journal of Volcanology and Geothermal Research 191, 15–32. https://doi.org/10.1016/j.jvolgeores.2010.01.008

Clark, R.N., 1999. Spectroscopy of rocks and minerals and principles of spectroscopy, in: Andrew N. Rencz (Ed.), Manual of Remote Sensing, Volume 3, Remote Sensing for the Earth Sciences. Wiley, pp. 3–58.

Clark, R.N., 1981. Water frost and ice: The near-infrared spectral reflectance 0.65–2.5 μm. J. Geophys. Res. 86, 3087–3096. https://doi.org/10.1029/JB086iB04p03087

Clark, R.N., King, T.V.V., Klejwa, M., Swayze, G.A., Vergo, N., 1990. High spectral resolution reflectance spectroscopy of minerals. J. Geophys. Res. 95, 12653–12680. https://doi.org/10.1029/JB095iB08p12653

Clark, R.N., Lucey, P.G., 1984. Spectral properties of ice-particulate mixtures and implications for remote sensing: 1. Intimate mixtures. J. Geophys. Res. 89, 6341–6348. https://doi.org/10.1029/JB089iB07p06341

Clark, R.N., Roush, T.L., 1984. Reflectance spectroscopy: Quantitative analysis techniques for remote sensing applications. J. Geophys. Res. 89, 6329–6340. https://doi.org/10.1029/JB089iB07p06329

Clark, R.N., Swayze, G.A., Livo, K.E., Kokaly, R.F., Sutley, S.J., Dalton, J.B., McDougal, R.R., Gent, C.A., 2003. Imaging spectroscopy: Earth and planetary remote sensing with the USGS Tetracorder and expert systems. J.-Geophys.-Res. 108, 2002JE001847. https://doi.org/10.1029/2002JE001847

Clavero, J., Roa, H., 2004. Evolution of Villarrica Volcano. IAVCEI 2004. Jorge Clavero; Hugo Moreno. Servicio Nacional de Geología y Minería, Boletín No. 61. Special Publications of IAVCEI Bulletin No. 61, 17–27.

Cole, S.E., 2011. Geophysical investigation into the internal dynamics of moving lahars : a thesis presented in partial fulfilment of the requirements for the degree of Doctor of Philosophy in Earth Science at Massey University, Palmerston North, New Zealand (Doctoral). Massey University.

Coles, S.G., Sparks, R.S.J., 2006. Extreme value methods for modelling historical series of large volcanic magnitudes, in: Mader, H.M., Coles, S.G., Connor, C.B., Connor, L.J. (Eds.), Statistics in Volcanology. The Geological Society of London on behalf of The International Association of Volcanology and Chemistry of the Earth's Interior, pp. 47–56. https://doi.org/10.1144/IAVCEI001.5

Conway, C.E., 2016. Studies on the glaciovolcanic and magmatic evolution of Ruapehu Volcano, New Zealand. Open Access Te Herenga Waka-Victoria University of Wellington. https://doi.org/10.26686/wgtn.17014568

Conway, C.E., Gamble, J.A., Wilson, C.J.N., Leonard, G.S., Townsend, D.B., Calvert, A.T., 2018. New petrological, geochemical, and geochronological perspectives on andesite-dacite magma genesis at Ruapehu volcano, New Zealand. American Mineralogist 103, 565–581. https://doi.org/10.2138/am-2018-6199

Conway, C.E., Leonard, G.S., Townsend, D.B., Calvert, A.T., Wilson, C.J.N., Gamble, J.A., Eaves, S.R., 2016. A high-resolution 40Ar/39Ar lava chronology and edifice construction history for Ruapehu volcano, New Zealand. Journal of Volcanology and Geothermal Research 327, 152–179. https://doi.org/10.1016/j.jvolgeores.2016.07.006

Cook, R., C., 2002. Differentiation of three quaternary Mt. Hood lahars by particle size, clay mineralogical, bulk mineralogical, and geochemical analyses. Middlebury College.

Costa, J.E., 1988. Rheologic, geomorphic, and sedimentologic differentiation of water floods, hyperconcentrated flows, and debris flows.

Costa, J.E., 1984. Physical Geomorphology of Debris Flows, in: Costa, J.E., Fleisher, P.J. (Eds.), Developments and Applications of Geomorphology. Springer Berlin Heidelberg, Berlin, Heidelberg, pp. 268–317. https://doi.org/10.1007/978-3-642-69759-3_9

Coussot, P., Meunier, M., 1996. Recognition, classification and mechanical description of debris flows. Earth-Science Reviews 40, 209–227. https://doi.org/10.1016/0012-8252(95)00065-8

Crandell, D., 1987. Deposits of pre-1980 pyroclastic flows and lahars from Mount St. Helens Volcano, Washington (Report No. 1444), Professional Paper. https://doi.org/10.3133/pp1444

Crandell, D.R., 1971. Postglacial Lahars From Mount Rainier Volcano, Washington, Professional Paper.

Cronin, S.J., 1996. Late quarternary volcanic stratigraphy within a portion of the northeastern Tongariro volcanic centre: a thesis presented as partial fulfilment of the requirements for the degree of Doctor of Philosophy in Soil Science.
Cronin, S.J., Hodgson, K.A., Neall, V.E., Palmer, A.S., Lecointre, J.A., 1997a. 1995 Ruapehu lahars in relation to the late Holocene lahars of Whangaehu River, New Zealand. null 40, 507–520. https://doi.org/10.1080/00288306.1997.9514780
Cronin, S.J., Lecointre, J.A., Palmer, A.S., Neall, V.E., 2000. Transformation, internal stratification, and depositional processes within a channelised, multi-peaked lahar flow. null 43, 117–128. https://doi.org/10.1080/00288306.2000.9514874
Cronin, S.J., Neall, V.E., 1997. A late Quaternary stratigraphic framework for the northeastern Ruapehu and eastern Tongariro ring plains, New Zealand. New Zealand Journal of Geology and Geophysics 40, 185–197. https://doi.org/10.1080/00288306.1997.9514752
Cronin, S.J., Neall, V.E., Lecointre, J.A., Palmer, A.S., 1999. Dynamic interactions between lahars and stream flow: A case study from Ruapehu volcano, New Zealand. GSA Bulletin 111, 28–38. https://doi.org/10.1130/0016-7606(1999)111%3C0028:DIBLAS%3E2.3.CO;2
Cronin, S.J., Neall, V.E., Lecointre, J.A., Palmer, A.S., 1997b. Changes in Whangaehu river lahar characteristics during the 1995 eruption sequence, Ruapehu volcano, New Zealand. Journal of Volcanology and Geothermal Research 76, 47–61. https://doi.org/10.1016/S0377-0273(96)00064-9
Cronin, S.J., Neall, V.E., Lecointre, J.A., Palmer, A.S., 1996. Unusual “snow slurry” lahars from Ruapehu volcano, New Zealand, September 1995. Geology 24.
Cronin, S.J., Neall, V.E., Palmer, A.S., Stewart, R.B., 1997c. Methods of identifying late Quaternary rhyolitic tephras on the ring plains of Ruapehu and Tongariro volcanoes, New Zealand. New Zealand Journal of Geology and Geophysics 40, 175–184. https://doi.org/10.1080/00288306.1997.9514751
Cronin, S.J., Zernack, A.V., Ukstins, I.A., Turner, M.B., Torres-Orozco, R., Stewart, R.B., Smith, I.E.M., Procter, J.N., Price, R., Platz, T., Petterson, M., Neall, V.E., McDonald, G.S., Lerner, G.A., Damaschcke, M., Bebbington, M.S., 2021. The geological history and hazards of a long-lived stratovolcano, Mt. Taranaki, New Zealand. New Zealand Journal of Geology and Geophysics 64, 456–478. https://doi.org/10.1080/00288306.2021.1895231
Crowley, J.K., Zimbelman, D.R., 1997. Mapping hydrothermally altered rocks on Mount Rainier, Washington, with Airborne Visible/Infrared Imaging Spectrometer (AVIRIS) data. Geol 25, 559. https://doi.org/10.1130/0091-7613(1997)025%3C0559:MHAROM%3E2.3.CO;2
Deligne, N.I., Coles, S.G., Sparks, R.S.J., 2010. Recurrence rates of large explosive volcanic eruptions. J. Geophys. Res. 115, 2009JB006554. https://doi.org/10.1029/2009JB006554
Delos Reyes, P.J., Bornas, Ma.A.V., Dominey-Howes, D., Pidlaoan, A.C., Magill, C.R., Solidum, Jr., R.U., 2018. A synthesis and review of historical eruptions at Taal Volcano, Southern Luzon, Philippines. Earth-Science Reviews 177, 565–588. https://doi.org/10.1016/j.earscirev.2017.11.014
Deon, F., Van Ruitenbeek, F., Van Der Werff, H., Van Der Meijde, M., Marcatelli, C., 2022. Detection of Interlayered Illite/Smectite Clay Minerals with XRD, SEM Analyses and Reflectance Spectroscopy. Sensors 22, 3602. https://doi.org/10.3390/s22093602
Detienne, M., Delmelle, P., Guevara, A., Samaniego, P., Opfergelt, S., Mothes, P.A., 2017. Contrasting origin of two clay-rich debris flows at Cayambe Volcanic Complex, Ecuador. Bull Volcanol 79, 27. https://doi.org/10.1007/s00445-017-1111-2
Dittmer, M., 2008. The Clockwork Lahar: Examining issues management in a New Zealand public service context (Master of Science (MSc)). Massey University, Palmerston North.
Dolan, M., 2004. Observations of lahars along the Sacobia-Bamban River systems, Mount Pinatubo, Philippines (48 pp.).

Donoghue, S.L., 1991. Late quaternary volcanic stratigraphy of the southeastern sector of the Mount Ruapehu ring plain New Zealand : a thesis presented as partial fulfilment of the requirements for the degree of Doctor of Philosophy in Soil Science (Doctoral). Massey University.
Donoghue, S.L., Neall, V.E., 2001. Late Quaternary constructional history of the southeastern Ruapehu ring plain, New Zealand. null 44, 439–466. https://doi.org/10.1080/00288306.2001.9514949
Donoghue, S.L., Neall, V.E., Palmer, A.S., 1995. Stratigraphy and chronology of late Quaternary tephra deposits, Tongariro Volcanic Centre, New Zealand. J. Royal Soc. of New Zealand 25.
Donoghue, S.L., Neall, V.E., Palmer, A.S., Stewart, R.B., 1997. The volcanic history of Ruapehu during the last 2 millennia based on the record of the Tufa Trig Tephras. Bull. Volcanol. 59.
Donoghue, S.L., Palmer, A.S., McClelland, E., Hobson, K., Stewart, R.B., Neall, V.E., Lecointre, J.A., Price, R., 1999. The Taurewa Eruptive Episode: evidence for climactic eruptions at Ruapehu volcano, New Zealand. Bulletin of Volcanology 61, 223–240. https://doi.org/10.1007/s004450050273
Douglas, A., Kereszturi, G., Schaefer, L.N., Kennedy, B., 2022. Rock alteration mapping in and around fossil shallow intrusions at Mt. Ruapehu New Zealand with laboratory and aerial hyperspectral imaging. Journal of Volcanology and Geothermal Research 432, 107700. https://doi.org/10.1016/j.jvolgeores.2022.107700
Dzierma, Y., Wehrmann, H., 2010. Eruption time series statistically examined: Probabilities of future eruptions at Villarrica and Llaima Volcanoes, Southern Volcanic Zone, Chile. Journal of Volcanology and Geothermal Research 193, 82–92. https://doi.org/10.1016/j.jvolgeores.2010.03.009
Fagents, S.A., Baloga, S.M., 2006. Toward a model for the bulking and debulking of lahars. J. Geophys. Res. 111, B10201. https://doi.org/10.1029/2005JB003986
Farifteh, J., Van Der Meer, F., Carranza, E.J.M., 2007. Similarity measures for spectral discrimination of salt-affected soils. International Journal of Remote Sensing 28, 5273–5293. https://doi.org/10.1080/01431160701227604
Finn, C.A., Deszcz-Pan, M., Anderson, E.D., John, D.A., 2007. Three-dimensional geophysical mapping of rock alteration and water content at Mount Adams, Washington: Implications for lahar hazards. J. Geophys. Res. 112, 2006JB004783. https://doi.org/10.1029/2006JB004783
Flores, F.A., 2022. Dynamics and Modelling of the 2015 Calbuco eruption Volcanic Debris Flows (Chile). From field evidence to a primary lahar model (Masters). University of Bristol, Bristol.
Folk, R.L., Ward, W.C., 1957. Brazos River bar [Texas]; a study in the significance of grain size parameters. Journal of sedimentary research 27, 3–26.
Frank, D., 1995. Surficial extent and conceptual model of hydrothermal system at Mount Rainier, Washington. Journal of Volcanology and Geothermal Research 65, 51–80. https://doi.org/10.1016/0377-0273(94)00081-Q
Frank, D.G., 1985. Hydrothermal processes at Mount Rainier (PhD). University of Washington, Seattle, Washington.
Freundt, A., 2003. Entrance of hot pyroclastic flows into the sea: experimental observations. Bulletin of Volcanology 65, 144–164. https://doi.org/10.1007/s00445-002-0250-1
Freundt, A., Strauch, W., Kutterolf, S., Schmincke, H.-U., 2007. Volcanogenic Tsunamis in Lakes: Examples from Nicaragua and General Implications. Pure appl. geophys. 164, 527–545. https://doi.org/10.1007/s00024-006-0178-z
Frimberger, T., Andrade, S.D., Weber, S., Krautblatter, M., 2021. Modelling future lahars controlled by different volcanic eruption scenarios at Cotopaxi (Ecuador) calibrated

with the massively destructive 1877 lahar. Earth Surf. Process. Landforms 46, 680–700. https://doi.org/10.1002/esp.5056
Gabrielsen, H., Procter, J.N., Rainforth, H., Black, T., Harmsworth, G., Pardo, N., 2018. Reflections from an Indigenous Community on Volcanic Event Management, Communications and Resilience, in: Fearnley, C.J., Bird, D.K., Haynes, K., McGuire, W.J., Jolly, G. (Eds.), Observing the Volcano World: Volcano Crisis Communication. Springer International Publishing, Cham, pp. 463–479. https://doi.org/10.1007/11157_2016_44
Gamble, J.A., Price, R.C., Smith, I.E.M., McIntosh, W.C., Dunbar, N.W., 2003. 40Ar/39Ar geochronology of magmatic activity, magma flux and hazards at Ruapehu volcano, Taupo Volcanic Zone, New Zealand. Journal of Volcanology and Geothermal Research 120, 271–287. https://doi.org/10.1016/S0377-0273(02)00407-9
Gattuso, A., Bonadonna, C., Frischknecht, C., Cuomo, S., Baumann, V., Pistolesi, M., Biass, S., Arrowsmith, J.R., Moscariello, M., Rosi, M., 2021. Lahar risk assessment from source identification to potential impact analysis: the case of Vulcano Island, Italy. Journal of Applied Volcanology 10, 9. https://doi.org/10.1186/s13617-021-00107-6
George, D.L., Iverson, R.M., Cannon, C.M., 2022. Modeling the dynamics of lahars that originate as landslides on the west side of Mount Rainier, Washington (Report No. 2021–1118), Open-File Report. Reston, VA. https://doi.org/10.3133/ofr20211118
Gómez-Vasconcelos, M.G., Villamor, P., Cronin, S.J., Procter, J., Palmer, A., Townsend, D., Leonard, G., 2017. Crustal extension in the Tongariro graben, New Zealand: Insights into volcano-tectonic interactions and active deformation in a young continental rift. GSA Bulletin 129, 1085–1099. https://doi.org/10.1130/B31657.1
Graettinger, A.H., 2008. Depositional record of historic lahars in the Whangaehu Gorge, Mt. Ruapehu (Masters). University of Waikato, Hamilton, New Zealand.
Graettinger, A.H., Manville, V.R., Briggs, R.M., 2010. Depositional record of historic lahars in the upper Whangaehu Valley, Mt. Ruapehu, New Zealand: implications for trigger mechanisms, flow dynamics and lahar hazards. Bulletin of Volcanology 72, 279–296. https://doi.org/10.1007/s00445-009-0318-2
Graham, I.J., Hackett, W.R., 1987. Petrology of Calc-alkaline Lavas from Ruapehu Volcano and Related Vents, Taupo Volcanic Zone, New Zealand. Journal of Petrology 28, 531–567. https://doi.org/10.1093/petrology/28.3.531
Gran, K.B., Montgomery, D.R., 2005. Spatial and temporal patterns in fluvial recovery following volcanic eruptions: Channel response to basin-wide sediment loading at Mount Pinatubo, Philippines. GSA Bulletin 117, 195–211. https://doi.org/10.1130/B25528.1
Green, R.M., Bebbington, M.S., Cronin, S.J., Jones, G., 2013. Geochemical precursors for eruption repose length. Geophysical Journal International 193, 855–873. https://doi.org/10.1093/gji/ggt044
Grilli, S.T., Ioualalen, M., Asavanant, J., Shi, F., Kirby, J.T., Watts, P., 2007. Source Constraints and Model Simulation of the December 26, 2004, Indian Ocean Tsunami. J. Waterway, Port, Coastal, Ocean Eng. 133, 414–428. https://doi.org/10.1061/(ASCE)0733-950X(2007)133:6(414)
Grilli, S.T., Tappin, D.R., Carey, S., Watt, S.F.L., Ward, S.N., Grilli, A.R., Engwell, S.L., Zhang, C., Kirby, J.T., Schambach, L., Muin, M., 2019. Modelling of the tsunami from the December 22, 2018 lateral collapse of Anak Krakatau volcano in the Sunda Straits, Indonesia. Sci Rep 9, 11946. https://doi.org/10.1038/s41598-019-48327-6
Grilli, S.T., Zhang, C., Kirby, J.T., Grilli, A.R., Tappin, D.R., Watt, S.F.L., Hunt, J.E., Novellino, A., Engwell, S., Nurshal, M.E.M., Abdurrachman, M., Cassidy, M., Madden-Nadeau, A.L., Day, S., 2021. Modeling of the Dec. 22nd 2018 Anak Krakatau volcano lateral collapse and tsunami based on recent field surveys: Comparison with observed tsunami impact. Marine Geology 440, 106566. https://doi.org/10.1016/j.margeo.2021.106566

Hackett, W.R., Houghton, B.F., 1989. A facies model for a quaternary andesitic composite volcano: Ruapehu, New Zealand. Bulletin of Volcanology 51, 51–68. https://doi.org/10.1007/BF01086761
Hales, T.C., 2000. The geology of the Summit Area, Mt Ruapehu. https://doi.org/10.26021/14517
Hall, M., Mothes, P., 2008. The rhyolitic–andesitic eruptive history of Cotopaxi volcano, Ecuador. Bull Volcanol 70, 675–702. https://doi.org/10.1007/s00445-007-0161-2
Hampton, M.A., 1972. The Role of Subaqueous Debris Flow in Generating Turbidity Currents. SEPM JSR Vol. 42. https://doi.org/10.1306/74D7262B-2B21-11D7-8648000102C1865D
Hancox, G., Otway, P., Webby, M., 1995. Possible effects of a lahar caused by future collapse of the tephra barrier formed at the Mt. Ruapehu Crater Lake outlet by the 96.
Hayward, M.W., 2023. Non-hydrostatic Numerical Modelling of Tsunami Generation from Subaqueous Eruptions and Explosions. The University of Auckland.
Hayward, M.W., Whittaker, C.N., Lane, E.M., Power, W.L., Popinet, S., White, J.D.L., 2022. Multilayer modelling of waves generated by explosive subaqueous volcanism. Nat. Hazards Earth Syst. Sci. 22, 617–637. https://doi.org/10.5194/nhess-22-617-2022
Healy, J., Lloyd, E.F., Rishworth, D.E.H., Wood, C.P., Glover, R.B., Dibble, R.R., 1978. The eruption of Ruapehu, New Zealand on 22 June 1969. New Zealand Dept. of Sci. and Ind. Res. Bull. 224.
Heinrich, M., Cronin, S.J., Pardo, N., 2020. Understanding multi-vent Plinian eruptions at Mt. Tongariro Volcanic Complex, New Zealand. Bull Volcanol 82, 30. https://doi.org/10.1007/s00445-020-1369-7
Hodgson, K.A., 1993. Late quaternary lahars from Mount Ruapehu in the Whangaehu River, North Island, New Zealand : a thesis presented in partial fulfilment of the requirements for the degree of Doctor of Philosoophy in Soil Science at Massey University Doctor of Philosophy (Ph.D.).
Hodgson, K.A., Lecointre, J.A., Neall, V.E., 2007. Onetapu Formation: The last 2000 yr of laharic activity at Ruapehu volcano, New Zealand. null 50, 81–99. https://doi.org/10.1080/00288300709509823
Hodgson, K.A., Manville, V.R., 1999. Sedimentology and flow behavior of a rain-triggered lahar, Mangatoetoenui Stream, Ruapehu volcano, New Zealand. GSA Bulletin 111, 743–754. https://doi.org/10.1130/0016-7606(1999)111%3C0743:SAFBOA%3E2.3.CO;2
Houghton, B.F., Latter, J.H., Hackett, W.R., 1987. Volcanic hazard assessment for Ruapehu composite volcano, taupo volcanic zone, New Zealand. Bull Volcanol 49, 737–751. https://doi.org/10.1007/BF01079825
Houghton, B.F., Neall, V.E., Johnston, D.M., 1996. Eruption! Mount Ruapehu Awakes. Penguin Books (NZ), Auckland.
Hunt, G.R., 1977. SPECTRAL SIGNATURES OF PARTICULATE MINERALS IN THE VISIBLE AND NEAR INFRARED. GEOPHYSICS 42, 501–513. https://doi.org/10.1190/1.1440721
Hurst, T., 1981. Pattern recognition applied to temperature and chemical measurem ents of Crater Lake, Ruapehu. Wellington, New Zealand : Geophysics Division, Department of Scientific and Industrial Research, 1981.
Hurst, T., Smith, W., 2010. Volcanic ashfall in New Zealand – probabilistic hazard modelling for multiple sources. New Zealand Journal of Geology and Geophysics 53, 1–14. https://doi.org/10.1080/00288301003631129
Inoue, A., 1995. Formation of Clay Minerals in Hydrothermal Environments, in: Velde, B. (Ed.), Origin and Mineralogy of Clays. Springer Berlin Heidelberg, Berlin, Heidelberg, pp. 268–329. https://doi.org/10.1007/978-3-662-12648-6_7
Irwin, M.E., 2016. Mapping hydrothermal alteration products on Mt Tongariro using multispectral satellite data, XRD analysis and reflectance spectroscopy : a thesis

presented in partial fulfilment of the requirements for the degree of Masters of Science, at Massey University, Palmerston North, New Zealand. Massey University.
Janda, R., S., D., Reyes, P., Newhall, C., Pierson, T., Punongbayan, R., Rodolfo, K., Solidum, R., Umbal, J., 1996. Assessment and response to lahar hazard around Mount Pinatubo, 1991-1993.
Janda, R.J., Scott, K., Nolan, K.M., Martinson, H.A., 1981. Lahar movement, effects and deposits (around Mount St. Helens). U.S. Geological Survey Professional Paper 1250, 461–478.
John, D.A., Lee, R.G., Breit, G.N., Dilles, J.H., Calvert, A.T., Muffler, L.J.P., Clynne, M.A., 2019. Pleistocene hydrothermal activity on Brokeoff volcano and in the Maidu volcanic center, Lassen Peak area, northeast California: Evolution of magmatic-hydrothermal systems on stratovolcanoes. Geosphere 15, 946–982. https://doi.org/10.1130/GES02049.1
John, D.A., Sisson, T.W., Breit, G.N., Rye, R.O., Vallance, J.W., 2008. Characteristics, extent and origin of hydrothermal alteration at Mount Rainier Volcano, Cascades Arc, USA: Implications for debris-flow hazards and mineral deposits. Journal of Volcanology and Geothermal Research 175, 289–314. https://doi.org/10.1016/j.jvolgeores.2008.04.004
Johnston, D.M., Houghton, B.F., Neall, V.E., Ronan, K.R., Paton, D., 2000. Impacts of the 1945 and 1995–1996 Ruapehu eruptions, in: GSA Bull. An example of increasing societal vulnerability, New Zealand.
Jumadi, Heppenstall, A., Malleson, N., Carver, S., Quincey, D., Manville, V., 2018. Modelling Individual Evacuation Decisions during Natural Disasters: A Case Study of Volcanic Crisis in Merapi, Indonesia. Geosciences 8, 196. https://doi.org/10.3390/geosciences8060196
Kastl, B., Fagents, S., Houghton, B.F., 2010. Erosional and Depositional Processes of the 18 March 2007 Lahar at Mt. Ruapehu, New Zealand. AGU Fall Meeting Abstracts.
Kataoka, K., 2005. Distal fluvio-lacustrine volcaniclastic resedimentation in response to an explosive silicic eruption: The Pliocene Mushono tephra bed, central Japan. GSA Bulletin 117, 3–17. https://doi.org/10.1130/B25379.1
Kataoka, K.S., Matsumoto, T., Saito, T., Kawashima, K., Nagahashi, Y., Iyobe, T., Sasaki, A., Suzuki, K., 2018. Lahar characteristics as a function of triggering mechanism at a seasonally snow-clad volcano: contrasting lahars following the 2014 phreatic eruption of Ontake Volcano, Japan. Earth Planets Space 70, 113. https://doi.org/10.1186/s40623-018-0873-x
Keigler, R., Thouret, J.-C., Hodgson, K.A., Neall, V.E., Lecointre, J.A., Procter, J.N., Cronin, S.J., 2011. The Whangaehu Formation: Debris-avalanche and lahar deposits from ancestral Ruapehu volcano, New Zealand. Geomorphology 133, 57–79. https://doi.org/10.1016/j.geomorph.2011.06.019
Kereszturi, G., Schaefer, L., Mead, S., Miller, C., Procter, J., Kennedy, B., 2021. Synthesis of hydrothermal alteration, rock mechanics and geophysical mapping to constrain failure and debris avalanche hazards at Mt. Ruapehu (New Zealand). New Zealand Journal of Geology and Geophysics 64, 421–442. https://doi.org/10.1080/00288306.2021.1885048
Kereszturi, G., Schaefer, L.N., Miller, C., Mead, S., 2020. Hydrothermal Alteration on Composite Volcanoes: Mineralogy, Hyperspectral Imaging, and Aeromagnetic Study of Mt Ruapehu, New Zealand. Geochem Geophys Geosyst 21, e2020GC009270. https://doi.org/10.1029/2020GC009270
Kereszturi, G., Schaefer, L.N., Schleiffarth, W.K., Procter, J., Pullanagari, R.R., Mead, S., Kennedy, B., 2018. Integrating airborne hyperspectral imagery and LiDAR for volcano mapping and monitoring through image classification. International Journal of Applied Earth Observation and Geoinformation 73, 323–339. https://doi.org/10.1016/j.jag.2018.07.006

Keys, H., Green, P.M., 2010. Mitigation of volcanic risks at Mt Ruapehu, New Zealand. Proceedings of the Mountain Risks International Conference, Firenze, Italy, 24-26 November 2010 485–490.
Keys, H.J.R., 2007. Lahars of Ruapehu Volcano, New Zealand: risk mitigation. Annals of Glaciology 45, 155–162. https://doi.org/10.3189/172756407782282390
Keys, H.J.R., Green, P.M., Department of Conservation, Private Bag, Turangi, NZ, 2008. Ruapehu Lahar New Zealand 18 March 2007: Lessons for Hazard Assessment and Risk Mitigation 1995-2007. J. Disaster Res. 3, 284–296. https://doi.org/10.20965/jdr.2008.p0284
Khangaonkar, T., Mehaute, B.L., 1991. Original surface disturbances from wave records. Applied Ocean Research 13, 110–115. https://doi.org/10.1016/S0141-1187(05)80058-6
Kilgour, G., Manville, V.R., Della Pasqua, F., Graettinger, A., Hodgson, K.A., Jolly, G., 2010. The 25 September 2007 eruption of Mount Ruapehu, New Zealand: directed ballistics, surtseyan jets, and ice-slurry lahars. Journal of Volcanology and Geothermal Research 191, 1–14.
King, D.N., Clark, K., Chagué, C., Li, X., Lane, E., McFadgen, B.G., Hippolite, J., Meihana, P., Wilson, B., Dobson, J., Geiger, P., Robb, H., Hikuroa, D., Williams, S., Morgenstern, R., Scheele, F., 2023. Tsunami or storm deposit? A late Holocene sedimentary record from Swamp Bay, Rangitoto ki te Tonga/D'Urville Island, Aotearoa – New Zealand. New Zealand Journal of Geology and Geophysics 66, 629–645. https://doi.org/10.1080/00288306.2022.2087692
Kochel, R.C., Baker, V.R., 1982. Paleoflood Hydrology. Science 215, 353–361. https://doi.org/10.1126/science.215.4531.353
Lane, E., Borrero, J., Whittaker, C., Bind, J., Chagué, C., Goff, J., Goring, D., Hoyle, J., Mueller, C., Power, W., Reid, C., Williams, J., Williams, S., 2017. Effects of Inundation by the 14th November, 2016 Kaikōura Tsunami on Banks Peninsula, Canterbury, New Zealand. Pure and Applied Geophysics 174, 1–20. https://doi.org/10.1007/s00024-017-1534-x
Langridge, R., Ries, W., Litchfield, N., Villamor, P., Van Dissen, R., Barrell, D., Rattenbury, M., Heron, D., Haubrock, S., Townsend, D., Lee, J., Berryman, K., Nicol, A., Cox, S., Stirling, M., 2016. The New Zealand Active Faults Database. New Zealand Journal of Geology and Geophysics 59, 86–96. https://doi.org/10.1080/00288306.2015.1112818
Lavigne, F., Thouret, J.C., Voight, B., Suwa, H., Sumaryono, A., 2000. Lahars at Merapi volcano, Central Java: an overview. Journal of Volcanology and Geothermal Research 100, 423–456. https://doi.org/10.1016/S0377-0273(00)00150-5
Lecointre, J.A., Hodgson, K.A., Neall, V.E., Cronin, S.J., 2004a. Lahar-Triggering Mechanisms and Hazard at Ruapehu Volcano, New Zealand. Natural Hazards 31, 85–109. https://doi.org/10.1023/B:NHAZ.0000020256.16645.eb
Lecointre, J.A., Neall, V.E., Hodgson, K.A., 1999. Onetapu Lahars are a key to understanding the history of Crater Lake, Ruapehu, 2,000 14C years to the present. Geol. Soc. of New Zealand Misc. Publication 107A.
Lecointre, J.A., Neall, V.E., Palmer, A.S., 1998. Quaternary lahar stratigraphy of the western Ruapehu ring plain, New Zealand. null 41, 225–245. https://doi.org/10.1080/00288306.1998.9514807
Lecointre, J.A., Neall, V.E., Wallace, C.R., Prebble, W.M., 2002. The 55- to 60-ka Te Whaiau Formation: a catastrophic, avalanche-induced, cohesive debris-flow deposit from Proto-Tongariro Volcano, New Zealand. Bull Volcanol 63, 509–525. https://doi.org/10.1007/s004450100167
Lecointre, J.A., Neall, V.E., Wallace, R.C., Elliot, M.B., Sparks, R., 2004b. Late Quaternary evolution of the Rotoaira Basin, northern Tongariro ring plain, New Zealand. null 47, 549–565. https://doi.org/10.1080/00288306.2004.9515075

Lee, J., Irish, J.L., Weiss, R., 2021. Probabilistic Near-Field Tsunami Source and Tsunami Run-up Distribution Inferred From Tsunami Run-up Records in Northern Chile. JGR Oceans 126, e2021JC017289. https://doi.org/10.1029/2021JC017289

Lee, J.-W., Irish, J.L., Weiss, R., 2020. Rapid prediction of alongshore run-up distribution from near-field tsunamis. Nat Hazards 104, 1157–1180. https://doi.org/10.1007/s11069-020-04209-z

Leonard, G.S., Cole, R.P., Christenson, B.W., Conway, C.E., Cronin, S.J., Gamble, J.A., Hurst, T., Kennedy, B.M., Miller, C.A., Procter, J.N., Pure, L.R., Townsend, D.B., White, J.D.L., Wilson, C.J.N., 2021. Ruapehu and Tongariro stratovolcanoes: a review of current understanding. New Zealand Journal of Geology and Geophysics 64, 389–420. https://doi.org/10.1080/00288306.2021.1909080

Lipman, P.W., 1976. Caldera-collapse breccias in the western San Juan Mountains, Colorado. GSA Bulletin 87, 1397–1410. https://doi.org/10.1130/0016-7606(1976)87%3C1397:CBITWS%3E2.0.CO;2

Loughlin, S.C., Sparks, S., Brown, S.K., Jenkins, S.F., Vye-Brown, C. (Eds.), 2015. Global Volcanic Hazards and Risk, 1st ed. Cambridge University Press. https://doi.org/10.1017/CBO9781316276273

Lowe, D., Percival, H.J., 1993. Clay mineralogy of tephras and associated paleosols and soils, and hydrothermal deposits, North Island [New Zealand].

Lube, G., Cronin, S.J., Manville, V.R., Procter, J.N., Cole, S.E., Freundt, A., 2012. Energy growth in laharic mass flows. Geology 40, 475–478. https://doi.org/10.1130/G32818.1

Lube, G., Cronin, S.J., Procter, J.N., 2009. Explaining the extreme mobility of volcanic ice-slurry flows, Ruapehu volcano, New Zealand. Geology 37, 15–18. https://doi.org/10.1130/G25352A.1

Maghsoudi Moud, F., Deon, F., Van Der Meijde, M., Van Ruitenbeek, F., Hewson, R., 2021. Mineral Interpretation Discrepancies Identified between Infrared Reflectance Spectra and X-ray Diffractograms. Sensors 21, 6924. https://doi.org/10.3390/s21206924

Major, J.J., Newhall, C.G., 1989. Snow and ice perturbation during historical volcanic eruptions and the formation of lahars and floods: A global review. Bull Volcanol 52, 1–27. https://doi.org/10.1007/BF00641384

Manville, V., 2015. Volcano-Hydrologic Hazards from Volcanic Lakes, in: Rouwet, D., Christenson, B., Tassi, F., Vandemeulebrouck, J. (Eds.), Volcanic Lakes, Advances in Volcanology. Springer Berlin Heidelberg, Berlin, Heidelberg, pp. 21–71. https://doi.org/10.1007/978-3-642-36833-2_2

Manville, V., 2002. Sedimentary and Geomorphic Responses to Ignimbrite Emplacement: Readjustment of the Waikato River after the a.d. 181 Taupo Eruption, New Zealand. The Journal of Geology 110, 519–541. https://doi.org/10.1086/341596

Manville, V., 2001. Techniques for evaluating the size of potential dam-break floods from natural dams. Institute of Geological & Nuclear Sciences, Lower Hutt, N.Z.

Manville, V., Cronin, S.J., 2007. Breakout Lahar from New Zealand's Crater Lake. Eos, Transactions American Geophysical Union 88, 441–442. https://doi.org/10.1029/2007EO430001

Manville, V., Hodgson, K.A., 2011. Paleohydrology of Volcanogenic Lake Break-Out Floods in the Taupo Volcanic Zone, New Zealand, in: Evans, S.G., Hermanns, R.L., Strom, A., Scarascia-Mugnozza, G. (Eds.), Natural and Artificial Rockslide Dams, Lecture Notes in Earth Sciences. Springer Berlin Heidelberg, Berlin, Heidelberg, pp. 519–541. https://doi.org/10.1007/978-3-642-04764-0_21

Manville, V., Hodgson, K.A., Houghton, B.F., Keys, J.R. (H.), White, J.D.L., 2000. Tephra, snow and water: complex sedimentary responses at an active snow-capped stratovolcano, Ruapehu, New Zealand. Bulletin of Volcanology 62, 278–293. https://doi.org/10.1007/s004450000096

Manville, V., Hodgson, K.A., Nairn, I.A., 2007. A review of break-out floods from volcanogenic lakes in New Zealand. New Zealand Journal of Geology and Geophysics 50, 131–150. https://doi.org/10.1080/00288300709509826
Manville, V., Newton, E.H., White, J.D.L., 2005. Fluvial responses to volcanism: resedimentation of the 1800a Taupo ignimbrite eruption in the Rangitaiki River catchment, North Island, New Zealand. Geomorphology 65, 49–70. https://doi.org/10.1016/j.geomorph.2004.07.007
Manville, V.R., 2004. Palaeohydraulic analysis of the 1953 Tangiwai lahar; New Zealand's worst volcanic disaster. Palaeohydraulic Analysis of the 1953 Tangiwai Lahar; New Zealand's Worst Volcanic Disaster 1000–1015.
Manville, V.R., Hodgson, K.A., White, J.D.L., 1998. Rheological properties of a remobilised-tephra lahar associated with the 1995 eruptions of Ruapehu volcano, New Zealand. null 41, 157–164. https://doi.org/10.1080/00288306.1998.9514800
Manville, V.R., Major, J.J., Fagents, S.A., 2013. Modeling lahar behavior and hazards, in: Modeling Volcanic Processes: The Physics and Mathematics of Volcanism. Cambridge University Press, Cambridge, pp. 300–330. https://doi.org/10.1017/CBO9781139021562.014
Mars, J.C., Hubbard, B.E., Pieri, D., Linick, J., 2015. Alteration, slope-classified alteration, and potential lahar inundation maps of volcanoes for the Advanced Spaceborne Thermal Emission and Reflection Radiometer (ASTER) Volcano Archive (Report No. 2015–5035), Scientific Investigations Report. Reston, VA. https://doi.org/10.3133/sir20155035
Massey, C.I., Manville, V., Hancox, G.H., Keys, H.J., Lawrence, C., McSaveney, M., 2010. Out-burst flood (lahar) triggered by retrogressive landsliding, 18 March 2007 at Mt Ruapehu, New Zealand—a successful early warning. Landslides 7, 303–315. https://doi.org/10.1007/s10346-009-0180-5
Mastin, L.G., Witter, J.B., 2000. The hazards of eruptions through lakes and seawater. Journal of Volcanology and Geothermal Research 97, 195–214. https://doi.org/10.1016/S0377-0273(99)00174-2
McArthur, J.L., Shepherd, M.J., 1990. Late Quaternary glaciation of Mt Ruapehu, North Island, New Zealand. Journal of the Royal Society of New Zealand 20, 287–296. https://doi.org/10.1080/03036758.1990.10416823
Mead, S.R., Magill, C.R., 2017. Probabilistic hazard modelling of rain-triggered lahars. Journal of Applied Volcanology 6, 8. https://doi.org/10.1186/s13617-017-0060-y
Mead, S.R., Magill, C.R., Hilton, J., 2016. Rain-triggered lahar susceptibility using a shallow landslide and surface erosion model. Geomorphology 273, 168–177. https://doi.org/10.1016/j.geomorph.2016.08.022
Mead, S.R., Procter, J.N., Bebbington, M.S., 2021. Ruapehu Volcano Lahar hazard assessment.
Mehaute, B.L., Wang, S., 1996. Water Waves Generated by Underwater Explosions (No. DNA-TR-94-128). Defense Nuclear Agency, Alexandria, VA.
Miall, A.D., 1977. A review of the braided-river depositional environment. Earth-Science Reviews 13, 1–62. https://doi.org/10.1016/0012-8252(77)90055-1
Miller, C.A., Schaefer, L.N., Kereszturi, G., Fournier, D., 2020. Three-Dimensional Mapping of Mt. Ruapehu Volcano, New Zealand, From Aeromagnetic Data Inversion and Hyperspectral Imaging. JGR Solid Earth 125, e2019JB018247. https://doi.org/10.1029/2019JB018247
Minami, Y., 2024. Geological and geomorphological characteristics of a crater lake breakout lahar at Akita-Yakeyama Volcano, NE Japan. https://doi.org/10.21203/rs.3.rs-4203702/v1
Minami Y., Ohba T., Hayashi S., Kataoka K.S., 2015. Depositional processes and temporal component-change of lahar deposits at the northern foot of Chokai volcano, NE Japan. https://doi.org/10.18940/kazan.60.1_1

Minami, Y., Ohba, T., Hayashi, S., Saito-Kokubu, Y., Kataoka, K.S., 2019. Lahar record during the last 2500 years, Chokai Volcano, northeast Japan: Flow behavior, sourced volcanic activity, and hazard implications. Journal of Volcanology and Geothermal Research 387, 106661. https://doi.org/10.1016/j.jvolgeores.2019.106661

Moebis, A., 2010. Understanding the Holocene explosive eruption record of the Tongariro Volcanic Centre, New Zealand : a thesis presented in partial fulfilment of the requirements for the degree of Doctor of Philosophy in Earth Science at Massey University, Palmerston North, New Zealand (Doctoral). Massey University.

Moebis, A., Cronin, S.J., Neall, V.E., Smith, I.E., 2011. Unravelling a complex volcanic history from fine-grained, intricate Holocene ash sequences at the Tongariro Volcanic Centre, New Zealand. Quaternary International 246, 352–363. https://doi.org/10.1016/j.quaint.2011.05.035

Montgomery, R.L., Keys, J.R., New Zealand, Department of Conservation, 1993. Volcanic hazard management in Tongariro National Park. Head Office, Dept of Conservation, Wellington, N.Z.

Moore, J.G., Nakamura, K., Alcaraz, A., 1966. The 1965 Eruption of Taal Volcano: Catastrophic explosions are caused by lake water entering a volcanic conduit. Science 151, 955–960. https://doi.org/10.1126/science.151.3713.955

Morrissey, M., Gisler, G., Weaver, R., Gittings, M., 2010. Numerical model of crater lake eruptions. Bull Volcanol 72, 1169–1178. https://doi.org/10.1007/s00445-010-0392-5

Mothes, P.A., Hall, M.L., Janda, R.J., 1998. The enormous Chillos Valley Lahar: an ash-flow-generated debris flow from Cotopaxi Volcano, Ecuador. Bulletin of Volcanology 59, 233–244. https://doi.org/10.1007/s004450050188

Mothes, P.A., Vallance, J.W., 2015. Lahars at Cotopaxi and Tungurahua Volcanoes, Ecuador, in: Volcanic Hazards, Risks and Disasters. Elsevier, pp. 141–168. https://doi.org/10.1016/B978-0-12-396453-3.00006-X

Mulder, V.L., Plötze, M., De Bruin, S., Schaepman, M.E., Mavris, C., Kokaly, R.F., Egli, M., 2013. Quantifying mineral abundances of complex mixtures by coupling spectral deconvolution of SWIR spectra (2.1–2.4 μm) and regression tree analysis. Geoderma 207–208, 279–290. https://doi.org/10.1016/j.geoderma.2013.05.011

Müller, K., Schwalb-Willmann, J., Wegmann, M., Leutner, B., 2025. RStoolbox: An R package for remote sensing data analysis. Methods Ecol Evol 16, 486–495. https://doi.org/10.1111/2041-210X.14451

Mullineaux, D.R., 1974. Pumice and other pyroclastic deposits in Mount Rainier National Park, Washington (USGS Numbered Series), Bulletin. https://doi.org/10.3133/b1326

Muravyev, Y., Fedotov, S., Budnikov, V., 1997. Activity in the Karymsky Center in 1996: summit eruption at Karymsky and phreatomagmatic eruption in the Akademii Nauk. Vulcanologiya i Seismologiya [Volcanology and Seismology] 5, 38–71.

Nairn, I.A., Wood, C.P., Hewson, C.A.Y., 1979. Phreatic eruptions of Ruapehu: April 1975. New Zealand J. Geol. and Geophys. 22.

Naranjo, J., Moreno Roa, H., 2004. Laharic debris-flows from Villarrica Volcano. IAVCEI 2004. Naranjo, J.A., Moreno Roa, H. Servicio Nacional de Geología y Minería, Boletín No. 61. Special Publications of IAVCEI Boletín No 61, 28–38.

Neall, V.E., 1976. Lahars as major geological hazards. Bulletin of the International Association of Engineering Geology 13, 233–240. https://doi.org/10.1007/BF02634799

Neall, V.E., Cronin, S.J., Donoghue, S.L., Hodgson, K.A., Lecointre, J.A., Palmer, A.S., Procter, J.N., Purves, A.M., Stewart, R.B., 2004. Lahar Hazards map for Ruapehu Volcano. Soil and Earth Sciences Occasional Publication No. 3.

Neall, V.E., Houghton, B.F., Cronin, S.J., Donoghue, S.L., Hodgson, K.A., Johnston, D.M., Lecointre, J.A., Mitchell, A.R., 1999. Volcanic hazards at Ruapehu. Ministry of Civil Defence. Volcanic Hazards Information Series 8.

Nemec, W., 2009. What is a hyperconcentrated flow?
Newhall, C.G., Punongbayan, R. (Eds.), 1996. Fire and mud: eruptions and lahars of Mount Pinatubo, Philippines. Philippine Institute of Volcanology and Seismology ; University of Washington Press, Quezon City : Seattle.
Nolan, E., 2008. Relative age dating of the Wahianoa moraines, Mount Ruapehu, New Zealand : thesis submitted in partial fulfilment of the degree of Master of Science in Quaternary Science at Massey University, Palmerston North, New Zealand.
O'Connor, J.E., Clague, J.J., Walder, J.S., Manville, V., Beebee, R.A., 2022. Outburst Floods, in: Treatise on Geomorphology. Elsevier, pp. 765–819. https://doi.org/10.1016/B978-0-12-818234-5.00007-9
O'Shea, B., 1954. Ruapehu and the Tangiwai disaster. New Zealand Journal of Science and Technology B 36, 174–189.
Paguican, E.M.R., Lagmay, A.M.F., Rodolfo, K.S., Rodolfo, R.S., Tengonciang, A.M.P., Lapus, M.R., Baliatan, E.G., Obille, E.C., 2009. Extreme rainfall-induced lahars and dike breaching, 30 November 2006, Mayon Volcano, Philippines. Bull Volcanol 71, 845–857. https://doi.org/10.1007/s00445-009-0268-8
Pallister, J., Papale, P., Eichelberger, J., Newhall, C., Mandeville, C., Nakada, S., Marzocchi, W., Loughlin, S., Jolly, G., Ewert, J., Selva, J., 2019. Volcano observatory best practices (VOBP) workshops - a summary of findings and best-practice recommendations. J Appl. Volcanol. 8, 2. https://doi.org/10.1186/s13617-019-0082-8
Palmer, B.A., 1991. Holocene lahar deposits in the Whakapapa catchment, northwestern ring plain, Ruapehu volcano (North Island, New Zealand). null 34, 177–190. https://doi.org/10.1080/00288306.1991.9514455
Palmer, B.A., Neall, V.E., 1991a. Contrasting lithofacies architecture in ring-plain deposits related to edifice construction and destruction, the Quaternary Stratford and Opunake Formations, Egmont Volcano, New Zealand. Sedimentary Geology 74, 71–88. https://doi.org/10.1016/0037-0738(91)90035-C
Palmer, B.A., Neall, V.E., 1991b. Contrasting lithofacies architecture in ring-plain deposits related to edifice construction and destruction, the Quaternary Stratford and Opunake Formations, Egmont Volcano, New Zealand. Sedimentary Geology 74, 71–88. https://doi.org/10.1016/0037-0738(91)90035-C
Palmer, B.A., Neall, V.E., 1989. The Murimotu Formation—9500 year old deposits of a debris avalanche and associated lahars, Mount Ruapehu, North Island, New Zealand. null 32, 477–486. https://doi.org/10.1080/00288306.1989.10427555
Palmer, B.A., Purves, A.M., Donoghue, S.L., 1993. Controls on accumulation of a volcaniclastic fan, Ruapehu composite volcano, New Zealand. Bulletin of Volcanology 55, 176–189. https://doi.org/10.1007/BF00301515
Pardo, N., 2012. Andesitic Plinian eruptions at Mt. Ruapehu (New Zealand) : from lithofacies to eruption dynamics : a thesis presented in partial fulfilment of the requirements for the degree of Doctor of Philosophy in Earth Science at Massey University, (Palmerston North, Manawatu), New Zealand (Doctoral). Massey University.
Pardo, N., Cronin, S.J., Palmer, A., Procter, J., Smith, I., 2012a. Andesitic Plinian eruptions at Mt. Ruapehu: quantifying the uppermost limits of eruptive parameters. Bull Volcanol 74, 1161–1185. https://doi.org/10.1007/s00445-012-0588-y
Pardo, N., Cronin, S.J., Palmer, A.S., Németh, K., 2012b. Reconstructing the largest explosive eruptions of Mt. Ruapehu, New Zealand: lithostratigraphic tools to understand subplinian–plinian eruptions at andesitic volcanoes. Bulletin of Volcanology 74, 617–640. https://doi.org/10.1007/s00445-011-0555-z
Paris, A., Heinrich, P., Paris, R., Abadie, S., 2020. The December 22, 2018 Anak Krakatau, Indonesia, Landslide and Tsunami: Preliminary Modeling Results. Pure Appl. Geophys. 177, 571–590. https://doi.org/10.1007/s00024-019-02394-y

Paris, R., Ulvrova, M., 2019. Tsunamis generated by subaqueous volcanic explosions in Taal Caldera Lake, Philippines. Bull Volcanol 81, 14. https://doi.org/10.1007/s00445-019-1272-2
Paris, R., Ulvrova, M., Selva, J., Brizuela, B., Costa, A., Grezio, A., Lorito, S., Tonini, R., 2019. Probabilistic hazard analysis for tsunamis generated by subaqueous volcanic explosions in the Campi Flegrei caldera, Italy. Journal of Volcanology and Geothermal Research 379, 106–116. https://doi.org/10.1016/j.jvolgeores.2019.05.010
Pasternack, G.B., Varekamp, J.C., 1997. Volcanic lake systematics I. Physical constraints. Bulletin of Volcanology 58, 528–538. https://doi.org/10.1007/s004450050160
Paterson, B.R., 1980. The Hazard of Lahars to the Tongariro Power Development, New Zealand. Presented at the Third Australia - New Zealand Conference on Geomechanics, Department of Scientific and Industrial Research, Wellington, N.Z.
Phillips, E., 2011. Forecasting the consequences of the failure of the eastern rim of Crater Lake, Mount Ruapehu: a thesis presented in partial fulfilment of the requirements for the degree of Master of Science in Earth Science at Massey University, Palmerston North, New Zealand.
Pierson, T.C., 2005a. Distinguishing between debris flows and floods from field evidence in small watersheds (No. 2327–6932). US Geological Survey.
Pierson, T.C., 2005b. Hyperconcentrated flow — transitional process between water flow and debris flow, in: Jakob, M., Hungr, O. (Eds.), Debris-Flow Hazards and Related Phenomena. Springer Berlin Heidelberg, Berlin, Heidelberg, pp. 159–202. https://doi.org/10.1007/3-540-27129-5_8
Pierson, T.C., 1980. Erosion and deposition by debris flows at Mt Thomas, North Canterbury, New Zealand. Earth Surface Processes 5, 227–247. https://doi.org/10.1002/esp.3760050302
Pierson, T.C., Daag, A.S., Reyes, P.J.D., Regalado, M.T.M., Solidum, R.U., Tubianosa, B.S., 1996. Flow and Deposition of Posteruption Hot Lahars on the East Side of Mount Pinatubo, July–October 1991, in: Newhall, C.G., Punongbayan, R.S. (Eds.), Fire and Mud: Eruptions and Lahars of Mount Pinatubo, Philippines. University of Washington Press in association with the Philippine Institute of Volcanology and Seismology, Seattle, pp. 921–950.
Pierson, T.C., Janda, R.J., Thouret, J.-C., Borrero, C.A., 1990. Perturbation and melting of snow and ice by the 13 November 1985 eruption of Nevado del Ruiz, Colombia, and consequent mobilization, flow and deposition of lahars. Journal of Volcanology and Geothermal Research 41, 17–66. https://doi.org/10.1016/0377-0273(90)90082-Q
Pierson, T.C., Scott, K.M., 1985. Downstream Dilution of a Lahar: Transition From Debris Flow to Hyperconcentrated Streamflow. Water Resources Research 21, 1511–1524. https://doi.org/10.1029/WR021i010p01511
Pierson, T.C., Siebert, L., Scott, K.M., 2025. Deposits of Volcanic Wet Flows: Identifying Deposits of Lahars, Debris Avalanches, and Water Floods in Volcanic Terrain, Advances in Volcanology. Springer Nature Switzerland, Cham. https://doi.org/10.1007/978-3-031-66574-5
Pirrie, D., Dawson, L., Graham, G., 2017. Predictive geolocation: forensic soil analysis for provenance determination. Episodes 40, 141–147. https://doi.org/10.18814/epiiugs/2017/v40i2/017016
Pirrung, M., Büchel, G., Lorenz, V., Treutler, H.-C., 2008. Post-eruptive development of the Ukinrek East Maar since its eruption in 1977 A.D. in the periglacial area of south-west Alaska. Sedimentology 55, 305–334. https://doi.org/10.1111/j.1365-3091.2007.00900.x
Ponomareva, V.V., Pevzner, M.M., Melekestsev, I.V., 1998. Large debris avalanches and associated eruptions in the Holocene eruptive history of Shiveluch Volcano,

Kamchatka, Russia. Bulletin of Volcanology 59, 490–505. https://doi.org/10.1007/s004450050206
Popinet, S., 2018. Basilisk, a free-software program for the solution of partial differential equations on adaptive cartesian meshes. URL http://basilisk
Popinet, S., 2012. Adaptive modelling of long-distance wave propagation and fine-scale flooding during the Tohoku tsunami. Nat. Hazards Earth Syst. Sci. 12, 1213–1227. https://doi.org/10.5194/nhess-12-1213-2012
Popinet, S., 2011. Quadtree-adaptive tsunami modelling. Ocean Dynamics 61, 1261–1285. https://doi.org/10.1007/s10236-011-0438-z
Procter, J.N., Cronin, S.J., Fuller, I.C., Lube, G., Manville, V.R., 2010a. Quantifying the geomorphic impacts of a lake-breakout lahar, Mount Ruapehu, New Zealand. Geology 38, 67–70. https://doi.org/10.1130/G30129.1
Procter, J.N., Cronin, S.J., Fuller, I.C., Sheridan, M., Neall, V.E., Keys, H.J.R., 2010b. Lahar hazard assessment using Titan2D for an alluvial fan with rapidly changing geomorphology: Whangaehu River, Mt. Ruapehu. Geomorphology 116, 162–174. https://doi.org/10.1016/j.geomorph.2009.10.016
Procter, J.N., Cronin, S.J., Sheridan, M.F., 2012. Evaluation of Titan2D modelling forecasts for the 2007 Crater Lake break-out lahar, Mt. Ruapehu, New Zealand. Geomorphology 136, 95–105. https://doi.org/10.1016/j.geomorph.2011.05.001
Procter, J.N., Zernack, A.V., Cronin, S.J., Singh, E., 2018. A complex interplay of sediment erosion and deposition during the 18 March 2007 crater-lake breakout lahar at Mt. Ruapehu, New Zealand. Presented at the EGU General Assembly Conference Abstracts, p. 19225.
Procter, J.N., Zernack, A.V., Mead, S.R., Morgan, M., Cronin, S.J., 2021. A review of lahars; past deposits, historic events and present-day simulations from Mt. Ruapehu and Mt. Taranaki, New Zealand. New Zealand Journal of Geology and Geophysics 64, 479–503. https://doi.org/10.1080/00288306.2020.1824999
Pure, L., 2020. The volcanic and magmatic evolution of Tongariro volcano, New Zealand. Open Access Te Herenga Waka-Victoria University of Wellington. https://doi.org/10.26686/wgtn.17145692
Purves, A., 1990. Landscape ecology of the Rangipo Desert. Unpublished M. Sc. thesis, lodged in the Library, Massey University, Palmerston North, New Zealand.
Rasmussen, C., Matsuyama, N., Dahlgren, R.A., Southard, R.J., Brauer, N., 2007. Soil Genesis and Mineral Transformation Across an Environmental Gradient on Andesitic Lahar. Soil Science Soc of Amer J 71, 225–237. https://doi.org/10.2136/sssaj2006.0100
Regassa, A., Van Daele, K., De Paepe, P., Dumon, M., Deckers, J., Asrat, A., Van Ranst, E., 2014. Characterizing weathering intensity and trends of geological materials in the Gilgel Gibe catchment, southwestern Ethiopia. Journal of African Earth Sciences 99, 568–580. https://doi.org/10.1016/j.jafrearsci.2014.05.012
Reverend Richard Taylor, 1861. Journal of Rev. Richard Taylor 1833–1873.
Rodolfo, K.S., 1989. Origin and early evolution of lahar channel at Mabinit, Mayon Volcano, Philippines. GSA Bulletin 101, 414–426. https://doi.org/10.1130/0016-7606(1989)101%3C0414:OAEEOL%3E2.3.CO;2
Rosenberg, M.D., 2000. The Whakapapaiti lahar: a snow-rich debris flow from the 23rd September 1995 eruption of Mt Ruapehu. Institute of Geological & Nuclear Sciences.
Rossel, R.A.V., Chen, C., 2011. Digitally mapping the information content of visible–near infrared spectra of surficial Australian soils. Remote Sensing of Environment 115, 1443–1455. https://doi.org/10.1016/j.rse.2011.02.004
Roudier, P., 2015. asdreader: Reading ASD Binary Files in R. https://doi.org/10.32614/CRAN.package.asdreader

Rougier, J., Sparks, S.R., Cashman, K.V., 2016. Global recording rates for large eruptions. J Appl. Volcanol. 5, 11. https://doi.org/10.1186/s13617-016-0051-4
Rowe, G.L., Brantley, S.L., Fernandez, M., Fernandez, J.F., Borgia, A., Barquero, J., 1992. Fluid-volcano interaction in an active stratovolcano: the crater lake system of Poás volcano, Costa Rica. Journal of Volcanology and Geothermal Research 49, 23–51. https://doi.org/10.1016/0377-0273(92)90003-V
Rowland, J.V., Wilson, C.J.N., Gravley, D.M., 2010. Spatial and temporal variations in magma-assisted rifting, Taupo Volcanic Zone, New Zealand. Journal of Volcanology and Geothermal Research 190, 89–108. https://doi.org/10.1016/j.jvolgeores.2009.05.004
Savitri, K.P., Hecker, C., Van Der Meer, F.D., Sidik, R.P., 2021. VNIR-SWIR infrared (imaging) spectroscopy for geothermal exploration: Current status and future directions. Geothermics 96, 102178. https://doi.org/10.1016/j.geothermics.2021.102178
Schaefer, L.N., Kennedy, B.M., Villeneuve, M.C., Cook, S.C.W., Jolly, A.D., Keys, H.J.R., Leonard, G.S., 2018. Stability assessment of the Crater Lake/Te Wai-ā-moe overflow channel at Mt. Ruapehu (New Zealand), and implications for volcanic lake break-out triggers. Journal of Volcanology and Geothermal Research 358, 31–44. https://doi.org/10.1016/j.jvolgeores.2018.06.011
Schaefer, L.N., Kereszturi, G., Kennedy, B.M., Villeneuve, M., 2023. Characterizing lithological, weathering, and hydrothermal alteration influences on volcanic rock properties via spectroscopy and laboratory testing: a case study of Mount Ruapehu volcano, New Zealand. Bull Volcanol 85, 43. https://doi.org/10.1007/s00445-023-01657-w
Scott, B., 2013. A revised catalogue of Ruapehu volcano eruptive activity: 1830-2012. GNS Science.
Scott, B.J., Sherburn, S., 2003. Volcano and geothermal observations 1996 (science report No. 2003/27), New Zealand Volcanological Record 25. Institute of Geological & Nuclear Sciences.
Scott, K.M., 1988. Origins, behavior, and sedimentology of lahars and lahar-runout flows in the Toutle-Cowlitz River system (No. 2330–7102).
Scott, K.M., Vallance, J.W., Kerle, N., Luis Macías, J., Strauch, W., Devoli, G., 2005. Catastrophic precipitation-triggered lahar at Casita volcano, Nicaragua: occurrence, bulking and transformation. Earth Surface Processes and Landforms 30, 59–79. https://doi.org/10.1002/esp.1127
Scott, K.M., Vallance, J.W., Pringle, P.T., 1995. Sedimentology, Behavior, and Hazards of Debris Flows at Mount Rainier, Washington (Report No. 1547), Professional Paper. https://doi.org/10.3133/pp1547
Scrivenor, J.B., 1929. The Mudstreams ("Lahars") of Gunong Keloet in Java. Geological Magazine 66, 433–434. https://doi.org/10.1017/S0016756800102304
Segschneider, B., Landis, C.A., Manville, V., White, J.D.L., Wilson, C.J.N., 2002. Environmental response to a large, explosive rhyolite eruption: sedimentology of post-1.8 ka pumice-rich Taupo volcaniclastics in the Hawke's Bay region, New Zealand. Sedimentary Geology 150, 275–299. https://doi.org/10.1016/S0037-0738(01)00200-7
Sherburn, S., Bryan, C.J., 1999. The Eruption Detection System: Mt. Ruapehu, New Zealand. Seismological Research Letters 70, 505–511. https://doi.org/10.1785/gssrl.70.5.505
Sherburn, S., Bryan, C.J., Hurst, A.W., Latter, J.H., Scott, B.J., 1999. Seismicity of Ruapehu volcano, New Zealand, 1971–1996: a review. Journal of Volcanology and Geothermal Research 88, 255–278. https://doi.org/10.1016/S0377-0273(99)00014-1
Shultz, A.W., 1984. Subaerial Debris-Flow Deposition in the Upper Paleozoic Cutler Formation, Western Colorado. SEPM JSR Vol. 54. https://doi.org/10.1306/212F84EF-2B24-11D7-8648000102C1865D
Siebert, L., Glicken, H., Ui, T., 1987. Volcanic hazards from Bezymianny- and Bandai-type eruptions. Bull Volcanol 49, 435–459. https://doi.org/10.1007/BF01046635

Siebert, L., Kimberly, P., Simkin, T., 2011. Volcanoes of the World: Third Edition. University of California Press, Berkeley, CA. https://doi.org/10.1525/9780520947931
Smith, G.A., 1988. Sedimentology of proximal to distal volcaniclastics dispersed across an active foldbelt: Ellensburg Formation (late Miocene), central Washington. Sedimentology 35, 953–977. https://doi.org/10.1111/j.1365-3091.1988.tb01740.x
Smith, G.A., Fritz, W.J., 1989. Volcanic influences on terrestrial sedimentation. Geology 17, 375–376. https://doi.org/10.1130/0091-7613(1989)017%3C0375:VIOTS%3E2.3.CO;2
Smith, G.A., Lowe, D.R., 1991. LAHARS: VOLCANO-HYDROLOGIC EVENTS AND DEPOSITION IN THE DEBRIS FLOW—HYPERCONCENTRATED FLOW CONTINUUM. Sedimentation in Volcanic Settings 59–70. https://doi.org/10.2110/pec.91.45.0059
Stern, T.A., Stratford, W.R., Salmon, M.L., 2006. Subduction evolution and mantle dynamics at a continental margin: Central North Island, New Zealand. Rev. Geophys. 44, RG4002. https://doi.org/10.1029/2005RG000171
Stevens, A., Ramirez-Lopez, L., 2013. prospectr: Miscellaneous Functions for Processing and Sample Selection of Spectroscopic Data. https://doi.org/10.32614/CRAN.package.prospectr
Stilwell, W., Hopkins, H., Appleton, W., 1954. Tangiwai railway disaster: report of board of inquiry. Wellington, NZ.
Suryaningtyas, D.T., 1998. Characteristics of volcanic ash soils of southern area of Mount Ruapehu, North Island, New Zealand : a thesis presented in partial fulfilment of the requirements for the degree of Master of Applied Science in Soil Science at Massey University (Masters). Massey University.
Suryo, I., Clarke, M.C.G., 1985. The occurrence and mitigation of volcanic hazards in Indonesia as exemplified at the Mount Merapi, Mount Kelut and Mount Galunggung volcanoes. QJEGH 18, 79–98. https://doi.org/10.1144/GSL.QJEG.1985.018.01.09
Taig, T., 2002. Ruapehu Lahar Residual Risk Assessment. Ministry of Civil Defence & Emergency Management.
Thompson, A.J.B., Hauff, P.L., Robitaille, A.J., 1999. Alteration Mapping in Exploration: Application of Short-Wave Infrared (SWIR) Spectroscopy. SEG Discovery 1–27. https://doi.org/10.5382/SEGnews.1999-39.fea
Thouret, J.-C., Abdurachman, K.E., Bourdier, J.-L., Bronto, S., 1998. Origin, characteristics, and behaviour of lahars following the 1990 eruption of Kelud volcano, eastern Java (Indonesia). Bulletin of Volcanology 59, 460–480. https://doi.org/10.1007/s004450050204
Tighe, M., Forster, N., Guppy, C., Savage, D., Grave, P., Young, I.M., 2018. Georeferenced soil provenancing with digital signatures. Sci Rep 8, 3162. https://doi.org/10.1038/s41598-018-21530-7
Tongariro District Office, 2023. DOC-1130183: Guidelines for DOC volcanic risk management in Tongariro National Park.
Topping, W.W., 1974. Some Aspects of Quaternary History of Tongariro Volcanic Centre. Open Access Te Herenga Waka-Victoria University of Wellington. https://doi.org/10.26686/wgtn.19252133
Topping, W.W., 1973. Tephrostratigraphy and chronology of late quaternary eruptives from the Tongariro Volcanic Centre, New Zealand. null 16, 397–423. https://doi.org/10.1080/00288306.1973.10431368
Tuñgol, N.M., 2002. Lahar Initiation and Sediment Yield in the Pasig-Potrero River Basin, Mount Pinatubo, Philippines (PhD). University of Canterbury, Christchurch, New Zealand.
Tuñgol, N.M., Regalado, M.T.M., 1996. Rainfall, acoustic flow monitor records, and observed lahars of the Sacobia River in 1992, in: Newhall, C.G., Punongbayan, R.S. (Eds.), Fire and Mud: Eruptions and Lahars of Mount Pinatubo, Philippines. Philippine Institute of Volcanology and Seismology & University of Washington Press, Quezon City / Seattle.

Ulvrová, M., Paris, R., Kelfoun, K., Nomikou, P., 2014. Numerical simulations of tsunamis generated by underwater volcanic explosions at Karymskoye lake (Kamchatka, Russia) and Kolumbo volcano (Aegean Sea, Greece). Nat. Hazards Earth Syst. Sci. 14, 401–412. https://doi.org/10.5194/nhess-14-401-2014

Umbal, J., Rodolfo, K., 1996. The 1991 Lahars of Southwestern Mount Pinatubo and Evolution of the Lahar-Dammed Mapanuepe Lake. pp. 951–970.

Umbal, J.V., Rodolfo, K.S., 1996. The 1991 lahars of southwestern Mount Pinatubo and evolution of the lahar-dammed Mapanuepe Lake, in: Newhall, C.G., Punongbayan, R.S. (Eds.), Fire and Mud: Eruptions and Lahars of Mount Pinatubo, Philippines. Philippine Institute of Volcanology and Seismology & University of Washington Press, Quezon City / Seattle.

U.S. Geological Survey, 2006. FGDC Digital Cartographic Standard for Geologic Map Symbolization (PostScript Implementation), U.S. Geological Survey Techniques and Methods 11-A2.

Vallance, J.W., 2005. Volcanic debris flows, in: Jakob, M., Hungr, O. (Eds.), Debris-Flow Hazards and Related Phenomena. Springer Berlin Heidelberg, Berlin, Heidelberg, pp. 247–274. https://doi.org/10.1007/3-540-27129-5_10

Vallance, J.W., 2000. Lahars, in: Sigurdsson, H., Houghton, B.F., McNutt, S.R., Rymer, H., Styx, J. (Eds.), Encyclopedia of Volcanoes. Academic Press, San Diego.

Vallance, J.W., Iverson, R.M., 2015. Lahars and Their Deposits, in: The Encyclopedia of Volcanoes. Elsevier, pp. 649–664. https://doi.org/10.1016/B978-0-12-385938-9.00037-7

Vallance, J.W., Scott, K.M., 1997. The Osceola Mudflow from Mount Rainier: Sedimentology and hazard implications of a huge clay-rich debris flow. GSA Bulletin 109, 143–163. https://doi.org/10.1130/0016-7606(1997)109%3C0143:TOMFMR%3E2.3.CO;2

Van Daele, M., Moernaut, J., Silversmit, G., Schmidt, S., Fontijn, K., Heirman, K., Vandoorne, W., De Clercq, M., Van Acker, J., Wolff, C., Pino, M., Urrutia, R., Roberts, S.J., Vincze, L., De Batist, M., 2014. The 600 yr eruptive history of Villarrica Volcano (Chile) revealed by annually laminated lake sediments. Geological Society of America Bulletin 126, 481–498. https://doi.org/10.1130/B30798.1

Vignaux, M., Weir, G.J., 1990. A general model for Mt. Ruapehu lahars. Bulletin of Volcanology 52, 381–390. https://doi.org/10.1007/BF00302050

Voloschina, M., 2020. Eruption dynamics and frequency-magnitude relationships of explosive eruptions at Mt. Ruapehu, New Zealand over the past 1800 years : a thesis presented in partial fulfilment of the requirements for the degree of Doctor of Philosophy in Earth Science at Massey University, Palmerston North, New Zealand (Doctoral). Massey University.

Waiser, T.H., Morgan, C.L.S., Brown, D.J., Hallmark, C.T., 2007. In Situ Characterization of Soil Clay Content with Visible Near-Infrared Diffuse Reflectance Spectroscopy. Soil Science Soc of Amer J 71, 389–396. https://doi.org/10.2136/sssaj2006.0211

Walker, G.P.L., Self, S., Froggatt, P.C., 1981. The ground layer of the taupo ignimbrite: A striking example of sedimentation from a pyroclastic flow. Journal of Volcanology and Geothermal Research 10, 1–11. https://doi.org/10.1016/0377-0273(81)90051-2

Wallace, L.M., 2004. Subduction zone coupling and tectonic block rotations in the North Island, New Zealand. J. Geophys. Res. 109, B12406. https://doi.org/10.1029/2004JB003241

Wallace, N.R., Baird, C.W., 1968. Explosions Generated Waves 1965 Mono Lake Test Series. Oceanographic Services, Inc., Santa Barbara, CA.

Walsh, B., Lormand, C., Procter, J., Williams-Jones, G., 2023. Characterizing the evolution of mass flow properties and dynamics through analysis of seismic signals: insights from the 18 March 2007 Mt. Ruapehu lake-breakout lahar. Nat. Hazards Earth Syst. Sci. 23, 1029–1044. https://doi.org/10.5194/nhess-23-1029-2023

Ward, J.H., 1963. Hierarchical Grouping to Optimize an Objective Function. Journal of the American Statistical Association 58, 236–244. https://doi.org/10.1080/01621459.1963.10500845
Webby, P.M., 1999. Mt Ruapehu Crater Lake lahar hazard.
Wentworth, C.K., 1922. A Scale of Grade and Class Terms for Clastic Sediments. The Journal of Geology 30, 377–392.
Whalin, R.W., Pace, C.E., Lane, W.F., 1970. Mono Lake explosion test series, 1965 analysis of surface wave and wave runup data (No. N-70-12). U.S. Army Engineer Waterways Experiment Station, Vicksburg, MI.
Whitehead, M.G., Bebbington, M.S., Procter, J.N., Irwin, M.E., Viskovic, G.P.D., 2022. An initial assessment of short-term eruption forecasting options in New Zealand. New Zealand Journal of Geology and Geophysics 1–18. https://doi.org/10.1080/00288306.2022.2080236
Williams, D.B., Ramsey, M.S., 2024. Infrared spectroscopy of volcanoes: from laboratory to orbital scale. Front. Earth Sci. 12, 1308103. https://doi.org/10.3389/feart.2024.1308103
Wilson, C.J.N., Gravley, D.M., Leonard, G.S., Rowland, J.V., 2009. Volcanism in the central Taupo volcanic zone, New Zealand: tempo, styles and controls, in: Thordarson, T., Self, S., Larsen, G., Rowland, S.K., Hoskuldsson, A. (Eds.), Studies in Volcanology: The Legacy of George Walker. The Geological Society of London on behalf of The International Association of Volcanology and Chemistry of the Earth's Interior, pp. 225–247. https://doi.org/10.1144/IAVCEI002.12
Wilson, C.J.N., Walker, G.P.L., 1985. The Taupo eruption, New Zealand I. General aspects. Phil. Trans. R. Soc. Lond. A 314, 199–228. https://doi.org/10.1098/rsta.1985.0019
Yamamoto, T., Nakamura, Y., Glicken, H., 1999. Pyroclastic density current from the 1888 phreatic eruption of Bandai volcano, NE Japan. Journal of Volcanology and Geothermal Research 90, 191–207. https://doi.org/10.1016/S0377-0273(99)00025-6
Zemeny, A., Procter, J.N., Németh, K., Zellmer, G.F., Zernack, A.V., Cronin, S.J., 2021. Elucidating stratovolcano construction from volcaniclastic mass-flow deposits: The medial ring-plain of Taranaki Volcano, New Zealand. Sedimentology 68, 2422–2449. https://doi.org/10.1111/sed.12857
Zeng, R., Rossiter, D.G., Zhao, Y.G., Li, D.C., Liu, F., Zheng, G.H., Zhang, G.L., 2023. The choice of spectral similarity algorithms influences suspected soil sample provenance. Forensic Science International 347, 111688. https://doi.org/10.1016/j.forsciint.2023.111688
Zernack, A.V., 2021. Volcanic Debris-Avalanche Deposits in the Context of Volcaniclastic Ring Plain Successions—A Case Study from Mt. Taranaki, in: Roverato, M., Dufresne, A., Procter, J.N. (Eds.), Volcanic Debris Avalanches, Advances in Volcanology. Springer International Publishing, Cham, pp. 211–254. https://doi.org/10.1007/978-3-030-57411-6_9
Zernack, A.V., Procter, J.N., Cronin, S.J., 2009. Sedimentary signatures of cyclic growth and destruction of stratovolcanoes: A case study from Mt. Taranaki, New Zealand. Sedimentary Geology 220, 288–305. https://doi.org/10.1016/j.sedgeo.2009.04.024
Zhang, G., Wasyliuk, K., Pan, Y., 2001. THE CHARACTERIZATION AND QUANTITATIVE ANALYSIS OF CLAY MINERALS IN THE ATHABASCA BASIN, SASKATCHEWAN: APPLICATION OF SHORTWAVE INFRARED REFLECTANCE SPECTROSCOPY. The Canadian Mineralogist 39, 1347–1363. https://doi.org/10.2113/gscanmin.39.5.1347

Appendix A

Appendix A1 Field sites, sample locations, and stratigraphic columns (.pptx)

Appendix A2 Weight size categories (.csv)

Appendix A3 Gradistat sample analysis results (.csv)

Appendix B

Appendix B1 XRD analysis spectra (.rasx)

Appendix B2 Individual sample SWIR spectra and sample matrix spectral angle similarity table (.csv)

Appendix B3 Leachate analysis results (.xlsx)

Appendix C

Appendix C1 Example Basilisk code (.c)

Appendix D

Appendix D1 Lahar events table (.xlsx)

Appendix E

Appendix E1 Statement of Contribution forms (.pdf)